



HAL
open science

**Contribution à l'étude de la propagation et de
l'atténuation des ondes guidées dans les laminés
composites anisotropes constitués de matériaux
composites viscoélastiques : Application à des pièces de
nacelle de l'A380**

Shuanglin Guo

► **To cite this version:**

Shuanglin Guo. Contribution à l'étude de la propagation et de l'atténuation des ondes guidées dans les laminés composites anisotropes constitués de matériaux composites viscoélastiques : Application à des pièces de nacelle de l'A380. Mécanique des matériaux [physics.class-ph]. HESAM Université, 2021. Français. NNT : 2021HESAE079 . tel-03709032

HAL Id: tel-03709032

<https://pastel.hal.science/tel-03709032v1>

Submitted on 29 Jun 2022

HAL is a multi-disciplinary open access archive for the deposit and dissemination of scientific research documents, whether they are published or not. The documents may come from teaching and research institutions in France or abroad, or from public or private research centers.

L'archive ouverte pluridisciplinaire **HAL**, est destinée au dépôt et à la diffusion de documents scientifiques de niveau recherche, publiés ou non, émanant des établissements d'enseignement et de recherche français ou étrangers, des laboratoires publics ou privés.

ÉCOLE DOCTORALE SCIENCES ET MÉTIERS DE L'INGÉNIEUR
Laboratoire de PIMM - Campus de Paris

THÈSE

présentée par : **Shuanglin GUO**
soutenue le : **9 Décembre 2021**

pour obtenir le grade de : **Docteur d'HESAM Université**

préparée à : **École Nationale Supérieure d'Arts et Métiers**
Spécialité : **Mécanique et Matériaux**

Contribution to the study of guided waves propagation and attenuation in anisotropic composite laminates made up of viscoelastic composite materials : Application to A380 mounted nacelle parts

THÈSE dirigée par :
Prof. MECHBAL Nazih

et co-encadrée par :
Dr. REBILLAT Marc

Jury

M. Alain LHEMERY

Mme. Zahra SHARIF KHODAEI

M. Kerem EGE

M. Zhenghua QIAN

M. Marc REBILLAT

M. Nazih MECHBAL

Directeur de Recherche, CEA

Associate Professor, Imperial College, London

Maitre de conférences (HDR), INSA Lyon

Professor, Nanjing University of Aeronautics & Astronautics

Maitre de Conférences, ENSAM

Professeur, ENSAM

Président

Rapporteur

Rapporteur

Examineur

Examineur

Examineur

**T
H
È
S
E**

In dedication to my parents. If without their constant support, this thesis was not possible.

Acknowledgements

I would like to thank my principal supervisor Prof. Nazih Mechbal for your kind guidance during the past four years. Your strict supervision expedited me so much for doing research with critical thinking and acute insight. For every manuscript I wrote, you can always give me the detailed comments and constructive revisions, which persistently improved my scientific writing skills. You also processed a lot of administrative affairs during the course of my Ph.D. study, like annually organizing the CSID audition, frequently communicating with the journal editor who was responsible for my manuscript, and managing the evaluation for my funding. Your patience to process these affairs liberated me that I can whole-heartedly concentrate on my research and complete my thesis smoothly.

I would also like to appreciate my co-supervisor Dr. Marc Rébillat. We had a wonderful experience during my Ph.D. journey. For each time when I entered in a dilemma in my research, I always turned to find help from you because you can always give me meaningful suggestions. Each discussion with you is nutritive and I enjoyed it. You also taught me a lot of scientific skills, for example, teaching me how to read scientific paper and make academic presentation, training my experimental skills, improving my programming ability. You still financially supported me to attend international conference, which greatly broadened my horizon. Under your supervision for these four years, I have grown into an independent researcher that I can independently discover, study and analyze various problems in different angles. Thank you very much.

In the past four years, I have received many supports, help and guidance from the PIMM laboratory to conduct my research works. At this point, I would like to sincerely express my thanks to everyone in the laboratory, especially for Nassim Benbara, Xixi Li, Shaobo Yang, William Briand, Emmanuel Lizé, Erika Bayona, Quentin Jacquemin, Eric Monteiro, Mikhail Guskov, Christine Schrive, who helped me a lot during the course of completing this thesis.

ACKNOWLEDGEMENTS

My research works were funded by the China Scholarship Council (CSC). My special appreciation goes to CSC.

Finally, I would like to thank my family. The achievement of this thesis would not have been possible if without your support and understanding.

ACKNOWLEDGEMENTS

ACKNOWLEDGEMENTS

Résumé

Les plaques composites anisotropes constituées de matériaux composites viscoélastiques sont de plus en plus utilisées dans l'industrie aéronautique et les stratégies de surveillance de la santé des structures (SHM) basées sur des ondes guidées apparaissent comme un outil très prometteur pour surveiller leur état de santé. Dans ce contexte, cette thèse est dédiée à l'étude de la propagation et de l'atténuation des ondes guidées dans de telles plaques composites.

Les équations fondamentales de la théorie de l'élasticité tridimensionnelle (3D) sont d'abord passées en revue. Divers matériaux composites sont introduits en mettant l'accent sur les caractéristiques de leurs matrices de rigidité. L'approche par superposition d'ondes partielles (PWSA) basée sur l'élasticité 3D est utilisée pour dériver les équations de dispersion des ondes guidées se propageant dans une plaque composite monocouche.

Dans une plaque composite multi-couches, la PWSA est étendue à la méthode de la matrice de transfert (TMM) qui relie les variables de champ des couches voisines (déplacement et contrainte) à travers les matrices des couches locales. Pour un stratifié composite arbitrairement orienté, un problème d'incompatibilité de matrice est rencontré en raison de l'anisotropie des matériaux composites, et une stratégie originale de matrice hybride (HMS) est proposée pour résoudre ce problème en refondant les matrices locales des couches incompatibles en une formulation hybride garantissant le bon déroulement de la TMM. Cette méthodologie est validée dans une plaque quasi-isotrope et une plaque métallique-composite.

Pour améliorer l'efficacité de calcul de la méthode de la matrice globale (GMM), une approche GMM optimisée est développée qui introduit une condition de symétrie dans la matrice globale pour réduire son ordre et tire parti des techniques de calcul matriciel et parallèle pour promouvoir les performances de calcul. La GMM optimisée est appliquée à une plaque composite aérospatiale comportant

400 couches, ce qui est le plus grand nombre de couches signalé à ce jour, pour calculer ses courbes de dispersion. En raison de la complexité de cette structure, le diagramme de dispersion subit un fort effet de “*veering*” qui correspond à des courbes de dispersions de même symétrie s’approchant l’une de l’autre mais ne se croisant jamais. L’analyse de la forme des modes et la tomographie des valeurs MAC sont utilisées pour analyser cet effet. Les résultats révèlent que les courbes modales s’approchant l’une de l’autre échangent leurs formes modales rapidement dans ces régions.

Il est en outre démontré que les équations de dispersion construites avec PWSA pour une plaque monocouche et avec les approches TMM et GMM pour un système de plaques multicouches possèdent une propriété de dichotomie dans le cas de matériaux élastiques purs. Cette propriété indique que ces équations à valeurs complexes a priori deviennent des équations à valeurs réelles ou imaginaires pures, en fonction du comportement de certains paramètres intermédiaires. Ceci est extrêmement utile pour surmonter les instabilités numériques rencontrées lors du processus de résolution d’équations. Avec la propriété de dichotomie, le problème des grand fd de l’approche TMM qui résulte de la disparition de la partie utile entre les parties réelle et imaginaire des équations de dispersion en raison du mauvais conditionnement de la matrice de transfert de monodromie est résolu.

Les matériaux composites possèdent une viscoélasticité inhérente qui produit des amplitudes d’ondes guidées qui s’atténuent avec la distance de propagation. Pour prédire les coefficients d’atténuation des stratifiés composites anisotropes, trois modèles d’amortissement (modèles hystérétique, Kelvin-Voigt et Biot) sont intégrés dans l’approche GMM pour former l’approche GMM amortie (dGMM). Le coefficient d’atténuation est calculé à partir des solutions d’équations de dispersion complexes construites avec la dGMM. Deux composants aéronautiques de l’avion A380, tous deux montés ou non montés sur l’avion, sont utilisés pour valider la dGMM développée. La première est une structure de capot de soufflante ayant des propriétés quasi-isotropes et la seconde une structure interne fixe étant une plaque sandwich. Les analyses théoriques et expérimentales révèlent que les coefficients d’atténuation des deux structures ont des propriétés anisotropes en termes de distribution spatiale malgré leur empilement quasi-isotrope. L’existence de contraintes dans les structures montées peut grandement modifier les propriétés d’atténuation par rapport aux structures non-montées. Dans les deux structures, le mode A0 subit beaucoup plus d’atténuation que le mode S0, ce qui indique que la sélection du mode S0 pour le SHM de structures aéronautiques similaires est plus souhaitable dans la gamme de fréquences sélectionnée.

Les travaux menés dans la thèse fournissent ainsi des inspirations pour déployer de manière optimale des réseaux de capteurs en considérant l'influence de l'atténuation des ondes et pour améliorer les méthodes de localisation des dommages qui tirent parti de l'analyse fréquence-nombre d'onde.

Mots-clés : Surveillance de la santé structurelle, Ondes guidées, Equations et courbes de dispersion, Stratifiés composites anisotropes, Approche par superposition d'ondes partielles, Méthodes de transfert et de matrice globale, Propriété de dichotomie, Modèles d'amortissement viscoélastique, Composant de nacelle A380.

RESUME

Abstract

Anisotropic composite plates made up of viscoelastic composite materials are increasingly used in aeronautic industry and structural health monitoring (SHM) strategies based on guided waves appear as a very promising tool to monitor their health state. In that context, this thesis is dedicated to the study of guided waves propagation and attenuation in such composite plates.

The fundamental equations of three-dimensional (3D) elasticity theory are first reviewed. Various composite materials are introduced with an emphasis on their characteristics of stiffness matrix rotation. The partial wave superposition approach (PWSA) based on 3D elasticity is used to derive the dispersion equations of guided waves propagating in a single layer composite lamina.

In a multi-layered composite plate system, the PWSA is extended to the transfer matrix method (TMM) which connects the neighboring layers' field variables (displacement and stress) through the local lamina matrices. For an arbitrarily oriented composite laminate, the matrix incompatibility issue of TMM is encountered due to the anisotropy of composite materials, and an original hybrid matrix strategy (HMS) is proposed to address this issue that recasts the incompatible layers' local lamina matrices into a hybrid form to guarantee the successful proceeding of the transferring process of TMM. The HMS is validated in a quasi-isotropic plate and a metallic-composite plate.

To improve the computational efficiency of the global matrix method (GMM), an optimized GMM is developed that introduces the symmetry condition into the global matrix to reduce matrix order and takes advantage of sparse matrix and parallel computing techniques to promote computing performance. The optimized GMM is applied to an aerospace composite plate having 400 layers, which is the largest number of layers reported so far, for computing its phase velocity dispersion curves. Due to the complexity of this structure, the dispersion diagram experiences heavy veering effect which is the phenomenon of dispersion curves belong to the same symmetry mutually closing but never crossing in

a small region. Mode shape analysis and MAC value tomography are used to analyze veering effect. Results reveal that the closing modal curves exchange their mode shapes rapidly in these regions.

It is furthermore demonstrated that dispersion equations built with PWSA for a single layer plate and with TMM and GMM for a multi-layered plate system possess a dichotomy property in the case of pure elastic materials. This property states that these a priori complex-valued equations collapse to pure real or imaginary valued equations, depending on the behavior of some intermediate parameters. This is extremely helpful for overcoming numerical instabilities encountered during the equation solving process. With the dichotomy property, the *large fd problem* of TMM results from the vanishing of effective part between the real and imaginary parts of dispersion equations due to the poor conditioning of the monodromy transfer matrix.

Composite materials possess inherent viscoelasticity which produces guided wave amplitudes attenuating with propagation distance. To predict attenuation coefficients of anisotropic composite laminates, three damping models (Hysteretic, Kelvin-Voigt and Biot models) are integrated into GMM to form the damped GMM framework (dGMM). Attenuation coefficient is computed from the solutions of complex dispersion equations built with dGMM. Two aeronautic components of A380 plane both which are either mounted or unmounted on the plane are employed to validate the developed dGMM. The first one is a fan cowl structure having quasi-isotropic property and the second one an inner fixed structure being a sandwich plate. Theoretical and experimental analysis reveal that the attenuation coefficients of both structures hold anisotropic property in terms of spatial distribution despite the quasi-isotropic stacking layups of them. The existence of stress in the mounted case can greatly change the property of attenuation as compared to the unmounted case. In both structures, A0 mode undergoes much attenuation than S0 mode, which gives the guidance that selecting S0 mode for SHM of similar aeronautic structures is more desired in the selected frequency range.

The works conducted in the thesis provides inspirations for optimally deploying sensor networks by considering the influence of wave attenuation and for improving damage localization methods that takes advantage of frequency-wavenumber analysis.

Keywords : Structural health monitoring, Guided waves, Dispersion equations and curves, Anisotropic composite laminates, Partial wave superposition approach, Transfer and global matrix methods, Dichotomy property, Viscoelastic damping models, Component of A380 nacelle.

Contents

Acknowledgements	5
Résumé	9
Abstract	13
List of tables	24
List of figures	31
List of acronyms	34
1 Introduction	35
1.1 Background of structural health monitoring	35
1.2 The history of elastic waves in homogeneous isotropic media	38
1.3 Modeling methods of guided waves in composite structures	39
1.3.1 The origin of matrix-based methods for modeling guided waves propagation in layered structure	41
1.3.2 The modern matrix-based methods	42
1.3.3 Finite element methods	44
1.3.4 Other methods	45
1.4 Organization of the thesis	46

2	Fundamentals of wave propagation in solids	49
2.1	Basic equations of 3D elasticity	49
2.1.1	Stress-strain relation	49
2.1.2	Strain-displacement relation	51
2.1.3	Elastodynamic equations of motion	51
2.2	Stiffness matrix types of various materials	51
2.2.1	Triclinic material	51
2.2.2	Monoclinic material	52
2.2.3	Orthotropic material	52
2.2.4	Transversely isotropic material	53
2.2.5	Isotropic material	53
2.3	Stiffness matrix rotation	54
2.3.1	Voigt notation and tensor rotation rule	54
2.3.2	Example of stiffness matrix rotation	56
2.3.3	Characteristics of stiffness matrix rotation	57
2.4	Expanded elastodynamic equations of motion of triclinic material	58
2.5	Bulk wave	60
2.5.1	Derivation of bulk wave	60
2.5.2	Numerical example	62
2.6	Conclusion	63
3	Guided waves propagation in a single-layered plate	65
3.1	Wave propagation model of a single layer plate	65
3.2	Dispersion equations of coupled Lamb and SH waves in triclinic material	67
3.2.1	Christoffel equation	67
3.2.2	Displacement and stress fields	68

CONTENTS

3.2.3	Dispersion equations	69
3.2.4	Mode shape	71
3.3	Dispersion equations of coupled Lamb and SH waves in monoclinic material	72
3.3.1	Christoffel equation	72
3.3.2	Displacement and stress fields	73
3.3.3	Dispersion equations	74
3.4	Dispersion equations of decoupled Lamb and SH waves in orthotropic material	76
3.4.1	Christoffel equation	76
3.4.2	Displacement and stress fields of Lamb wave	77
3.4.3	Dispersion equations of Lamb wave	78
3.4.4	Displacement and stress fields of SH wave	79
3.4.5	Dispersion relation of SH wave	79
3.5	Derivation of the classical Rayleigh-Lamb equation via PWSA	81
3.6	Conclusion	82
4	Guided wave propagation in a multi-layered plate: transfer matrix method	83
4.1	The multi-layered composite plate model	83
4.2	Local lamina matrices along the wave propagation direction	85
4.2.1	Local lamina matrices of coupled Lamb and SH waves	85
4.2.2	Local lamina matrices of pure Lamb waves	88
4.2.3	Local lamina matrices of pure SH waves	89
4.3	Transfer matrix method	90
4.3.1	Local transfer matrix in a lamina	90
4.3.2	The monodromy transfer matrix of the laminate system	91
4.3.3	Dispersion equation	92
4.3.4	Wave mode shapes	96

CONTENTS

4.4	Hybrid matrix strategy	96
4.4.1	The incompatibility issue of matrix dimension of the local transfer matrices	96
4.4.2	Hybrid local lamina matrices of pure Lamb and SH waves	98
4.5	Four classes of composite laminates	102
4.6	Numerical example on a cross-ply laminate	103
4.6.1	The pure Lamb and SH waves when $\theta = 0^\circ$	103
4.6.2	The coupled Lamb and SH waves when $\theta = 45^\circ$	104
4.6.3	Displacement and stress mode shapes	105
4.7	Numerical example on a quasi-isotropic laminate	107
4.7.1	The hybrid Lamb and SH waves when $\theta = 0^\circ, 45^\circ$ or 90°	108
4.7.2	The coupled Lamb and SH waves when $\theta = 30^\circ$	109
4.7.3	Illustration of Pant's pseudo correction measure	112
4.8	Numerical example on a metallic-composite laminate	112
4.8.1	The pure Lamb and SH waves when $\theta = 0^\circ$ or 90°	113
4.8.2	The hybrid Lamb and SH waves when $\theta = 20^\circ, 45^\circ$ or 70°	116
4.8.3	Superiority of HMS over Pant's pseudo correction measure	117
4.9	Conclusion	117
5	Guided wave propagation in a multi-layered plate: global matrix method	119
5.1	The standard global matrix method	119
5.2	Benchmark test of GMM through the dataset Open Guided Waves	122
5.2.1	Dispersion curves comparison between GMM and TMM	123
5.2.2	Dispersion curves comparison between GMM and experimental data	124
5.2.3	Dispersion curves comparison between GMM and ESM	124
5.3	The optimized global matrix method	126
5.3.1	The symmetry condition in the global matrix	126

5.3.2	Sparsity of global matrix	129
5.3.3	Parallelization of GMM	129
5.4	Application of the optimized GMM to an aerospace composite laminate with 400 layers	130
5.4.1	Dispersion curves	130
5.4.2	Study the veering effect to avoid mode jumping problem	131
5.4.2.1	Displacement mode shape analysis	132
5.4.2.2	MAC value tomography of displacement mode shapes	134
5.4.2.3	Stress mode shape analysis	135
5.4.3	Computational efficiency	135
5.5	Conclusion	137
6	Dichotomy property of dispersion equation of guided waves propagating in anisotropic composite plates	139
6.1	Problem statement	139
6.2	Properties of Christoffel equation of monoclinic materials	142
6.2.1	Property of the polynomial discriminant Δ	142
6.2.2	Illustration of the property of polynomial discriminant Δ	143
6.2.3	Properties of intermediate parameters	144
6.3	Dichotomy property of dispersion equation of a single layer plate	146
6.3.1	Dichotomy property of dispersion equation when sweeping ξ	147
6.3.1.1	Case 1: all $\alpha_1, \alpha_3, \alpha_5$ are real numbers.	147
6.3.1.2	Case 2: only α_1 is a purely imaginary number.	148
6.3.1.3	Case 3: only α_1, α_3 are purely imaginary numbers.	148
6.3.1.4	Case 4: all $\alpha_1, \alpha_3, \alpha_5$ are purely imaginary numbers.	149
6.3.1.5	Numerical validation of the dichotomy property when sweeping ξ	149
6.3.2	Dichotomy property of dispersion equation when sweeping v	154

CONTENTS

6.3.3	Dichotomy property of dispersion equation in $f - \xi$ and $f - v$ domains	156
6.3.4	Dichotomy property of evanescent waves	157
6.4	Dichotomy property of dispersion equation of a multi-layered plate	158
6.5	Overcoming common numerical issues using dichotomy property	160
6.5.1	Overcoming numerical instability of the phase change method	160
6.5.2	Overcoming numerical instability of TMM	160
6.6	Exploring the <i>large fd problem</i> of TMM using dichotomy property	163
6.7	Discussion	165
6.7.1	Comparison of computational efficiencies of two sweeping schemes	165
6.7.2	Generalization of dichotomy property in other material classes	166
6.8	Conclusion	167
7	Prediction of frequency and spatially dependent attenuation of guided waves propagating in anisotropic viscoelastic composite laminates	169
7.1	Background of guided waves attenuation	170
7.2	Wave propagation theory in the viscoelastic composite laminate	172
7.2.1	Viscoelastic damping models of composite materials	173
7.2.2	Damped global matrix method	175
7.2.3	Numerical algorithm of solving the complex DE	178
7.3	Data-driven structural parameters estimation	180
7.3.1	Identification of attenuation coefficient	181
7.3.2	Estimation of viscoelastic loss factors	182
7.3.3	Overview of the attenuation prediction method	183
7.4	Case study on an unmounted and mounted FCS of A380 plane	184
7.4.1	Experimental setup	184
7.4.2	Dispersion curve identification for energy velocity and attenuation coefficient	187

CONTENTS

7.4.2.1	Energy velocity and attenuation coefficient identification at 100 kHz	187
7.4.2.2	Identified dispersion curves of energy velocity and attenuation coefficient	190
7.4.3	Estimation of viscoelastic material properties of the unmounted FCS	191
7.4.4	Attenuation coefficient prediction for the unmounted FCS	193
7.5	Case study on an unmounted and mounted IFS of A380 plane	195
7.5.1	Experimental setup	195
7.5.2	Dispersion curve identification for energy velocity and attenuation coefficient	197
7.5.2.1	Comparison of energy velocity and attenuation coefficient at 100 kHz between the mounted and unmounted IFS	197
7.5.2.2	Identified dispersion curves of energy velocity and attenuation coefficient	199
7.5.3	Estimation of viscoelastic material properties of the unmounted IFS	200
7.5.4	Prediction of dispersion curves in various forms for the unmounted IFS	202
7.6	Discussion	207
7.7	Conclusion	207
8	General conclusions and perspectives	209
8.1	General conclusions	209
8.2	Perspectives	212
8.3	Publications related to the thesis	215
	Bibliography	217
	List of appendix	228
A	Proof of the properties of the intermediate parameters in Section 6.2.3	229
B	Introduction (Français/French)	231
B.1	Contexte général de la thèse	231

CONTENTS

B.2	Etat de l'art	233
B.2.1	Les méthodes matricielles	233
B.2.1.1	Méthode de la matrice de transfert	234
B.2.1.2	Méthode matricielle globale	235
B.2.1.3	Méthode de la matrice de rigidité	236
B.2.2	Méthodes basées sur les éléments finis	236
B.2.3	Autres méthodes	237
B.2.4	Atténuation des ondes guidées	238
B.3	Apport de la thèse	239
B.3.1	Chapitre 2 - Aspects fondamentaux de la propagation des ondes dans les solides	240
B.3.2	Chapitre 3 - Propagation des ondes guidées dans une plaque monocouche . . .	240
B.3.3	Chapitre 4 - Propagation des ondes guidées dans une plaque multicouche : méthode de la matrice de transfert	241
B.3.4	Chapitre 5 - Propagation des ondes guidées dans une plaque multicouche : méthode matricielle globale	241
B.3.5	Chapitre 6 - Propriété de dichotomie de l'équation de dispersion des ondes guidées se propageant dans des plaques composites anisotropes	244
B.3.6	Chapitre 7 - Prédiction de l'atténuation des ondes guidées se propageant dans les stratifiés composites viscoélastiques anisotropes en fonction de la fréquence et de la direction de propagation	247
B.4	Conclusion	250

List of Tables

2.1	The characteristics of stiffness matrix rotation	58
4.1	Four classes of composite laminates and the wave type dependence on the propagation angle.	102
4.2	Material properties of a transversely isotropic lamina	103
4.3	Material properties of a carbon-fiber epoxy lamina	108
4.4	Material properties of aluminum	113
4.5	Material properties of glass fiber	113
5.1	Material properties of composite laminate of Open Guided Waves	123
5.2	The computational time of the 400-layered laminate using the optimized GMM (unit: seconds)	137
6.1	The composite materials that automatically exclude the case $\Delta > 0$	145
6.2	The composite materials that invoke the case $\Delta > 0$ in a limited phase velocity range.	145
6.3	The ranges of phase velocity v [m/s] that correspond to the four cases.	150
6.4	The presence or absence of <i>large fd problem</i> of TMM in classical references.	165
6.5	The computational time of the 50-layered plate (unit: seconds).	166
7.1	Elastic and viscoelastic material properties of composite lamina of the unmounted FCS.	184
7.2	Identified energy velocities from Figure 7.9(a). R^2 is the correlation coefficient.	188
7.3	Identified attenuation coefficient from Figure 7.9(b). R^2 is the correlation coefficient.	188

LIST OF TABLES

7.4	Elastic material properties of the carbon epoxy ply in the unmounted IFS.	195
7.5	Elastic material properties of the aluminum core layer in the unmounted IFS.	195
7.6	Viscoelastic material properties of the carbon epoxy ply and aluminum core in the unmounted IFS.	197
B.1	Caractérisation des matrices de rigidité avant et après rotation	240
B.2	Classes de stratifiés composites et la dépendance du type d'onde à l'angle de propagation.242	
B.3	Le temps de calcul du stratifié à 400 couches en utilisant le GMM optimisé (unité : secondes)	245

List of Figures

1.1	SHM procedures of aeronautic structures to prevent accidents [1].	36
1.2	Increasing usage of composite materials in aircraft structures over the past 40 years [2].	36
1.3	Picture of a nacelle [3]	37
1.4	Guided waves based SHM system [4].	37
1.5	Dispersion and directivity properties of guided waves velocity [4].	38
1.6	Elastic waves in solid media [5].	40
1.7	Symmetric and anti-symmetric mode shapes of Lamb waves [4].	40
1.8	Labeling system for multilayered plate [6].	41
1.9	SAFE model of wave propagation, (a) discretization along thickness direction, (b) three-node element and degrees of freedom of each node [7].	45
2.1	The stress state of a cubic element of a solid material.	50
2.2	The schematic diagram of a composite lamina.	54
2.3	The example of Voigt notation.	55
2.4	The schematic diagram of bulk wave propagation.	61
2.5	Elementary bulk waves.	63
3.1	Wave propagation model of a single-layered plate showing (a) boundary condition, (b) symmetric condition and (c) anti-symmetric condition.	66
3.2	The polynomial coefficients about α in Eq. (3.9).	68

LIST OF FIGURES

4.1 A three-layered composite plate model $[0/\theta/90]$. The wave propagation direction is along the fiber direction of the middle layer. 83

4.2 Guided wave propagation model in a n -layered composite laminate. 85

4.3 Pant’s pseudo correction measure to deal with the incompatibility issue [8]. 97

4.4 Barazanchy’s vector orthogonality analysis to deal with the incompatibility issue [9]. . . 98

4.5 Conceptual diagram of determining the wave type existing in the cross-ply laminate $[(0/90)_s]_2$ at wave propagation angle $\theta = 0^\circ$ 104

4.6 Dispersion curves of pure Lamb and SH waves of the cross-ply laminate when $\theta = 0^\circ$. 104

4.7 Conceptual diagram of determining the wave type existing in the cross-ply laminate $[(0/90)_s]_2$ at wave propagation angle $\theta = 45^\circ$ 105

4.8 Dispersion curves of the coupled Lamb and SH waves of the cross-ply laminate at $\theta = 45^\circ$. 105

4.9 Displacement mode shapes of the cross-ply laminate for $\theta = 0^\circ$ and 45° at $f = 400$ kHz. 106

4.10 Stress mode shapes of the cross-ply laminate for $\theta = 0^\circ$ and 45° at $f = 400$ kHz. . . . 106

4.11 Conceptual diagram of determining the wave type existing in the quasi-isotropic laminate $[0/90/+45/-45]_s$ at the wave propagation angle (a) $\theta = 0^\circ$, (b) $\theta = 30^\circ$, (c) $\theta = 45^\circ$ 110

4.12 Dispersion curves of the hybrid or coupled Lamb and SH waves of the quasi-isotropic laminate. The experimental data points are extracted from [8]. 111

4.13 Polar plot of wave velocities. The experimental data points are extracted from [8]. . . 111

4.14 Conceptual diagram of Pant’s pseudo correction to deal with the incompatibility issue of the quasi-isotropic laminate $[0/90/+45/-45]_s$ when $\theta = 0^\circ$ 112

4.15 Conceptual diagram of determining the wave type existing in the metallic-composite laminate $[Al/0/90/Al/90/0/Al]$ at the wave propagation angle (a) $\theta = 0^\circ$, (b) $\theta = 45^\circ$ and (c) $\theta = 45^\circ$ for Pant’s pseudo correction. 114

4.16 Dispersion curves of the hybrid or pure Lamb and SH waves of the metallic-composite laminate. The experimental data points are extracted from [8]. 115

4.17 Polar plot of wave velocities. The experimental data points are extracted from [8]. . . 116

LIST OF FIGURES

5.1 Dispersion curves of Open Guided Waves at the propagation angle $\theta = 0^\circ$ computed via TMM and GMM. 123

5.2 Dispersion curves of Open Guided Waves at the propagation angle $\theta = 0^\circ$ computed via GMM and ESM. 124

5.3 Polar plot of Open Guided Waves plate at frequency=260 kHz. 125

5.4 Equations of ESM to compute the effective stiffness matrix [10]. 125

5.5 A symmetric laminate showing only the upper half layers. In the SC $\zeta_{\text{bot}}^{X,lm}$ and $\zeta_{\text{mid}}^{X,lm}$, the superscript $X = s$ and a represent the symmetric and anti-symmetric condition, respectively. 127

5.6 Dispersion curves of the 400-layered aerospace laminate at $\theta = 0^\circ$ direction. 131

5.7 MAC value tomography of displacement mode shapes in the region R1 of symmetric modes. 132

5.8 Displacement mode shapes. 133

5.9 MAC value tomography of stress mode shapes in the region R1 of symmetric modes. 135

5.10 Stress mode shapes. 136

6.1 A summary of the solving strategy adopted by *Dispersion Calculator* [11]. 141

6.2 The complex-to-real strategy for solving Rayleigh-Lamb equation [12]. 142

6.3 The typical $\Delta - v$ relation showing (a) the absence of $\Delta > 0$ and (b) the presence of $\Delta > 0$ in a narrow phase velocity range. 144

6.4 Using bisection method to solve the equation $\mathcal{D}_a(v_0 = 9000, \xi) = 0$ 151

6.5 Using phase change method to solve the equation $\mathcal{D}_a(v_0 = 9000, \xi) = 0$ 152

6.6 Using bisection method to solve the equation $\mathcal{D}_a(v_0 = 5000, \xi) = 0$ 153

6.7 The schematic diagram of phase change method for case 2. 154

6.8 Using phase change method to solve the equation $\mathcal{D}_a(v_0 = 5000, \xi) = 0$ 154

6.9 Using bisection and phase change methods to solve the equation $\mathcal{D}_a(v, \xi_0 = 1750) = 0$. The small width of case 3 is caused by the degree of anisotropy. 156

LIST OF FIGURES

6.10 Dispersion curves of the monoclinic lamina. 156

6.11 Concluding figures: (a) the strategy to determine the dichotomy property of dispersion equation, (b) the computational efficiency of solving methods adapted to dichotomy property. 159

6.12 Dispersion curves propagating at 0° for the $[0]_{50}$ unidirectional laminate. 161

6.13 Phase angle curve of $\mathcal{D}_G(v, \xi_0 = 3000) = 0$ for the $[0]_{50}$ unidirectional laminate. 161

6.14 Dispersion curves in frequency-wavenumber domain propagating at 45° of the single-layered unidirectional composite plate. 162

6.15 Dichotomy property of dispersion equation at $v_0 = 1000$ m/s that invokes $\Delta > 0$ 162

6.16 Function curves of $\mathcal{D}_X(v_0, \xi) = 0$ at $v_0 = 1000$ m/s of the Open Guided Waves. 164

6.17 The condition number of matrices of the Open Guided Waves at $v_0 = 1000$ m/s for (a) the monodromy transfer matrix \mathbf{T}^{mono} and (b) the global matrix \mathbf{D}_G 164

6.18 Function curve of the symmetric modes of dispersion equation $\mathcal{D}_s(v_0, \xi)$ for a triclinic material at $v_0 = 4000$ m/s. 167

7.1 The studied aircraft nacelles of an A380 plane for (a) fan cowl structure and (b) inner fixed structure. 172

7.2 Schematical diagram of a n -layered aeronautic composite laminate. 173

7.3 The schematic diagram of the curve tracing technique. 180

7.4 The flowchart of the two-step dGMM algorithm for solving the complex DE. 181

7.5 Overview of the proposed method to predict guided waves attenuation. 184

7.6 The PZT deployments of FCS for (a) the unmounted case and (b) the mounted case on an instrumented A380 plane. 185

7.7 The experimental setup of the unmounted FCS. 186

7.8 Typical guided wave signals of the unmounted FCS at 100 kHz. 186

7.9 Example of identifying (a) energy velocity and (b) attenuation coefficient via LR method at 100 kHz for the unmounted FCS. Both figures share the same legend and α is used to give the confidence level with $100(1 - \alpha)\%$ 187

LIST OF FIGURES

7.10 Polar plot of S0 mode of (a) energy velocity [m/s] and (b) attenuation coefficient [Np/m] at 100 kHz for the unmounted FCS. Both subfigures share the same legend. 188

7.11 Bar chart to display regression results of (a) energy velocity and (b) attenuation coefficient via LR method for the mounted FCS at 100 kHz. The horizontal line represents the reference value of the unmounted FCS, and the triangles denote that the marked bars correspond to a R^2 larger than 0.7. 189

7.12 The identified dispersion curves of (a) energy velocity, (b) attenuation coefficient and (c) correlation coefficient. These subfigures relate to the S0 mode propagating at 0° direction of the unmounted FCS. 191

7.13 Comparison between the computed and experimentally identified dispersion curves of (a) energy velocity and (b) attenuation coefficient for the unmounted FCS at $\theta = 0^\circ$. . . 192

7.14 For the unmounted FCS, HR model's prediction of (a) dispersion curve of phase velocity at $\theta = 180^\circ$, (b) dispersion curve of attenuation coefficient at $\theta = 180^\circ$, (c) polar plot of phase velocity [m/s] at $f = 500$ kHz, (d) polar plot of attenuation coefficient [Np/m] at $f = 500$ kHz. The open circles in the four subfigures are the solutions computed by SAFE method. 194

7.15 For the unmounted FCS, surface plot of phase velocity (left) and attenuation coefficient (right): (a) and (b) S0 mode, (c) and (d) A0 mode, (e) and (f) SH0 mode. The inner and outer surfaces in subfigures (b)(d)(f) correspond to HR and KV models, respectively. 196

7.16 The transducers layout of IFS for (a) the unmounted case and (b) the mounted case on an instrumented A380 plane. 197

7.17 Comparison between the mounted and unmounted IFS for (a) energy velocity and (b) attenuation coefficient at 100 kHz. In the two subfigures, the bars relate to the left y-axis and the lines correlate to the right y-axis. 198

7.18 Polar plot of S0 mode energy velocity [km/s] in the mounted IFS at 100 kHz. The contour of dGMM prediction 1 and dGMM prediction 2 are computed by using the (E_1, E_2, E_3) values 1 and 2 in Table 7.4, respectively. 199

7.19 The identified S0 mode dispersion curves of (a) energy velocity and (b) attenuation coefficient for the unmounted IFS. 200

LIST OF FIGURES

7.20 Comparison between the computed and experimentally identified dispersion curves of (a) energy velocity and (b) attenuation coefficient for the unmounted IFS at $\theta = 0^\circ$ 201

7.21 The computed group velocity via the pure elastic GMM for the unmounted IFS at $\theta = 0^\circ$. 202

7.22 For the unmounted IFS, the predicted dispersion curves at $\theta = 90^\circ$ for HR+BT model (left) and KV+BT model (right): (a) and (b) 3D space of (f, k_r, k_i) , (c) and (d) projection onto (f, k_r) plane, (e) and (f) projection onto (f, k_i) plane. 204

7.23 For the unmounted IFS, HR+BT model's prediction of (a) dispersion curve of phase velocity at $\theta = 90^\circ$, (b) dispersion curve of attenuation coefficient at $\theta = 90^\circ$, (c) polar plot of phase velocity [m/s] at $f = 200$ kHz, (d) polar plot of attenuation coefficient [Np/m] at $f = 200$ kHz. 205

7.24 For the unmounted IFS, surface plot of phase velocity (left) and attenuation coefficient (right): (a) and (b) S0 mode, (c) and (d) A0 mode, (e) and (f) SH0 mode. 206

B.1 Image d'une nacelle d'Airbus A380 [3]. 232

B.2 Système d'étiquetage pour plaque multicouche [6]. 234

B.3 Modèle SAFE de propagation des ondes, (a) discrétisation dans le sens de l'épaisseur, (b) élément à trois nœuds et degrés de liberté de chaque nœud [7]. 237

B.4 Courbes de dispersion pour le cas d'étude *Open Guided Waves* pour un angle de propagation $\theta = 0^\circ$ calculées via la TMM et la GMM. 242

B.5 Courbes de dispersion des ondes guidées ouvertes à l'angle de propagation $\theta = 0^\circ$ calculées via GMM et ESM. 243

B.6 Courbes de dispersion du stratifié aérospatial à 400 couches dans la direction $\theta = 0^\circ$ 244

B.7 Formes de mode de déplacement. 244

B.8 Tomographie à valeur MAC des formes de mode de déplacement dans la région R1 des modes symétriques. 245

B.9 (a) Stratégie à adopter pour déterminer la propriété de dichotomie de l'équation de dispersion. (b) Efficacité de calcul des méthodes de résolution basées sur la propriété de dichotomie. 246

LIST OF FIGURES

B.10 Le nombre de conditionnement des matrices pour le cas Open Guided Waves à $v_0 = 1000$ m/s pour (a) la matrice de transfert de monodromie \mathbf{T}^{mono} (méthode TMM) et (b) la matrice globale \mathbf{D}_G (méthode GMM).	246
B.11 L'organigramme de l'algorithme dGMM en deux étapes pour résoudre le DE complexe.	248
B.12 Le réseau de PZT pour le FCS: (a) le cas où la structure n'est pas montée sur l'A380 et (b) le cas où la structure est montée sur un A380 instrumenté.	249
B.13 Le réseau de PZTs pour l'IFS: (a) le cas où la structure n'est pas montée sur l'A380 et (b) le cas où la structure est montée sur un A380 instrumenté.	249
B.14 Prédiction du modèle HR + BT pour l'IFS non monté: (a) courbe de dispersion de la vitesse de phase à $\theta = 90^\circ$, (b) courbe de dispersion du coefficient d'atténuation à $\theta = 90^\circ$, (c) tracé polaire de la vitesse de phase [m/s] à $f = 200$ kHz, (d) tracé polaire du coefficient d'atténuation [Np/m] à $f = 200$ kHz.	250

LIST OF FIGURES

List of acronyms

2D MRCM	<i>2D module ratio convergence method</i>
BC	<i>Boundary condition</i>
BT	<i>Biot damping model</i>
CC	<i>Continuity condition</i>
CFRP	<i>Carbon fiber reinforced polymer</i>
CPCM	<i>Corrected phase change method</i>
DEs	<i>Dispersion equations</i>
dGMM	<i>Damped global matrix method</i>
ESM	<i>Effective stiffness matrix method</i>
ESPRIT	<i>Estimation of signal parameters via rotational invariance techniques</i>
FCS	<i>Fan cowl structure</i>
FEM	<i>Finite element method</i>
GMM	<i>Global matrix method</i>
HMS	<i>Hybrid matrix strategy</i>
HOPT	<i>Higher order plate theory</i>
HR	<i>Hysteretic damping model</i>
IFS	<i>Inner fixed structure</i>
KV	<i>Kelvin-Voigt damping model</i>
L	<i>Longitudinal wave</i>
LR	<i>Linear regression method</i>
MAC	<i>Modal assurance criteria</i>
NDE	<i>Non-destructive evaluation</i>
OGW	<i>Open Guided Waves</i>
PWSA	<i>Partial wave superposition approach</i>
PZT	<i>Piezoelectric transducer</i>
SAFE	<i>Semi-analytical finite element method</i>
SC	<i>Symmetry condition</i>
SCM	<i>Spectral collocation method</i>

LIST OF FIGURES

SH	<i>Shear horizontal wave</i>
SHM	<i>Structural health monitoring</i>
SLS	<i>Standard linear solid damping model</i>
SMM	<i>Stiffness matrix method</i>
SNR	<i>Signal to noise ratio</i>
STMM	<i>Stiffness transfer matrix method</i>
SV	<i>Shear vertical wave</i>
TMM	<i>Transfer matrix method</i>
ToF	<i>Time of flight</i>
WFEM	<i>Wave finite element method</i>

Chapter 1

Introduction

1.1 Background of structural health monitoring

One of the most important issues in engineering concerns the monitoring and the early detection and localization of structural damages in order to prevent catastrophic failures. This process is referred to as structural health monitoring (SHM) and is expected to provide considerable improvements with respect to safety and maintenance costs. A SHM procedure is generally made up of five steps: damage detection, localization, classification, quantification and prognosis [1, 13]. Over half a century, modern SHM techniques have reached maturity in engineering practice, playing a significant role in evaluating the integrity and durability of engineered structures and assets [5]. These techniques are typified by radioscopy, ultrasonic scanning, shearography, dye penetrant testing, magnetic resonance imagery, laser interferometry, acoustic holography, infrared thermography and eddy-current [14, 15], leading to vast achievements in scientific and industrial areas. With efficient, continuous and automated SHM techniques it is possible to identify structural damage at an early stage so as to prevent further failure occurrence, producing huge economic and human benefit [16].

In aeronautic and aerospace industries, composite materials are increasingly used from the past decades to the future due to their high performances to other engineering materials, such as the high strength-to-weight ratio [2]. However, the complexity of damage mechanism of composite materials increases the difficulty to develop effective SHM techniques for aeronautic composite structures. Composite materials generally experience various damage types during the manufacturing and in-service process, for example delamination between layers, porosity in the matrix, impact induced matrix crack, fiber breakage, fiber-matrix debonding and fatigue caused defects [1]. All these occurred damages can

1.1. BACKGROUND OF STRUCTURAL HEALTH MONITORING

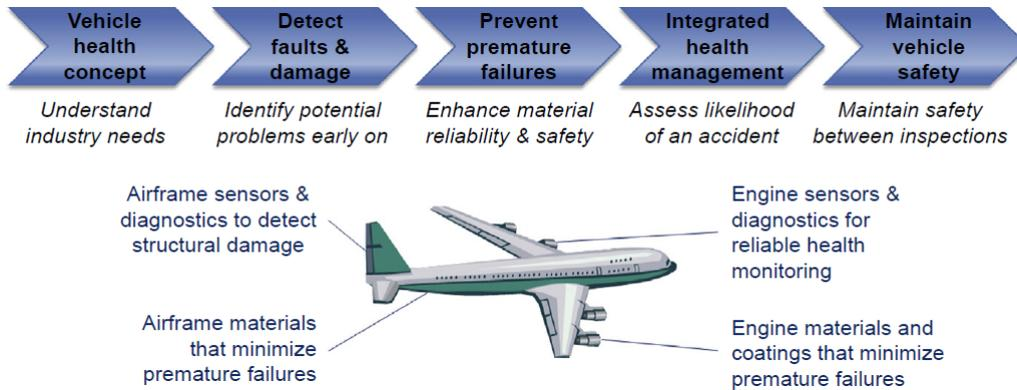


Figure 1.1 – SHM procedures of aeronautic structures to prevent accidents [1].

cause a significant loss in mechanical properties of the composite structures. Besides, different from metallic materials, the strong anisotropic nature of composite materials has introduced new challenges for developing effective inspection techniques suitable for composite materials.

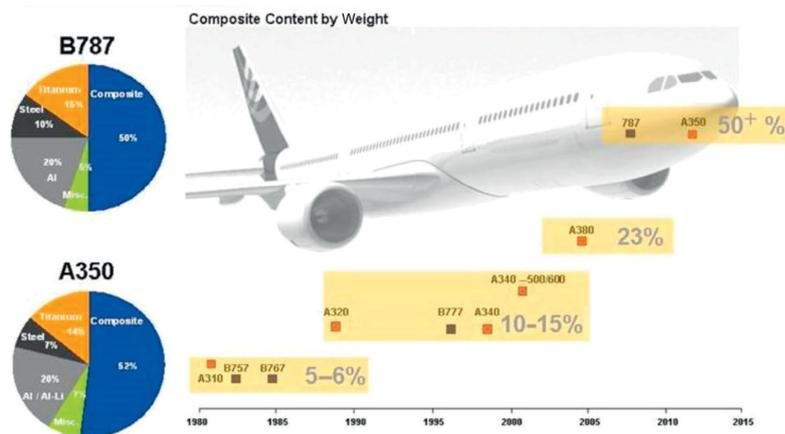


Figure 1.2 – Increasing usage of composite materials in aircraft structures over the past 40 years [2].

The nacelle of an airplane is a complex structure, which is composed of several components with different materials. Two main components are Fan Cowl and Inlet Cowl as indicated in Figure 1.3(b). The Fan Cowl structure is made of multi-layered composite materials (carbon fiber reinforced polymers) and the Inlet Cowl structure is made of sandwich materials (composite skins and aluminum alloy honeycomb core). These materials present heavy anisotropy which poses a challenge for monitoring the healthy state of nacelles. In the thesis, the anisotropic property of the Fan Cowl structure and the Inlet Cowl structure will be examined with an emphasis on the attenuation coefficient of composite materials.

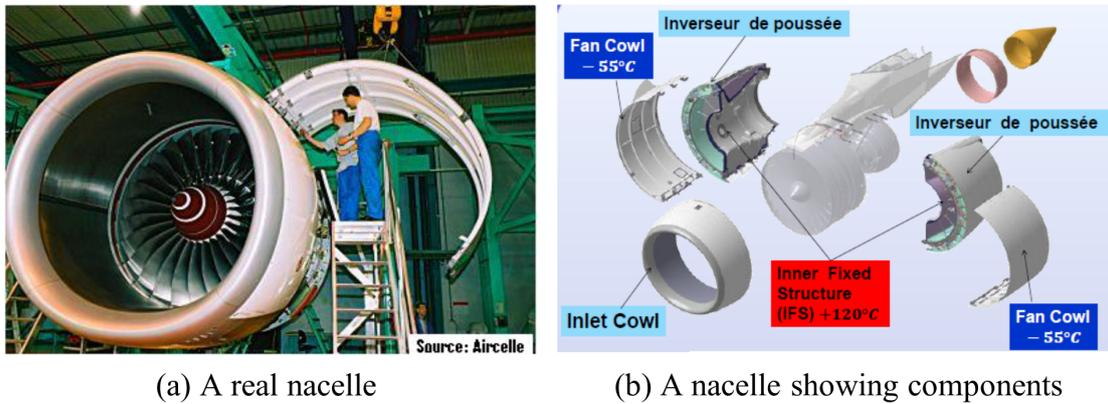


Figure 1.3 – Picture of a nacelle [3]

In the family of elastic waves, the theoretical basis of a number of wave types such as bulk waves, surface waves, interface waves, guided waves, etc., have been well-established and they have received a variety of applications in engineering problems [17]. Among all kinds of existing SHM techniques, ultrasonic guided wave strategy is particularly effective in accomplishing the task of monitoring the health and integrity state of aeronautic composite structures [18]. Guided waves possess the characteristic that they are able to propagate over broad distances and thus can cover a large area with few sensors and few testing durations. This benefit results in reduced labor and equipment to perform a test, and makes long-range inspection possible [19]. Moreover, some guided wave modes are rather sensitive to damage occurring within the inspected structure. Thus, by appropriately configuring the excitation frequency and transducer polarization, geometry, and shape, effective modes can be excited to match the application at hand, making ultrasonic wave strategies very versatile [4, 20].

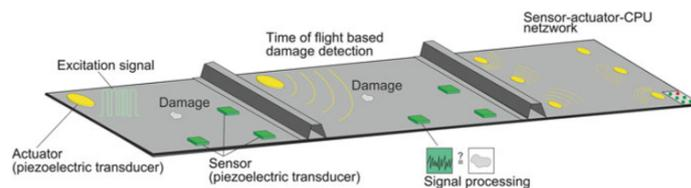


Figure 1.4 – Guided waves based SHM system [4].

When adopting guided waves as an inspection tool for aeronautic composite structures, dispersion properties of these waves are an essential aspect that should be considered carefully. More precisely, dispersion behavior describes the evolution of wave velocity with modes and frequency [21]. Due to the dispersion property, multiple wave modes can propagate simultaneously in the same frequency range

1.2. THE HISTORY OF ELASTIC WAVES IN HOMOGENEOUS ISOTROPIC MEDIA

and thus superpose to each other, a combination of several propagating modes is probably unavoidable [22]. In addition, aeronautic composite materials possess inherent anisotropy that causes directional dependence of guided waves properties, e.g. varying wave speed along different directions [4]. Both properties of guided waves complexified the analysis of the received wave signal, because wave packets change their shape with frequency and propagation direction. As a consequence, the aim of this manuscript is to increase the knowledge of guided waves propagation in composite aeronautic structures for SHM purposes.

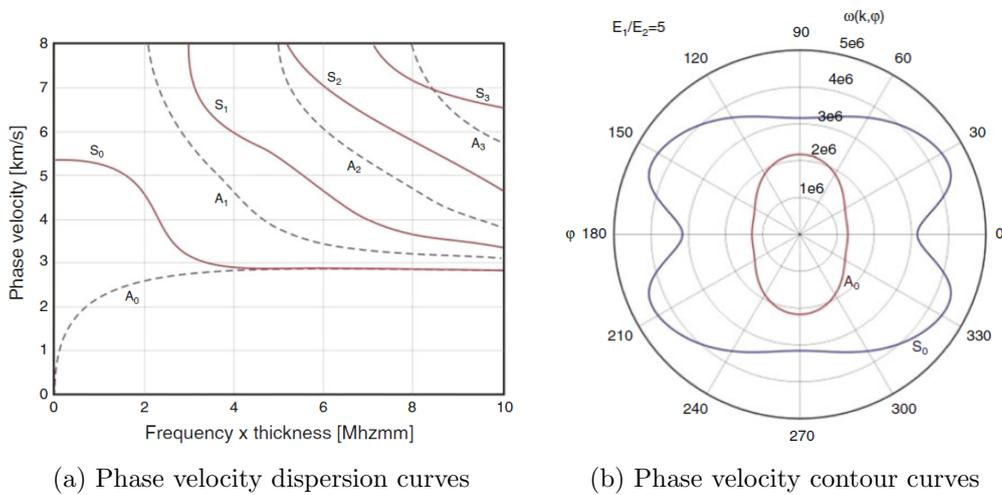


Figure 1.5 – Dispersion and directivity properties of guided waves velocity [4].

1.2 The history of elastic waves in homogeneous isotropic media

The earlier works of investigating elastic waves propagation in layered isotropic media were performed for geophysical applications in that era. There are mainly the following five wave types having the name of the corresponding discoverer.

As early as in 1885, Lord Rayleigh studied the wave propagation on the free surface of a semi-infinite solid, which is a surface wave and now named Rayleigh wave. His investigation determined the velocity of the propagating surface wave [23, 24]. In 1911, Love solved the simplest problem of wave propagation in a finite thickness layer, which was attached to a semi-space solid having a different material to the thick layer, and now this wave has been defined as the horizontal polarized SH wave due to the nature of particles' horizontally shear motion in the plane of the layer in addition to the alternative name Love wave [25]. In 1917, Horace Lamb deeply studied the classical free plate

wave problem, formed the well-known Lamb wave, and his solutions led to two types of wave modes including symmetric (longitudinal) and anti-symmetric (transverse) ones but they are coupled to each other during propagation. One important characteristic of Lamb waves is the dispersion, i.e. phase velocity of a specific mode varies with frequency [26]. Lamb's pioneering research, at present, laid the foundation of non-destructive evaluation (NDE) based on Lamb waves techniques [19]. In 1924, Stoneley wave was discovered by Robert Stoneley who explored the wave behavior propagation along the interface of two solid semi-space [27]. In 1947, when Scholte studied the Stoneley's problem, he replaced one solid medium with water and afterwards discovered a new wave type, now named Scholte wave, which possesses the property of a lower speed than the bulk wave speeds of both the solid and the water. Scholte's work mainly focused on the wave propagation without energy leaking into neighboring solids but later works by Pilant in 1979 completed the works of wave leaking energy during its propagation [28].

The above introduced works mainly dedicated to the class of isotropic media. In these works, the Helmholtz decomposition method is widely used to study the corresponding wave propagation problem that decouples the equations of motion into two separate wave equations governing two potential [29]. However, in anisotropic media especially for composite materials, the **partial wave superposition approach** based on the linear 3D elasticity theory becomes the prevalent way since it demonstrates closer physical relations between guided and bulk waves, which are further extended to a class of matrix-based methods. In the thesis, partial wave superposition approach will be particularly adopted to study guided waves propagation in a single-layered composite lamina.

1.3 Modeling methods of guided waves in composite structures

Accurately and efficiently computing dispersion curves of guided waves is mandatory to design a guided wave-based SHM system of aeronautic composite structures. It is the basis of selecting appropriate excitation frequency and designing the optimal piezoelectric transducer (PZT) network (position and size of the PZT elements) [30, 31]. However, strong anisotropy and multiple layers stacking of composite laminates complicate the theory of guided wave propagation in these structures, thus the conventional single-layered isotropic model, i.e. Rayleigh-Lamb equation [26], is no longer applicable to composite laminates. In the past two decades, multifarious methods have been developed to realize this purpose. For anisotropic material its dispersion equations are efficiently built, and the

1.3. MODELING METHODS OF GUIDED WAVES IN COMPOSITE STRUCTURES

Wave type	Definition and characteristics	Graphic description
<i>Longitudinal wave</i>	Travelling in a medium as a series of alternate compressions and rarefactions, a longitudinal wave vibrates particles back and forth in the direction of wave propagation.	
<i>Shear wave</i>	Also termed a <i>transverse wave</i> , a shear wave is generated under vibration of particles perpendicular to the direction of wave propagation.	
<i>Rayleigh wave</i>	Also defined as a <i>surface wave</i> , a Rayleigh wave exists along the free surface of a semi-infinite (or very thick) solid, decaying exponentially in displacement magnitude with distance from the surface.	
Wave type	Definition and characteristics	Graphic description
<i>Lamb wave</i>	Also known as a <i>plate wave</i> , a Lamb wave exists in a thin plate-like medium, guided by the free upper and lower surfaces. Infinite wave modes are available in a finite body, and their propagation characteristics vary with entry angle, frequency and structural geometry.	
<i>Stonely wave</i>	A Stonely wave is a kind of wave existing at the interface between two media or in the neighbourhood of a free surface.	
<i>Creep wave</i>	Also called a <i>head wave</i> , a creep wave is generated by refraction of a longitudinal wave from a boundary with the same propagation velocity. It has similar behaviour to a longitudinal wave.	

Figure 1.6 – Elastic waves in solid media [5].

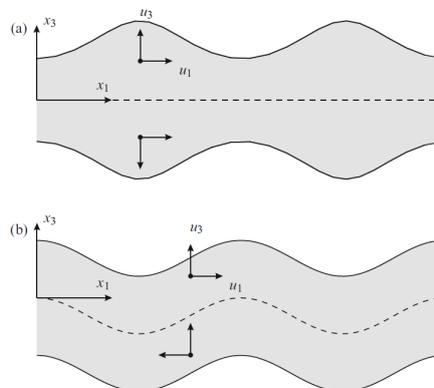


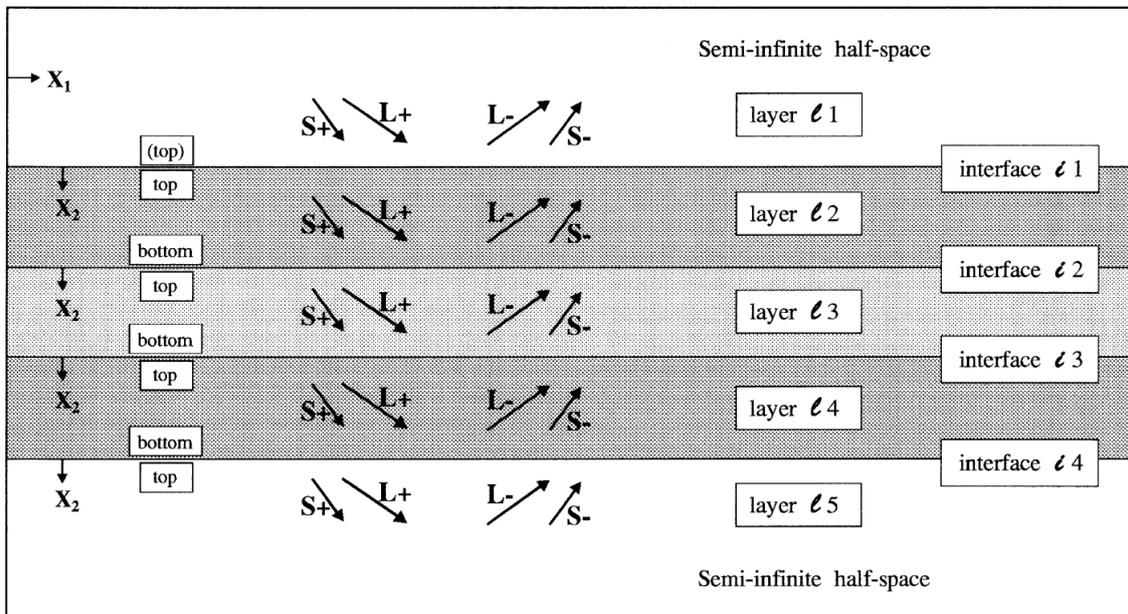
Figure 1.7 – Symmetric and anti-symmetric mode shapes of Lamb waves [4].

1.3. MODELING METHODS OF GUIDED WAVES IN COMPOSITE STRUCTURES

dispersion curves are stably computed. These methods include matrix-based methods, finite element methods and other methods.

1.3.1 The origin of matrix-based methods for modeling guided waves propagation in layered structure

Matrix-based methods are mainly applied to multi-layered problems, and they have received a great development since 1950s from theoretical advancements to engineering applications. There are three specific methods including transfer matrix method, global matrix method and stiffness matrix method.



Example, using three-layer plate with semi-infinite half-spaces.

Figure 1.8 – Labeling system for multilayered plate [6].

Thomson proposed the first version of the transfer matrix method (TMM) in 1950 to relate the field variables, i.e. the stress and displacement components, at the top and bottom surfaces of the plate through a series of transfer matrices, which simultaneously takes account of the continuity of field variables at the interfaces of adjacent layers and the traction-free boundary conditions at the two outer surfaces of the plate. Haskell subsequently polished Thomson's version by correcting several small errors [32]. The Thomson-Haskell formulation conceptualized the simplicity of TMM and thereafter received a significant number of applications in both seismological and ultrasonic fields [33].

But one fatal flaw of TMM is the notorious *large fd problem* which means that at the large product value of frequency f and plate's thickness d , the dispersion curves obtained from the solutions of the dispersion equation built with TMM become unstable. The reason of this problem is attributed to the poor conditioning of the transfer matrices thanks to the coexisted growing and decaying wave types.

In contrast to TMM, an alternative global matrix method (GMM) was proposed originally by Knopoff in 1964 [34]. The principal idea of GMM is to assemble all the sub-matrices representing the continuity conditions of field variables in each layer into a global matrix, along with all layers' wave amplitudes to be determined by the traction-free boundary conditions. The main merit of GMM rests on its numerical stability even at large fd range but at the cost of increasing computational burden. Limited by the poor computational capabilities in the twentieth century, when the application was focused on the media having massive number of layers, the global matrix possesses a large size, thus the issue of computational inefficiency is unavoidable.

In order to fix the *large fd problem* of TMM, Rokhlin and Wang (2001) developed a new stiffness matrix method (SMM) by recasting the layer's transfer matrix to form the stiffness matrix that relates displacement to stress at the top and bottom side of a layer [35, 36]. Then, the continuity conditions used in TMM and GMM are now transformed to the recursive procedure from the first to the last layer in SMM to produce a global stiffness matrix of the whole plate. Finally, the traction-free boundary condition is applied to the generated global stiffness matrix to obtain the dispersion equation. It has been proved that SMM is unconditionally stable. One shortcoming of SMM is the degeneration of the conceptual simplicity in comparison to TMM and GMM. Due to this reason, we do not consider SMM in the thesis.

1.3.2 The modern matrix-based methods

The modern matrix-based methods are the successors of the classical TMM, GMM and SMM as introduced above. There are a significant number of references in pursuit of theoretical improvements and practical applications to these methods. We cannot refer each reference but only concern the representatives.

Wang and Yuan (2007) exerted symmetry condition in TMM to study the anisotropic property of composite laminates in terms of the wave characteristic curves in polar coordinate system, i.e. phase velocity, slowness and group velocity [37]. The improved TMM was successfully validated by

1.3. MODELING METHODS OF GUIDED WAVES IN COMPOSITE STRUCTURES

the experimental data. However, their works cast a veil over the *large fd problem* inherent in TMM as stated previously. Maghsoodi et al. (2014) applied TMM to predict the dispersion curves of metallic-composite plates [38]. They decomposed the coupled numerical problem into two cases, wave propagation along principal and off-principal axes of material respectively. Whereas, their method, like any other attempts, is invalid when dealing with the special case that the wave propagation direction corresponds to the off-principal direction of the composite layers but always to the principal direction of the metallic layers due to the isotropic property of metal. This causes the underlying different elastic matrix types issue between the two materials. Nandyala et al. (2019) proposed an effective stiffness matrix method (ESM) to compute dispersion curves by regarding a multi-layered laminate as a single monoclinic layer, viz. from lamination to homogenization, such that it improves the computational efficiency of the traditional TMM [10]. ESM is an approximation method. It fails to predict dispersion curves at larger frequencies and higher orders [10].

Lowe et al. (2003) developed the software *Disperse* via GMM which became the pioneering computing program in the past two decades [39]. However, some problems still exist in *Disperse* such as missing roots or producing outliers in a mode [40], as well as the limited computational capability that it can only cope with laminates containing no more than 64 layers [11] (this incapability does not work for a 400-layered laminate considered in [11]). Pant et al. (2014) recast the conventional GMM based on 3D elasticity and partial wave superposition approach [8] to compute the dispersion curves of fiber-metal laminate. Although their method was well examined by experiments, only lower modes' data were compared (S0, A0, SH0 modes) and the comparison was made in the lower frequency range (0-600 kHz). Besides, one deficiency of their method is that they did not technically solve the numerically unstable issue, when waves propagate in the metallic-composite plates, that mismatched stiffness matrix types are used for the two materials also encountered in [38] (see the comments to this reference in the prior paragraph). In Pant's paper, a pseudo-correction measure was employed to circumvent the issue of mismatched stiffness matrix type by subtracting 1° from the wave propagation angle when the direction of wave propagation is at the material's principal axis. But this measure is still invalid for metallic-composite plates because composite layers remain orthotropic and monoclinic type of elastic matrix in the principal and off-principal axes, respectively; conversely, the metal layers always keep the isotropic type in all directions. To solve the same problem of incompatible elastic matrix type, Barazanchy and Giurgiutiu (2016) proposed a unified formulation [9] by taking all elastic

1.3. MODELING METHODS OF GUIDED WAVES IN COMPOSITE STRUCTURES

matrix types into consideration. However, their method failed to pass the benchmark test for an unidirectional 50-layered plate due to another numerical instability issue. Ramasawmy et al. (2020) developed a toolbox to compute dispersion curves of composite materials implemented in MATLAB called *ElasticMatrix* based on GMM [41]. This toolbox has limited functionality that it can only deal with isotropic and transversely isotropic materials, as well as restricting the wave propagation direction along the principal axes of material, which is evidently not suitable for aeronautic composite materials having strong anisotropic property.

In order to get stable dispersion solutions, Kamal and Giurgiutiu (2014) combined SMM and TMM to form the stiffness transfer matrix method (STMM) [42]. In this method, SMM can produce stable solutions at higher wavenumber region and TMM can give correct solutions at lower wavenumber region. Combining two independent methods is a bit superfluous in the author's opinion. Huber et al. (2018) adopted SMM to compute the dispersion curves of anisotropic composites with large to 400 layers being a component of the rocket Ariane 6 [11]. Computing such complex structure is time consuming but that paper did not report the computational time, which is the sole inadequacy. That work contributed to a stand-alone freeware *Dispersion Calculator*, which has received substantial updates by Huber after its creation since 2018.

1.3.3 Finite element methods

Another effective route of modeling dispersion relation is to use finite element methods (FEM), among which the mainstream is the semi-analytical finite element method (SAFE). Just as its name implied, SAFE assumes the displacement field of a laminate in two separated forms: in the cross-section of waveguide 1D or 2D finite element discretization is utilized and in the propagation direction an analytical harmonic function of propagation distance and time is applied [7]. Benefiting from the flexible discretization in the cross-section, SAFE has natural advantages for modeling wave propagation in waveguides of arbitrary cross-section. Bocchini et al. (2011) developed the freeware GUIGUW [43] based on SAFE to compute dispersion curves of various waveguides containing multi-layered plate, cylinder, circular tube, square tube and railroad tracks, etc. Recently, a spectral method similar to SAFE has received increasing attention called spectral collocation method (SCM) based on Chebyshev polynomials [44] that allocates spectral points in the thickness direction of the plate to discretize each layer of a laminate, instead of elements in SAFE. This method is promising but may still encounter

1.3. MODELING METHODS OF GUIDED WAVES IN COMPOSITE STRUCTURES

numerical issues such as unstable solutions caused by the non-uniform Chebyshev grid points [45]. In order to take full advantage of the commercial FEM software such as ANSYS, a wave finite element method (WFEM) was developed by some researchers, e.g. Mace and Manconi (2008) [46] and Sorohan et al. (2011) [47]. In the thickness direction, WFEM discretizes the waveguide with finite elements as the SAFE strategy, but in the propagation direction, only a nominal length, usually a wavelength, is discretized by an element. In WFEM, the boundary condition is replaced by the Floquet periodic condition. Given that the wavelength changes with frequency, the elements in the propagation direction should be re-meshed for different frequencies to retain the consistent accuracy [47], thus WFEM is not as flexible as SAFE and SCM.

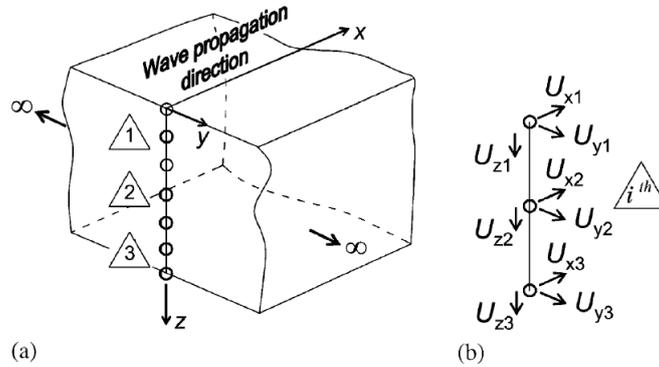


Figure 1.9 – SAFE model of wave propagation, (a) discretization along thickness direction, (b) three-node element and degrees of freedom of each node [7].

It should be stated here that the focus of the thesis is the **matrix based methods** (specifically, TMM and GMM) since these methods are based on the linear 3D elasticity theory and thus become the standard manner to derive the analytical dispersion equations of multi-layered plate system [40]. SAFE method will be adopted for validation.

1.3.4 Other methods

The remaining available methods to build dispersion equation for a plate waveguide are partly based on the higher order plate theory (HOPT) [48, 49], Ritz-Rayleigh method [50, 51], Green's function [52], and Green's matrix [53]. Although the HOPT can take the higher order shear deformation of plates into consideration, it is still an approximation method. The number of modes accessible from HOPT cannot be larger than six (three symmetric and three anti-symmetric modes) due to the limited characteristic matrix orders [49]. Besides, in the higher order modes, e.g. S2 and A2, or at larger frequencies, HOPT

may produce a poor accuracy of dispersion solutions. The Ritz-Rayleigh and Green's function based methods have superiority on characterizing material parameters through ultrasonic acoustic waves, and have led to some applications for metallic austenite [50, 52], but not for composite materials, which has been done by the Green's matrix-based method [53].

1.4 Organization of the thesis

The objective of the thesis is to study guided waves propagation and attenuation in an arbitrarily oriented composite plate for its potential application to SHM. The thesis is organized as follows:

In Chapter 2, classical equations of three-dimensional (3D) elasticity are reviewed with an emphasis on the characteristics of stiffness matrix rotation of composite materials.

In Chapter 3, the partial wave superposition approach is used to derive the classical dispersion equations of guided waves propagating in a single layer composite lamina.

In Chapter 4, the transfer matrix method is introduced to model guided waves propagation in a multi-layered composite plate. An original hybrid matrix strategy is proposed to cope with the matrix incompatibility issue encountered in quasi-isotropic plates and metallic-composite plates.

In Chapter 5, the standard global matrix method is introduced. Based on it, an optimized global matrix method is developed that can greatly improve the computational efficiency of the standard global matrix method. The optimized version is applied to an aerospace composite structure having 400 layers which is the largest number of layers reported so far.

In Chapter 6, an important property of dispersion equations, named dichotomy property, is originally explored, which states that the a priori complex-valued dispersion equations in the case of pure elastic materials collapse to pure real or imaginary valued equations, depending on the behavior of some intermediate parameters. This property is extremely helpful for overcoming numerical instabilities encountered during the equation solving process.

In Chapter 7, the methodology of predicting the frequency and spatially dependent attenuation is proposed by using the damped global matrix method. Two engineering case studies are conducted to validate the effectiveness of the methodology. The two involved structures are the components of AIRBUS A380. Using the actual and in-service data of the practical aeronautic structures makes a great contribution to the state-of-the-art and thus this chapter escorts the initiative of closing the gap

1.4. ORGANIZATION OF THE THESIS

between research and industrial deployment for SHM [54].

The general conclusions and major contributions of the thesis are presented in Chapter 8, along with several perspectives for future works. To finish the thesis, a short list of publications is provided in the end of this chapter.

1.4. ORGANIZATION OF THE THESIS

Chapter 2

Fundamentals of wave propagation in solids

In this chapter, some fundamentals of elastic wave propagation in solids will be reviewed [2, 4, 33], including the basic equations of 3D elasticity, stiffness matrix types of various materials, stiffness matrix rotation, the expanded field equations of triclinic material and bulk wave propagation in solids. These contents are the basis of the subsequent chapters.

2.1 Basic equations of 3D elasticity

The mechanism of wave propagation in solid media is governed by the 3D elasticity theory. Thus, the basic equations of 3D elasticity will be introduced firstly, including stress-strain relation, strain-displacement relation and elastodynamic equations of motion.

2.1.1 Stress-strain relation

For a cubic element representing a tiny volume of a certain solid material, its 3D stress state can be illustrated in Figure 2.1 in Cartesian coordinate system $O - x_1x_2x_3$. In this figure, the labelled quantities $(\sigma_{11}, \sigma_{22}, \sigma_{33})$ are the normal stresses, and $(\sigma_{12}, \sigma_{21}, \sigma_{13}, \sigma_{31}, \sigma_{23}, \sigma_{32})$ are the shear stresses. Due to the reciprocal condition, i.e. $\sigma_{12} = \sigma_{21}$, $\sigma_{13} = \sigma_{31}$, $\sigma_{23} = \sigma_{32}$, the nine variables of stresses reduce to six, that form the stress vector $\boldsymbol{\sigma}$. Correspondingly, there are six variables of strain $(\varepsilon_{11}, \varepsilon_{22}, \varepsilon_{33}, \varepsilon_{23}, \varepsilon_{13}, \varepsilon_{12})$ that form the strain vector $\boldsymbol{\varepsilon}$. For a typical 3D elastic problem, there are three displacement variables (u_1, u_2, u_3) that form the displacement vector \mathbf{u} . The relation between

2.1. BASIC EQUATIONS OF 3D ELASTICITY

stress and strain is characterized by the general Hookes' law as formalized in Eq. (2.4).

$$\boldsymbol{\sigma} = [\sigma_{11}, \sigma_{22}, \sigma_{33}, \sigma_{23}, \sigma_{13}, \sigma_{12}]^T \quad (2.1)$$

$$\boldsymbol{\varepsilon} = [\varepsilon_{11}, \varepsilon_{22}, \varepsilon_{33}, \varepsilon_{23}, \varepsilon_{13}, \varepsilon_{12}]^T \quad (2.2)$$

$$\mathbf{u} = [u_1, u_2, u_3]^T \quad (2.3)$$

where, T is the matrix transpose operator.

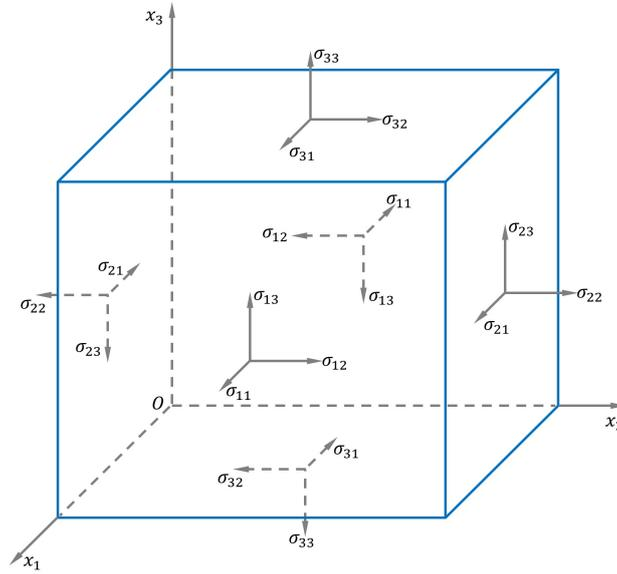


Figure 2.1 – The stress state of a cubic element of a solid material.

$$\begin{bmatrix} \sigma_{11} \\ \sigma_{22} \\ \sigma_{33} \\ \sigma_{23} \\ \sigma_{13} \\ \sigma_{12} \end{bmatrix} = \begin{bmatrix} C_{11} & C_{12} & C_{13} & C_{14} & C_{15} & C_{16} \\ & C_{22} & C_{23} & C_{24} & C_{25} & C_{26} \\ & & C_{33} & C_{34} & C_{35} & C_{36} \\ & & & C_{44} & C_{45} & C_{46} \\ \text{sym} & & & & C_{55} & C_{56} \\ & & & & & C_{66} \end{bmatrix} \begin{bmatrix} \varepsilon_{11} \\ \varepsilon_{22} \\ \varepsilon_{33} \\ 2\varepsilon_{23} \\ 2\varepsilon_{13} \\ 2\varepsilon_{12} \end{bmatrix} \quad (2.4)$$

where, the coefficients matrix in Eq. (2.4) is denoted by $\mathbf{C} \in \mathbb{C}^{6 \times 6}$ which is the stiffness matrix of the material having symmetric property. Since it characterizes the elastic or viscoelastic behavior of stress and strain, it is also called elastic matrix in pure elastic materials or viscoelastic matrix in viscoelastic materials.

2.1.2 Strain-displacement relation

The relation between strain and displacement is characterized by the geometric equations as formalized in Eq. (2.5).

$$\begin{cases} \varepsilon_{11} = \frac{\partial u_1}{\partial x_1}, & \varepsilon_{12} = \frac{1}{2} \left(\frac{\partial u_1}{\partial x_2} + \frac{\partial u_2}{\partial x_1} \right), \\ \varepsilon_{22} = \frac{\partial u_2}{\partial x_2}, & \varepsilon_{23} = \frac{1}{2} \left(\frac{\partial u_2}{\partial x_3} + \frac{\partial u_3}{\partial x_2} \right), \\ \varepsilon_{33} = \frac{\partial u_3}{\partial x_3}, & \varepsilon_{13} = \frac{1}{2} \left(\frac{\partial u_1}{\partial x_3} + \frac{\partial u_3}{\partial x_1} \right). \end{cases} \quad (2.5)$$

2.1.3 Elastodynamic equations of motion

Inherently, the dynamic behavior of particles in material is governed by its elastodynamic equations of motion, representing the equilibrium condition in the dynamic sense, as presented in Eq. (2.6), where ρ is the mass density.

$$\begin{cases} \frac{\partial \sigma_{11}}{\partial x_1} + \frac{\partial \sigma_{12}}{\partial x_2} + \frac{\partial \sigma_{13}}{\partial x_3} = \rho \frac{\partial^2 u_1}{\partial t^2} \\ \frac{\partial \sigma_{21}}{\partial x_1} + \frac{\partial \sigma_{22}}{\partial x_2} + \frac{\partial \sigma_{23}}{\partial x_3} = \rho \frac{\partial^2 u_2}{\partial t^2} \\ \frac{\partial \sigma_{31}}{\partial x_1} + \frac{\partial \sigma_{32}}{\partial x_2} + \frac{\partial \sigma_{33}}{\partial x_3} = \rho \frac{\partial^2 u_3}{\partial t^2} \end{cases} \quad (2.6)$$

2.2 Stiffness matrix types of various materials

In Eq. (2.4), there are 21 elements in the stiffness matrix \mathbf{C} . However, for different materials, the number of elements in \mathbf{C} and its types are different. In material science, materials are physically classified into five types according to the number of symmetry axes inherent in it, i.e. triclinic, monoclinic, orthotropic, transversely isotropic and isotropic materials [55]. Mathematically, this classification is equivalent to count the different number of independent elements in the stiffness matrix \mathbf{C} , in other words, depending on the stiffness matrix type. During deriving the wave propagation equations in the next chapter, the stiffness matrix types play a significant role for the wave propagation property. Thus, the five materials along with their specific stiffness matrix types should be introduced firstly.

2.2.1 Triclinic material

For triclinic material, there are 21 independent constants in the stiffness matrix \mathbf{C}_T , which directly succeeds from the general type of the stiffness matrix \mathbf{C} in Eq. (2.4). The set of all stiffness matrices

of triclinic materials is denoted as $\mathcal{C}_{\mathcal{T}}$.

$$\mathbf{C}_{\mathcal{T}} = \begin{bmatrix} C_{11} & C_{12} & C_{13} & C_{14} & C_{15} & C_{16} \\ & C_{22} & C_{23} & C_{24} & C_{25} & C_{26} \\ & & C_{33} & C_{34} & C_{35} & C_{36} \\ & & & C_{44} & C_{45} & C_{46} \\ \text{sym} & & & & C_{55} & C_{56} \\ & & & & & C_{66} \end{bmatrix} \quad (2.7)$$

2.2.2 Monoclinic material

For monoclinic material, the number of independent constants in its stiffness matrix $\mathbf{C}_{\mathcal{M}}$ reduces to 13, as presented in Eq. (2.8). All stiffness matrices of monoclinic materials constitute the set $\mathcal{C}_{\mathcal{M}}$.

$$\mathbf{C}_{\mathcal{M}} = \begin{bmatrix} C_{11} & C_{12} & C_{13} & 0 & 0 & C_{16} \\ & C_{22} & C_{23} & 0 & 0 & C_{26} \\ & & C_{33} & 0 & 0 & C_{36} \\ & & & C_{44} & C_{45} & 0 \\ \text{sym} & & & & C_{55} & 0 \\ & & & & & C_{66} \end{bmatrix} \quad (2.8)$$

2.2.3 Orthotropic material

For orthotropic material, there are nine independent constants in its stiffness matrix $\mathbf{C}_{\mathcal{O}}$, which belongs to the set of stiffness matrices of orthotropic materials denoted as $\mathcal{C}_{\mathcal{O}}$.

$$\mathbf{C}_{\mathcal{O}} = \begin{bmatrix} C_{11} & C_{12} & C_{13} & 0 & 0 & 0 \\ & C_{22} & C_{23} & 0 & 0 & 0 \\ & & C_{33} & 0 & 0 & 0 \\ & & & C_{44} & 0 & 0 \\ \text{sym} & & & & C_{55} & 0 \\ & & & & & C_{66} \end{bmatrix} \quad (2.9)$$

In engineering, $\mathbf{C}_{\mathcal{O}}$ is generally obtained from the elastic constants ($E_1, E_2, E_3, G_{23}, G_{31}, G_{12}, \nu_{23}, \nu_{13}, \nu_{12}$) measured through the standard mechanical test for the normal shaped specimens [55].

$$\mathbf{C}_{\mathcal{O}} = \begin{bmatrix} 1/E_1 & -\nu_{12}/E_1 & -\nu_{13}/E_1 & 0 & 0 & 0 \\ & 1/E_2 & -\nu_{23}/E_2 & 0 & 0 & 0 \\ & & 1/E_3 & 0 & 0 & 0 \\ & & & 1/G_{23} & 0 & 0 \\ \text{sym} & & & & 1/G_{31} & 0 \\ & & & & & 1/G_{12} \end{bmatrix}^{-1} \quad (2.10)$$

2.2.4 Transversely isotropic material

For transversely isotropic material, there are five independent constants in its stiffness matrix \mathbf{C}_{TI} . The widely used unidirectional composite materials in aeronautic and aerospace engineering just belong to this type. This material possesses the transversely isotropic property, i.e. in the plane transverse to the fiber direction, material properties are isotropic [2]. In the thesis, we classify $\mathbf{C}_{\text{TI}} \in \mathcal{C}_{\mathcal{O}}$ based on the fact that \mathbf{C}_{TI} has the same shape as $\mathcal{C}_{\mathcal{O}}$ in terms of number and positions of zero elements but with less number of independent coefficients.

$$\mathbf{C}_{\text{TI}} = \begin{bmatrix} C_{11} & C_{12} & C_{12} & 0 & 0 & 0 \\ & C_{22} & C_{23} & 0 & 0 & 0 \\ & & C_{22} & 0 & 0 & 0 \\ & & & \frac{C_{22}-C_{23}}{2} & 0 & 0 \\ \text{sym} & & & & C_{55} & 0 \\ & & & & & C_{55} \end{bmatrix} \quad (2.11)$$

In engineering, \mathbf{C}_{TI} can be obtained from the experimentally measured elastic constants ($E_1, E_2, G_{12}, \nu_{12}, \nu_{23}$).

$$\mathbf{C}_{\text{TI}} = \begin{bmatrix} 1/E_1 & -\nu_{12}/E_1 & -\nu_{12}/E_1 & 0 & 0 & 0 \\ & 1/E_2 & -\nu_{23}/E_2 & 0 & 0 & 0 \\ & & 1/E_2 & 0 & 0 & 0 \\ & & & 1/G_{23} & 0 & 0 \\ \text{sym} & & & & 1/G_{12} & 0 \\ & & & & & 1/G_{12} \end{bmatrix}^{-1} \quad (2.12)$$

where, $G_{23} = \frac{E_2}{2(1+\nu_{23})}$.

2.2.5 Isotropic material

Isotropic materials only have two independent constants in its stiffness matrix \mathbf{C}_{I} . Most metallic materials belong to isotropic type, which is denoted by the set notation $\mathcal{C}_{\mathcal{I}}$. In Section 2.3.3, we further classify $\mathbf{C}_{\text{I}} \in \mathcal{C}_{\mathcal{I}} \subseteq \mathcal{C}_{\mathcal{O}}$.

$$\mathbf{C}_{\text{I}} = \begin{bmatrix} C_{11} & C_{12} & C_{12} & 0 & 0 & 0 \\ & C_{11} & C_{12} & 0 & 0 & 0 \\ & & C_{11} & 0 & 0 & 0 \\ & & & \frac{C_{11}-C_{12}}{2} & 0 & 0 \\ \text{sym} & & & & \frac{C_{11}-C_{12}}{2} & 0 \\ & & & & & \frac{C_{11}-C_{12}}{2} \end{bmatrix} \quad (2.13)$$

2.3. STIFFNESS MATRIX ROTATION

The Lamé constants λ and μ are widely used to represent the elastic properties of isotropic materials.

$$\mathbf{C}_I = \begin{bmatrix} \lambda + 2\mu & \lambda & \lambda & 0 & 0 & 0 \\ & \lambda + 2\mu & \lambda & 0 & 0 & 0 \\ & & \lambda + 2\mu & 0 & 0 & 0 \\ & & & \mu & 0 & 0 \\ \text{sym} & & & & \mu & 0 \\ & & & & & \mu \end{bmatrix} \quad (2.14)$$

where, the Lamé constants can be computed from Young's modulus E and Poisson's ratio ν according to $\lambda = \frac{E\nu}{(1+\nu)(1-2\nu)}$, $\mu = \frac{E}{2(1+\nu)}$. E and ν are generally measured from experiments.

2.3 Stiffness matrix rotation

Eqs. (2.9)(2.11)(2.13) show the stiffness matrix types of orthotropic, transversely isotropic and isotropic materials, which are measured along their respective material's symmetry axes, i.e. the principal axis x_1 illustrated in Figure 2.2. However, in plate, guided waves can propagate at a general off-principal direction. Thus, it is necessary to study the stiffness matrix types of these materials along the off-principal axis direction (x'_1 as illustrated in Figure 2.2). In elasticity theory, this task can be completed based on the tensor rotation rule, which is introduced in this section.

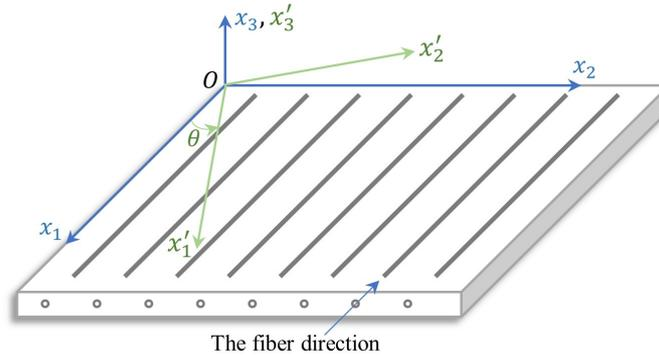


Figure 2.2 – The schematic diagram of a composite lamina.

2.3.1 Voigt notation and tensor rotation rule

The first step is to transform the general stiffness matrix C_{pq} into the fourth order tensor c_{ijkl} via the Voigt notation, which is exemplified in Figure 2.3 and detailed in Eq. (2.15).

2.3. STIFFNESS MATRIX ROTATION

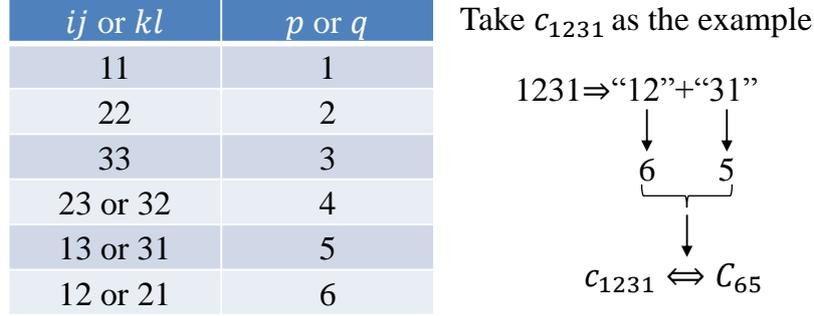


Figure 2.3 – The example of Voigt notation.

$$\mathbf{C} = \begin{bmatrix} C_{11} & C_{12} & C_{13} & C_{14} & C_{15} & C_{16} \\ C_{12} & C_{22} & C_{23} & C_{24} & C_{25} & C_{26} \\ C_{13} & C_{23} & C_{33} & C_{34} & C_{35} & C_{36} \\ C_{14} & C_{24} & C_{34} & C_{44} & C_{45} & C_{46} \\ C_{15} & C_{25} & C_{35} & C_{45} & C_{55} & C_{56} \\ C_{16} & C_{26} & C_{36} & C_{46} & C_{56} & C_{66} \end{bmatrix} \Leftrightarrow \mathbf{C} = \begin{bmatrix} c_{1111} & c_{1122} & c_{1133} & c_{1123} & c_{1131} & c_{1112} \\ c_{2211} & c_{2222} & c_{2233} & c_{2223} & c_{2231} & c_{2212} \\ c_{3311} & c_{3322} & c_{3333} & c_{3323} & c_{3331} & c_{3312} \\ c_{2311} & c_{2322} & c_{2333} & c_{2323} & c_{2331} & c_{2312} \\ c_{3111} & c_{3122} & c_{3133} & c_{3123} & c_{3131} & c_{3112} \\ c_{1211} & c_{1222} & c_{1233} & c_{1223} & c_{1231} & c_{1212} \end{bmatrix} \quad (2.15)$$

The second step is to compute the rotation matrix shown in Eq. (2.16) that is based on the rotation of coordinate system around the axis x_3 as illustrated in Figure 2.2.

$$\mathbf{R}(\theta) = \begin{bmatrix} \cos(\theta) & \sin(\theta) & 0 \\ -\sin(\theta) & \cos(\theta) & 0 \\ 0 & 0 & 1 \end{bmatrix} \quad (2.16)$$

where, θ is the rotation angle being positive for counterclockwise direction and negative for clockwise direction.

The third step is to compute the rotated tensor c'_{mnop} based on the tensor multiplication rule formalized in Eq. (2.17a), where the Einstein summation convention is implied for the repeated indices. To ease computation, the tensor multiplication form in Eq. (2.17a) is expanded to the linear summation form in Eq. (2.17b).

$$c'_{mnop} = R_{mi}R_{nj}R_{ok}R_{pl}c_{ijkl} \quad (2.17a)$$

$$c'_{mnop} = \sum_{i=1}^3 \sum_{j=1}^3 \sum_{k=1}^3 \sum_{l=1}^3 R_{mi}R_{nj}R_{ok}R_{pl}c_{ijkl} \quad (2.17b)$$

Finally, by inversely applying the Voigt notation shown in Eq. (2.15), the rotated tensor c'_{mnop} can be transformed back to the matrix form C'_{pq} , and the rotated stiffness matrix \mathbf{C}' is just obtained. Note

2.3. STIFFNESS MATRIX ROTATION

that although the original stiffness tensor c_{ijkl} in Eq. (2.17a) represents the type of triclinic material, it can be written for any other types.

2.3.2 Example of stiffness matrix rotation

The orthotropic, transversely isotropic and pure isotropic materials are widely used in aeronautic engineering. Their stiffness matrices are employed here to demonstrate the process of stiffness matrix rotation. To this end, the four rotation steps are firstly applied to the stiffness matrix of the orthotropic material \mathbf{C}_O defined in Eq. (2.9) with an arbitrary angle θ . The rotated matrix \mathbf{C}'_O is obtained in Eq. (2.18), with the detailed elements listed in Eq. (2.19).

Among all possible rotation angles, there is a special one $\theta = 90^\circ$ which makes the elements C'_{16} , C'_{26} , C'_{36} , $C'_{45} = 0$ in the rotated \mathbf{C}'_O , see Eq. (2.20). This angle corresponds to the transverse direction in relation to the fibers in the plate plane, in other words, the axis x'_1 is rotated to coincide with the axis x_2 in Figure 2.2.

$$\mathbf{C}_O = \begin{bmatrix} C_{11} & C_{12} & C_{13} & 0 & 0 & 0 \\ & C_{22} & C_{23} & 0 & 0 & 0 \\ & & C_{33} & 0 & 0 & 0 \\ & & & C_{44} & 0 & 0 \\ \text{sym} & & & & C_{55} & 0 \\ & & & & & C_{66} \end{bmatrix} \xrightarrow{\text{Rot}\{\mathbf{C}_O, \theta\}} \mathbf{C}'_O = \begin{bmatrix} C'_{11} & C'_{12} & C'_{13} & 0 & 0 & C'_{16} \\ & C'_{22} & C'_{23} & 0 & 0 & C'_{26} \\ & & C'_{33} & 0 & 0 & C'_{36} \\ & & & C'_{44} & C'_{45} & 0 \\ \text{sym} & & & & C'_{55} & 0 \\ & & & & & C'_{66} \end{bmatrix} \quad (2.18)$$

where, $\text{Rot}\{\mathbf{C}_O, \theta\}$ is the rotation operator that rotates the stiffness matrix \mathbf{C}_O with angle θ .

$$\begin{cases} C'_{11} = C_{11} \cos^4 \theta + C_{22} \sin^4 \theta + (2C_{12} + 4C_{66}) \sin^2 \theta \cos^2 \theta, \\ C'_{12} = (C_{11} + C_{22} - 4C_{66}) \sin^2 \theta \cos^2 \theta + C_{12}(\sin^4 \theta + \cos^4 \theta), \\ C'_{13} = C_{13} \cos^2 \theta + C_{23} \sin^2 \theta, \\ C'_{16} = (C_{12} + 2C_{66} - C_{11}) \sin \theta \cos^3 \theta + (C_{22} - C_{12} - 2C_{66}) \cos \theta \sin^3 \theta, \\ C'_{22} = C_{11} \sin^4 \theta + C_{22} \cos^4 \theta + (2C_{12} + 4C_{66}) \sin^2 \theta \cos^2 \theta, \\ C'_{23} = C_{23} \cos^2 \theta + C_{13} \sin^2 \theta, \\ C'_{26} = (C_{12} + 2C_{66} - C_{11}) \cos \theta \sin^3 \theta + (C_{22} - C_{12} - 2C_{66}) \sin \theta \cos^3 \theta, \\ C'_{33} = C_{33}, \\ C'_{36} = (C_{23} - C_{13}) \sin \theta \cos \theta, \\ C'_{44} = C_{44} \cos^2 \theta + C_{55} \sin^2 \theta, \\ C'_{45} = (C_{44} - C_{55}) \sin \theta \cos \theta, \\ C'_{55} = C_{55} \cos^2 \theta + C_{44} \sin^2 \theta, \\ C'_{66} = C_{66}(\sin^4 \theta + \cos^4 \theta) + (C_{11} + C_{22} - 2C_{12} - 2C_{66}) \sin^2 \theta \cos^2 \theta. \end{cases} \quad (2.19)$$

2.3. STIFFNESS MATRIX ROTATION

$$\mathbf{C}_O = \begin{bmatrix} C_{11} & C_{12} & C_{13} & 0 & 0 & 0 \\ & C_{22} & C_{23} & 0 & 0 & 0 \\ & & C_{33} & 0 & 0 & 0 \\ & & & C_{44} & 0 & 0 \\ \text{sym} & & & & C_{55} & 0 \\ & & & & & C_{66} \end{bmatrix} \xrightarrow{\text{Rot}\{\mathbf{C}_O, 90^\circ\}} \mathbf{C}'_O = \begin{bmatrix} C_{22} & C_{12} & C_{23} & 0 & 0 & 0 \\ & C_{11} & C_{13} & 0 & 0 & 0 \\ & & C_{33} & 0 & 0 & 0 \\ & & & C_{55} & 0 & 0 \\ \text{sym} & & & & C_{44} & 0 \\ & & & & & C_{66} \end{bmatrix} \quad (2.20)$$

For the rotated stiffness matrix of the transversely isotropic material \mathbf{C}'_{TI} , it can be directly obtained based on Eq. (2.19) in which the four constants C_{13} , C_{33} , C_{44} , C_{66} are now replaced by $C_{13} = C_{12}$, $C_{33} = C_{22}$, $C_{44} = \frac{C_{22}-C_{23}}{2}$, $C_{66} = C_{55}$ because there are only five independent constants in \mathbf{C}_{TI} as indicated in Eq. (2.11). After substitution, one can know that the resulting \mathbf{C}'_{TI} keeps the same form as \mathbf{C}'_O in Eq. (2.18). This is the reason that we classify $\mathbf{C}_{\text{TI}} \in \mathcal{C}_O$ in Section 2.2.4.

The elements of \mathbf{C}_I in Eq. (2.13) are further substituted into Eq. (2.19) to derive the rotated stiffness matrix of the isotropic material \mathbf{C}'_I as concluded in Eq. (2.21), which shows that $\mathbf{C}'_I = \mathbf{C}_I$. This outcome conforms with the property of isotropic materials that has the highest symmetry such that its mechanical properties do not change with wave propagation direction.

$$\mathbf{C}_I = \begin{bmatrix} C_{11} & C_{12} & C_{12} & 0 & 0 & 0 \\ & C_{11} & C_{12} & 0 & 0 & 0 \\ & & C_{11} & 0 & 0 & 0 \\ & & & \frac{C_{11}-C_{12}}{2} & 0 & 0 \\ \text{sym} & & & & \frac{C_{11}-C_{12}}{2} & 0 \\ & & & & & \frac{C_{11}-C_{12}}{2} \end{bmatrix} \xrightarrow{\text{Rot}\{\mathbf{C}_I, \theta\}} \mathbf{C}'_I = \begin{bmatrix} C_{11} & C_{12} & C_{12} & 0 & 0 & 0 \\ & C_{11} & C_{12} & 0 & 0 & 0 \\ & & C_{11} & 0 & 0 & 0 \\ & & & \frac{C_{11}-C_{12}}{2} & 0 & 0 \\ \text{sym} & & & & \frac{C_{11}-C_{12}}{2} & 0 \\ & & & & & \frac{C_{11}-C_{12}}{2} \end{bmatrix} \quad (2.21)$$

2.3.3 Characteristics of stiffness matrix rotation

From the presented results of examples, the following characteristics can be observed. These characteristics is the basis of Chapter 3 and 4.

1. After rotation from the principal axis x_1 to the off-principal axis x'_1 when $\theta \neq 0^\circ$ and 90° , the rotated $\mathbf{C}'_O, \mathbf{C}'_{\text{TI}} \in \mathcal{C}_M$, see Eq. (2.18).

2.4. EXPANDED ELASTODYNAMIC EQUATIONS OF MOTION OF TRICLINIC MATERIAL

2. When $\theta = 0^\circ$ or 90° ,¹ the rotated $\mathbf{C}'_{\mathcal{O}}, \mathbf{C}'_{\mathcal{TI}} \in \mathcal{C}_{\mathcal{O}}$, see Eq. (2.20).
3. Regardless of the rotation angle θ , the rotated $\mathbf{C}'_{\mathcal{I}} \in \mathcal{C}_{\mathcal{I}}$, see Eq. (2.21). Mathematically, we can classify $\mathbf{C}'_{\mathcal{I}} \in \mathcal{C}_{\mathcal{O}}$ by defining $\mathcal{C}_{\mathcal{I}} \subseteq \mathcal{C}_{\mathcal{O}}$. In Section 4.8, we will see the benefit of this classification during the study of the coupling issue between Lamb and SH waves in a composite laminate.
4. For completeness purpose, the characteristics of the rotated $\mathbf{C}'_{\mathcal{M}} \in \mathcal{C}_{\mathcal{M}}$ and $\mathbf{C}'_{\mathcal{T}} \in \mathcal{C}_{\mathcal{T}}$ are given here even if they are not presented in section 2.3.2 thanks to the complexity of the two cases. This characteristic manifests that for monoclinic and triclinic materials, the rotation process does not change their respective stiffness matrix types.

The above characteristics of stiffness matrix rotation are summarized in Table 2.1.

Table 2.1 – The characteristics of stiffness matrix rotation

Matrix form in the (minor-)principal axis direction	Number of independent coefficients	Matrix form in the off-principal axis direction
$\mathbf{C}_{\mathcal{T}} \in \mathcal{C}_{\mathcal{T}}$	21	$\mathbf{C}'_{\mathcal{T}} \in \mathcal{C}_{\mathcal{T}}$
$\mathbf{C}_{\mathcal{M}} \in \mathcal{C}_{\mathcal{M}}$	13	$\mathbf{C}'_{\mathcal{M}} \in \mathcal{C}_{\mathcal{M}}$
$\mathbf{C}_{\mathcal{O}} \in \mathcal{C}_{\mathcal{O}}$	9	$\mathbf{C}'_{\mathcal{O}} \in \mathcal{C}_{\mathcal{M}}$
$\mathbf{C}_{\mathcal{TI}} \in \mathcal{C}_{\mathcal{O}}$	5	$\mathbf{C}'_{\mathcal{TI}} \in \mathcal{C}_{\mathcal{M}}$
$\mathbf{C}_{\mathcal{I}} \in \mathcal{C}_{\mathcal{I}} \subseteq \mathcal{C}_{\mathcal{O}}$	2	$\mathbf{C}'_{\mathcal{I}} = \mathbf{C}_{\mathcal{I}} \in \mathcal{C}_{\mathcal{I}} \subseteq \mathcal{C}_{\mathcal{O}}$

2.4 Expanded elastodynamic equations of motion of triclinic material

The elastodynamic equations of motion, Eq. (2.6), are the basis of deriving wave propagation equations in the next chapters. To facilitate the derivation, the contracted Eq. (2.6) are expanded in this section being representative of triclinic material. To this end, we substitute Eq. (2.5) into Eq. (2.4) to get the stresses described by displacements as presented in Eq. (2.22). Then, substituting Eq. (2.22) into Eq. (2.6), the deduced elastodynamic equations of motion are now expanded in Eqs. (2.23)(2.24)(2.25). For other kind of materials and different wave types (bulk waves, SH and Lamb waves as well as their coupling) involved in the next chapters, all the counterparts can be

1. Although $\theta = 0^\circ$ does not mean an effective rotation, it is still applied here for notation homogeneity purpose.

2.4. EXPANDED ELASTODYNAMIC EQUATIONS OF MOTION OF TRICLINIC MATERIAL

simplified from the equations corresponding to triclinic material [33].

$$\begin{cases} \sigma_{11} = C_{11} \frac{\partial u_1}{\partial x_1} + C_{12} \frac{\partial u_2}{\partial x_2} + C_{13} \frac{\partial u_3}{\partial x_3} + C_{14} \left(\frac{\partial u_2}{\partial x_3} + \frac{\partial u_3}{\partial x_2} \right) + C_{15} \left(\frac{\partial u_1}{\partial x_3} + \frac{\partial u_3}{\partial x_1} \right) + C_{16} \left(\frac{\partial u_1}{\partial x_2} + \frac{\partial u_2}{\partial x_1} \right) \\ \sigma_{22} = C_{12} \frac{\partial u_1}{\partial x_1} + C_{22} \frac{\partial u_2}{\partial x_2} + C_{23} \frac{\partial u_3}{\partial x_3} + C_{24} \left(\frac{\partial u_2}{\partial x_3} + \frac{\partial u_3}{\partial x_2} \right) + C_{25} \left(\frac{\partial u_1}{\partial x_3} + \frac{\partial u_3}{\partial x_1} \right) + C_{26} \left(\frac{\partial u_1}{\partial x_2} + \frac{\partial u_2}{\partial x_1} \right) \\ \sigma_{33} = C_{13} \frac{\partial u_1}{\partial x_1} + C_{23} \frac{\partial u_2}{\partial x_2} + C_{33} \frac{\partial u_3}{\partial x_3} + C_{34} \left(\frac{\partial u_2}{\partial x_3} + \frac{\partial u_3}{\partial x_2} \right) + C_{35} \left(\frac{\partial u_1}{\partial x_3} + \frac{\partial u_3}{\partial x_1} \right) + C_{36} \left(\frac{\partial u_1}{\partial x_2} + \frac{\partial u_2}{\partial x_1} \right) \\ \sigma_{23} = C_{14} \frac{\partial u_1}{\partial x_1} + C_{24} \frac{\partial u_2}{\partial x_2} + C_{34} \frac{\partial u_3}{\partial x_3} + C_{44} \left(\frac{\partial u_2}{\partial x_3} + \frac{\partial u_3}{\partial x_2} \right) + C_{45} \left(\frac{\partial u_1}{\partial x_3} + \frac{\partial u_3}{\partial x_1} \right) + C_{46} \left(\frac{\partial u_1}{\partial x_2} + \frac{\partial u_2}{\partial x_1} \right) \\ \sigma_{13} = C_{15} \frac{\partial u_1}{\partial x_1} + C_{25} \frac{\partial u_2}{\partial x_2} + C_{35} \frac{\partial u_3}{\partial x_3} + C_{45} \left(\frac{\partial u_2}{\partial x_3} + \frac{\partial u_3}{\partial x_2} \right) + C_{55} \left(\frac{\partial u_1}{\partial x_3} + \frac{\partial u_3}{\partial x_1} \right) + C_{56} \left(\frac{\partial u_1}{\partial x_2} + \frac{\partial u_2}{\partial x_1} \right) \\ \sigma_{12} = C_{16} \frac{\partial u_1}{\partial x_1} + C_{26} \frac{\partial u_2}{\partial x_2} + C_{36} \frac{\partial u_3}{\partial x_3} + C_{46} \left(\frac{\partial u_2}{\partial x_3} + \frac{\partial u_3}{\partial x_2} \right) + C_{56} \left(\frac{\partial u_1}{\partial x_3} + \frac{\partial u_3}{\partial x_1} \right) + C_{66} \left(\frac{\partial u_1}{\partial x_2} + \frac{\partial u_2}{\partial x_1} \right) \end{cases} \quad (2.22)$$

$$\begin{aligned} & C_{11} \frac{\partial^2 u_1}{\partial x_1^2} + C_{66} \frac{\partial^2 u_1}{\partial x_2^2} + C_{55} \frac{\partial^2 u_1}{\partial x_3^2} + 2C_{16} \frac{\partial^2 u_1}{\partial x_1 \partial x_2} + 2C_{15} \frac{\partial^2 u_1}{\partial x_1 \partial x_3} + 2C_{56} \frac{\partial^2 u_1}{\partial x_2 \partial x_3} \\ & + C_{16} \frac{\partial^2 u_2}{\partial x_1^2} + C_{26} \frac{\partial^2 u_2}{\partial x_2^2} + C_{45} \frac{\partial^2 u_2}{\partial x_3^2} + (C_{12} + C_{66}) \frac{\partial^2 u_2}{\partial x_1 \partial x_2} + (C_{14} + C_{56}) \frac{\partial^2 u_2}{\partial x_1 \partial x_3} \\ & + (C_{46} + C_{25}) \frac{\partial^2 u_2}{\partial x_2 \partial x_3} + C_{15} \frac{\partial^2 u_3}{\partial x_1^2} + C_{46} \frac{\partial^2 u_3}{\partial x_2^2} + C_{35} \frac{\partial^2 u_3}{\partial x_3^2} + (C_{14} + C_{56}) \frac{\partial^2 u_3}{\partial x_1 \partial x_2} \\ & + (C_{13} + C_{55}) \frac{\partial^2 u_3}{\partial x_1 \partial x_3} + (C_{36} + C_{45}) \frac{\partial^2 u_3}{\partial x_2 \partial x_3} = \rho \frac{\partial^2 u_1}{\partial t^2} \end{aligned} \quad (2.23)$$

$$\begin{aligned} & C_{16} \frac{\partial^2 u_1}{\partial x_1^2} + C_{26} \frac{\partial^2 u_1}{\partial x_2^2} + C_{45} \frac{\partial^2 u_1}{\partial x_3^2} + (C_{12} + C_{66}) \frac{\partial^2 u_1}{\partial x_1 \partial x_2} + (C_{14} + C_{56}) \frac{\partial^2 u_1}{\partial x_1 \partial x_3} \\ & + (C_{46} + C_{25}) \frac{\partial^2 u_1}{\partial x_2 \partial x_3} + C_{66} \frac{\partial^2 u_2}{\partial x_1^2} + C_{22} \frac{\partial^2 u_2}{\partial x_2^2} + C_{44} \frac{\partial^2 u_2}{\partial x_3^2} + 2C_{26} \frac{\partial^2 u_2}{\partial x_1 \partial x_2} \\ & + 2C_{46} \frac{\partial^2 u_2}{\partial x_1 \partial x_3} + 2C_{24} \frac{\partial^2 u_2}{\partial x_2 \partial x_3} + C_{56} \frac{\partial^2 u_3}{\partial x_1^2} + C_{24} \frac{\partial^2 u_3}{\partial x_2^2} + C_{34} \frac{\partial^2 u_3}{\partial x_3^2} \\ & + (C_{46} + C_{25}) \frac{\partial^2 u_3}{\partial x_1 \partial x_2} + (C_{36} + C_{45}) \frac{\partial^2 u_3}{\partial x_1 \partial x_3} + (C_{23} + C_{44}) \frac{\partial^2 u_3}{\partial x_2 \partial x_3} = \rho \frac{\partial^2 u_2}{\partial t^2} \end{aligned} \quad (2.24)$$

$$\begin{aligned} & C_{15} \frac{\partial^2 u_1}{\partial x_1^2} + C_{46} \frac{\partial^2 u_1}{\partial x_2^2} + C_{35} \frac{\partial^2 u_1}{\partial x_3^2} + (C_{14} + C_{56}) \frac{\partial^2 u_1}{\partial x_1 \partial x_2} + (C_{13} + C_{55}) \frac{\partial^2 u_1}{\partial x_1 \partial x_3} \\ & + (C_{36} + C_{45}) \frac{\partial^2 u_1}{\partial x_2 \partial x_3} + C_{56} \frac{\partial^2 u_2}{\partial x_1^2} + C_{24} \frac{\partial^2 u_2}{\partial x_2^2} + C_{34} \frac{\partial^2 u_2}{\partial x_3^2} + (C_{46} + C_{25}) \frac{\partial^2 u_2}{\partial x_1 \partial x_2} \\ & + (C_{36} + C_{45}) \frac{\partial^2 u_2}{\partial x_1 \partial x_3} + (C_{23} + C_{44}) \frac{\partial^2 u_2}{\partial x_2 \partial x_3} + C_{55} \frac{\partial^2 u_3}{\partial x_1^2} + C_{44} \frac{\partial^2 u_3}{\partial x_2^2} + C_{33} \frac{\partial^2 u_3}{\partial x_3^2} \\ & + 2C_{45} \frac{\partial^2 u_3}{\partial x_1 \partial x_2} + 2C_{35} \frac{\partial^2 u_3}{\partial x_1 \partial x_3} + 2C_{34} \frac{\partial^2 u_3}{\partial x_2 \partial x_3} = \rho \frac{\partial^2 u_3}{\partial t^2} \end{aligned} \quad (2.25)$$

2.5 Bulk wave

Bulk wave is the basis of the partial wave superposition approach (PWSA) used to derive the dispersion equations of guided waves in a single-layered plate studied in the next chapter. Thus, the concept of bulk wave in solids will be introduced briefly in this section for monoclinic material. For other kind of materials, all the counterparts can be simplified from the corresponding equations.

2.5.1 Derivation of bulk wave

In the stiffness matrix of monoclinic material, the following elements are zero: $C_{14} = 0$, $C_{15} = 0$, $C_{24} = 0$, $C_{25} = 0$, $C_{34} = 0$, $C_{35} = 0$, $C_{46} = 0$, $C_{56} = 0$. Applying this condition to Eqs. (2.23)(2.24)(2.25), the simplified equations are obtained as follows.

$$\begin{aligned} C_{11} \frac{\partial^2 u_1}{\partial x_1^2} + C_{66} \frac{\partial^2 u_1}{\partial x_2^2} + C_{55} \frac{\partial^2 u_1}{\partial x_3^2} + 2C_{16} \frac{\partial^2 u_1}{\partial x_1 \partial x_2} + C_{16} \frac{\partial^2 u_2}{\partial x_1^2} + C_{26} \frac{\partial^2 u_2}{\partial x_2^2} + C_{45} \frac{\partial^2 u_2}{\partial x_3^2} \\ + (C_{12} + C_{66}) \frac{\partial^2 u_2}{\partial x_1 \partial x_2} + (C_{13} + C_{55}) \frac{\partial^2 u_3}{\partial x_1 \partial x_3} + (C_{36} + C_{45}) \frac{\partial^2 u_3}{\partial x_2 \partial x_3} = \rho \frac{\partial^2 u_1}{\partial t^2} \end{aligned} \quad (2.26)$$

$$\begin{aligned} C_{16} \frac{\partial^2 u_1}{\partial x_1^2} + C_{26} \frac{\partial^2 u_1}{\partial x_2^2} + C_{45} \frac{\partial^2 u_1}{\partial x_3^2} + (C_{12} + C_{66}) \frac{\partial^2 u_1}{\partial x_1 \partial x_2} + C_{66} \frac{\partial^2 u_2}{\partial x_1^2} + C_{22} \frac{\partial^2 u_2}{\partial x_2^2} \\ + C_{44} \frac{\partial^2 u_2}{\partial x_3^2} + 2C_{26} \frac{\partial^2 u_2}{\partial x_1 \partial x_2} + (C_{36} + C_{45}) \frac{\partial^2 u_3}{\partial x_1 \partial x_3} + (C_{23} + C_{44}) \frac{\partial^2 u_3}{\partial x_2 \partial x_3} = \rho \frac{\partial^2 u_2}{\partial t^2} \end{aligned} \quad (2.27)$$

$$\begin{aligned} (C_{13} + C_{55}) \frac{\partial^2 u_1}{\partial x_1 \partial x_3} + (C_{36} + C_{45}) \frac{\partial^2 u_1}{\partial x_2 \partial x_3} + (C_{36} + C_{45}) \frac{\partial^2 u_2}{\partial x_1 \partial x_3} \\ + (C_{23} + C_{44}) \frac{\partial^2 u_2}{\partial x_2 \partial x_3} + C_{55} \frac{\partial^2 u_3}{\partial x_1^2} + C_{44} \frac{\partial^2 u_3}{\partial x_2^2} + C_{33} \frac{\partial^2 u_3}{\partial x_3^2} + 2C_{45} \frac{\partial^2 u_3}{\partial x_1 \partial x_2} = \rho \frac{\partial^2 u_3}{\partial t^2} \end{aligned} \quad (2.28)$$

For bulk wave propagation in a solid in the direction provided by the wave vector $\vec{\xi}$ as illustrated in Figure 2.4,² the displacement fields can be expressed as the sinusoidal form shown in Eq. (2.29).

$$u_j = U_j e^{i\xi(n_1 x_1 + n_2 x_2 + n_3 x_3 - vt)} \quad (j = 1, 2, 3) \quad (2.29)$$

2. The media admissible for bulk wave propagation should be an unbounded solid space, however the unidirectional composite plate shown in Figure 2.4 is only for illustration purpose.

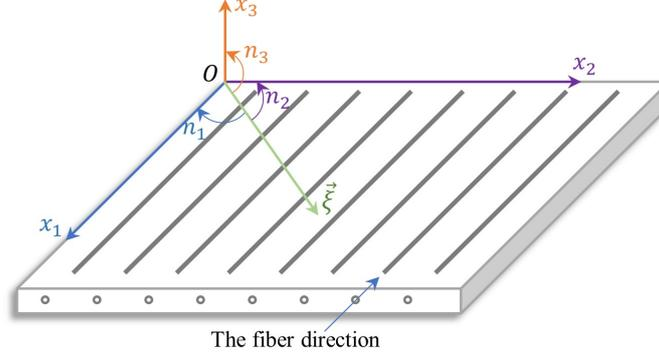


Figure 2.4 – The schematic diagram of bulk wave propagation.

where, i is the imaginary number unit, ξ and v are wavenumber and velocity, respectively, t is the time variable, U_j is the amplitude of u_j along axis x_j , and n_1, n_2, n_3 are the directional cosines of the wave vector $\vec{\xi}$.

With Eq. (2.29), the first order partial derivative of u_j can be easily computed as follows [2, 33].

$$\begin{cases} \frac{\partial u_j}{\partial x_1} = i\xi n_1 U_j e^{i\xi(n_1 x_1 + n_2 x_2 + n_3 x_3 - vt)} = i\xi n_1 u_j \\ \frac{\partial u_j}{\partial x_2} = i\xi n_2 U_j e^{i\xi(n_1 x_1 + n_2 x_2 + n_3 x_3 - vt)} = i\xi n_2 u_j \\ \frac{\partial u_j}{\partial x_3} = i\xi n_3 U_j e^{i\xi(n_1 x_1 + n_2 x_2 + n_3 x_3 - vt)} = i\xi n_3 u_j \\ \frac{\partial u_j}{\partial t} = -i\xi v U_j e^{i\xi(n_1 x_1 + n_2 x_2 + n_3 x_3 - vt)} = -i\xi v u_j \end{cases} \quad (j = 1, 2, 3) \quad (2.30)$$

Furthermore, Eq. (2.31) shows the second order partial derivative of u_j .

$$\begin{cases} \frac{\partial^2 u_j}{\partial x_1^2} = -\xi^2 n_1^2 u_j, & \frac{\partial^2 u_j}{\partial x_1 \partial x_2} = -\xi^2 n_1 n_2 u_j, \\ \frac{\partial^2 u_j}{\partial x_2^2} = -\xi^2 n_2^2 u_j, & \frac{\partial^2 u_j}{\partial x_2 \partial x_3} = -\xi^2 n_2 n_3 u_j, \\ \frac{\partial^2 u_j}{\partial x_3^2} = -\xi^2 n_3^2 u_j, & \frac{\partial^2 u_j}{\partial x_1 \partial x_3} = -\xi^2 n_1 n_3 u_j, \\ \frac{\partial^2 u_j}{\partial t^2} = -\xi^2 v^2 u_j, & (j = 1, 2, 3). \end{cases} \quad (2.31)$$

Substituting Eq. (2.31) into Eqs. (2.26)(2.27)(2.28) finally leads to the following eigen equation, $\mathbf{K}\mathbf{U} = \lambda\mathbf{U}$, which is termed as the Christoffel equation in wave propagation problems.

$$\begin{bmatrix} A & D & E \\ D & B & F \\ E & F & C \end{bmatrix} \begin{bmatrix} U_1 \\ U_2 \\ U_3 \end{bmatrix} = \rho v^2 \begin{bmatrix} U_1 \\ U_2 \\ U_3 \end{bmatrix} \quad (2.32)$$

where, the elements of the matrix \mathbf{K} are listed below, $\lambda = \rho v^2$ and $\mathbf{U} = [U_1, U_2, U_3]^T$ are the eigenvalue

and eigenvector, respectively.

$$\begin{cases} A = C_{11}n_1^2 + C_{66}n_2^2 + C_{55}n_3^2 + 2C_{16}n_1n_2, \\ B = C_{66}n_1^2 + C_{22}n_2^2 + C_{44}n_3^2 + 2C_{26}n_1n_2, \\ C = C_{55}n_1^2 + C_{44}n_2^2 + C_{33}n_3^2 + 2C_{45}n_1n_2, \\ D = C_{16}n_1^2 + C_{26}n_2^2 + C_{45}n_3^2 + (C_{12} + C_{66})n_1n_2, \\ E = (C_{13} + C_{55})n_1n_3 + (C_{36} + C_{45})n_2n_3, \\ F = (C_{36} + C_{45})n_1n_3 + (C_{23} + C_{44})n_2n_3. \end{cases} \quad (2.33)$$

For pure elastic media,³ \mathbf{K} is a real symmetric matrix since all the parameters in Eq. (2.33) are real numbers, which immediately leads to the two properties based on the fundamentals of linear algebra that all the three eigenvalues $(\lambda_1, \lambda_2, \lambda_3)$ are real numbers, and the three eigenvectors $(\mathbf{U}_1, \mathbf{U}_2, \mathbf{U}_3)$ are mutually orthogonal [56].

Each pair of eigenvalue and eigenvector of the Christoffel equation corresponds to a certain wave type amongst the shear horizontal wave (SH), shear vertical wave (SV) and longitudinal wave (L) that are characterized by the dominated component of polarization U_2 , U_3 and U_1 , respectively. In some situations, if there is not a dominated component for the solved eigenvector $[U_1, U_2, U_3]^T$ (that can always happen in anisotropic materials), a prefix *quasi* or *q* could be attached to the abbreviations SH, SV and L to represent the coupled waves, namely, qSH, qSV and qL waves. This usage is accepted by some references [37, 57, 8], but we do not emphasize it in the thesis, thus the prefix *quasi* or *q* is omitted unless stated otherwise.

2.5.2 Numerical example

A transversely isotropic material is adopted to illustrate the three elementary bulk waves. Its material properties are cited from [58] and listed in Eq. (2.34) for convenience. The (minor-)principal axes of this material are consistent with the coordinate system of Figure 2.4. We study the bulk waves propagating in the $x_1 - x_2$ plane, thus $n_3 = 0$, $E = 0$ and $F = 0$ in Eq. (2.33), which leads to the decoupled polarization U_3 from U_1 and U_2 . n_1 and n_2 can be easily computed from the specific directional angle of the wave vector $\vec{\xi}$ in Figure 2.4. Thus, for each direction angle, the three bulk wave velocities can be obtained by solving the eigenvalue problem in Eq. (2.32). By rotating the wave vector $\vec{\xi}$ from 0° to 360° , the polar plot of the three bulk wave velocities, characterizing the anisotropic

3. Elastic material makes the real-valued stiffness matrix and is considered in Chapters 3, 4, 5, 6 of the thesis. In contrast, viscoelastic material leads to the complex-valued stiffness matrix and is studied in Chapter 7.

2.6. CONCLUSION

effect of the three waves, is illustrated in Figure 2.5(a). In literature, the slowness curves being the inverse of wave velocity are also widely used [37], and they are presented in Figure 2.5(b). One can see that SH and L waves hold an anisotropic effect, and SV wave is quasi-isotropic. This is due to the reason that SV wave polarizes along U_3 direction which is decoupled from U_1 and U_2 directions.

$$\mathbf{C} = \begin{bmatrix} 155.6 & 3.7 & 3.7 & 0 & 0 & 0 \\ & 15.95 & 4.33 & 0 & 0 & 0 \\ & & 15.95 & 0 & 0 & 0 \\ & & & 5.81 & 0 & 0 \\ \text{sym} & & & & 7.46 & 0 \\ & & & & & 7.46 \end{bmatrix} \text{ GPa}, \quad \rho = 1600 \text{ kg/m}^3. \quad (2.34)$$

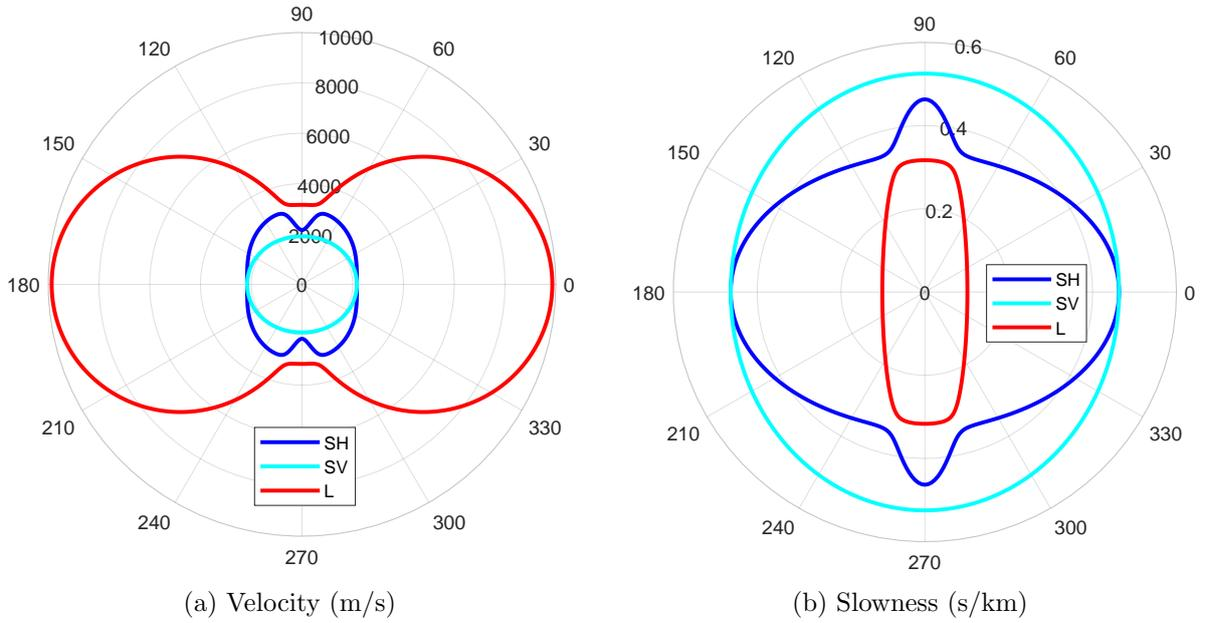


Figure 2.5 – Elementary bulk waves.

2.6 Conclusion

This chapter reviews the fundamental equations of 3D elasticity including stress-strain relation, strain-displacement relation and elastodynamic equations of motion. Five widely used composite materials are introduced in terms of their respective stiffness matrix, specifically, triclinic, monoclinic, orthotropic, transversely isotropic and isotropic materials. Stiffness matrix rotation is achieved by using Voigt notation and tensor rotation rule, along with the characteristics of the rotated matrix

2.6. CONCLUSION

shown in Table 2.1. The expanded field equations of triclinic materials lead to bulk wave equations in solids. This chapter defines many concepts and presents some fundamental equations and characteristics, and thus establishes the basis of subsequent chapters for studying guided waves propagation in plate structure.

Chapter 3

Guided waves propagation in a single-layered plate

This chapter mainly introduces the partial wave superposition approach (PWSA) which is based on 3D elasticity of Chapter 2 to model guided waves propagation in a single-layered composite plate. Traction-free boundary condition and symmetry condition will be employed to derive dispersion equations. For different composite materials, Lamb and SH waves will be coupled or separated according to the specific material characteristics. This chapter is a prerequisite for the following chapters that focus on guided waves propagation in a multi-layered composite laminate.

3.1 Wave propagation model of a single layer plate

The guided waves propagating in a single-layered plate schematically shown in Figure 3.1(a) is considered in this chapter. The plate extends infinitely in both directions of x_1 and x_2 axes, and the wave is guided for propagation along the direction of x_1 axis. In this condition, the plane-strain state in x_2 direction is satisfied which leads to the displacement field being invariant to x_2 . Thus, the time harmonic displacement expression in Eq. (2.29), which characterizes bulk waves, is now changed to the following one.

$$\mathbf{u} = \begin{bmatrix} u_1 \\ u_2 \\ u_3 \end{bmatrix} = \begin{bmatrix} U_1 \\ U_2 \\ U_3 \end{bmatrix} e^{i\xi(x_1 + \alpha x_3 - vt)} = \begin{bmatrix} U \\ V \\ W \end{bmatrix} e^{i\xi(x_1 + \alpha x_3 - vt)} \quad (3.1)$$

where, α is the ratio of wavenumbers between x_3 and x_1 direction as illustrated in Figure 3.1(a), v is the phase velocity,¹ $U = U_1$, $V = U_2$, $W = U_3$ are the amplitudes of displacements along x_1 , x_2 , x_3

1. In somewhere of the thesis, phase velocity is signified by c_p .

3.1. WAVE PROPAGATION MODEL OF A SINGLE LAYER PLATE

direction, respectively.

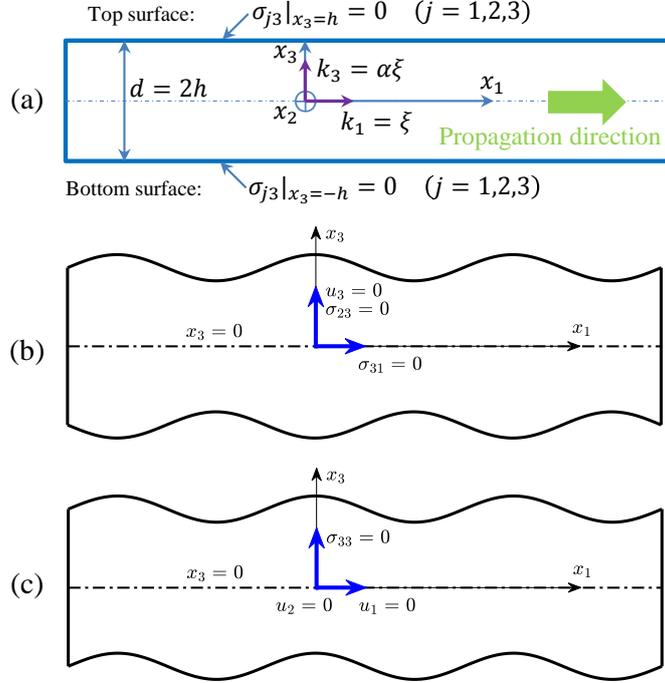


Figure 3.1 – Wave propagation model of a single-layered plate showing (a) boundary condition, (b) symmetric condition and (c) anti-symmetric condition.

Considering the traction-free boundary condition (BC) at the two surfaces of plate as illustrated in Figure 3.1(a), the three stresses (σ_{33} , σ_{23} , σ_{13}) should be zero when $x_3 = \pm h$ as formulated in Eq. (3.2). Furthermore, the displacement and stress fields have symmetry condition (SC) at the midplane of the plate [37] that is presented in Eqs. (3.3) and (3.4).

$$[\sigma_{33}, \sigma_{23}, \sigma_{13}]_{x_3=\pm h}^T = [0, 0, 0]^T \quad \text{for boundary condition} \quad (3.2)$$

$$[u_3, \sigma_{13}, \sigma_{23}]_{x_3=0}^T = [0, 0, 0]^T \quad \text{for symmetric condition} \quad (3.3)$$

$$[u_1, u_2, \sigma_{33}]_{x_3=0}^T = [0, 0, 0]^T \quad \text{for anti-symmetric condition} \quad (3.4)$$

where, h is the plate's half thickness and $x_3 = 0$ indicates the midplane of the plate.

To facilitate the following derivation of dispersion equations, the first and second order partial

3.2. DISPERSION EQUATIONS OF COUPLED LAMB AND SH WAVES IN TRICLINIC MATERIAL

derivative of displacement has been presented in Eqs. (3.5) and (3.6), respectively, based on Eq. (3.1).

$$\begin{cases} \frac{\partial u_j}{\partial x_1} = i\xi U_j e^{i\xi(x_1 + \alpha x_3 - vt)} = i\xi u_j \\ \frac{\partial u_j}{\partial x_2} = 0 \\ \frac{\partial u_j}{\partial x_3} = i\xi \alpha U_j e^{i\xi(x_1 + \alpha x_3 - vt)} = i\xi \alpha u_j \\ \frac{\partial u_j}{\partial t} = -i\xi v U_j e^{i\xi(x_1 + \alpha x_3 - vt)} = -i\xi v u_j \end{cases} \quad (j = 1, 2, 3) \quad (3.5)$$

$$\begin{cases} \frac{\partial^2 u_j}{\partial x_1^2} = -\xi^2 u_j, & \frac{\partial^2 u_j}{\partial x_1 \partial x_2} = 0, \\ \frac{\partial^2 u_j}{\partial x_2^2} = 0, & \frac{\partial^2 u_j}{\partial x_2 \partial x_3} = 0, \\ \frac{\partial^2 u_j}{\partial x_3^2} = -\xi^2 \alpha^2 u_j, & \frac{\partial^2 u_j}{\partial x_1 \partial x_3} = -\xi^2 \alpha u_j, \\ \frac{\partial^2 u_j}{\partial t^2} = -\xi^2 v^2 u_j, & (j = 1, 2, 3). \end{cases} \quad (3.6)$$

3.2 Dispersion equations of coupled Lamb and SH waves in triclinic material

With the specific form of wave field in Eq. (3.1), the boundary condition in Eq. (3.2) and the symmetry condition in Eqs. (3.3)(3.4), dispersion equations of guided waves propagating in a single-layered plate with triclinic material will be derived in this chapter. The same derivation procedure will be applied to other materials.

3.2.1 Christoffel equation

Substituting Eq. (3.6) into Eqs. (2.23)(2.24)(2.25), the following Christoffel equation $\mathbf{K}(\alpha)\mathbf{U} = \mathbf{0}$ can be derived.

$$\begin{bmatrix} K_{11}(\alpha) & K_{12}(\alpha) & K_{13}(\alpha) \\ K_{12}(\alpha) & K_{22}(\alpha) & K_{23}(\alpha) \\ K_{13}(\alpha) & K_{23}(\alpha) & K_{33}(\alpha) \end{bmatrix} \begin{bmatrix} U \\ V \\ W \end{bmatrix} = \begin{bmatrix} 0 \\ 0 \\ 0 \end{bmatrix} \quad (3.7)$$

where,

$$\begin{cases} K_{11}(\alpha) = C_{11} - \rho v^2 + 2C_{15}\alpha + C_{55}\alpha^2, & K_{12}(\alpha) = C_{16} + (C_{14} + C_{56})\alpha + C_{45}\alpha^2, \\ K_{13}(\alpha) = C_{15} + (C_{13} + C_{55})\alpha + C_{35}\alpha^2, & K_{22}(\alpha) = C_{66} - \rho v^2 + 2C_{46}\alpha + C_{44}\alpha^2, \\ K_{23}(\alpha) = C_{56} + (C_{36} + C_{45})\alpha + C_{34}\alpha^2, & K_{33}(\alpha) = C_{55} - \rho v^2 + 2C_{35}\alpha + C_{33}\alpha^2. \end{cases} \quad (3.8)$$

To make sure that Eq. (3.7) has nontrivial amplitudes of displacement \mathbf{U} , the matrix $\mathbf{K}(\alpha)$ should be singular, namely $\det\{\mathbf{K}(\alpha)\} = 0$, where $\det\{\cdot\}$ means the operator computing the determinant for a square matrix. Expanding this determinant results in a sixth order polynomial equation in terms of α as expressed in Eq. (3.9).

$$A_6\alpha^6 + A_5\alpha^5 + A_4\alpha^4 + A_3\alpha^3 + A_2\alpha^2 + A_1\alpha + A_0 = 0 \quad (3.9)$$

3.2. DISPERSION EQUATIONS OF COUPLED LAMB AND SH WAVES IN TRICLINIC MATERIAL

where, the seven polynomial coefficients are presented in Figure 3.2 and obtained via the software *Mathematica* due to its powerful capability of symbolic computing.

$$\begin{aligned}
 \text{Out}[70]= & -C35^2 C44 + 2 C34 C35 C45 - C33 C45^2 - C34^2 C55 + C33 C44 C55 \quad \text{A6} \\
 \text{Out}[71]= & 2 (-C15 C34^2 + C14 C34 C35 + C15 C33 C44 - C13 C35 C44 - C14 C33 C45 + C13 C34 C45 + C35 C36 C45 - C35^2 C46 - C34 C36 C55 + C33 C46 C55 + C34 C35 C56 - C33 C45 C56) \quad \text{A5} \\
 \text{Out}[72]= & -C14^2 C33 - C11 C34^2 + 2 C16 C34 C35 - 4 C15 C34 C36 - C13^2 C44 + C11 C33 C44 + 2 C15 C35 C44 - 2 C16 C33 C45 - 2 C15 C34 C45 + 2 C13 C36 C45 + 2 C13 C45^2 + \\
 & 4 C15 C33 C46 - 4 C13 C35 C46 - C36^2 C55 - 2 C13 C44 C55 + 2 C13 C34 C56 + 2 C35 C36 C56 - C33 C56^2 + 2 C14 (C13 C34 + C35 C36 - C35 C45 + C34 C55 - C33 C56) - \\
 & C35^2 C66 + C33 C55 C66 + C34^2 v^2 \rho + C35^2 v^2 \rho - C33 C44 v^2 \rho + C45^2 v^2 \rho - C33 C55 v^2 \rho - C44 C55 v^2 \rho \quad \text{A4} \\
 \text{Out}[74]= & 2 (-C14^2 C35 - C11 C34 C36 + C16 C35 C36 - C15 C36^2 + C11 C35 C44 - C11 C34 C45 - C16 C35 C45 - C15 C36 C45 - C13^2 C46 + C11 C33 C46 + 2 C15 C35 C46 + C16 C34 C55 - \\
 & C16 C33 C56 - C15 C34 C56 + C14 (-C16 C33 + C15 C34 + C13 C36 + C13 C45 + C36 C55 - C35 C56) + C15 C33 C66 + C13 (C16 C34 - C15 C44 - 2 C46 C55 + C36 C56 + 2 C45 C56 - C35 C66) + \\
 & 2 (C13 C35 + C34 C36 - C35 C44 - C15 (C33 + C44) + C14 C45 + C34 C45 - C33 C46 - C46 C55 + C45 C56) v^2 \rho \quad \text{A3} \\
 \text{Out}[75]= & -C16^2 C33 - C11 C36^2 - C15^2 C44 - 2 C11 C36 C45 - C11 C45^2 - 4 C13 C15 C46 + 4 C11 C35 C46 - C14^2 C55 + C11 C44 C55 - 2 C11 C34 C56 - 2 C15 C36 C56 + 2 C13 C56^2 + \\
 & 2 C14 (C15 (C36 + C45) + C13 C56) + 2 C16 (C15 C34 - 2 C14 C35 + C13 C36 + C13 C45 + C36 C55 - C35 C56) - C13^2 C66 + C11 C33 C66 + 2 C15 C35 C66 - 2 C13 C55 C66 + \\
 & (C13^2 + C14^2 - C11 C33 - 2 C15 C35 + C36^2 - C11 C44 + 2 C16 C45 + 2 C36 C45 + C45^2 - 4 C15 C46 - 4 C35 C46 + 2 C13 C55 - C44 C55 + 2 C14 C56 + 2 C34 C56 + C56^2 - C33 C66 - C55 C66) v^2 \rho + \\
 & C33 v^4 \rho^2 + C44 v^4 \rho^2 + C55 v^4 \rho^2 \quad \text{A2} \\
 \text{Out}[78]= & 2 (-C16^2 C35 - C15^2 C46 + C16 (C15 (C36 + C45) - C14 C55 + C13 C56) + C15 (C14 C56 - C13 C66) + C11 (C46 C55 - C36 C56 - C45 C56 + C35 C66)) + \\
 & 2 (C13 C15 + C14 C16 - C11 C35 - C11 C46 - C46 C55 + C16 C56 + C36 C56 + C45 C56 - C15 C66 - C35 C66) v^2 \rho + 2 (C15 + C35 + C46) v^4 \rho^2 \quad \text{A1} \\
 \text{Out}[80]= & -C16^2 C55 + 2 C15 C16 C56 - C11 C56^2 - C15^2 C66 + C11 C55 C66 + (C15^2 + C16^2 - C11 C55 + C56^2 - C11 C66 - C55 C66) v^2 \rho + C11 v^4 \rho^2 + C55 v^4 \rho^2 + C66 v^4 \rho^2 - v^6 \rho^3 \quad \text{A0}
 \end{aligned}$$

Figure 3.2 – The polynomial coefficients about α in Eq. (3.9).

Once the elastic coefficients C_{pq} and mass density ρ are known, meanwhile phase velocity v is provided as a specific value $v = v_0$, the seven polynomial coefficients can be computed based on Figure 3.2. Then, the six α 's roots can be solved via polynomial root-finding algorithms [59, 60], or by directly calling the MATLAB built-in function *roots*.

3.2.2 Displacement and stress fields

For each α_r ($r = 1, \dots, 6$), there will be a corresponding solution vector of displacement amplitude $\mathbf{U}_r = [U_r, V_r, W_r]^T$ according to Eq. (3.7), which is one degree on indeterminacy according to the theory of linear algebra [56]. The three displacement amplitudes can be determined by assigning a specific value for a certain term, for example $U_r = 1$, and V_r and W_r are found from the resulted equation set via Cramer's Rule as presented in Eq. (3.10).

$$V_r = \frac{K_{11}(\alpha_r)K_{23}(\alpha_r) - K_{12}(\alpha_r)K_{13}(\alpha_r)}{K_{13}(\alpha_r)K_{22}(\alpha_r) - K_{12}(\alpha_r)K_{23}(\alpha_r)}, \quad W_r = \frac{K_{11}(\alpha_r)K_{23}(\alpha_r) - K_{12}(\alpha_r)K_{13}(\alpha_r)}{K_{12}(\alpha_r)K_{33}(\alpha_r) - K_{13}(\alpha_r)K_{23}(\alpha_r)} \quad (3.10)$$

With the predefined form of displacements in Eq. (3.1) and the obtained amplitudes in Eq. (3.10), the displacement field $\mathbf{u} = [u_1, u_2, u_3]^T$ now can be written as the superposition of the six solutions as shown in Eq. (3.11), in which each term within the summation represents a partial wave. Therefore,

3.2. DISPERSION EQUATIONS OF COUPLED LAMB AND SH WAVES IN TRICLINIC MATERIAL

the denomination partial wave superposition approach (PWSA) is chosen.

$$\begin{cases} u_1 = \left(\sum_{r=1}^6 \eta_r e^{i\xi\alpha_r x_3} \right) e^{i\xi(x_1-vt)} \\ u_2 = \left(\sum_{r=1}^6 \eta_r V_r e^{i\xi\alpha_r x_3} \right) e^{i\xi(x_1-vt)} \\ u_3 = \left(\sum_{r=1}^6 \eta_r W_r e^{i\xi\alpha_r x_3} \right) e^{i\xi(x_1-vt)} \end{cases} \quad (3.11)$$

where, η_r is the participation factor of partial wave to be determined, which can be organized into a vector $\boldsymbol{\eta} = [\eta_1, \eta_2, \eta_3, \eta_4, \eta_5, \eta_6]^T$.

Substituting Eq. (3.11) into Eq. (2.22), the PWSA is also applied to the stress tensor as presented in Eq. (3.12).

$$\begin{cases} \sigma_{11} = \left\{ \sum_{r=1}^6 [(C_{11} + C_{15}\alpha_r) + (C_{16} + C_{14}\alpha_r)V_r + (C_{15} + C_{13}\alpha_r)W_r] e^{i\xi\alpha_r x_3} \eta_r \right\} i\xi e^{i\xi(x_1-vt)} \\ \sigma_{22} = \left\{ \sum_{r=1}^6 [(C_{12} + C_{25}\alpha_r) + (C_{26} + C_{24}\alpha_r)V_r + (C_{25} + C_{23}\alpha_r)W_r] e^{i\xi\alpha_r x_3} \eta_r \right\} i\xi e^{i\xi(x_1-vt)} \\ \sigma_{33} = \left\{ \sum_{r=1}^6 [(C_{13} + C_{35}\alpha_r) + (C_{36} + C_{34}\alpha_r)V_r + (C_{35} + C_{33}\alpha_r)W_r] e^{i\xi\alpha_r x_3} \eta_r \right\} i\xi e^{i\xi(x_1-vt)} \\ \sigma_{23} = \left\{ \sum_{r=1}^6 [(C_{14} + C_{45}\alpha_r) + (C_{46} + C_{44}\alpha_r)V_r + (C_{45} + C_{34}\alpha_r)W_r] e^{i\xi\alpha_r x_3} \eta_r \right\} i\xi e^{i\xi(x_1-vt)} \\ \sigma_{13} = \left\{ \sum_{r=1}^6 [(C_{15} + C_{55}\alpha_r) + (C_{56} + C_{45}\alpha_r)V_r + (C_{55} + C_{35}\alpha_r)W_r] e^{i\xi\alpha_r x_3} \eta_r \right\} i\xi e^{i\xi(x_1-vt)} \\ \sigma_{12} = \left\{ \sum_{r=1}^6 [(C_{16} + C_{56}\alpha_r) + (C_{66} + C_{46}\alpha_r)V_r + (C_{56} + C_{36}\alpha_r)W_r] e^{i\xi\alpha_r x_3} \eta_r \right\} i\xi e^{i\xi(x_1-vt)} \end{cases} \quad (3.12)$$

Considering that in the stress tensor, only the three terms (σ_{33} , σ_{23} , σ_{13}) are useful because they correspond to the boundary conditions (see Eq. (3.2)), the three terms are extracted into Eq. (3.13).

$$\begin{cases} \sigma_{33} = \left(\sum_{r=1}^6 \beta_{1r} e^{i\xi\alpha_r x_3} \eta_r \right) i\xi e^{i\xi(x_1-vt)} \\ \sigma_{23} = \left(\sum_{r=1}^6 \beta_{2r} e^{i\xi\alpha_r x_3} \eta_r \right) i\xi e^{i\xi(x_1-vt)} \\ \sigma_{13} = \left(\sum_{r=1}^6 \beta_{3r} e^{i\xi\alpha_r x_3} \eta_r \right) i\xi e^{i\xi(x_1-vt)} \end{cases} \quad (3.13)$$

where, β_{ir} is the amplitude of partial wave in terms of stress and is defined in Eq. (3.14).

$$\begin{cases} \beta_{1r} = (C_{13} + C_{35}\alpha_r) + (C_{36} + C_{34}\alpha_r)V_r + (C_{35} + C_{33}\alpha_r)W_r \\ \beta_{2r} = (C_{14} + C_{45}\alpha_r) + (C_{46} + C_{44}\alpha_r)V_r + (C_{45} + C_{34}\alpha_r)W_r \\ \beta_{3r} = (C_{15} + C_{55}\alpha_r) + (C_{56} + C_{45}\alpha_r)V_r + (C_{55} + C_{35}\alpha_r)W_r \end{cases} \quad (r = 1, \dots, 6) \quad (3.14)$$

3.2.3 Dispersion equations

Substituting Eq. (3.13) into Eq. (3.2) to apply the BC, the following linear homogeneous equation set $\mathbf{D}(v, \xi)\boldsymbol{\eta} = \mathbf{0}$ is obtained, where $\mathbf{D}(v, \xi)$ is the coefficient matrix in Eq. (3.15) depending on phase velocity v and wavenumber ξ . In order to produce non-trivial solution of $\boldsymbol{\eta}$, $\mathbf{D}(v, \xi)$ should vanish as presented in Eq. (3.16), which is the dispersion equation for coupled symmetric and anti-symmetric

3.2. DISPERSION EQUATIONS OF COUPLED LAMB AND SH WAVES IN TRICLINIC MATERIAL

modes in implicit² form.

$$\begin{bmatrix} \beta_{11}e^{-i\xi\alpha_1h} & \beta_{12}e^{-i\xi\alpha_2h} & \beta_{13}e^{-i\xi\alpha_3h} & \beta_{14}e^{-i\xi\alpha_4h} & \beta_{15}e^{-i\xi\alpha_5h} & \beta_{16}e^{-i\xi\alpha_6h} \\ \beta_{21}e^{-i\xi\alpha_1h} & \beta_{22}e^{-i\xi\alpha_2h} & \beta_{23}e^{-i\xi\alpha_3h} & \beta_{24}e^{-i\xi\alpha_4h} & \beta_{25}e^{-i\xi\alpha_5h} & \beta_{26}e^{-i\xi\alpha_6h} \\ \beta_{31}e^{-i\xi\alpha_1h} & \beta_{32}e^{-i\xi\alpha_2h} & \beta_{33}e^{-i\xi\alpha_3h} & \beta_{34}e^{-i\xi\alpha_4h} & \beta_{35}e^{-i\xi\alpha_5h} & \beta_{36}e^{-i\xi\alpha_6h} \\ \beta_{11}e^{i\xi\alpha_1h} & \beta_{12}e^{i\xi\alpha_2h} & \beta_{13}e^{i\xi\alpha_3h} & \beta_{14}e^{i\xi\alpha_4h} & \beta_{15}e^{i\xi\alpha_5h} & \beta_{16}e^{i\xi\alpha_6h} \\ \beta_{21}e^{i\xi\alpha_1h} & \beta_{22}e^{i\xi\alpha_2h} & \beta_{23}e^{i\xi\alpha_3h} & \beta_{24}e^{i\xi\alpha_4h} & \beta_{25}e^{i\xi\alpha_5h} & \beta_{26}e^{i\xi\alpha_6h} \\ \beta_{31}e^{i\xi\alpha_1h} & \beta_{32}e^{i\xi\alpha_2h} & \beta_{33}e^{i\xi\alpha_3h} & \beta_{34}e^{i\xi\alpha_4h} & \beta_{35}e^{i\xi\alpha_5h} & \beta_{36}e^{i\xi\alpha_6h} \end{bmatrix} \begin{bmatrix} \eta_1 \\ \eta_2 \\ \eta_3 \\ \eta_4 \\ \eta_5 \\ \eta_6 \end{bmatrix} = \begin{bmatrix} 0 \\ 0 \\ 0 \\ 0 \\ 0 \\ 0 \end{bmatrix} \quad (3.15)$$

$$\mathcal{D}(v, \xi) = \mathcal{D}^R(v, \xi) + i\mathcal{D}^I(v, \xi) \triangleq \det\{\mathbf{D}(v, \xi)\} = 0 \quad \text{for sym. and anti. modes} \quad (3.16)$$

Note that $\mathbf{D}(v, \xi)$ is a complex-valued matrix due to the existence of complex exponential terms in it. Thus, its determinant $\mathcal{D}(v, \xi)$ is a complex number in general and can be separated as real part $\mathcal{D}^R(v, \xi)$ and imaginary part $\mathcal{D}^I(v, \xi)$ as indicated in Eq. (3.16).

If the SC is added along with the BC to derive dispersion equation, the option $x_3 = -h$ in Eq. (3.2) is redundant. Thus, the BC at $x_3 = h$ in Eq. (3.2) and the SC in Eq. (3.3) are employed to derive the dispersion equation of symmetric modes. Substituting Eqs. (3.11) and (3.13) into the two equations, meanwhile reorganizing the resulted equation set to matrix form with the participation factors $\boldsymbol{\eta}$ being the unknown vector, one obtains Eqs. (3.17) and (3.18).

$$\begin{bmatrix} W_1 & W_2 & W_3 & W_4 & W_5 & W_6 \\ \beta_{21} & \beta_{22} & \beta_{23} & \beta_{24} & \beta_{25} & \beta_{26} \\ \beta_{31} & \beta_{32} & \beta_{33} & \beta_{34} & \beta_{35} & \beta_{36} \\ \beta_{11}e^{i\xi\alpha_1h} & \beta_{12}e^{i\xi\alpha_2h} & \beta_{13}e^{i\xi\alpha_3h} & \beta_{14}e^{i\xi\alpha_4h} & \beta_{15}e^{i\xi\alpha_5h} & \beta_{16}e^{i\xi\alpha_6h} \\ \beta_{21}e^{i\xi\alpha_1h} & \beta_{22}e^{i\xi\alpha_2h} & \beta_{23}e^{i\xi\alpha_3h} & \beta_{24}e^{i\xi\alpha_4h} & \beta_{25}e^{i\xi\alpha_5h} & \beta_{26}e^{i\xi\alpha_6h} \\ \beta_{31}e^{i\xi\alpha_1h} & \beta_{32}e^{i\xi\alpha_2h} & \beta_{33}e^{i\xi\alpha_3h} & \beta_{34}e^{i\xi\alpha_4h} & \beta_{35}e^{i\xi\alpha_5h} & \beta_{36}e^{i\xi\alpha_6h} \end{bmatrix} \begin{bmatrix} \eta_1 \\ \eta_2 \\ \eta_3 \\ \eta_4 \\ \eta_5 \\ \eta_6 \end{bmatrix} = \begin{bmatrix} 0 \\ 0 \\ 0 \\ 0 \\ 0 \\ 0 \end{bmatrix} \quad (3.17)$$

$$\mathcal{D}_s(v, \xi) = \mathcal{D}_s^R(v, \xi) + i\mathcal{D}_s^I(v, \xi) \triangleq \det\{\mathbf{D}_s(v, \xi)\} = 0 \quad \text{for symmetric modes} \quad (3.18)$$

where, the subscript ‘s’ denotes the symmetric modes.

Substituting Eqs. (3.11) and (3.13) into Eqs. (3.2) and (3.4), the dispersion equation of anti-symmetric modes can be derived as presented in Eqs. (3.19) and (3.20).

$$\begin{bmatrix} 1 & 1 & 1 & 1 & 1 & 1 \\ V_1 & V_2 & V_3 & V_4 & V_5 & V_6 \\ \beta_{11} & \beta_{12} & \beta_{13} & \beta_{14} & \beta_{15} & \beta_{16} \\ \beta_{11}e^{i\xi\alpha_1h} & \beta_{12}e^{i\xi\alpha_2h} & \beta_{13}e^{i\xi\alpha_3h} & \beta_{14}e^{i\xi\alpha_4h} & \beta_{15}e^{i\xi\alpha_5h} & \beta_{16}e^{i\xi\alpha_6h} \\ \beta_{21}e^{i\xi\alpha_1h} & \beta_{22}e^{i\xi\alpha_2h} & \beta_{23}e^{i\xi\alpha_3h} & \beta_{24}e^{i\xi\alpha_4h} & \beta_{25}e^{i\xi\alpha_5h} & \beta_{26}e^{i\xi\alpha_6h} \\ \beta_{31}e^{i\xi\alpha_1h} & \beta_{32}e^{i\xi\alpha_2h} & \beta_{33}e^{i\xi\alpha_3h} & \beta_{34}e^{i\xi\alpha_4h} & \beta_{35}e^{i\xi\alpha_5h} & \beta_{36}e^{i\xi\alpha_6h} \end{bmatrix} \begin{bmatrix} \eta_1 \\ \eta_2 \\ \eta_3 \\ \eta_4 \\ \eta_5 \\ \eta_6 \end{bmatrix} = \begin{bmatrix} 0 \\ 0 \\ 0 \\ 0 \\ 0 \\ 0 \end{bmatrix} \quad (3.19)$$

2. In the thesis, the term *implicit* means that the dispersion equation is defined in matrix-determinant form.

3.2. DISPERSION EQUATIONS OF COUPLED LAMB AND SH WAVES IN TRICLINIC MATERIAL

$$\mathcal{D}_a(v, \xi) = \mathcal{D}_a^R(v, \xi) + i\mathcal{D}_a^I(v, \xi) \triangleq \det\{\mathbf{D}_a(v, \xi)\} = 0 \quad \text{for anti-symmetric modes} \quad (3.20)$$

where, the subscript ‘ a ’ denotes the anti-symmetric modes.

Once the dispersion equation is built regardless of which SC being considered, for example, $\mathcal{D}(v, \xi) = 0$ in Eq. (3.16), it can be solved through some root-finding methods such as Newton-Raphson method or bisection method. From numerical realization perspective, Newton-Raphson method is not suitable for this problem because it requires the derivative information of the characteristic function $\mathcal{D}(v, \xi)$ which is not available since $\mathcal{D}(v, \xi)$ is transcendental. Thus, bisection method is the desired one. With such method, the solutions can be found by fixing $v = v_0$ to sweep the roots of ξ ($\mathcal{D}(v_0, \xi) = 0$) or by fixing $\xi = \xi_0$ to sweep the roots of v ($\mathcal{D}(v, \xi_0) = 0$). The two sweeping schemes will be comprehensively investigated in Chapter 6.

The continuous loci of solutions (v, ξ) form the dispersion curves in $v - \xi$ domain in which each individual branch represents a single modal curve. The dispersion curves in $\omega - \xi$ and $\omega - v$ domains can be obtained from the relation $\omega = \xi v$, where ω is the angular frequency. For (quasi-)isotropic materials, the group velocity c_g is computed from each individual branch of dispersion curves based on Eq. (3.21a) in $\omega - \xi$ domain or Eq. (3.21b) in $\omega - v$ domain. For anisotropic materials, the steering effect should be taken into account when computing group velocity in these materials. The related work was reported in [37]. In the subsequent chapters of the thesis, we directly present the computed dispersion curves of group velocity in anisotropic materials by taking advantage of the approach reported in [37] without a statement.

$$c_g = \frac{\partial \omega}{\partial \xi} \quad (3.21a)$$

$$c_g = \frac{v^2}{v - \omega \frac{\partial v}{\partial \omega}} \quad (3.21b)$$

3.2.4 Mode shape

When a solution point (v, ξ) of the symmetry-omitted dispersion equation $\mathcal{D}(v, \xi) = 0$ in Eq. (3.16) is obtained, it can be substituted back in Eq. (3.15) to compute the vector $\boldsymbol{\eta}$ which corresponds to the zero-eigenvalue correlated eigenvector of the matrix $\mathbf{D}(v, \xi)$ in Eq. (3.15). Once all the required quantities are obtained, the displacement and stress fields described in Eqs. (3.11) and (3.13) can be

3.3. DISPERSION EQUATIONS OF COUPLED LAMB AND SH WAVES IN MONOCLINIC MATERIAL

reconstructed. At a fixed section of the waveguide, i.e. omitting the phase term $e^{i\xi(x_1-vt)}$ in Eqs. (3.11) and (3.13), the displacement and stress mode shapes of the plate can be portrayed along the plate thickness direction x_3 through Eqs. (3.11) and (3.13), respectively, which are further classified into symmetric and anti-symmetric modes by checking the symmetry condition at the midplane of the plate stated in Eqs. (3.3) and (3.4). Undoubtedly, if the solution point (v, ξ) is substituted into Eq. (3.17) or (3.19), the computed displacement and stress mode shapes will meet the symmetry condition automatically.

3.3 Dispersion equations of coupled Lamb and SH waves in monoclinic material

The dispersion equations of monoclinic material is a simpler case of triclinic material, which will be obtained by making a series of simplifications for the equations of triclinic material.

3.3.1 Christoffel equation

For monoclinic material, the following stiffness coefficients are zero in addition to the triclinic material, $C_{14}, C_{15}, C_{24}, C_{25}, C_{34}, C_{35}, C_{46}, C_{56} = 0$. Thus, the Christoffel equation of triclinic material in Eq. (3.7) changes to Eq. (3.22), though it remains the same form as Eq. (3.7) yet with different elements in the matrix $\mathbf{K}(\alpha)$ as shown in Eq. (3.23).

$$\begin{bmatrix} K_{11}(\alpha) & K_{12}(\alpha) & K_{13}(\alpha) \\ K_{12}(\alpha) & K_{22}(\alpha) & K_{23}(\alpha) \\ K_{13}(\alpha) & K_{23}(\alpha) & K_{33}(\alpha) \end{bmatrix} \begin{bmatrix} U \\ V \\ W \end{bmatrix} = \begin{bmatrix} 0 \\ 0 \\ 0 \end{bmatrix} \quad (3.22)$$

$$\begin{cases} K_{11}(\alpha) = C_{11} - \rho v^2 + C_{55}\alpha^2, & K_{12}(\alpha) = C_{16} + C_{45}\alpha^2, & K_{13}(\alpha) = (C_{13} + C_{55})\alpha, \\ K_{22}(\alpha) = C_{66} - \rho v^2 + C_{44}\alpha^2, & K_{23}(\alpha) = (C_{36} + C_{45})\alpha, & K_{33}(\alpha) = C_{55} - \rho v^2 + C_{33}\alpha^2. \end{cases} \quad (3.23)$$

The singular condition of matrix $\mathbf{K}(\alpha)$ leads to $\det\{\mathbf{K}(\alpha)\} = 0$. Expanding this determinant produces a third order polynomial equation in terms of α^2 as expressed in Eq. (3.24).

$$A_6\alpha^6 + A_4\alpha^4 + A_2\alpha^2 + A_0 = 0 \quad (3.24)$$

where, the coefficients A_6, A_4, A_2, A_0 are presented in Eq. (3.25), and can be computed from the

3.3. DISPERSION EQUATIONS OF COUPLED LAMB AND SH WAVES IN MONOCLINIC MATERIAL

constant elastic coefficients C_{pq} and mass density ρ at a specified phase velocity $v = v_0$.

$$\left\{ \begin{array}{l} A_6 = C_{33}C_{44}C_{55} - C_{33}C_{45}^2 \\ A_4 = (C_{44}C_{55} - C_{45}^2)(C_{55} - \rho v^2) + C_{33}C_{55}(C_{66} - \rho v^2) + C_{33}C_{44}(C_{11} - \rho v^2) \\ \quad - 2C_{16}C_{45}C_{33} + 2(C_{36} + C_{45})(C_{13} + C_{55})C_{45} \\ \quad - (C_{13} + C_{55})^2C_{44} - (C_{45} + C_{36})^2C_{55} \\ A_2 = C_{33}(C_{11} - \rho v^2)(C_{66} - \rho v^2) + C_{44}(C_{11} - \rho v^2)(C_{55} - \rho v^2) \\ \quad + C_{55}(C_{66} - \rho v^2)(C_{55} - \rho v^2) - (C_{11} - \rho v^2)(C_{45} + C_{36})^2 \\ \quad - (C_{66} - \rho v^2)(C_{13} + C_{55})^2 - 2(C_{55} - \rho v^2)C_{16}C_{45} \\ \quad + 2C_{16}(C_{45} + C_{36})(C_{13} + C_{55}) - C_{16}^2C_{33} \\ A_0 = [(C_{11} - \rho v^2)(C_{66} - \rho v^2) - C_{16}^2] (C_{55} - \rho v^2) \end{array} \right. \quad (3.25)$$

The three α^2 roots can be solved from Eq. (3.24) via Cardano's Formula or polynomial root-finding algorithms. The six α 's roots are further obtained by satisfying the conditions in Eq. (3.26).

$$\alpha_2 = -\alpha_1, \alpha_4 = -\alpha_3, \alpha_6 = -\alpha_5 \quad (3.26)$$

3.3.2 Displacement and stress fields

For each α_r ($r = 1, \dots, 6$), the three displacement amplitudes (U_r, V_r, W_r) can be solved from Eq. (3.22) by assigning $U_r = 1$, then V_r and W_r are found from the resulted equation set via Cramer's Rule as presented in Eq. (3.27).

$$V_r = \frac{K_{11}(\alpha_r)K_{23}(\alpha_r) - K_{12}(\alpha_r)K_{13}(\alpha_r)}{K_{13}(\alpha_r)K_{22}(\alpha_r) - K_{12}(\alpha_r)K_{23}(\alpha_r)}, \quad W_r = \frac{K_{11}(\alpha_r)K_{23}(\alpha_r) - K_{12}(\alpha_r)K_{13}(\alpha_r)}{K_{12}(\alpha_r)K_{33}(\alpha_r) - K_{13}(\alpha_r)K_{23}(\alpha_r)} \quad (3.27)$$

With the negative reciprocity in Eq. (3.26), it is easy to get the relation of Eq. (3.28) if one substitutes Eq. (3.26) and the detailed expression of $K_{ij}(\alpha)$ of Eq. (3.23) into Eq. (3.27).

$$V_2 = V_1, V_4 = V_3, V_6 = V_5; \quad W_2 = -W_1, W_4 = -W_3, W_6 = -W_5 \quad (3.28)$$

By applying PWSA, the displacement field of monoclinic material is now presented in Eq. (3.29), which remains the same form as Eq. (3.11) but has different forms of V_r and W_r thanks to Eq. (3.23).

$$\left\{ \begin{array}{l} u_1 = \left(\sum_{r=1}^6 \eta_r e^{i\xi \alpha_r x_3} \right) e^{i\xi(x_1 - vt)} \\ u_2 = \left(\sum_{r=1}^6 \eta_r V_r e^{i\xi \alpha_r x_3} \right) e^{i\xi(x_1 - vt)} \\ u_3 = \left(\sum_{r=1}^6 \eta_r W_r e^{i\xi \alpha_r x_3} \right) e^{i\xi(x_1 - vt)} \end{array} \right. \quad (3.29)$$

3.3. DISPERSION EQUATIONS OF COUPLED LAMB AND SH WAVES IN MONOCLINIC MATERIAL

The stress field $(\sigma_{33}, \sigma_{23}, \sigma_{13})$ of monoclinic material is expressed in Eq. (3.30) based on PWSA, which keeps the same form as Eq. (3.13) but has different forms of $(\beta_{1r}, \beta_{2r}, \beta_{3r})$ as shown in Eq. (3.31).

$$\begin{cases} \sigma_{33} = \left(\sum_{r=1}^6 \beta_{1r} e^{i\xi\alpha_r x_3} \eta_r \right) i\xi e^{i\xi(x_1-vt)} \\ \sigma_{23} = \left(\sum_{r=1}^6 \beta_{2r} e^{i\xi\alpha_r x_3} \eta_r \right) i\xi e^{i\xi(x_1-vt)} \\ \sigma_{13} = \left(\sum_{r=1}^6 \beta_{3r} e^{i\xi\alpha_r x_3} \eta_r \right) i\xi e^{i\xi(x_1-vt)} \end{cases} \quad (3.30)$$

$$\begin{cases} \beta_{1r} = C_{13} + C_{36}V_r + C_{33}\alpha_r W_r \\ \beta_{2r} = C_{45}\alpha_r + C_{44}\alpha_r V_r + C_{45}W_r \\ \beta_{3r} = C_{55}\alpha_r + C_{45}\alpha_r V_r + C_{55}W_r \end{cases} \quad (r = 1, \dots, 6) \quad (3.31)$$

Like in Eq. (3.28), β_{ir} exhibits some relationships described in Eq. (3.32).

$$\begin{aligned} \beta_{12} &= \beta_{11}, \quad \beta_{14} = \beta_{13}, \quad \beta_{16} = \beta_{15} \\ \beta_{22} &= -\beta_{21}, \quad \beta_{24} = -\beta_{23}, \quad \beta_{26} = -\beta_{25} \\ \beta_{32} &= -\beta_{31}, \quad \beta_{34} = -\beta_{33}, \quad \beta_{36} = -\beta_{35} \end{aligned} \quad (3.32)$$

3.3.3 Dispersion equations

Under the condition of Eqs. (3.26)(3.28)(3.32), the linear homogeneous equation set of the symmetric modes of triclinic material in Eq. (3.17) is now changed to Eq. (3.33). Thus, the dispersion equation of symmetric modes of monoclinic material is generated in Eq. (3.34) in implicit form.

$$\begin{bmatrix} W_1 & -W_1 & W_3 & -W_3 & W_5 & -W_5 \\ \beta_{21} & -\beta_{21} & \beta_{23} & -\beta_{23} & \beta_{25} & -\beta_{25} \\ \beta_{31} & -\beta_{31} & \beta_{33} & -\beta_{33} & \beta_{35} & -\beta_{35} \\ \beta_{11}e^{i\xi\alpha_1 h} & \beta_{11}e^{-i\xi\alpha_1 h} & \beta_{13}e^{i\xi\alpha_3 h} & \beta_{13}e^{-i\xi\alpha_3 h} & \beta_{15}e^{i\xi\alpha_5 h} & \beta_{15}e^{-i\xi\alpha_5 h} \\ \beta_{21}e^{i\xi\alpha_1 h} & -\beta_{21}e^{-i\xi\alpha_1 h} & \beta_{23}e^{i\xi\alpha_3 h} & -\beta_{23}e^{-i\xi\alpha_3 h} & \beta_{25}e^{i\xi\alpha_5 h} & -\beta_{25}e^{-i\xi\alpha_5 h} \\ \beta_{31}e^{i\xi\alpha_1 h} & -\beta_{31}e^{-i\xi\alpha_1 h} & \beta_{33}e^{i\xi\alpha_3 h} & -\beta_{33}e^{-i\xi\alpha_3 h} & \beta_{35}e^{i\xi\alpha_5 h} & -\beta_{35}e^{-i\xi\alpha_5 h} \end{bmatrix} \begin{bmatrix} \eta_1 \\ \eta_2 \\ \eta_3 \\ \eta_4 \\ \eta_5 \\ \eta_6 \end{bmatrix} = \begin{bmatrix} 0 \\ 0 \\ 0 \\ 0 \\ 0 \\ 0 \end{bmatrix} \quad (3.33)$$

$$\mathcal{D}_s(v, \xi) = \mathcal{D}_s^R(v, \xi) + i\mathcal{D}_s^I(v, \xi) \triangleq \det\{\mathbf{D}_s(v, \xi)\} = 0 \quad \text{for symmetric modes} \quad (3.34)$$

where, the subscript 's' denotes the symmetric modes.

For the dispersion equation of anti-symmetric modes of monoclinic material, it can be derived from Eq. (3.19) which belongs to the triclinic material by applying Eqs. (3.26)(3.28)(3.32). Thus, Eq. (3.35)

3.3. DISPERSION EQUATIONS OF COUPLED LAMB AND SH WAVES IN MONOCLINIC MATERIAL

is generated and the desired dispersion equation is expressed as implicit form in Eq. (3.36).

$$\begin{bmatrix} 1 & 1 & 1 & 1 & 1 & 1 \\ V_1 & V_1 & V_3 & V_3 & V_5 & V_5 \\ \beta_{11} & \beta_{11} & \beta_{13} & \beta_{13} & \beta_{15} & \beta_{15} \\ \beta_{11}e^{i\xi\alpha_1h} & \beta_{11}e^{-i\xi\alpha_1h} & \beta_{13}e^{i\xi\alpha_3h} & \beta_{13}e^{-i\xi\alpha_3h} & \beta_{15}e^{i\xi\alpha_5h} & \beta_{15}e^{-i\xi\alpha_5h} \\ \beta_{21}e^{i\xi\alpha_1h} & -\beta_{21}e^{-i\xi\alpha_1h} & \beta_{23}e^{i\xi\alpha_3h} & -\beta_{23}e^{-i\xi\alpha_3h} & \beta_{25}e^{i\xi\alpha_5h} & -\beta_{25}e^{-i\xi\alpha_5h} \\ \beta_{31}e^{i\xi\alpha_1h} & -\beta_{31}e^{-i\xi\alpha_1h} & \beta_{33}e^{i\xi\alpha_3h} & -\beta_{33}e^{-i\xi\alpha_3h} & \beta_{35}e^{i\xi\alpha_5h} & -\beta_{35}e^{-i\xi\alpha_5h} \end{bmatrix} \begin{bmatrix} \eta_1 \\ \eta_2 \\ \eta_3 \\ \eta_4 \\ \eta_5 \\ \eta_6 \end{bmatrix} = \begin{bmatrix} 0 \\ 0 \\ 0 \\ 0 \\ 0 \\ 0 \end{bmatrix} \quad (3.35)$$

$$\mathcal{D}_a(v, \xi) = \mathcal{D}_a^R(v, \xi) + i\mathcal{D}_a^I(v, \xi) \triangleq \det\{\mathbf{D}_a(v, \xi)\} = 0 \quad \text{for anti-symmetric modes} \quad (3.36)$$

where, the subscript ‘a’ denotes the anti-symmetric modes.

To facilitate computation, the explicit³ formula of the determinant of $\mathbf{D}_s(v, \xi)$ in Eq. (3.34) and $\mathbf{D}_a(v, \xi)$ in Eq. (3.36) are derived into Eqs. (3.37a) and (3.37b) by right of the software *Mathematica* due to its powerful capability of symbolic computing. Note that during manipulation using *Mathematica*, the Euler’s equation should be used, for example, $e^{i\xi\alpha_1h} = \cos(\xi\alpha_1h) + i\sin(\xi\alpha_1h)$.

$$\begin{aligned} \mathcal{D}_s(v, \xi) = & [B_1 \cos(\xi\alpha_1h) \sin(\xi\alpha_3h) \sin(\xi\alpha_5h) + B_2 \sin(\xi\alpha_1h) \cos(\xi\alpha_3h) \sin(\xi\alpha_5h) \\ & + B_3 \sin(\xi\alpha_1h) \sin(\xi\alpha_3h) \cos(\xi\alpha_5h)] B_4 \end{aligned} \quad (3.37a)$$

$$\begin{aligned} \mathcal{D}_a(v, \xi) = & [B_1 \sin(\xi\alpha_1h) \cos(\xi\alpha_3h) \cos(\xi\alpha_5h) + B_2 \cos(\xi\alpha_1h) \sin(\xi\alpha_3h) \cos(\xi\alpha_5h) \\ & + B_3 \cos(\xi\alpha_1h) \cos(\xi\alpha_3h) \sin(\xi\alpha_5h)] B_5 \end{aligned} \quad (3.37b)$$

where,

$$\begin{cases} B_1 = \beta_{11}(\beta_{25}\beta_{33} - \beta_{23}\beta_{35}), & B_2 = \beta_{13}(\beta_{21}\beta_{35} - \beta_{25}\beta_{31}), & B_3 = \beta_{15}(\beta_{23}\beta_{31} - \beta_{21}\beta_{33}) \\ B_4 = 8 [W_1(\beta_{25}\beta_{33} - \beta_{23}\beta_{35}) + W_3(\beta_{21}\beta_{35} - \beta_{25}\beta_{31}) + W_5(\beta_{23}\beta_{31} - \beta_{21}\beta_{33})] \\ B_5 = 8i [V_1(\beta_{15} - \beta_{13}) + V_3(\beta_{11} - \beta_{15}) + V_5(\beta_{13} - \beta_{11})] \end{cases} \quad (3.38)$$

With Eqs. (3.37a) and (3.37b), the implicit dispersion equations, Eqs. (3.34) and (3.36), of the monoclinic material have been exposed in Eqs. (3.39a) and (3.39b), which are classically presented in many textbooks [33, 4]. Considering that the tangent functions are discontinuous, it is preferred to adopt Eqs. (3.37a) and (3.37b) for computation.

$$B_1 \cot(\xi\alpha_1h) + B_2 \cot(\xi\alpha_3h) + B_3 \cot(\xi\alpha_5h) = 0 \quad \text{for symmetric modes} \quad (3.39a)$$

$$B_1 \tan(\xi\alpha_1h) + B_2 \tan(\xi\alpha_3h) + B_3 \tan(\xi\alpha_5h) = 0 \quad \text{for anti-symmetric modes} \quad (3.39b)$$

3. In this thesis, the term *explicit* means that the dispersion equation is simplified from the original one defined in matrix-determinant form.

3.4. DISPERSION EQUATIONS OF DECOUPLED LAMB AND SH WAVES IN ORTHOTROPIC MATERIAL

Once a solution point (v, ξ) of a certain dispersion equation, specifically $\mathcal{D}_s(v, \xi) = 0$ in Eq. (3.34) or $\mathcal{D}_a(v, \xi) = 0$ in Eq. (3.36), is found, the displacement and stress mode shapes of monoclinic material can be obtained easily by following the same strategy as triclinic material stated in section 3.2.4.

Note that due to the complexity of triclinic materials, there is not a simple explicit form of the dispersion equations in Section 3.2.3 like for monoclinic materials presented in this section.

3.4 Dispersion equations of decoupled Lamb and SH waves in orthotropic material

In orthotropic plate, guided waves will be decoupled into Lamb and SH waves, which will be demonstrated in this section.

3.4.1 Christoffel equation

For orthotropic material, the following stiffness coefficients are zero in addition to the monoclinic material, $C_{16}, C_{26}, C_{36}, C_{45} = 0$, which makes the Christoffel equation of monoclinic material in Eq. (3.22) change to Eq. (3.40).

$$\begin{bmatrix} C_{11} - \rho v^2 + C_{55}\alpha^2 & 0 & (C_{13} + C_{55})\alpha \\ 0 & C_{66} - \rho v^2 + C_{44}\alpha^2 & 0 \\ (C_{13} + C_{55})\alpha & 0 & C_{55} - \rho v^2 + C_{33}\alpha^2 \end{bmatrix} \begin{bmatrix} U \\ V \\ W \end{bmatrix} = \begin{bmatrix} 0 \\ 0 \\ 0 \end{bmatrix} \quad (3.40)$$

Naturally, Eq. (3.40) can be separated as Eqs. (3.42) and (3.41). Since Eq. (3.41) only involves in the displacement u_2 (shear horizontal direction), the wave derived from Eq. (3.41) is termed as SH wave. Correspondingly, the wave derived from Eq. (3.42) is termed as Lamb wave because this equation involves in the displacements u_1 (longitudinal direction) and u_3 (shear vertical direction).

$$(C_{66} - \rho v^2 + C_{44}\alpha^2)V = 0 \quad (3.41)$$

$$\begin{bmatrix} C_{11} - \rho v^2 + C_{55}\alpha^2 & (C_{13} + C_{55})\alpha \\ (C_{13} + C_{55})\alpha & C_{55} - \rho v^2 + C_{33}\alpha^2 \end{bmatrix} \begin{bmatrix} U \\ W \end{bmatrix} = \begin{bmatrix} 0 \\ 0 \end{bmatrix} \quad (3.42)$$

In the next subsections, the dispersion equations of Lamb and SH waves will be derived separately.

3.4.2 Displacement and stress fields of Lamb wave

The nontrivial solution of $[U_1, U_3]^T$ in Eq. (3.42) requires the singular condition of the coefficient matrix as presented in Eq. (3.43). It is the possibility to expand the determinant results in a quadratic equation in terms of α^2 in Eq. (3.44) and the polynomial coefficients are listed in Eq. (3.45).

$$\begin{vmatrix} C_{11} - \rho v^2 + C_{55}\alpha^2 & (C_{13} + C_{55})\alpha \\ (C_{13} + C_{55})\alpha & C_{55} - \rho v^2 + C_{33}\alpha^2 \end{vmatrix} = 0 \quad (3.43)$$

$$A_4\alpha^4 + A_2\alpha^2 + A_0 = 0 \quad (3.44)$$

$$\begin{cases} A_4 = C_{33}C_{55} \\ A_2 = (C_{11} - \rho v^2)C_{33} + (C_{55} - \rho v^2)C_{55} - (C_{13} + C_{55})^2 \\ A_0 = (C_{11} - \rho v^2)(C_{55} - \rho v^2) \end{cases} \quad (3.45)$$

From Eq. (3.44), the four α 's roots can be easily obtained that have the negative reciprocity $\alpha_2 = -\alpha_1$, $\alpha_4 = -\alpha_3$. For each α_r ($r = 1, 2, 3, 4$), the displacement amplitude vector $[U_r, W_r]^T$ can be solved from Eq. (3.42) by letting $U_r = 1$, and W_r is calculated using the first row of Eq. (3.42).

$$W_r = \frac{\rho v^2 - C_{11} - C_{55}\alpha_r^2}{(C_{13} + C_{55})\alpha_r} \quad (r = 1, 2, 3, 4) \quad (3.46)$$

It is easy to get the relation $W_2 = -W_1$ and $W_4 = -W_3$ under the fact $\alpha_2 = -\alpha_1$, $\alpha_4 = -\alpha_3$. For the displacement field equations of Lamb wave, the four α 's solutions manifest that there are four partial waves to compose Lamb wave with two longitudinal waves and two shear vertical waves.

$$\begin{cases} u_1 = \left(\sum_{r=1}^4 \eta_r e^{i\xi\alpha_r x_3} \right) e^{i\xi(x_1 - vt)} \\ u_3 = \left(\sum_{r=1}^4 \eta_r W_r e^{i\xi\alpha_r x_3} \right) e^{i\xi(x_1 - vt)} \end{cases} \quad (3.47)$$

where, η_r ($r = 1, 2, 3, 4$) is the participation factors of partial waves and they can be organized into a vector $\boldsymbol{\eta} = [\eta_1, \eta_2, \eta_3, \eta_4]^T$.

Unlike Eqs. (3.13)(3.30), the stress field of Lamb wave only involves in σ_{33} and σ_{13} terms which are stated in Eq. (3.48) based on PWSA.

$$\begin{cases} \sigma_{33} = \left(\sum_{r=1}^4 \beta_{1r} \eta_r e^{i\xi\alpha_r x_3} \right) i\xi e^{i\xi(x_1 - vt)} \\ \sigma_{31} = \left(\sum_{r=1}^4 \beta_{3r} \eta_r e^{i\xi\alpha_r x_3} \right) i\xi e^{i\xi(x_1 - vt)} \end{cases} \quad (3.48)$$

3.4. DISPERSION EQUATIONS OF DECOUPLED LAMB AND SH WAVES IN ORTHOTROPIC MATERIAL

where, the stress amplitude of partial wave β_{ir} is derived into Eq. (3.49), from which the relationship among β_{ir} can be easily obtained: $\beta_{12} = \beta_{11}$, $\beta_{14} = \beta_{13}$, $\beta_{32} = -\beta_{31}$, $\beta_{34} = -\beta_{33}$.

$$\begin{cases} \beta_{1r} = C_{13} + C_{33}\alpha_r W_r \\ \beta_{3r} = C_{55}\alpha_r + C_{55}W_r \end{cases} \quad (r = 1, 2, 3, 4) \quad (3.49)$$

3.4.3 Dispersion equations of Lamb wave

For the displacement and stress field equations shown in Eqs. (3.47)(3.48), substituting them into the boundary condition of Eq. (3.2) (only σ_{33} and σ_{13} are evaluated) and the symmetric condition of Eq. (3.3) (only u_3 and σ_{13} are evaluated) allows to derive the dispersion equation of symmetric modes of Lamb wave, which is presented in Eqs. (3.50)(3.51).

$$\begin{bmatrix} W_1 & -W_1 & W_3 & -W_3 \\ \beta_{31} & -\beta_{31} & \beta_{33} & -\beta_{33} \\ \beta_{11}e^{i\xi\alpha_1 h} & \beta_{11}e^{-i\xi\alpha_1 h} & \beta_{13}e^{i\xi\alpha_3 h} & \beta_{13}e^{-i\xi\alpha_3 h} \\ \beta_{31}e^{i\xi\alpha_1 h} & -\beta_{31}e^{-i\xi\alpha_1 h} & \beta_{33}e^{i\xi\alpha_3 h} & -\beta_{33}e^{-i\xi\alpha_3 h} \end{bmatrix} \begin{bmatrix} \eta_1 \\ \eta_2 \\ \eta_3 \\ \eta_4 \end{bmatrix} = \begin{bmatrix} 0 \\ 0 \\ 0 \\ 0 \end{bmatrix} \quad (3.50)$$

$$\mathcal{D}_s(v, \xi) = \mathcal{D}_s^R(v, \xi) + i\mathcal{D}_s^I(v, \xi) \triangleq \det\{\mathbf{D}_s(v, \xi)\} = 0 \quad \text{for symmetric modes} \quad (3.51)$$

By using the software *Mathematica*, the determinant of the coefficient matrix $\mathbf{D}_s(v, \xi)$ in Eq. (3.50) is simplified into Eq. (3.52).

$$\det\{\mathbf{D}_s(v, \xi)\} = -4i(W_3\beta_{31} - W_1\beta_{33}) [\cos(\xi\alpha_3 h) \sin(\xi\alpha_1 h)\beta_{13}\beta_{31} - \cos(\xi\alpha_1 h) \sin(\xi\alpha_3 h)\beta_{11}\beta_{33}] \quad (3.52)$$

Upon simplification, the Lamb wave dispersion equation of symmetric modes for a single-layered orthotropic plate is explicitly stated in Eq. (3.53), which is also presented in [33].

$$\frac{\tan(\xi\alpha_1 h)}{\tan(\xi\alpha_3 h)} = \frac{\beta_{11}\beta_{33}}{\beta_{13}\beta_{31}} \quad \text{for symmetric modes} \quad (3.53)$$

To obtain the dispersion equation of anti-symmetric modes, the displacement and stress field equations in Eqs. (3.47)(3.48) are substituted into the boundary condition of Eq. (3.2) (only σ_{33} and σ_{13} are evaluated) and the anti-symmetric condition of Eq. (3.4) (only u_1 and σ_{33} are evaluated). The resulted equations are presented in Eqs. (3.54)(3.55).

$$\begin{bmatrix} 1 & 1 & 1 & 1 \\ \beta_{11} & \beta_{11} & \beta_{13} & \beta_{13} \\ \beta_{11}e^{i\xi\alpha_1 h} & \beta_{11}e^{-i\xi\alpha_1 h} & \beta_{13}e^{i\xi\alpha_3 h} & \beta_{13}e^{-i\xi\alpha_3 h} \\ \beta_{31}e^{i\xi\alpha_1 h} & -\beta_{31}e^{-i\xi\alpha_1 h} & \beta_{33}e^{i\xi\alpha_3 h} & -\beta_{33}e^{-i\xi\alpha_3 h} \end{bmatrix} \begin{bmatrix} \eta_1 \\ \eta_2 \\ \eta_3 \\ \eta_4 \end{bmatrix} = \begin{bmatrix} 0 \\ 0 \\ 0 \\ 0 \end{bmatrix} \quad (3.54)$$

3.4. DISPERSION EQUATIONS OF DECOUPLED LAMB AND SH WAVES IN ORTHOTROPIC MATERIAL

$$\mathcal{D}_a(v, \xi) = \mathcal{D}_a^R(v, \xi) + i\mathcal{D}_a^I(v, \xi) \triangleq \det\{\mathbf{D}_a(v, \xi)\} = 0 \quad \text{for anti-symmetric modes} \quad (3.55)$$

With the software *Mathematica*, the determinant of the coefficient matrix $\mathbf{D}_a(v, \xi)$ in Eq. (3.54) is simplified into Eq. (3.56).

$$\det\{\mathbf{D}_a(v, \xi)\} = 4i(\beta_{11} - \beta_{13}) [-\cos(\xi\alpha_1 h) \sin(\xi\alpha_3 h)\beta_{13}\beta_{31} + \cos(\xi\alpha_3 h) \sin(\xi\alpha_1 h)\beta_{11}\beta_{33}] \quad (3.56)$$

Upon simplification, the Lamb wave dispersion equation of anti-symmetric modes for a single-layered orthotropic plate is explicitly stated in Eq. (3.57), still presented in [33].

$$\frac{\tan(\xi\alpha_1 h)}{\tan(\xi\alpha_3 h)} = \frac{\beta_{13}\beta_{31}}{\beta_{11}\beta_{33}} \quad \text{for anti-symmetric modes} \quad (3.57)$$

3.4.4 Displacement and stress fields of SH wave

Eq. (3.41) characterizes the displacement and stress fields of SH wave, from which the two α 's roots can be easily solved as shown in Eq. (3.58) with the indices 5 and 6 given that the indices from 1 to 4 have been occupied by Lamb wave in Eq. (3.44). Accordingly, there are two partial waves to compose SH wave. The displacement u_2 and stress σ_{23} are expressed in Eqs. (3.59) and (3.60) respectively based on PWSA.

$$\alpha^2 = \frac{\rho v^2 - C_{66}}{C_{44}} \Rightarrow \alpha_5 = \sqrt{\frac{\rho v^2 - C_{66}}{C_{44}}}, \quad \alpha_6 = -\sqrt{\frac{\rho v^2 - C_{66}}{C_{44}}} \quad (3.58)$$

$$u_2 = \left(\sum_{r=5}^6 \eta_r e^{i\xi\alpha_r x_3} \right) e^{i\xi(x_1 - vt)} \quad (3.59)$$

$$\sigma_{23} = \left(\sum_{r=5}^6 \beta_{2r} \eta_r e^{i\xi\alpha_r x_3} \right) i\xi e^{i\xi(x_1 - vt)} \quad (3.60)$$

where, $\alpha_6 = -\alpha_5$, $\beta_{25} = C_{44}\alpha_5$, $\beta_{26} = C_{44}\alpha_6$.

3.4.5 Dispersion relation of SH wave

For deriving dispersion equation of SH wave, only the traction-free boundary condition of Eq. (3.2) (only σ_{23} is evaluated) can be applied.

$$\sigma_{23}|_{x_3=\pm h} = 0 \Rightarrow \begin{cases} \alpha_5 e^{-i\xi\alpha_5 h} \eta_5 + \alpha_6 e^{-i\xi\alpha_6 h} \eta_6 = 0 \\ \alpha_5 e^{+i\xi\alpha_5 h} \eta_5 + \alpha_6 e^{+i\xi\alpha_6 h} \eta_6 = 0 \end{cases} \quad (3.61)$$

3.4. DISPERSION EQUATIONS OF DECOUPLED LAMB AND SH WAVES IN ORTHOTROPIC MATERIAL

Rewrite Eq. (3.61) as the matrix form as follows,

$$\begin{bmatrix} \alpha_5 e^{-i\xi\alpha_5 h} & \alpha_6 e^{-i\xi\alpha_6 h} \\ \alpha_5 e^{i\xi\alpha_5 h} & \alpha_6 e^{i\xi\alpha_6 h} \end{bmatrix} \begin{bmatrix} \eta_5 \\ \eta_6 \end{bmatrix} = \begin{bmatrix} 0 \\ 0 \end{bmatrix} \Rightarrow \begin{vmatrix} \alpha_5 e^{-i\xi\alpha_5 h} & \alpha_6 e^{-i\xi\alpha_6 h} \\ \alpha_5 e^{i\xi\alpha_5 h} & \alpha_6 e^{i\xi\alpha_6 h} \end{vmatrix} = 0 \quad (3.62)$$

Expand the determinant in Eq. (3.62) to get Eq. (3.63),

$$e^{i\xi(\alpha_5 - \alpha_6)h} = e^{i\xi(\alpha_6 - \alpha_5)h} \xrightarrow{\alpha_6 = -\alpha_5, d=2h} \cos(\xi\alpha_5 d) + i \sin(\xi\alpha_5 d) = \cos(\xi\alpha_5 d) - i \sin(\xi\alpha_5 d) \quad (3.63)$$

$$\sin(\xi\alpha_5 d) = 0 \Rightarrow \xi\alpha_5 d = n\pi \Rightarrow \xi d \sqrt{\frac{\rho v^2 - C_{66}}{C_{44}}} = n\pi \quad (n = 0, 1, 2, \dots) \quad (3.64)$$

The dispersion relation of SH wave linking phase velocity v and wavenumber ξ can be obtained in Eq. (3.65).

$$v = \sqrt{\frac{C_{66}}{\rho} + \frac{C_{44}}{\rho} \left(\frac{n\pi}{\xi d}\right)^2} \quad (n = 0, 1, 2, \dots) \quad (3.65)$$

Or substitute $\xi = \frac{\omega}{v}$ into Eq. (3.65) to get another form of Eq. (3.66) linking v and ω .

$$v = \sqrt{\frac{d^2 \omega^2 C_{66}}{\rho d^2 \omega^2 - C_{44} n^2 \pi^2}} \quad (n = 0, 1, 2, \dots) \quad (3.66)$$

Obviously, letting $n = 0$ in Eq. (3.66) produces the fundamental SH0 mode which possesses a constant phase velocity as written in Eq. (3.67), indicating the non-dispersive characteristic with respect to frequency ω or wavenumber ξ .

$$v = \sqrt{\frac{C_{66}}{\rho}} \quad (n = 0) \quad (3.67)$$

For each (v, ξ) solution point of a SH mode, the corresponding displacement and stress mode shapes computed via Eqs. (3.59)(3.60) can be also classified into symmetric and anti-symmetric modes via the symmetry condition stated in Eqs. (3.3)(3.4) in which only u_2 and σ_{23} are evaluated. Specifically, the symmetric mode corresponds to the condition $\sigma_{23}|_{x_3=0} = 0$ and the anti-symmetric mode makes the requirement $u_2|_{x_3=0} = 0$, where $x_3 = 0$ indicates the midplane.

It should be noted that although Eqs. (3.53)(3.57)(3.65) are derived through the stiffness matrix of orthotropic material, they are still compatible with transversely isotropic and isotropic materials given that the stiffness matrix of the two materials belong to the stiffness matrix set of orthotropic materials, i.e. $\mathbf{C}_{\text{TI}}, \mathbf{C}_{\text{I}} \in \mathcal{C}_{\mathcal{O}}$ (see Section 2.2.4 and 2.3.3). Thus, one just needs to substitute the corresponding elements in the stiffness matrix of transversely isotropic or isotropic material into Eqs. (3.53)(3.57)(3.65) to get the corresponding dispersion equations of the two materials, respectively.

3.5 Derivation of the classical Rayleigh-Lamb equation via PWSA

The classical Rayleigh-Lamb equation is originally derived through the Helmholtz decomposition method [26]. In this section, we dedicate to retrieve it by following Eqs. (3.53)(3.57) which are based on PWSA to complete the wave propagation theory. When it comes to Rayleigh-Lamb equation, it belongs to the isotropic material case. Thus, all the derivations in section 3.4.2 should be replaced by the parameters of isotropic material. The derivation starts from Eq. (3.44). Thus, the polynomial coefficients A_4, A_2, A_0 in Eq. (3.45) are now computed by using the stiffness coefficients of the isotropic material (see Eq. (2.14)) as follows.

$$\begin{cases} A_4 = (\lambda + 2\mu)\mu \\ A_2 = [(\lambda + 2\mu) - \rho v^2] (\lambda + 2\mu) + (\mu - \rho v^2)\mu - (\lambda + \mu)^2 \\ A_0 = [(\lambda + 2\mu) - \rho v^2] (\mu - \rho v^2) \end{cases} \quad (3.68)$$

The discriminant of the quadratic equation on α^2 in Eq. (3.44) can be derived easily via the software *Mathematica*.

$$\Delta = A_2^2 - 4A_4A_0 = (\lambda + \mu)^2 \rho^2 v^4 \quad (3.69)$$

The two solutions about α^2 can be further obtained for which the smaller one is assigned as α_L^2 and the larger one α_T^2 .

$$\begin{cases} \alpha_L^2 = \alpha_1^2 = \frac{-A_2 - \sqrt{\Delta}}{2A_4} = \frac{\rho v^2 - (\lambda + 2\mu)}{\lambda + 2\mu} = \frac{v^2}{c_L^2} - 1 \\ \alpha_T^2 = \alpha_3^2 = \frac{-A_2 + \sqrt{\Delta}}{2A_4} = \frac{\rho v^2 - \mu}{\mu} = \frac{v^2}{c_T^2} - 1 \end{cases} \quad (3.70)$$

where, $c_L = \sqrt{\frac{\lambda + 2\mu}{\rho}}$ and $c_T = \sqrt{\frac{\mu}{\rho}}$ represent the velocity of longitudinal and transverse modes, respectively.

Substitute Eq. (3.70) into Eq. (3.46) to get W_L and W_T .

$$\begin{aligned} W_L = W_1 &= \frac{\rho v^2 - C_{11} - C_{55}\alpha_L^2}{(C_{13} + C_{55})\alpha_L} = \frac{\rho v^2 - (\lambda + 2\mu) - \mu \frac{\rho v^2 - (\lambda + 2\mu)}{\lambda + 2\mu}}{(\lambda + \mu)\alpha_L} \\ &= \frac{\rho v^2 - (\lambda + 2\mu)}{(\lambda + 2\mu)\alpha_L} = \frac{v^2 - c_L^2}{c_L^2 \alpha_L} = \left(\frac{v^2}{c_L^2} - 1 \right) \frac{1}{\alpha_L} = \frac{\alpha_L^2}{\alpha_L} = \alpha_L \end{aligned} \quad (3.71)$$

$$W_T = W_3 = \frac{\rho v^2 - C_{11} - C_{55}\alpha_T^2}{(C_{13} + C_{55})\alpha_T} = \frac{\rho v^2 - (\lambda + 2\mu) - \mu \frac{\rho v^2 - \mu}{\mu}}{(\lambda + \mu)\alpha_T} = \frac{-(\lambda + \mu)}{(\lambda + \mu)\alpha_T} = -\frac{1}{\alpha_T} \quad (3.72)$$

3.6. CONCLUSION

Substitute Eqs. (3.71) and (3.72) into Eq. (3.49) to compute β_{11} , β_{31} , β_{13} , β_{33} .

$$\begin{cases} \beta_{11} = \lambda + (\lambda + 2\mu)\alpha_L W_L = \lambda + (\lambda + 2\mu)\alpha_L^2 = \lambda + (\lambda + 2\mu)\frac{\rho v^2 - (\lambda + 2\mu)}{\lambda + 2\mu} = \rho v^2 - 2\mu \\ \beta_{31} = \mu\alpha_L + \mu W_L = \mu\alpha_L + \mu\alpha_L = 2\mu\alpha_L \\ \beta_{13} = \lambda + (\lambda + 2\mu)\alpha_T W_T = \lambda + (\lambda + 2\mu)\alpha_T \frac{-1}{\alpha_T} = -2\mu \\ \beta_{33} = \mu\alpha_T + \mu W_T = \mu\alpha_T + \mu \frac{-1}{\alpha_T} = \mu \frac{\alpha_T^2 - 1}{\alpha_T} \end{cases} \quad (3.73)$$

The right hand side of Eq. (3.53) can be computed by substituting Eq. (3.73) into it.

$$\begin{aligned} \frac{\beta_{11}\beta_{33}}{\beta_{13}\beta_{31}} &= \frac{(\rho v^2 - 2\mu)\mu \frac{\alpha_T^2 - 1}{\alpha_T}}{(-2\mu)(2\mu\alpha_L)} = \frac{(\rho v^2 - 2\mu)(\alpha_T^2 - 1)}{-4\mu\alpha_L\alpha_T} = \frac{(v^2 - 2\frac{\mu}{\rho})(\alpha_T^2 - 1)}{-4\frac{\mu}{\rho}\alpha_L\alpha_T} \\ &= \frac{(v^2 - 2c_T^2)(\alpha_T^2 - 1)}{-4c_T^2\alpha_L\alpha_T} = \frac{(\frac{v^2}{c_T^2} - 2)(\alpha_T^2 - 1)}{-4\alpha_L\alpha_T} = \frac{(\alpha_T^2 - 1)(\alpha_T^2 - 1)}{-4\alpha_L\alpha_T} = \frac{(\alpha_T^2 - 1)^2}{-4\alpha_L\alpha_T} \end{aligned} \quad (3.74)$$

Let $p = \xi\alpha_L$, $q = \xi\alpha_T$. Substitute Eq. (3.74) into Eqs. (3.53) and (3.57) to retrieve the classical Rayleigh-Lamb equation.

For symmetric modes,

$$\frac{\tan(ph)}{\tan(qh)} = \frac{(\alpha_T^2 - 1)^2}{-4\alpha_L\alpha_T} = \frac{(\alpha_T^2 - 1)^2\xi^4}{-4\alpha_L\alpha_T\xi^4} = \frac{[(\xi\alpha_T)^2 - \xi^2]^2}{-4\xi^2(\xi\alpha_L)(\xi\alpha_T)} = \frac{(q^2 - \xi^2)^2}{-4\xi^2 pq} \quad (3.75)$$

For anti-symmetric modes,

$$\frac{\tan(ph)}{\tan(qh)} = \frac{-4\alpha_L\alpha_T}{(\alpha_T^2 - 1)^2} = \frac{-4\xi^2 pq}{(q^2 - \xi^2)^2} \quad (3.76)$$

where, $p^2 = \frac{\omega^2}{c_L^2} - \xi^2$, $q^2 = \frac{\omega^2}{c_T^2} - \xi^2$.

Eventually, the classical Rayleigh-Lamb equation is retrieved.

3.6 Conclusion

PWSA is a unified framework to derive dispersion equations of guided waves propagating in a single-layered composite lamina which integrates simultaneously the traction-free boundary condition and symmetry condition. In orthotropic, transversely isotropic and isotropic materials, guided waves will be decoupled into Lamb and SH waves, whereas in triclinic and monoclinic materials, both wave types are coupled to each other. The classical Rayleigh-Lamb equation is retrieved by using PWSA, which serves as an alternative to the Helmholtz decomposition method.

Chapter 4

Guided wave propagation in a multi-layered plate: transfer matrix method

This chapter comprehensively studies the various properties of guided waves propagation in a multi-layered composite plate through the classical transfer matrix method (TMM) [2, 10, 33, 38]. The core contribution of this chapter to the state-of-the-art is that a hybrid matrix strategy is originally proposed to address the matrix incompatibility issue that is usually encountered for arbitrarily oriented composite laminates. The hybrid matrix strategy is theoretically derived by following the PWSA of Chapter 3 and is numerically assessed for three commonly used composite laminates.

4.1 The multi-layered composite plate model

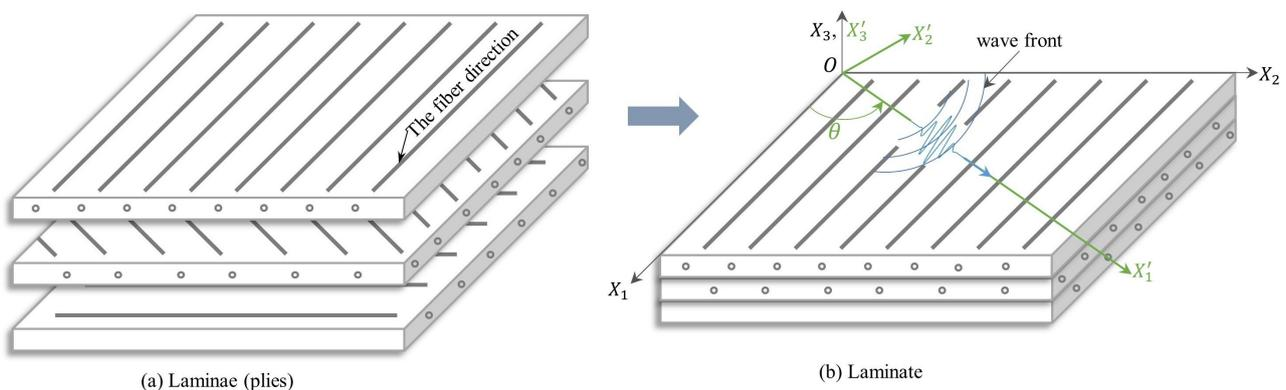


Figure 4.1 – A three-layered composite plate model $[0/\theta/90]$. The wave propagation direction is along the fiber direction of the middle layer.

In this chapter, we consider the multi-layered composite plate model schematically shown in Fig-

ure 4.1(a), which consists of laminae with various stacking angles of layups being a typical composite laminate widely used in aeronautical engineering. In the laminate, each lamina is reinforced by the carbon fibers within the composing matrix, thus producing orthotropic material property from macroscopical view. In the lamina plane, the fiber direction and transverse fiber direction are defined as the **principal** and **minor-principal** direction of the lamina, respectively. Naturally, all other directions are defined as its **off-principal** direction. The perfect interface condition between adjacent layers is assumed and thus leads to the continuity of field variables (displacement and stress) across all the interfaces, otherwise delamination problem [61] occurs which is not the concern of the thesis.

Guided waves propagation in a plate waveguide emanating from a point source is at arbitrary angles. The wave front behaves like a circular shape, see Figure 4.1(b). For an interested wave propagation direction, it may coincide with the principal direction of a certain lamina (see the middle layer in Figure 4.1(b)), but it may correspond to the off-principal direction of another lamina (see the top layer in Figure 4.1(b)) due to the varying stacking angles of layups. For each lamina, its stiffness matrix keeps the orthotropic type, i.e. \mathbf{C}_O , in the principal and minor-principal directions according to the Characteristic 2 of Section 2.3.3. However, for a lamina whose principal direction does not coincide with the wave propagation direction, its \mathbf{C}_O should be rotated to the wave propagation direction with angle θ , denoted as \mathbf{C}'_O . According to the Characteristic 1 of Section 2.3.3, it can be easily inferred that $\mathbf{C}'_O \in \mathcal{C}_M$.

In Sections 3.3 and 3.4, we have studied that \mathbf{C}_O and \mathbf{C}'_O (or \mathbf{C}_M) will lead to different coupling properties of Lamb and SH waves in a single lamina. Thus, in a laminate system, the mismatch issue between wave propagation direction and the fiber (principal) direction of a lamina will lead to different wave types among laminae. As a consequence, to model guided waves propagation in a unified multi-layered plate system, how to unite the various wave types in different laminae becomes an essential issue, which can be tackled through TMM (in this chapter) and GMM (in the next chapter) frameworks. In the following section, the displacement and stress equations of a specific wave type will be reorganized into a series of local lamina matrices which lay the foundation of TMM and GMM. Then, these local matrices are transferred into a monodromy one based on the TMM framework. Finally, the dispersion equation of the laminate system is generated and solving this equation just offers various wave solutions.

4.2 Local lamina matrices along the wave propagation direction

We consider a general n -layered laminate with various stacking angles of layups $[\phi_1/\phi_2/\dots/\phi_n]$ and the interested wave propagation direction at angle θ , as illustrated in Figure 4.2(a). The profile section of the laminate along the wave propagation direction is shown in Figure 4.2(b). For a general layer l_k , its rotation angle becomes $(\theta - \phi_k)$, thus the rotated stiffness matrix of this layer becomes $\mathbf{C}'_k = \text{Rot}\{\mathbf{C}_k, \theta - \phi_k\}$, where \mathbf{C}_k is the stiffness matrix of layer l_k in its principal direction, and the operator $\text{Rot}\{\cdot, \cdot\}$ is defined in Eq. (2.18).

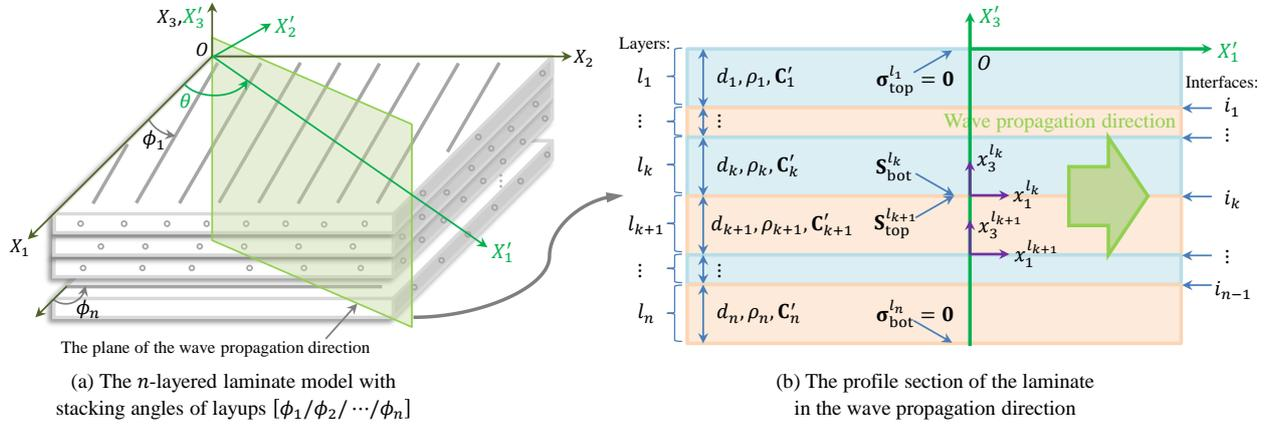


Figure 4.2 – Guided wave propagation model in a n -layered composite laminate.

According to the study in Sections 3.3 and 3.4, the different matrix type of \mathbf{C}'_k will lead to different wave types in layer l_k . If \mathbf{C}'_k is monoclinic type, the resulted waves are the coupled Lamb and SH waves in layer l_k (see Section 3.3); if \mathbf{C}'_k is orthotropic type, the guided waves are decoupled into pure Lamb and SH waves in layer l_k (see Section 3.4). Thus, in a multi-layered plate system, the wave type present in each layer should be determined separately.

4.2.1 Local lamina matrices of coupled Lamb and SH waves

When the interested wave propagation direction is along the off-principle direction of a general layer l_k , the rotated stiffness matrix of this layer $\mathbf{C}'_k \in \mathcal{C}_M$ produces the coupled Lamb and SH waves in this layer. In this case, the three displacement quantities (u_1, u_2, u_3) should be simultaneously solved, whose expressions are presented in Eq. (3.29). Rewrite it as the matrix form in Eq. (4.1) and the compact form in Eq. (4.2) is obtained.

4.2. LOCAL LAMINA MATRICES ALONG THE WAVE PROPAGATION DIRECTION

$$\begin{bmatrix} u_1 \\ u_2 \\ u_3 \end{bmatrix} = \begin{bmatrix} 1 & 1 & 1 & 1 & 1 & 1 \\ V_1 & V_2 & V_3 & V_4 & V_5 & V_6 \\ W_1 & W_2 & W_3 & W_4 & W_5 & W_6 \end{bmatrix} \begin{bmatrix} e^{i\xi\alpha_1x_3} & & & & & \\ & e^{i\xi\alpha_2x_3} & & & & \\ & & e^{i\xi\alpha_3x_3} & & & \\ & & & e^{i\xi\alpha_4x_3} & & \\ & & & & e^{i\xi\alpha_5x_3} & \\ & & & & & e^{i\xi\alpha_6x_3} \end{bmatrix} \begin{bmatrix} \eta_1 \\ \eta_2 \\ \eta_3 \\ \eta_4 \\ \eta_5 \\ \eta_6 \end{bmatrix} e^{i\xi(x_1-vt)} \quad (4.1)$$

$$\mathbf{u}_{3 \times 1} = \mathbf{U}_{3 \times 6} \mathbf{\Lambda}_{6 \times 6}(x_3) \boldsymbol{\eta}_{6 \times 1} e^{i\xi(x_1-vt)} \quad (4.2)$$

where, $\mathbf{u}_{3 \times 1}$, $\mathbf{U}_{3 \times 6}$, $\mathbf{\Lambda}_{6 \times 6}(x_3)$ and $\boldsymbol{\eta}_{6 \times 1}$ are defined as follows. The subscript “ $m \times n$ ” designates the matrix dimension.

$$\mathbf{u}_{3 \times 1} = [u_1, u_2, u_3]^T \quad (4.3)$$

$$\mathbf{U}_{3 \times 6} = \begin{bmatrix} 1 & 1 & 1 & 1 & 1 & 1 \\ V_1 & V_2 & V_3 & V_4 & V_5 & V_6 \\ W_1 & W_2 & W_3 & W_4 & W_5 & W_6 \end{bmatrix} \quad (4.4)$$

$$\mathbf{\Lambda}_{6 \times 6}(x_3) = \begin{bmatrix} e^{i\xi\alpha_1x_3} & & & & & \\ & e^{i\xi\alpha_2x_3} & & & & \\ & & e^{i\xi\alpha_3x_3} & & & \\ & & & e^{i\xi\alpha_4x_3} & & \\ & & & & e^{i\xi\alpha_5x_3} & \\ & & & & & e^{i\xi\alpha_6x_3} \end{bmatrix} \quad (4.5)$$

$$\boldsymbol{\eta}_{6 \times 1} = [\eta_1, \eta_2, \eta_3, \eta_4, \eta_5, \eta_6]^T \quad (4.6)$$

Correspondingly, the three stress quantities $(\sigma_{33}, \sigma_{23}, \sigma_{13})$ presented in Eq. (3.30) are rewritten as the matrix form in Eq. (4.7) and the compact form in Eq. (4.8) by suppressing the common factor $i\xi$ since this factor has no effect on the traction-free boundary condition to be evaluated in Section 4.3 for the TMM framework.

4.2. LOCAL LAMINA MATRICES ALONG THE WAVE PROPAGATION DIRECTION

$$\begin{bmatrix} \sigma_{33} \\ \sigma_{23} \\ \sigma_{13} \end{bmatrix} = \begin{bmatrix} \beta_{11} & \beta_{12} & \beta_{13} & \beta_{14} & \beta_{15} & \beta_{16} \\ \beta_{21} & \beta_{22} & \beta_{23} & \beta_{24} & \beta_{25} & \beta_{26} \\ \beta_{31} & \beta_{32} & \beta_{33} & \beta_{34} & \beta_{35} & \beta_{36} \end{bmatrix} \begin{bmatrix} e^{i\xi\alpha_1 x_3} \\ e^{i\xi\alpha_2 x_3} \\ e^{i\xi\alpha_3 x_3} \\ e^{i\xi\alpha_4 x_3} \\ e^{i\xi\alpha_5 x_3} \\ e^{i\xi\alpha_6 x_3} \end{bmatrix} \begin{bmatrix} \eta_1 \\ \eta_2 \\ \eta_3 \\ \eta_4 \\ \eta_5 \\ \eta_6 \end{bmatrix} e^{i\xi(x_1 - vt)} \quad (4.7)$$

$$\boldsymbol{\sigma}_{3 \times 1} = \boldsymbol{\beta}_{3 \times 6} \boldsymbol{\Lambda}_{6 \times 6}(x_3) \boldsymbol{\eta}_{6 \times 1} e^{i\xi(x_1 - vt)} \quad (4.8)$$

where, $\boldsymbol{\sigma}_{3 \times 1}$ and $\boldsymbol{\beta}_{3 \times 6}$ are defined as follows.

$$\boldsymbol{\sigma}_{3 \times 1} = [\sigma_{33}, \sigma_{23}, \sigma_{13}]^T \quad (4.9)$$

$$\boldsymbol{\beta}_{3 \times 6} = \begin{bmatrix} \beta_{11} & \beta_{12} & \beta_{13} & \beta_{14} & \beta_{15} & \beta_{16} \\ \beta_{21} & \beta_{22} & \beta_{23} & \beta_{24} & \beta_{25} & \beta_{26} \\ \beta_{31} & \beta_{32} & \beta_{33} & \beta_{34} & \beta_{35} & \beta_{36} \end{bmatrix} \quad (4.10)$$

Eqs. (4.1) and (4.7) can be concatenated into a single equation. Then, we have the matrix form in Eq. (4.11) and the compact form in Eq. (4.12).

$$\begin{bmatrix} u_1 \\ u_2 \\ u_3 \\ \sigma_{33} \\ \sigma_{23} \\ \sigma_{13} \end{bmatrix} = \begin{bmatrix} 1 & 1 & 1 & 1 & 1 & 1 \\ V_1 & V_2 & V_3 & V_4 & V_5 & V_6 \\ W_1 & W_2 & W_3 & W_4 & W_5 & W_6 \\ \beta_{11} & \beta_{12} & \beta_{13} & \beta_{14} & \beta_{15} & \beta_{16} \\ \beta_{21} & \beta_{22} & \beta_{23} & \beta_{24} & \beta_{25} & \beta_{26} \\ \beta_{31} & \beta_{32} & \beta_{33} & \beta_{34} & \beta_{35} & \beta_{36} \end{bmatrix} \begin{bmatrix} e^{i\xi\alpha_1 x_3} \\ e^{i\xi\alpha_2 x_3} \\ e^{i\xi\alpha_3 x_3} \\ e^{i\xi\alpha_4 x_3} \\ e^{i\xi\alpha_5 x_3} \\ e^{i\xi\alpha_6 x_3} \end{bmatrix} \begin{bmatrix} \eta_1 \\ \eta_2 \\ \eta_3 \\ \eta_4 \\ \eta_5 \\ \eta_6 \end{bmatrix} e^{i\xi(x_1 - vt)} \quad (4.11)$$

$$\mathbf{S}_{6 \times 1} = \mathbf{\Gamma}_{6 \times 6} \boldsymbol{\Lambda}_{6 \times 6}(x_3) \boldsymbol{\eta}_{6 \times 1} e^{i\xi(x_1 - vt)} = \mathbf{Z}_{6 \times 6}(x_3) \boldsymbol{\eta}_{6 \times 1} e^{i\xi(x_1 - vt)} \quad (4.12)$$

where, $\mathbf{S}_{6 \times 1} = [u_1, u_2, u_3, \sigma_{33}, \sigma_{23}, \sigma_{13}]^T$ represents the field variables of the coupled Lamb and SH waves in the layer l_k ; $\mathbf{Z}_{6 \times 6}(x_3) = \mathbf{\Gamma}_{6 \times 6} \boldsymbol{\Lambda}_{6 \times 6}(x_3)$ and $\mathbf{\Gamma}_{6 \times 6}$ is stated in Eq. (4.13).

It should be noted that those matrices, $\mathbf{\Gamma}_{6 \times 6}$, $\boldsymbol{\Lambda}_{6 \times 6}(x_3)$, $\mathbf{Z}_{6 \times 6}(x_3)$, only depend on the lamina properties of layer l_k . Thus, they are uniformly defined as the **local lamina matrices**. This terminology is applicable to the subsequent subsections.

4.2. LOCAL LAMINA MATRICES ALONG THE WAVE PROPAGATION DIRECTION

$$\mathbf{\Gamma}_{6 \times 6} = \begin{bmatrix} 1 & 1 & 1 & 1 & 1 & 1 \\ V_1 & V_2 & V_3 & V_4 & V_5 & V_6 \\ W_1 & W_2 & W_3 & W_4 & W_5 & W_6 \\ \beta_{11} & \beta_{12} & \beta_{13} & \beta_{14} & \beta_{15} & \beta_{16} \\ \beta_{21} & \beta_{22} & \beta_{23} & \beta_{24} & \beta_{25} & \beta_{26} \\ \beta_{31} & \beta_{32} & \beta_{33} & \beta_{34} & \beta_{35} & \beta_{36} \end{bmatrix} \quad (4.13)$$

4.2.2 Local lamina matrices of pure Lamb waves

When the interested wave propagation direction is just along the (minor-)principal direction of layer l_k , the rotated stiffness matrix of this layer $\mathbf{C}'_k \in \mathcal{C}_O$ according to the Characteristic 2 of Section 2.3.3 leads to the decoupled Lamb and SH waves in this layer. The current subsection aims to derive the local lamina matrices of pure Lamb waves and the next subsection pure SH waves. For pure Lamb waves, only the two displacement quantities (u_1, u_3) are involved, whose expressions are presented in Eq. (3.47). Rewrite it as the matrix form in Eq. (4.14) and the compact form in Eq. (4.15) is obtained.

$$\begin{bmatrix} u_1 \\ u_3 \end{bmatrix} = \begin{bmatrix} 1 & 1 & 1 & 1 \\ W_1 & W_2 & W_3 & W_4 \end{bmatrix} \begin{bmatrix} e^{i\xi\alpha_1 x_3} \\ e^{i\xi\alpha_2 x_3} \\ e^{i\xi\alpha_3 x_3} \\ e^{i\xi\alpha_4 x_3} \end{bmatrix} \begin{bmatrix} \eta_1 \\ \eta_2 \\ \eta_3 \\ \eta_4 \end{bmatrix} e^{i\xi(x_1 - vt)} \quad (4.14)$$

$$\mathbf{u}_{2 \times 1} = \mathbf{U}_{2 \times 4} \mathbf{\Lambda}_{4 \times 4}(x_3) \mathbf{\eta}_{4 \times 1} e^{i\xi(x_1 - vt)} \quad (4.15)$$

The stress terms regarding to pure Lamb waves are $(\sigma_{33}, \sigma_{13})$ which are presented in Eq. (3.48) and are rewritten as the matrix form in Eq. (4.16) and the compact form in Eq. (4.17) by suppressing the common factor $i\xi$.

$$\begin{bmatrix} \sigma_{33} \\ \sigma_{13} \end{bmatrix} = \begin{bmatrix} \beta_{11} & \beta_{12} & \beta_{13} & \beta_{14} \\ \beta_{31} & \beta_{32} & \beta_{33} & \beta_{34} \end{bmatrix} \begin{bmatrix} e^{i\xi\alpha_1 x_3} \\ e^{i\xi\alpha_2 x_3} \\ e^{i\xi\alpha_3 x_3} \\ e^{i\xi\alpha_4 x_3} \end{bmatrix} \begin{bmatrix} \eta_1 \\ \eta_2 \\ \eta_3 \\ \eta_4 \end{bmatrix} e^{i\xi(x_1 - vt)} \quad (4.16)$$

$$\mathbf{\sigma}_{2 \times 1} = \mathbf{\beta}_{2 \times 4} \mathbf{\Lambda}_{4 \times 4}(x_3) \mathbf{\eta}_{4 \times 1} e^{i\xi(x_1 - vt)} \quad (4.17)$$

Eqs. (4.14) and (4.16) can be concatenated into a single equation, see the matrix form in Eq. (4.18) and the compact form in Eq. (4.19).

4.2. LOCAL LAMINA MATRICES ALONG THE WAVE PROPAGATION DIRECTION

$$\begin{bmatrix} u_1 \\ u_3 \\ \sigma_{33} \\ \sigma_{13} \end{bmatrix} = \begin{bmatrix} 1 & 1 & 1 & 1 \\ W_1 & W_2 & W_3 & W_4 \\ \beta_{11} & \beta_{12} & \beta_{13} & \beta_{14} \\ \beta_{31} & \beta_{32} & \beta_{33} & \beta_{34} \end{bmatrix} \begin{bmatrix} e^{i\xi\alpha_1 x_3} & & & \\ & e^{i\xi\alpha_2 x_3} & & \\ & & e^{i\xi\alpha_3 x_3} & \\ & & & e^{i\xi\alpha_4 x_3} \end{bmatrix} \begin{bmatrix} \eta_1 \\ \eta_2 \\ \eta_3 \\ \eta_4 \end{bmatrix} e^{i\xi(x_1-vt)} \quad (4.18)$$

$$\mathbf{S}_{4 \times 1} = \mathbf{\Gamma}_{4 \times 4} \mathbf{\Lambda}_{4 \times 4}(x_3) \boldsymbol{\eta}_{4 \times 1} e^{i\xi(x_1-vt)} = \mathbf{Z}_{4 \times 4}(x_3) \boldsymbol{\eta}_{4 \times 1} e^{i\xi(x_1-vt)} \quad (4.19)$$

The local lamina matrices, $\mathbf{\Gamma}_{4 \times 4}$, $\mathbf{\Lambda}_{4 \times 4}(x_3)$, $\mathbf{Z}_{4 \times 4}(x_3)$, of the pure Lamb waves in layer l_k have been obtained according to Eq. (4.19).

4.2.3 Local lamina matrices of pure SH waves

The current subsection continues to derive the local lamina matrices of pure SH waves in layer l_k . The involved displacement is only u_2 , whose expression is presented in Eq. (3.59). It can be rewritten as the matrix form in Eq. (4.20) and the compact form in Eq. (4.21).

$$u_2 = \begin{bmatrix} 1 & 1 \end{bmatrix} \begin{bmatrix} e^{i\xi\alpha_5 x_3} & \\ & e^{i\xi\alpha_6 x_3} \end{bmatrix} \begin{bmatrix} \eta_5 \\ \eta_6 \end{bmatrix} e^{i\xi(x_1-vt)} \quad (4.20)$$

$$\mathbf{u}_{1 \times 1} = \mathbf{U}_{1 \times 2} \mathbf{\Lambda}_{2 \times 2}(x_3) \boldsymbol{\eta}_{2 \times 1} e^{i\xi(x_1-vt)} \quad (4.21)$$

The stress term regarding pure SH waves is σ_{23} which is presented in Eq. (3.60) and is rewritten as the matrix form in Eq. (4.22) and the compact form in Eq. (4.23) by suppressing the common factor $i\xi$.

$$\sigma_{23} = \begin{bmatrix} \beta_{25} & \beta_{26} \end{bmatrix} \begin{bmatrix} e^{i\xi\alpha_5 x_3} & \\ & e^{i\xi\alpha_6 x_3} \end{bmatrix} \begin{bmatrix} \eta_5 \\ \eta_6 \end{bmatrix} e^{i\xi(x_1-vt)} \quad (4.22)$$

$$\boldsymbol{\sigma}_{1 \times 1} = \boldsymbol{\beta}_{1 \times 2} \mathbf{\Lambda}_{2 \times 2}(x_3) \boldsymbol{\eta}_{2 \times 1} e^{i\xi(x_1-vt)} \quad (4.23)$$

Eqs. (4.20) and (4.22) can be concatenated into a single equation to form the field variables.

$$\begin{bmatrix} u_2 \\ \sigma_{23} \end{bmatrix} = \begin{bmatrix} 1 & 1 \\ \beta_{25} & \beta_{26} \end{bmatrix} \begin{bmatrix} e^{i\xi\alpha_5 x_3} & \\ & e^{i\xi\alpha_6 x_3} \end{bmatrix} \begin{bmatrix} \eta_5 \\ \eta_6 \end{bmatrix} e^{i\xi(x_1-vt)} \quad (4.24)$$

$$\mathbf{S}_{2 \times 1} = \mathbf{\Gamma}_{2 \times 2} \mathbf{\Lambda}_{2 \times 2}(x_3) \boldsymbol{\eta}_{2 \times 1} e^{i\xi(x_1-vt)} = \mathbf{Z}_{2 \times 2}(x_3) \boldsymbol{\eta}_{2 \times 1} e^{i\xi(x_1-vt)} \quad (4.25)$$

The local lamina matrices, $\mathbf{\Gamma}_{2 \times 2}$, $\mathbf{\Lambda}_{2 \times 2}(x_3)$, $\mathbf{Z}_{2 \times 2}(x_3)$, of the pure SH waves in layer l_k have been obtained based on Eq. (4.25).

4.3 Transfer matrix method

In this section, the local lamina matrices corresponding to each wave type will be transferred into a monodromy one under the TMM framework by applying the continuity condition.

4.3.1 Local transfer matrix in a lamina

The field variables \mathbf{S} (including displacement and stress) of a general layer l_k have been obtained in Eqs. (4.12), (4.19) and (4.25) for different wave types. Tentatively ignoring the matrix dimension of \mathbf{S} denoted in the subscript, the field variables \mathbf{S} of layer l_k at its top side ($x_3 = 0$ in the local coordinate system) and bottom side ($x_3 = d_k$) can be computed based on Eqs. (4.26) and (4.27), respectively, refer to Figure 4.2(b) for easy understanding.

$$\mathbf{S}_{\text{top}}^{l_k} = \mathbf{S}^{l_k}|_{x_3=0} = \mathbf{\Gamma}^{l_k} \mathbf{\Lambda}^{l_k}(0) \boldsymbol{\eta}^{l_k} e^{i\xi(x_1-vt)} = \mathbf{\Gamma}^{l_k} \boldsymbol{\eta}^{l_k} e^{i\xi(x_1-vt)} \quad (4.26)$$

$$\mathbf{S}_{\text{bot}}^{l_k} = \mathbf{S}^{l_k}|_{x_3=d_k} = \mathbf{\Gamma}^{l_k} \mathbf{\Lambda}^{l_k}(d_k) \boldsymbol{\eta}^{l_k} e^{i\xi(x_1-vt)} \quad (4.27)$$

where, the superscript ' l_k ' denotes that the associated terms belong to a general layer l_k ; the subscript 'bot' and 'top' represents bottom and top side, respectively; d_k is the thickness of layer l_k . Note that in Eq. (4.26), $\mathbf{\Lambda}^{l_k}(0) = \mathbf{I}$, where \mathbf{I} is the identity matrix.

The common term $\boldsymbol{\eta}^{l_k} e^{i\xi(x_1-vt)}$ in Eqs. (4.26) and (4.27) can be eliminated and thus the field variables of layer l_k at its top and bottom sides can be linked as shown in Eq. (4.28).

$$\mathbf{S}_{\text{bot}}^{l_k} = \mathbf{T}^{l_k} \mathbf{S}_{\text{top}}^{l_k} \quad (4.28)$$

where, \mathbf{T}^{l_k} is stated in Eq. (4.29) and is naturally defined as the **local transfer matrix** of layer l_k .

$$\mathbf{T}^{l_k} = \mathbf{\Gamma}^{l_k} \mathbf{\Lambda}^{l_k}(d_k) \left(\mathbf{\Gamma}^{l_k} \right)^{-1} \in \mathbb{C}^{p \times p} \quad (4.29)$$

where, $\mathbb{C}^{p \times p}$ represents the set of complex matrix with dimension $p \times p$ and p is the number of partial waves, specifically, for the coupled Lamb and SH waves in Section (4.2.1) ($p = 6$), for the pure Lamb waves in Section (4.2.2) ($p = 4$) and for the pure SH waves in Section (4.2.3) ($p = 2$).

4.3.2 The monodromy transfer matrix of the laminate system

The local transfer matrix \mathbf{T}^{l_k} in Eq. (4.29) can be synthesized to yield the monodromy transfer matrix of the laminate. Primarily, each layer's local transfer matrix should have the same dimension, i.e. $\mathbf{T}^{l_k} \in \mathbb{C}^{p \times p}$ for $k = 1, \dots, n$, otherwise the incompatibility issue of matrix dimension just occurs and it will be discussed in Section 4.4. By virtue of Eq. (4.28), the field variables at the top and bottom sides of each layer can be linked based on the following transferring rule.

$$\text{The transferring rule: } \begin{cases} \mathbf{S}_{\text{bot}}^{l_1} = \mathbf{T}^{l_1} \mathbf{S}_{\text{top}}^{l_1} \\ \mathbf{S}_{\text{bot}}^{l_2} = \mathbf{T}^{l_2} \mathbf{S}_{\text{top}}^{l_2} \\ \vdots \\ \mathbf{S}_{\text{bot}}^{l_n} = \mathbf{T}^{l_n} \mathbf{S}_{\text{top}}^{l_n} \end{cases} \quad (4.30)$$

On the other hand, the continuity condition (CC) at each interface as illustrated in Figure 4.2 should be satisfied. Thus, we have Eq. (4.31).

$$\text{The continuity condition: } \begin{cases} \mathbf{S}_{\text{top}}^{l_2} = \mathbf{S}_{\text{bot}}^{l_1} \\ \mathbf{S}_{\text{top}}^{l_3} = \mathbf{S}_{\text{bot}}^{l_2} \\ \vdots \\ \mathbf{S}_{\text{top}}^{l_n} = \mathbf{S}_{\text{bot}}^{l_{n-1}} \end{cases} \quad (4.31)$$

$\mathbf{S}_{\text{bot}}^{l_n}$ in the last equation of Eq. (4.30) can be consecutively transferred to $\mathbf{S}_{\text{top}}^{l_1}$ by recurrently substituting Eq. (4.31) into Eq. (4.30). This process is illustrated in Eq. (4.32).

$$\begin{aligned} \mathbf{S}_{\text{bot}}^{l_n} &= \mathbf{T}^{l_n} \mathbf{S}_{\text{top}}^{l_n} \\ &= \mathbf{T}^{l_n} \mathbf{T}^{l_{n-1}} \mathbf{S}_{\text{top}}^{l_{n-1}} \\ &\vdots \\ &= \mathbf{T}^{l_n} \mathbf{T}^{l_{n-1}} \mathbf{T}^{l_{n-2}} \dots \mathbf{T}^{l_2} \mathbf{T}^{l_1} \mathbf{S}_{\text{top}}^{l_1} \end{aligned} \quad (4.32)$$

Thus, the field variables at the bottom- and top-most surfaces of the laminate are linked with a monodromy matrix \mathbf{T}^{mono} as stated in Eq. (4.33) which characterizes the transfer matrix of the laminate system.

$$\mathbf{S}_{\text{bot}}^{l_n} = \mathbf{T}^{\text{mono}} \mathbf{S}_{\text{top}}^{l_1} \quad (4.33)$$

$$\mathbf{T}^{\text{mono}} = \mathbf{T}^{l_n} \mathbf{T}^{l_{n-1}} \mathbf{T}^{l_{n-2}} \dots \mathbf{T}^{l_2} \mathbf{T}^{l_1} \quad (4.34)$$

It is clear that $\mathbf{T}^{\text{mono}} \in \mathbb{C}^{p \times p}$ has the same dimension as \mathbf{T}^{l_k} ($k = 1, \dots, n$).

4.3.3 Dispersion equation

The monodromy transfer matrix of the laminate is then used to derive the dispersion equation.

1. The coupled Lamb and SH waves for $\mathbf{T}^{\text{mono}} \in \mathbb{C}^{6 \times 6}$

When $\mathbf{T}^{\text{mono}} \in \mathbb{C}^{6 \times 6}$, Eq. (4.33) can be expanded in Eq. (4.35), which characterizes the field variables regarding to the coupled Lamb and SH waves.

$$\begin{bmatrix} u_1 \\ u_2 \\ u_3 \\ \sigma_{33} \\ \sigma_{23} \\ \sigma_{13} \end{bmatrix}_{\text{bot}}^{l_n} = \begin{bmatrix} T_{11} & T_{12} & T_{13} & T_{14} & T_{15} & T_{16} \\ T_{21} & T_{22} & T_{23} & T_{24} & T_{25} & T_{26} \\ T_{31} & T_{32} & T_{33} & T_{34} & T_{35} & T_{36} \\ T_{41} & T_{42} & T_{43} & T_{44} & T_{45} & T_{46} \\ T_{51} & T_{52} & T_{53} & T_{54} & T_{55} & T_{56} \\ T_{61} & T_{62} & T_{63} & T_{64} & T_{65} & T_{66} \end{bmatrix} \begin{bmatrix} u_1 \\ u_2 \\ u_3 \\ \sigma_{33} \\ \sigma_{23} \\ \sigma_{13} \end{bmatrix}_{\text{top}}^{l_1} \quad (4.35)$$

The traction-free boundary condition at the bottom- and top-most surfaces of the multi-layered plate system is presented in Eq. (4.36), see Figure 4.2(b) for the illustration.

$$\text{The boundary condition: } \begin{bmatrix} \sigma_{33} \\ \sigma_{23} \\ \sigma_{13} \end{bmatrix}_{\text{bot}}^{l_n} = \begin{bmatrix} \sigma_{33} \\ \sigma_{23} \\ \sigma_{13} \end{bmatrix}_{\text{top}}^{l_1} = \begin{bmatrix} 0 \\ 0 \\ 0 \end{bmatrix} \quad (4.36)$$

Substituting Eq. (4.36) into Eq. (4.35) leads to Eq. (4.37).

$$\begin{bmatrix} u_1 \\ u_2 \\ u_3 \\ 0 \\ 0 \\ 0 \end{bmatrix}_{\text{bot}}^{l_n} = \begin{bmatrix} T_{11} & T_{12} & T_{13} & T_{14} & T_{15} & T_{16} \\ T_{21} & T_{22} & T_{23} & T_{24} & T_{25} & T_{26} \\ T_{31} & T_{32} & T_{33} & T_{34} & T_{35} & T_{36} \\ \hline T_{41} & T_{42} & T_{43} & T_{44} & T_{45} & T_{46} \\ T_{51} & T_{52} & T_{53} & T_{54} & T_{55} & T_{56} \\ T_{61} & T_{62} & T_{63} & T_{64} & T_{65} & T_{66} \end{bmatrix} \begin{bmatrix} u_1 \\ u_2 \\ u_3 \\ 0 \\ 0 \\ 0 \end{bmatrix}_{\text{top}}^{l_1} \quad (4.37)$$

For the purpose of deriving dispersion equation through TMM, only the bottom left corner of \mathbf{T}^{mono} is useful because this submatrix relates to the boundary condition. Extracting out this submatrix from Eq. (4.37) leads to Eq. (4.38).

$$\begin{bmatrix} 0 \\ 0 \\ 0 \end{bmatrix}_{\text{bot}}^{l_n} = \begin{bmatrix} T_{41} & T_{42} & T_{43} \\ T_{51} & T_{52} & T_{53} \\ T_{61} & T_{62} & T_{63} \end{bmatrix} \begin{bmatrix} u_1 \\ u_2 \\ u_3 \end{bmatrix}_{\text{top}}^{l_1} \quad (4.38)$$

Note that the displacement in the top-most surface, $\mathbf{u}_{\text{top}}^{l_1}$, should be non-trivial, thus the bottom left corner of \mathbf{T}^{mono} in Eq. (4.38) should have a vanishing determinant. This finally produces the dispersion equation of the coupled Lamb and SH waves linking v and ξ as presented in Eq. (4.39).

$$\mathcal{D}_T(v, \xi) = \mathcal{D}_T^R(v, \xi) + i\mathcal{D}_T^I(v, \xi) \triangleq \begin{vmatrix} T_{41} & T_{42} & T_{43} \\ T_{51} & T_{52} & T_{53} \\ T_{61} & T_{62} & T_{63} \end{vmatrix} = 0 \quad (4.39)$$

where, the subscript ‘T’ denotes that the dispersion equation is built with TMM.

2. The pure Lamb waves for $\mathbf{T}^{\text{mono}} \in \mathbb{C}^{4 \times 4}$

When $\mathbf{T}^{\text{mono}} \in \mathbb{C}^{4 \times 4}$, it characterizes the pure Lamb waves. The corresponding dispersion equation of the pure Lamb waves can be derived by expanding Eq. (4.33) into Eq. (4.40).

$$\begin{bmatrix} u_1 \\ u_3 \\ \sigma_{33} \\ \sigma_{13} \end{bmatrix}_{\text{bot}}^{l_n} = \begin{bmatrix} T_{11} & T_{12} & T_{13} & T_{14} \\ T_{21} & T_{22} & T_{23} & T_{24} \\ T_{31} & T_{32} & T_{33} & T_{34} \\ T_{41} & T_{42} & T_{43} & T_{44} \end{bmatrix} \begin{bmatrix} u_1 \\ u_3 \\ \sigma_{33} \\ \sigma_{13} \end{bmatrix}_{\text{top}}^{l_1} \quad (4.40)$$

By applying the traction-free boundary condition at the bottom- and top-most surfaces of the plate, $\begin{bmatrix} \sigma_{33} \\ \sigma_{13} \end{bmatrix}_{\text{bot}}^{l_n} = \begin{bmatrix} \sigma_{33} \\ \sigma_{13} \end{bmatrix}_{\text{top}}^{l_1} = \begin{bmatrix} 0 \\ 0 \end{bmatrix}$, Eq. (4.40) becomes Eq. (4.41).

$$\begin{bmatrix} u_1 \\ u_3 \\ 0 \\ 0 \end{bmatrix}_{\text{bot}}^{l_n} = \begin{bmatrix} T_{11} & T_{12} & T_{13} & T_{14} \\ T_{21} & T_{22} & T_{23} & T_{24} \\ T_{31} & T_{32} & T_{33} & T_{34} \\ T_{41} & T_{42} & T_{43} & T_{44} \end{bmatrix} \begin{bmatrix} u_1 \\ u_3 \\ 0 \\ 0 \end{bmatrix}_{\text{top}}^{l_1} \quad (4.41)$$

The requirement of the non-trivial displacement in the top-most surface, $\begin{bmatrix} u_1 \\ u_3 \end{bmatrix}_{\text{top}}^{l_1} \neq \begin{bmatrix} 0 \\ 0 \end{bmatrix}$, finally produces the dispersion equation of the pure Lamb waves linking v and ξ as presented in Eq. (4.42).

$$\mathcal{D}_T(v, \xi) = \mathcal{D}_T^R(v, \xi) + i\mathcal{D}_T^I(v, \xi) \triangleq \begin{vmatrix} T_{31} & T_{32} \\ T_{41} & T_{42} \end{vmatrix} = 0 \quad (4.42)$$

3. The pure SH waves for $\mathbf{T}^{\text{mono}} \in \mathbb{C}^{2 \times 2}$

When $\mathbf{T}^{\text{mono}} \in \mathbb{C}^{2 \times 2}$, it characterizes the pure SH waves. Expand Eq. (4.33) to derive the dispersion equation of the pure SH waves, as presented in Eq. (4.43).

$$\begin{bmatrix} u_2 \\ \sigma_{23} \end{bmatrix}_{\text{bot}}^{l_n} = \begin{bmatrix} T_{11} & T_{12} \\ T_{21} & T_{22} \end{bmatrix} \begin{bmatrix} u_2 \\ \sigma_{23} \end{bmatrix}_{\text{top}}^{l_1} \quad (4.43)$$

By applying the traction-free boundary condition at the bottom- and top-most surfaces of the plate, $\begin{bmatrix} \sigma_{23} \end{bmatrix}_{\text{bot}}^{l_n} = \begin{bmatrix} \sigma_{23} \end{bmatrix}_{\text{top}}^{l_1} = \begin{bmatrix} 0 \end{bmatrix}$, the dispersion equation of the pure SH waves linking v and ξ just come into being, as presented in Eq. (4.44).

$$\mathcal{D}_T(v, \xi) = \mathcal{D}_T^R(v, \xi) + i\mathcal{D}_T^I(v, \xi) \triangleq T_{21} = 0 \quad (4.44)$$

4.3. TRANSFER MATRIX METHOD

To this stage, the derivation process of TMM for various guided wave types has been completed. The pseudo-code for processing the three wave types is presented in Algorithm 2, 3 and 4, respectively. But before running the three algorithms, Algorithm 1 should be run to determine the correct wave type existing in the laminate system. Note that though this chapter concentrates on the multi-layered plate, the TMM framework is compatible with the single layer case given that for a single layer plate $\mathbf{T}^{\text{mono}} = \mathbf{T}^{l_1}$ in Eq. (4.34).

Algorithm 1 Judge wave type according to the rotated laminae's stiffness matrix type.

Input: Each layer's material properties $(\mathbf{C}_k, \rho_k, d_k, \phi_k)$ for $(k = 1, \dots, n)$;
The wave propagation angle of interest θ .

- 1: Compute the rotated stiffness matrix $\mathbf{C}'_k = \text{Rot}\{\mathbf{C}_k, \theta - \phi_k\}$ for $(k = 1, \dots, n)$.
- 2: **if** All $\mathbf{C}'_k \in \mathcal{C}_{\mathcal{M}}$ **then** % Branch 1
- 3: Call Algorithm 2 to process the coupled Lamb and SH waves.
- 4: **else if** All $\mathbf{C}'_k \in \mathcal{C}_{\mathcal{O}}$ **then** % Branch 2
- 5: Call Algorithm 3 and 4 to process the pure Lamb and SH waves.
- 6: **else if** Some $\mathbf{C}'_k \in \mathcal{C}_{\mathcal{M}}$ and other $\mathbf{C}'_k \in \mathcal{C}_{\mathcal{O}}$ **then** % Branch 3
- 7: Call Algorithm 5 to process the hybrid Lamb and SH waves.
- 8: **end if**

Algorithm 2 Process the coupled Lamb and SH waves via TMM

Input: Each layer's material properties $(\mathbf{C}_k, \rho_k, d_k, \phi_k)$ for $(k = 1, \dots, n)$;
The wave propagation angle of interest θ ;
The minimum and maximum wavenumber of interest (ξ_{\min}, ξ_{\max}) ;
The minimum, maximum and incremental velocity of interest $(v_{\min}, v_{\max}, \Delta v)$.

- 1: Compute $\mathbf{C}'_k = \text{Rot}\{\mathbf{C}_k, \theta - \phi_k\}$ for $(k = 1, \dots, n)$.
- 2: **if** Any $\mathbf{C}'_k \notin \mathcal{C}_{\mathcal{M}}$ **then**
- 3: Call Algorithm 1 to determine the correct wave type.
- 4: **end if**
- 5: **for** $v_0 = v_{\min} : \Delta v : v_{\max}$ **do** % Solve the dispersion equation at each fixed v_0 .
- 6: **for** $k = 1 : 1 : n$ **do** % Loop through each layer.
- 7: Compute $(\alpha_r, V_r, W_r, \beta_{1r}, \beta_{2r}, \beta_{3r})$ for $(r = 1, \dots, 6)$ via Eqs. (3.24)(3.27)(3.31) using the data $(\mathbf{C}'_k, \rho_k, v_0)$.
- 8: Compute the local lamina matrices $(\mathbf{\Gamma}_{6 \times 6}^{l_k}, \mathbf{\Lambda}_{6 \times 6}^{l_k}(d_k))$ via Eq. (4.11).
- 9: Compute the local transfer matrix $\mathbf{T}_{6 \times 6}^{l_k}$ via Eq. (4.29).
- 10: **end for**
- 11: Compute the monodromy transfer matrix $\mathbf{T}_{6 \times 6}^{\text{mono}}$ via Eq. (4.34).
- 12: Solve $\mathcal{D}_T(v_0, \xi) = 0$ in Eq. (4.39) to get multiple roots $(\xi_1, \xi_2, \dots) \in [\xi_{\min}, \xi_{\max}]$.
- 13: **end for**

Output: All solution points (v_i, ξ_i) in the range $[v_{\min}, v_{\max}] \times [\xi_{\min}, \xi_{\max}]$.
Plot dispersion curves of the coupled Lamb and SH waves in (v, ξ) , (ω, ξ) , (ω, v) and (ω, c_g) domains where $\omega = \xi v$ and $c_g = \frac{\partial \omega}{\partial \xi}$ is the group velocity.

4.3. TRANSFER MATRIX METHOD

Algorithm 3 Process the pure Lamb waves via TMM

Input: Each layer's material properties $(\mathbf{C}_k, \rho_k, d_k, \phi_k)$ for $(k = 1, \dots, n)$;
The wave propagation angle of interest θ ;
The minimum and maximum wavenumber of interest (ξ_{\min}, ξ_{\max}) ;
The minimum, maximum and incremental velocity of interest $(v_{\min}, v_{\max}, \Delta v)$.

- 1: Compute $\mathbf{C}'_k = \text{Rot}\{\mathbf{C}_k, \theta - \phi_k\}$ for $(k = 1, \dots, n)$.
- 2: **if** Any $\mathbf{C}'_k \notin \mathcal{C}_O$ **then**
- 3: Call Algorithm 1 to determine the correct wave type.
- 4: **end if**
- 5: **for** $v_0 = v_{\min} : \Delta v : v_{\max}$ **do** % Solve the dispersion equation at each fixed v_0 .
- 6: **for** $k = 1 : 1 : n$ **do** % Loop through each layer.
- 7: Compute $(\alpha_r, W_r, \beta_{1r}, \beta_{3r})$ for $(r = 1, \dots, 4)$ via Eqs. (3.44)(3.46)(3.49) using the data $(\mathbf{C}'_k, \rho_k, v_0)$.
- 8: Compute the local lamina matrices $(\mathbf{\Gamma}_{4 \times 4}^{l_k}, \mathbf{\Lambda}_{4 \times 4}^{l_k}(d_k))$ via Eq. (4.18).
- 9: Compute the local transfer matrix $\mathbf{T}_{4 \times 4}^{l_k}$ via Eq. (4.29).
- 10: **end for**
- 11: Compute the monodromy transfer matrix $\mathbf{T}_{4 \times 4}^{\text{mono}}$ via Eq. (4.34).
- 12: Solve $\mathcal{D}_T(v_0, \xi) = 0$ in Eq. (4.42) to get multiple roots $(\xi_1, \xi_2, \dots) \in [\xi_{\min}, \xi_{\max}]$.
- 13: **end for**

Output: All solution points (v_i, ξ_i) in the range $[v_{\min}, v_{\max}] \times [\xi_{\min}, \xi_{\max}]$.
Plot dispersion curves of the pure Lamb waves in (v, ξ) , (ω, ξ) , (ω, v) and (ω, c_g) domains.

Algorithm 4 Process the pure SH waves via TMM

Input: Each layer's material properties $(\mathbf{C}_k, \rho_k, d_k, \phi_k)$ for $(k = 1, \dots, n)$;
The wave propagation angle of interest θ ;
The minimum and maximum wavenumber of interest (ξ_{\min}, ξ_{\max}) ;
The minimum, maximum and incremental velocity of interest $(v_{\min}, v_{\max}, \Delta v)$.

- 1: Compute $\mathbf{C}'_k = \text{Rot}\{\mathbf{C}_k, \theta - \phi_k\}$ for $(k = 1, \dots, n)$.
- 2: **if** Any $\mathbf{C}'_k \notin \mathcal{C}_O$ **then**
- 3: Call Algorithm 1 to determine the correct wave type.
- 4: **end if**
- 5: **for** $v_0 = v_{\min} : \Delta v : v_{\max}$ **do** % Solve the dispersion equation at each fixed v_0 .
- 6: **for** $k = 1 : 1 : n$ **do** % Loop through each layer.
- 7: Compute (α_r, β_{2r}) for $(r = 5, 6)$ via Eqs. (3.58)(3.60) using the data $(\mathbf{C}'_k, \rho_k, v_0)$.
- 8: Compute the local lamina matrices $(\mathbf{\Gamma}_{2 \times 2}^{l_k}, \mathbf{\Lambda}_{2 \times 2}^{l_k}(d_k))$ via Eq. (4.24).
- 9: Compute the local transfer matrix $\mathbf{T}_{2 \times 2}^{l_k}$ via Eq. (4.29).
- 10: **end for**
- 11: Compute the monodromy transfer matrix $\mathbf{T}_{2 \times 2}^{\text{mono}}$ via Eq. (4.34).
- 12: Solve $\mathcal{D}_T(v_0, \xi) = 0$ in Eq. (4.44) to get multiple roots $(\xi_1, \xi_2, \dots) \in [\xi_{\min}, \xi_{\max}]$.
- 13: **end for**

Output: All solution points (v_i, ξ_i) in the range $[v_{\min}, v_{\max}] \times [\xi_{\min}, \xi_{\max}]$.
Plot dispersion curves of the pure SH waves in (v, ξ) , (ω, ξ) , (ω, v) and (ω, c_g) domains.

4.3.4 Wave mode shapes

Wave mode shapes are the displacement and stress fields across the thickness of the laminate at a fixed point in the wave propagation path. The key step to compute wave mode shapes is to compute the participation factors $\boldsymbol{\eta}^{l_k}$ of each layer, which can be regarded as, to some extent, the inverse process of the transfer matrix derivation in Section 4.3.1 and 4.3.2. In this section, we take the example of computing mode shapes of the coupled Lamb and SH waves. For other wave types, it can be achieved by a similar way.

For a known dispersion solution point (v_i, ξ_i) solved through Algorithm 2, each layer's various kinds of matrices are known as well, $(\mathbf{U}_{3 \times 6}^{l_k}, \boldsymbol{\beta}_{3 \times 6}^{l_k}, \boldsymbol{\Lambda}_{6 \times 6}^{l_k}(d_k), \mathbf{T}_{6 \times 6}^{l_k}, \mathbf{T}_{6 \times 6}^{l_k}, \mathbf{T}_{6 \times 6}^{\text{mono}})$. Then, $\mathbf{u}_{\text{top}}^{l_1}$ in Eq. (4.38) can be solved from the three-order linear homogeneous equation set, which is the zero-eigenvalue correlated eigenvector of the submatrix $\mathbf{T}_{6 \times 6}^{\text{mono}}(4 : 6, 1 : 3)$. Thanks to the traction-free boundary condition at the top side of layer l_1 (see Eq. (4.36)), $\boldsymbol{\sigma}_{\text{top}}^{l_1} = \mathbf{0}$, the field variables of layer l_1 at its top side are then obtained $\mathbf{S}_{\text{top}}^{l_1} = \begin{bmatrix} \mathbf{u}_{\text{top}}^{l_1} \\ \mathbf{0} \end{bmatrix}$. For other layer's field variables at its top side, it can be computed recurrently from $\mathbf{S}_{\text{top}}^{l_1}$ as follows based on Eq. (4.28).

$$\mathbf{S}_{\text{top}}^{l_k} = \mathbf{S}_{\text{bot}}^{l_{k-1}} = \mathbf{T}^{l_{k-1}} \mathbf{S}_{\text{top}}^{l_{k-1}} \quad (k = 2, \dots, n) \quad (4.45)$$

Each layer's participation factors $\boldsymbol{\eta}^{l_k}$ are then computed as follows based on Eq. (4.26) by omitting the phase term $e^{i\xi(x_1 - vt)}$.

$$\boldsymbol{\eta}^{l_k} = (\mathbf{T}^{l_k})^{-1} \mathbf{S}_{\text{top}}^{l_k} \quad (k = 1, \dots, n) \quad (4.46)$$

Finally, substitute $\boldsymbol{\eta}^{l_k}$ into Eqs. (4.2) and (4.8) to compute the layer l_k 's mode shapes of displacement and stress, respectively. The whole laminate's mode shapes are then concatenated from all layers' ones.

4.4 Hybrid matrix strategy

4.4.1 The incompatibility issue of matrix dimension of the local transfer matrices

In Eq. (4.34), there is a requirement that all layers' local transfer matrices \mathbf{T}^{l_k} ($k = 1, \dots, n$) should have the same dimension in order to produce the monodromy transfer matrix $\mathbf{T}^{\text{mono}} \in \mathbb{C}^{p \times p}$, otherwise an incompatibility issue of the local transfer matrices in terms of their matrix dimension

4.4. HYBRID MATRIX STRATEGY

is encountered. Physically, this issue corresponds to the case that the interested wave propagation direction is along the principal direction of one layer (producing the decoupled Lamb and SH waves in this layer) but along the off-principal direction of another layer (producing the coupled Lamb and SH waves in this layer). This issue is very common and it is usually present in multi-layered anisotropic composite plates owing to the various stacking angles of layups. However, this issue has not been given sufficient attention in the literature and only a few works attempted to tackle this issue.

The first work was presented by S. Pant in [8]. In this reference, a pseudo correction measure was adopted to avoid this issue. Specifically, along the interested wave propagation direction, when the rotated stiffness matrix in the layer l_i behaves like the orthotropic type but in another layer l_j like the monoclinic type, namely, $\mathbf{C}'_i \in \mathcal{C}_O$ and $\mathbf{C}'_j \in \mathcal{C}_M$, \mathbf{C}'_i is further rotated with an additional minor angle $\Delta\theta = -1^\circ$ such that it transitions to $\mathbf{C}''_i \in \mathcal{C}_M$. The screenshot of Pant's pseudo correction measure is presented in Figure 4.3. As the additional rotation angle is relatively small, the pseudo correction has very little effect on the overall stiffness of the laminate. Thus, it is doable but not orthodox from a mathematical perspective. Besides, there is a vital problem that, in metallic-composite structures, the stiffness matrix of the metallic layer always keeps the isotropic type regardless of the rotation angle, and the composite layers can be orthotropic or monoclinic type along an arbitrary propagation direction. Thus, in metallic-composite structures Pant's pseudo correction measure is invalid.

Fig. 8. Flow chart to numerically solve Lamb wave equations. *1: For orthotropic and higher symmetry materials during individual layer calculation; whenever the material orientation angle (fiber orientation angle within a layer) equals the sensor orientation angle (considered angle for wave propagation or the orientation angle between the wave source and sensor), the quasi-shear horizontal wave decoupled into pure shear horizontal wave. This reduced the total quasi waves from six to four and Eqs. (2.27) and (2.28) goes to zero. As such, the Global Matrix approach became numerically unstable when six waves were combined with four waves due to the decoupling effect and no solution was found. Therefore, a simple solution was purposed by subtracting the material orientation by 1° , which ensures the six waves travelling along the plane at any given material and sensor angles. Subtracting 1° from the material orientation angle has very minimal effect on the overall stiffness of the laminate. This is because fiber misalignments occur frequently in composite manufacturing process and it has been reported that misalignments of $\pm 10^\circ$ produces only a 3% change in the laminate Young's Modulus [48]. *2: The numerical solution was found to be stable when the entire Global Matrix was divided by the largest term within the matrix before calculating its determinant. The division also reduced the overall computational time.

Figure 4.3 – Pant's pseudo correction measure to deal with the incompatibility issue [8].

Another work was done by D. Barazanchy in [9] for isotropic materials, who considered the Christoffel equation of isotropic materials in Eq. (4.47) and the three solutions of α^2 in Eq. (4.48). The displacement amplitudes of the six partial waves $[U_r, V_r, W_r]^T$ ($r = 1, \dots, 6$) were obtained from the eigenvectors of the Christoffel matrix that corresponds to the zero eigenvalues. Due to the repeated solutions $\alpha_3^2 = \alpha_5^2$, the corresponding eigenvectors are linearly dependent. Thus, the vector orthogonality analysis was used to sort these eigenvectors to generate the six linearly independent eigenvectors being the admissible displacement amplitudes of the six partial waves. The screenshot of Barazanchy's

vector orthogonality analysis is presented in Figure 4.4. This method is only applicable to isotropic materials and it encountered numerical instability issue when applied to a 50-layered plate [9].

$$\begin{bmatrix} C_{11} - \rho v^2 + \frac{C_{11}-C_{12}}{2}\alpha^2 & 0 & \frac{C_{11}+C_{12}}{2}\alpha \\ 0 & \frac{C_{11}-C_{12}}{2} - \rho v^2 + \frac{C_{11}-C_{12}}{2}\alpha^2 & 0 \\ \frac{C_{11}+C_{12}}{2}\alpha & 0 & \frac{C_{11}-C_{12}}{2} - \rho v^2 + C_{11}\alpha^2 \end{bmatrix} \begin{bmatrix} U \\ V \\ W \end{bmatrix} = \begin{bmatrix} 0 \\ 0 \\ 0 \end{bmatrix} \quad (4.47)$$

$$\alpha_1^2 = \frac{\rho v^2}{C_{11}} - 1, \quad \alpha_3^2 = \frac{2\rho v^2}{C_{11} - C_{12}} - 1, \quad \alpha_5^2 = \frac{2\rho v^2}{C_{11} - C_{12}} - 1. \quad (4.48)$$

three α^2 values produced six α values, where, in the case of an isotropic material four of the six values were the same in magnitude. Substituting one of those four α values into equation (4) produced an eigenvalue problem which had two eigenvectors satisfying the equation corresponding to two zero eigenvalues. A total of ten, instead of an expected six, eigenvectors were obtained for the six α values. Therefore, the eigenvectors were sorted first based on their type (shear-horizontal or shear-vertical) and pressure, using the vector orthogonality principle. The sorted eigenvectors were matched with their corresponding α values resulting in six distinguished sets of eigenvectors and α values. Applying an uniqueness algorithm to the eigenvectors yielded no more duplicate eigenvectors for each α value.

Figure 4.4 – Barazanchy’s vector orthogonality analysis to deal with the incompatibility issue [9].

In the current thesis, we propose a new hybrid matrix strategy (HMS) to solve the incompatibility issue, which is effective for various material types including isotropic and orthotropic materials. The most important aspect of HMS is that it is directly derived from the layer-wise PWSA similar to the coupled Lamb and SH waves in Section 4.2.1. Thus, HMS is mathematically rigorous and numerically stable.

4.4.2 Hybrid local lamina matrices of pure Lamb and SH waves

The incompatibility issue mathematically corresponds to the case that in some layers their local transfer matrices are six-order $\mathbf{T}_{6 \times 6}^{l_i}$ (producing the coupled Lamb and SH waves) and in other layers they have two decoupled four-order and two-order of local transfer matrices $\mathbf{T}_{4 \times 4}^{l_j}$ (producing the pure Lamb waves) and $\mathbf{T}_{2 \times 2}^{l_j}$ (producing the pure SH waves). The process of deriving the HMS is to ‘re-couple’ $\mathbf{T}_{4 \times 4}^{l_j}$ and $\mathbf{T}_{2 \times 2}^{l_j}$ to yield a new six-order local transfer matrix $\tilde{\mathbf{T}}_{6 \times 6}^{l_j}$, which is compatible with $\mathbf{T}_{6 \times 6}^{l_i}$ in terms of the matrix order.

4.4. HYBRID MATRIX STRATEGY

The single-layer system studied in Chapter 3 is the basis to derive the equations regarding to the multi-layer system. Specifically, the displacement expressions of (u_1, u_3) in Eq. (3.47) and u_2 in Eq. (3.59) can be merged in Eq. (4.49).

$$\begin{cases} u_1 = \left(\sum_{r=1}^4 \eta_r e^{i\xi\alpha_r x_3} \right) e^{i\xi(x_1-vt)} \\ u_2 = \left(\sum_{r=5}^6 \eta_r e^{i\xi\alpha_r x_3} \right) e^{i\xi(x_1-vt)} \\ u_3 = \left(\sum_{r=1}^4 \eta_r W_r e^{i\xi\alpha_r x_3} \right) e^{i\xi(x_1-vt)} \end{cases} \quad (4.49)$$

It is equivalent to Eq. (4.50) under the concept of layer-wise PWSA.

$$\begin{cases} u_1 = \left(\sum_{r=1}^4 1 \times \eta_r e^{i\xi\alpha_r x_3} + \sum_{r=5}^6 0 \times \eta_r e^{i\xi\alpha_r x_3} \right) e^{i\xi(x_1-vt)} \\ u_2 = \left(\sum_{r=1}^4 0 \times \eta_r e^{i\xi\alpha_r x_3} + \sum_{r=5}^6 1 \times \eta_r e^{i\xi\alpha_r x_3} \right) e^{i\xi(x_1-vt)} \\ u_3 = \left(\sum_{r=1}^4 W_r \times \eta_r e^{i\xi\alpha_r x_3} + \sum_{r=5}^6 0 \times \eta_r e^{i\xi\alpha_r x_3} \right) e^{i\xi(x_1-vt)} \end{cases} \quad (4.50)$$

Rewrite Eq. (4.50) as the matrix form in Eq. (4.51) and the compact form in Eq. (4.52).

$$\begin{bmatrix} u_1 \\ u_2 \\ u_3 \end{bmatrix} = \begin{bmatrix} 1 & 1 & 1 & 1 & 0 & 0 \\ 0 & 0 & 0 & 0 & 1 & 1 \\ W_1 & W_2 & W_3 & W_4 & 0 & 0 \end{bmatrix} \begin{bmatrix} e^{i\xi\alpha_1 x_3} \\ e^{i\xi\alpha_2 x_3} \\ e^{i\xi\alpha_3 x_3} \\ e^{i\xi\alpha_4 x_3} \\ e^{i\xi\alpha_5 x_3} \\ e^{i\xi\alpha_6 x_3} \end{bmatrix} \begin{bmatrix} \eta_1 \\ \eta_2 \\ \eta_3 \\ \eta_4 \\ \eta_5 \\ \eta_6 \end{bmatrix} e^{i\xi(x_1-vt)} \quad (4.51)$$

$$\mathbf{u}_{3 \times 1} = \tilde{\mathbf{U}}_{3 \times 6} \mathbf{\Lambda}_{6 \times 6}(x_3) \boldsymbol{\eta}_{6 \times 1} e^{i\xi(x_1-vt)} \quad (4.52)$$

where, $\tilde{\mathbf{U}}_{3 \times 6}$ is used to distinguish $\mathbf{U}_{3 \times 6}$ defined in Eq. (4.4), and it is regarded as the hybrid matrix of $\mathbf{U}_{2 \times 4}$ in Eq. (4.14) and $\mathbf{U}_{1 \times 2}$ in Eq. (4.20). The tilde ‘~’ represents the hybrid sense. Physically, the zero elements in $\tilde{\mathbf{U}}_{3 \times 6}$ denote that the amplitudes of the corresponding partial waves are zero.

The stress equations of $(\sigma_{33}, \sigma_{13})$ in Eq. (3.48) and σ_{23} in Eq. (3.60) can be merged in Eq. (4.53) and are further equivalently written as the superposition form in Eq. (4.54).

$$\begin{cases} \sigma_{33} = \left(\sum_{r=1}^4 \eta_r \beta_{1r} e^{i\xi\alpha_r x_3} \right) e^{i\xi(x_1-vt)} \\ \sigma_{23} = \left(\sum_{r=5}^6 \eta_r \beta_{2r} e^{i\xi\alpha_r x_3} \right) e^{i\xi(x_1-vt)} \\ \sigma_{13} = \left(\sum_{r=1}^4 \eta_r \beta_{3r} e^{i\xi\alpha_r x_3} \right) e^{i\xi(x_1-vt)} \end{cases} \quad (4.53)$$

$$\begin{cases} \sigma_{33} = \left(\sum_{r=1}^4 \beta_{1r} \times \eta_r e^{i\xi\alpha_r x_3} + \sum_{r=5}^6 0 \times \eta_r e^{i\xi\alpha_r x_3} \right) e^{i\xi(x_1-vt)} \\ \sigma_{23} = \left(\sum_{r=1}^4 0 \times \eta_r e^{i\xi\alpha_r x_3} + \sum_{r=5}^6 \beta_{2r} \times \eta_r e^{i\xi\alpha_r x_3} \right) e^{i\xi(x_1-vt)} \\ \sigma_{13} = \left(\sum_{r=1}^4 \beta_{3r} \times \eta_r e^{i\xi\alpha_r x_3} + \sum_{r=5}^6 0 \times \eta_r e^{i\xi\alpha_r x_3} \right) e^{i\xi(x_1-vt)} \end{cases} \quad (4.54)$$

Rewrite Eq. (4.54) as the matrix form in Eq. (4.55) and the compact form in Eq. (4.56).

$$\begin{bmatrix} \sigma_{33} \\ \sigma_{23} \\ \sigma_{13} \end{bmatrix} = \begin{bmatrix} \beta_{11} & \beta_{12} & \beta_{13} & \beta_{14} & 0 & 0 \\ 0 & 0 & 0 & 0 & \beta_{25} & \beta_{26} \\ \beta_{31} & \beta_{32} & \beta_{33} & \beta_{34} & 0 & 0 \end{bmatrix} \begin{bmatrix} e^{i\xi\alpha_1 x_3} \\ e^{i\xi\alpha_2 x_3} \\ e^{i\xi\alpha_3 x_3} \\ e^{i\xi\alpha_4 x_3} \\ e^{i\xi\alpha_5 x_3} \\ e^{i\xi\alpha_6 x_3} \end{bmatrix} \begin{bmatrix} \eta_1 \\ \eta_2 \\ \eta_3 \\ \eta_4 \\ \eta_5 \\ \eta_6 \end{bmatrix} e^{i\xi(x_1-vt)} \quad (4.55)$$

$$\boldsymbol{\sigma}_{3 \times 1} = \tilde{\boldsymbol{\beta}}_{3 \times 6} \boldsymbol{\Lambda}_{6 \times 6}(x_3) \boldsymbol{\eta}_{6 \times 1} e^{i\xi(x_1-vt)} \quad (4.56)$$

where, $\tilde{\boldsymbol{\beta}}_{3 \times 6}$ is used to distinguish $\boldsymbol{\beta}_{3 \times 6}$ defined in Eq. (4.10), and it is regarded as the hybrid matrix of $\boldsymbol{\beta}_{2 \times 4}$ in Eq. (4.16) and $\boldsymbol{\beta}_{1 \times 2}$ in Eq. (4.22).

Eqs. (4.51) and (4.55) can be concatenated into a single equation, see the matrix form in Eq. (4.57) and the compact form in Eq. (4.58).

$$\begin{bmatrix} u_1 \\ u_2 \\ u_3 \\ \sigma_{33} \\ \sigma_{23} \\ \sigma_{13} \end{bmatrix} = \begin{bmatrix} 1 & 1 & 1 & 1 & 0 & 0 \\ 0 & 0 & 0 & 0 & 1 & 1 \\ W_1 & W_2 & W_3 & W_4 & 0 & 0 \\ \beta_{11} & \beta_{12} & \beta_{13} & \beta_{14} & 0 & 0 \\ 0 & 0 & 0 & 0 & \beta_{25} & \beta_{26} \\ \beta_{31} & \beta_{32} & \beta_{33} & \beta_{34} & 0 & 0 \end{bmatrix} \begin{bmatrix} e^{i\xi\alpha_1 x_3} \\ e^{i\xi\alpha_2 x_3} \\ e^{i\xi\alpha_3 x_3} \\ e^{i\xi\alpha_4 x_3} \\ e^{i\xi\alpha_5 x_3} \\ e^{i\xi\alpha_6 x_3} \end{bmatrix} \begin{bmatrix} \eta_1 \\ \eta_2 \\ \eta_3 \\ \eta_4 \\ \eta_5 \\ \eta_6 \end{bmatrix} e^{i\xi(x_1-vt)} \quad (4.57)$$

$$\mathbf{S}_{6 \times 1} = \tilde{\boldsymbol{\Gamma}}_{6 \times 6} \boldsymbol{\Lambda}_{6 \times 6}(x_3) \boldsymbol{\eta}_{6 \times 1} e^{i\xi(x_1-vt)} = \tilde{\mathbf{Z}}_{6 \times 6}(x_3) \boldsymbol{\eta}_{6 \times 1} e^{i\xi(x_1-vt)} \quad (4.58)$$

At this moment, $\tilde{\mathbf{U}}_{3 \times 6}$, $\tilde{\boldsymbol{\beta}}_{3 \times 6}$, $\tilde{\boldsymbol{\Gamma}}_{6 \times 6}$ are uniformly defined as the **hybrid local lamina matrices**, and they are further used to compute the **hybrid local transfer matrix** $\tilde{\mathbf{T}}_{6 \times 6}$ in Eq. (4.59), which is based on Eq. (4.29). It can be easily proved that any two rows of $\tilde{\boldsymbol{\Gamma}}_{6 \times 6}$ are linearly independent that makes it non-singular. Thus, the inverse of $\tilde{\boldsymbol{\Gamma}}_{6 \times 6}$ in Eq. (4.59) is defined and this property secures the numerical stability of the HMS.

$$\tilde{\mathbf{T}}_{6 \times 6} = \tilde{\boldsymbol{\Gamma}}_{6 \times 6} \boldsymbol{\Lambda}_{6 \times 6}(d_k) \left(\tilde{\boldsymbol{\Gamma}}_{6 \times 6} \right)^{-1} \in \mathbb{C}^{6 \times 6} \quad (4.59)$$

With the compatible transfer matrices between $\tilde{\mathbf{T}}_{6 \times 6}^{l_j}$ and $\mathbf{T}_{6 \times 6}^{l_i}$, the hybrid monodromy transfer matrix $\tilde{\mathbf{T}}_{6 \times 6}^{\text{mono}}$ is computed based on Eq. (4.34). The above derivations for the HMS is programmatically interpreted in Algorithm 5, which is logically accompanied by Algorithm 1 to make sure that the

4.4. HYBRID MATRIX STRATEGY

current guided wave type correctly corresponds to the hybrid case. Specifically, the Branch 3 of Algorithm 1 should be targeted. In response to the HMS, the wave solutions that are obtained via Algorithm 5 are classified into the **hybrid Lamb and SH waves** to distinguish the terminology of the coupled waves in Algorithm 2 and the pure waves in Algorithm 3 and 4.

Algorithm 5 HMS to process the matrix incompatibility issue of the hybrid Lamb and SH waves

Input: Each layer's material properties $(\mathbf{C}_k, \rho_k, d_k, \phi_k)$ for $(k = 1, \dots, n)$;
The wave propagation angle of interest θ ;
The minimum and maximum wavenumber of interest (ξ_{\min}, ξ_{\max}) ;
The minimum, maximum and incremental velocity of interest $(v_{\min}, v_{\max}, \Delta v)$.

- 1: Compute $\mathbf{C}'_k = \text{Rot}\{\mathbf{C}_k, \theta - \phi_k\}$ for $(k = 1, \dots, n)$.
- 2: **if** All $\mathbf{C}'_k \in \mathcal{C}_{\mathcal{M}}$ or all $\mathbf{C}'_k \in \mathcal{C}_{\mathcal{O}}$ **then**
- 3: Call Algorithm 1 to determine the correct wave type.
- 4: **end if**
- 5: **for** $v_0 = v_{\min} : \Delta v : v_{\max}$ **do**
- 6: **for** $k = 1 : 1 : n$ **do**
- 7: **if** $\mathbf{C}'_k \in \mathcal{C}_{\mathcal{M}}$ **then** % Process the coupled Lamb and SH waves.
- 8: Compute $(\alpha_r, W_r, W_r, \beta_{1r}, \beta_{2r}, \beta_{3r})$ for $(r = 1, \dots, 6)$ via Eqs. (3.24)(3.27)(3.31) using the data $(\mathbf{C}'_k, \rho_k, v_0)$.
- 9: Compute the local lamina matrices $(\mathbf{\Gamma}_{6 \times 6}^{l_k}, \mathbf{\Lambda}_{6 \times 6}^{l_k}(d_k))$ via Eq. (4.11).
- 10: Compute the local transfer matrix $\mathbf{T}_{6 \times 6}^{l_k}$ via Eq. (4.29).
- 11: **else if** $\mathbf{C}'_k \in \mathcal{C}_{\mathcal{O}}$ **then** % Process the hybrid Lamb and SH waves.
- 12: Compute $(\alpha_r, W_r, \beta_{1r}, \beta_{3r})$ for $(r = 1, \dots, 4)$ via Eqs. (3.44)(3.46)(3.49) using the data $(\mathbf{C}'_k, \rho_k, v_0)$.
- 13: Compute the local lamina matrices $(\mathbf{\Gamma}_{4 \times 4}^{l_k}, \mathbf{\Lambda}_{4 \times 4}^{l_k}(d_k))$ via Eq. (4.18).
- 14: Compute (α_r, β_{2r}) for $(r = 5, 6)$ via Eqs. (3.58)(3.60) using the data $(\mathbf{C}'_k, \rho_k, v_0)$.
- 15: Compute the local lamina matrices $(\mathbf{\Gamma}_{2 \times 2}^{l_k}, \mathbf{\Lambda}_{2 \times 2}^{l_k}(d_k))$ via Eq. (4.24).
- 16: Compute the hybrid local lamina matrices $\tilde{\mathbf{\Gamma}}_{6 \times 6}^{l_k}$ using the obtained $(\mathbf{\Gamma}_{4 \times 4}^{l_k}, \mathbf{\Gamma}_{2 \times 2}^{l_k})$ based on Eq. (4.57).
- 17: Compute the hybrid local transfer matrix $\tilde{\mathbf{T}}_{6 \times 6}^{l_k}$ using the obtained $(\tilde{\mathbf{\Gamma}}_{6 \times 6}^{l_k}, \mathbf{\Lambda}_{6 \times 6}^{l_k})$ based on Eq. (4.59).
- 18: **end if**
- 19: **end for**
- 20: Compute the monodromy transfer matrix $\tilde{\mathbf{T}}_{6 \times 6}^{\text{mono}}$ via Eq. (4.34).
- 21: Solve $\mathcal{D}_T(v_0, \xi) = 0$ in Eq. (4.39) to get multiple roots $(\xi_1, \xi_2, \dots) \in [\xi_{\min}, \xi_{\max}]$.
- 22: **end for**

Output: All solution points (v_i, ξ_i) in the range $[v_{\min}, v_{\max}] \times [\xi_{\min}, \xi_{\max}]$.
Plot dispersion curves of the hybrid Lamb and SH waves in (v, ξ) , (ω, ξ) , (ω, v) and (ω, c_g) domains.

4.5 Four classes of composite laminates

In aeronautic and aerospace industry, an arbitrarily oriented composite laminate can be classified into four classes according to the stacking angles and material compositions as listed in Table 4.1, in which the unidirectional, cross-ply and quasi-isotropic laminates are composed solely by orthotropic materials (the transversely isotropic materials are included in the type of orthotropic materials according to the Section 2.2.4.) and the metallic-composite laminate consists of orthotropic (for composite layers) and isotropic (for metallic layers) materials. The second column of Table 4.1 lists the representative for each laminate class. According to the remark below Table 4.1, the unidirectional laminate can be mathematically modeled as the single layer plate which is the focus of Chapter 3. Thus, in the next sections for numerical examples, only the latter three laminates are adopted to validate the developed TMM adapted to the coupled, pure and hybrid wave types as indicated in Table 4.1.

In an arbitrarily oriented composite laminate, if a certain wave propagation angle θ will lead to the incompatibility issue (causing the hybrid Lamb and SH waves), this angle is defined as the **singular angle** of this laminate. For example, $\theta = 45^\circ$ in the quasi-isotropic laminate of Table 4.1.

Table 4.1 – Four classes of composite laminates and the wave type dependence on the propagation angle.

Laminate class	Stacking angles	Propagation angle θ	Coupled waves	Pure waves	Hybrid waves
Unidirectional ¹	$[0]_8$	$\theta \in \{0^\circ, 90^\circ\}$		✓	
		$\theta \notin \{0^\circ, 90^\circ\}$	✓		
Cross-ply	$[(0/90)_s]_2$	$\theta \in \{0^\circ, 90^\circ\}$		✓	
		$\theta \notin \{0^\circ, 90^\circ\}$	✓		
Quasi-isotropic	$[0/90/+45/-45]_s$	$\theta \in \{0^\circ, 45^\circ, 90^\circ, -45^\circ\}$			✓
		$\theta \notin \{0^\circ, 45^\circ, 90^\circ, -45^\circ\}$	✓		
Metallic-composite	$[Al/0/90/Al/90/0/Al]_2^2$	$\theta \in \{0^\circ, 90^\circ\}$		✓	
		$\theta \notin \{0^\circ, 90^\circ\}$			✓

¹ Remark on the unidirectional laminate class: since the field variables (displacement and stress) are considered to be continuous across the interface of adjacent layers (the perfect interface condition is assumed), the unidirectional laminate $[0]_8$ is mathematically equivalent to the single layer plate $[0]_1$ that has the same thickness as the $[0]_8$ plate.

² Al: the aluminum layer that is an isotropic material.

4.6 Numerical example on a cross-ply laminate

The first example is the cross-ply laminate consisting of eight transversely isotropic laminae with stacking angles of layups $[(0/90)_s]_2$. The material properties of each ply are listed in Table 4.2 cited from [12]. The total thickness of the plate is 1.6 mm since the thickness of each ply is 0.2 mm. The stiffness matrix of each ply along its fiber direction is presented in Eq. (4.60) which is computed based on Eq. (2.12).

Table 4.2 – Material properties of a transversely isotropic lamina

Density [kg/m ³]	E_1 [GPa]	E_2 [GPa]	G_{12} [GPa]	ν_{12}	ν_{23}	Ply thickness	Stacking angles
1608	172	9.8	6.1	0.37	0.55	0.2 mm	$[(0/90)_s]_2$

$$\mathbf{C} = \begin{bmatrix} 178.2 & 8.347 & 8.347 & 0 & 0 & 0 \\ & 14.44 & 8.119 & 0 & 0 & 0 \\ & & 14.44 & 0 & 0 & 0 \\ & & & 3.161 & 0 & 0 \\ \text{sym} & & & & 6.1 & 0 \\ & & & & & 6.1 \end{bmatrix} \text{ GPa} \quad (4.60)$$

4.6.1 The pure Lamb and SH waves when $\theta = 0^\circ$

To clearly illustrate the process of stiffness matrix rotation and the existing wave types in the cross-ply laminate that is adapted to the rotated stiffness matrix of each layer, the profile section of this laminate is illustrated in Figure 4.5 for the current wave propagation angle $\theta = 0^\circ$. From this conceptual diagram, it can be seen that, after rotation of Eq. (4.60), the rotated stiffness matrix of each layer still keeps the orthotropic type, i.e. $\mathbf{C}'_i \in \mathcal{C}_O$ ($i = 1, \dots, 8$). According to the Algorithm 1, Branch 2 is targeted that corresponds to the case of the pure Lamb and SH waves. After running Algorithm 3 and 4, the resulted dispersion curves of the pure Lamb and SH waves are depicted in Figure 4.6.

For another wave propagation angle $\theta = 90^\circ$, a similar diagram than Figure 4.5 can be generated to determine the accessible wave type existing in the cross-ply laminate at the specified angle $\theta = 90^\circ$. Due to the reciprocal condition between $\theta = 0^\circ$ and $\theta = 90^\circ$ for the cross-ply stacking sequence $[(0/90)_s]_2$, it is easy to infer that the rotated $\mathbf{C}'_i \in \mathcal{C}_O$ ($i = 1, \dots, 8$) for $\theta = 90^\circ$. Thus, the accessible

4.6. NUMERICAL EXAMPLE ON A CROSS-PLY LAMINATE

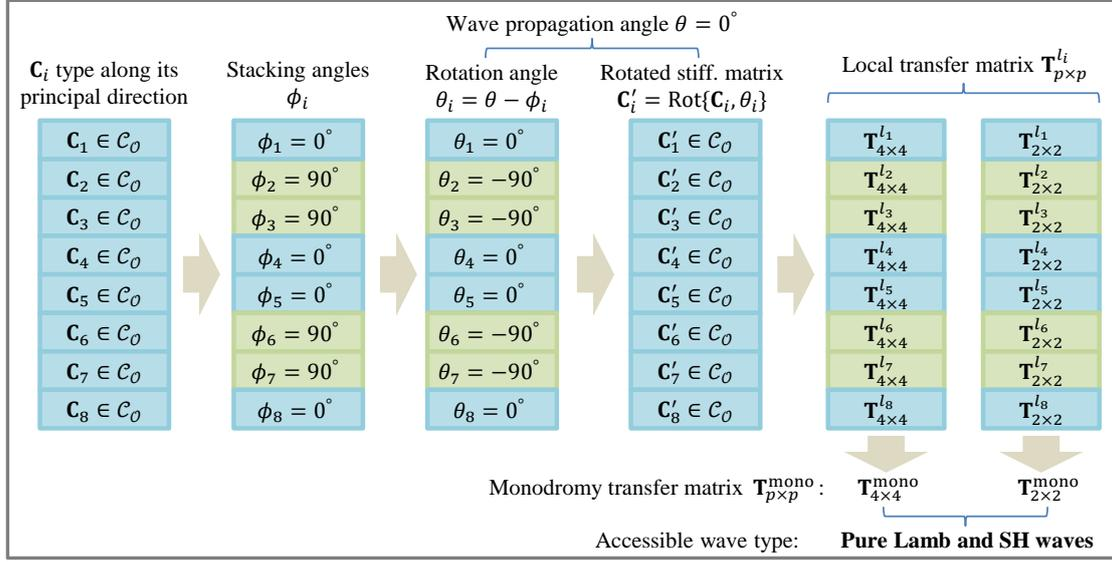


Figure 4.5 – Conceptual diagram of determining the wave type existing in the cross-ply laminate $[(0/90)_s]_2$ at wave propagation angle $\theta = 0^\circ$.

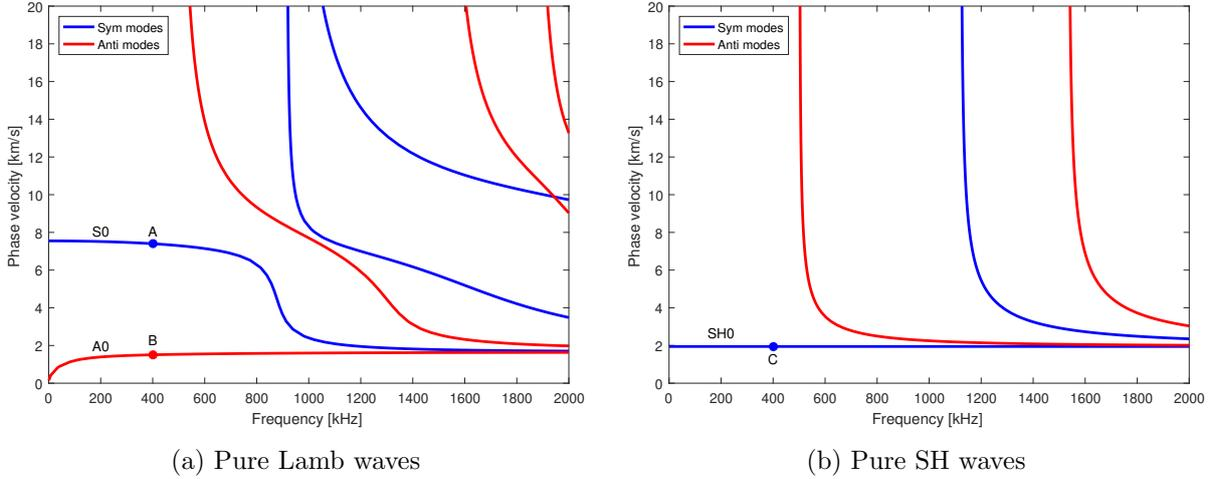


Figure 4.6 – Dispersion curves of pure Lamb and SH waves of the cross-ply laminate when $\theta = 0^\circ$.

wave type is still the pure Lamb and SH waves when $\theta = 90^\circ$. To avoid redundancy, the computed dispersion curves are not presented here.

4.6.2 The coupled Lamb and SH waves when $\theta = 45^\circ$

When we consider $\theta = 45^\circ$, the conceptual diagram of determining the plate's wave type is illustrated in Figure 4.7. It shows that each layer's stiffness matrix after rotation changes to $\mathbf{C}'_i \in$

4.6. NUMERICAL EXAMPLE ON A CROSS-PLY LAMINATE

$\mathcal{C}_M (i = 1, \dots, 8)$. This outcome immediately leads to the coupled Lamb and SH waves according to the Branch 1 of Algorithm 1, and Algorithm 2 should be adopted to compute the dispersion curves. After running Algorithm 2, the resulted dispersion curves of the coupled Lamb and SH waves are depicted in Figure 4.8.

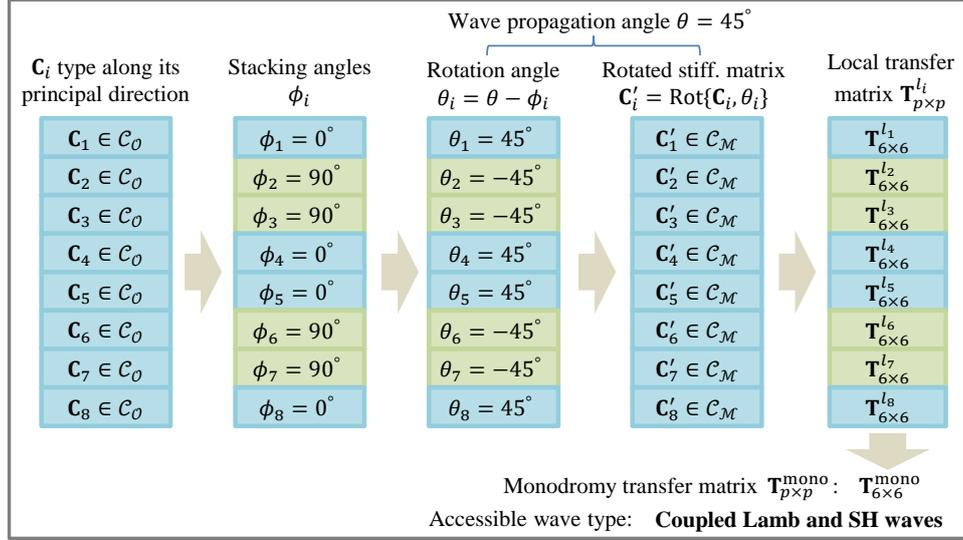


Figure 4.7 – Conceptual diagram of determining the wave type existing in the cross-ply laminate $[(0/90)_s]_2$ at wave propagation angle $\theta = 45^\circ$.

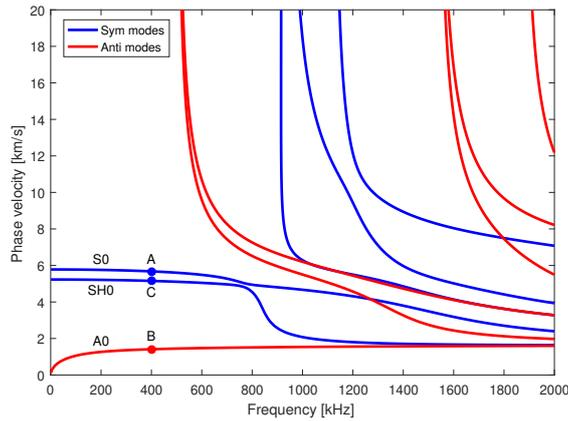


Figure 4.8 – Dispersion curves of the coupled Lamb and SH waves of the cross-ply laminate at $\theta = 45^\circ$.

4.6.3 Displacement and stress mode shapes

Each point of the dispersion curves is a solution of the dispersion equation. It can be used to compute the wave mode shapes introduced in Section 4.3.4. Here, we take the points A, B, C in

4.6. NUMERICAL EXAMPLE ON A CROSS-PLY LAMINATE

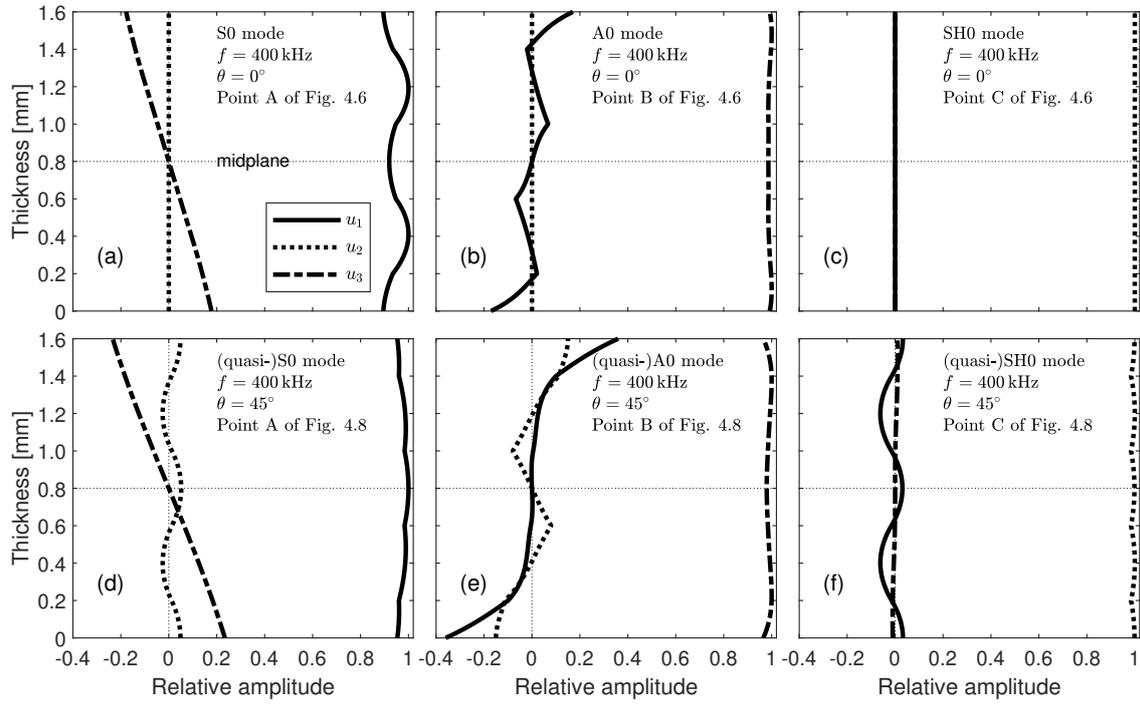


Figure 4.9 – Displacement mode shapes of the cross-ply laminate for $\theta = 0^\circ$ and 45° at $f = 400$ kHz.

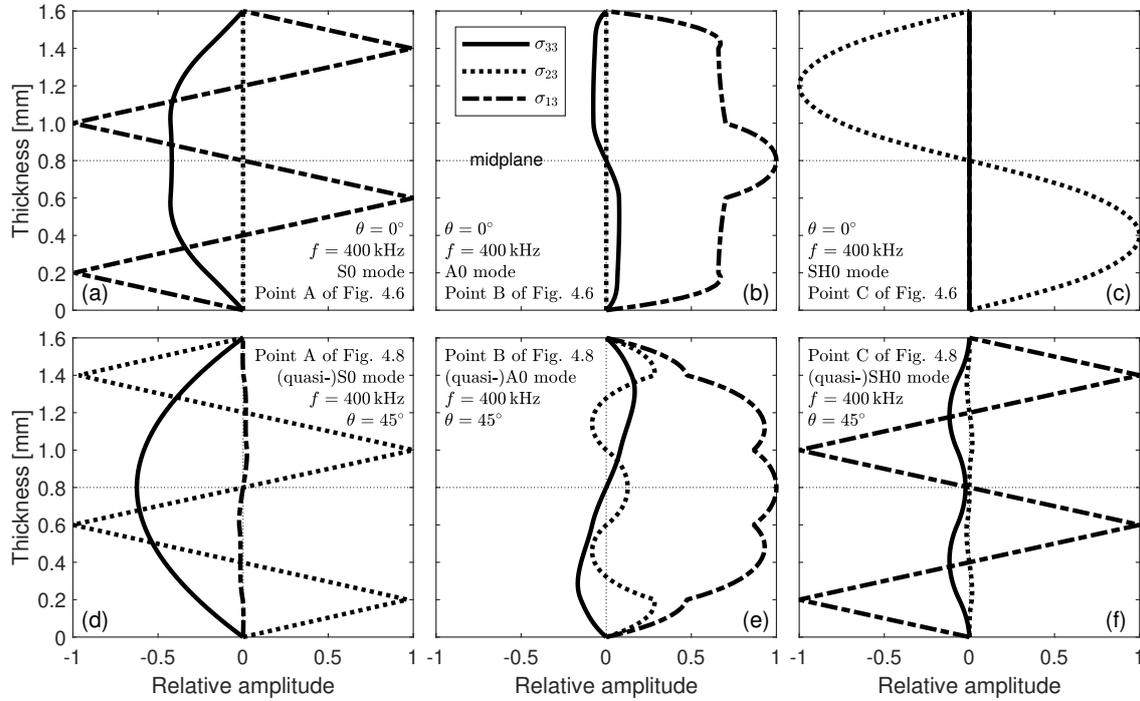


Figure 4.10 – Stress mode shapes of the cross-ply laminate for $\theta = 0^\circ$ and 45° at $f = 400$ kHz.

Figures 4.6 and 4.8 to compute their displacement mode shapes (see Figure 4.9) and stress mode shapes (see Figure 4.10).

In Figure 4.9(a)(b), the u_2 component is zero, but in Figure 4.9(c), the u_1 and u_3 component is zero. This is consistent with their respective wave types implied in Figure 4.6. Specifically, Figure 4.9(a) corresponds to the point A of Figure 4.6 that belongs to the pure Lamb modes. Thus, u_2 component vanished in a pure Lamb mode. Likewise, Figure 4.9(c) corresponds to the point C of Figure 4.6 belonging to the pure SH modes and thus the u_1 and u_3 components vanished in a pure SH mode.

Figure 4.9(d), (e), (f) corresponds to the point A, B, C of Figure 4.8, respectively, which belong to the coupled Lamb and SH waves. The three displacement components are coexisting in Figure 4.9(d)(e)(f). For the coupled modes, the mode order is named by following the terminology of the pure modes with a prefix *quasi* to distinguish the pure counterparts in some references [37, 57, 8], namely, quasi-S0, quasi-A0 and quasi-SH0 modes. In the thesis, we do not emphasize this point. The prefix *quasi* is omitted in the next sections unless stated otherwise.

From Figure 4.10, the zero-valued stress mode shapes at the top- and bottom-most surfaces can be observed thus demonstrating the traction-free boundary condition considered in Eq. (4.36). Besides, the continuous curves of the displacement and stress mode shapes reveal that the continuity condition postulated during deriving the TMM framework (see Eq. (4.31)) is legitimate. In Figures 4.9 and 4.10, the dotted horizontal line represents the midplane of the plate, which is mentioned here to validate the symmetry condition (see Figure 3.1(b)(c) and Eqs. (3.3)(3.4) for the single-layered system, where the midplane is represented by $x_3 = 0$). As a consequence, the dispersion curves in Figures 4.6 and 4.8 are further classified into symmetric and anti-symmetric modes.

4.7 Numerical example on a quasi-isotropic laminate

In this section, a carbon-fiber epoxy laminate is used to demonstrate the developed HMS. The laminate consists of eight unidirectional composite laminae with stacking angles of layups $[0/90/+45/-45]_s$, indicating the quasi-isotropic property of this plate. Each lamina is made up of carbon-fiber epoxy prepreg having transversely isotropic material properties as listed in Table 4.3, which is cited from [8]. This material is commonly used in the aeronautic and aerospace industry. The material properties are further used to compute the stiffness matrix in Eq. (4.61) along its principal direction

4.7. NUMERICAL EXAMPLE ON A QUASI-ISOTROPIC LAMINATE

based on Eq. (2.12).

Table 4.3 – Material properties of a carbon-fiber epoxy lamina

Density [kg/m ³]	E_1 [GPa]	E_2 [GPa]	G_{12} [GPa]	ν_{12}	ν_{23}	Ply thickness	Stacking angles
1650	143	9.1	4.8	0.3	0.3	0.17 mm	[0/90/+45/−45] _s

$$\mathbf{C} = \begin{bmatrix} 145.38 & 3.96 & 3.96 & 0 & 0 & 0 \\ & 10.11 & 3.11 & 0 & 0 & 0 \\ & & 10.11 & 0 & 0 & 0 \\ & & & 3.5 & 0 & 0 \\ \text{sym} & & & & 4.8 & 0 \\ & & & & & 4.8 \end{bmatrix} \text{GPa} \quad (4.61)$$

The quasi-isotropic stacking sequence of layups results in that there is not a common principal axis among the laminae and thus no pure Lamb or SH waves present in the plate for any propagation angle. For the specific stacking angles of layups [0/90/+45/−45]_s, when the interested wave propagation angle just coincides with one layer's private principal direction, i.e. $\theta \in \{0^\circ, 45^\circ, 90^\circ, -45^\circ\}$, the incompatibility issue is just encountered, which can be solved by virtue of the HMS. The related procedures are illustrated in this section.

4.7.1 The hybrid Lamb and SH waves when $\theta = 0^\circ, 45^\circ$ or 90°

Figure 4.11(a) illustrates the process of determining the wave type existing in the laminate at the current propagation angle $\theta = 0^\circ$. It is clear that the stiffness matrices of some layers after rotation (specifically, the 1st, 2nd, 7th, 8th layer) belong to the set \mathcal{C}_O but another layers (from the 3rd to the 6th layer) belong to the set \mathcal{C}_M . For the rotated $\mathbf{C}'_j \in \mathcal{C}_O$, there exists two kinds of local transfer matrix $\mathbf{T}_{4 \times 4}^{l_j}$ and $\mathbf{T}_{2 \times 2}^{l_j}$ according to the Section 4.2.2 and 4.2.3, which correspond to the pure Lamb and SH waves in this layer. But for another rotated $\mathbf{C}'_i \in \mathcal{C}_M$, it has only the local transfer matrix $\mathbf{T}_{6 \times 6}^{l_i}$ according to the Section 4.2.1, which corresponds to the coupled Lamb and SH waves in this layer. Immediately, we are encountering the incompatibility issue between $\mathbf{T}_{6 \times 6}^{l_i}$ and $(\mathbf{T}_{4 \times 4}^{l_j}, \mathbf{T}_{2 \times 2}^{l_j})$. The HMS developed in Section 4.4 just dedicates to solve this issue, which is achieved by reconstructing $(\mathbf{T}_{4 \times 4}^{l_j}, \mathbf{T}_{2 \times 2}^{l_j})$ to the hybrid local transfer matrix $\tilde{\mathbf{T}}_{6 \times 6}^{l_j}$. By doing so, all layers' local transfer matrices are now compatible and they are assembled together to yield the hybrid monodromy transfer matrix $\tilde{\mathbf{T}}_{6 \times 6}^{\text{mono}}$ based on the TMM framework. After running Algorithm 1 and 5, the dispersion solutions of

the hybrid Lamb and SH waves are obtained and the dispersion curves are depicted in Figure 4.12(a) which corresponds to the current propagation angle $\theta = 0^\circ$.

$$\left(\mathbf{T}_{4 \times 4}^{l_j}, \mathbf{T}_{2 \times 2}^{l_j} \right) \xrightarrow{\text{HMS based on Eqs. (4.57)(4.59)}} \tilde{\mathbf{T}}_{6 \times 6}^{l_j}$$

The incompatibility issue is still occurring at $\theta = \pm 45^\circ$ and 90° due to the stacking angles of layups $[0/90/+45/-45]_s$, and it can be qualitatively analyzed by making the same kind of conceptual diagram as the angle $\theta = 0^\circ$ in Figure 4.11(a). To avoid redundancy, we only illustrate the angle $\theta = 45^\circ$ in Figure 4.11(c). It shows that, after rotation, the stiffness matrices of the 3rd to the 6th layer keep the orthotropic type, i.e. $\mathbf{C}'_j \in \mathcal{C}_O$ ($j = 3, 4, 5, 6$), which is conjugated with Figure 4.11(a) in the graphical sense. Thus, the HMS should be applied to these layers. After running Algorithm 1 and 5, the dispersion curves of the hybrid Lamb and SH waves are depicted in Figure 4.12(c) and (d) for $\theta = 45^\circ$ and $\theta = 90^\circ$, respectively.

4.7.2 The coupled Lamb and SH waves when $\theta = 30^\circ$

When the wave direction of interest does not coincide with any principal axis of all layers, i.e. $\theta \notin \{0^\circ, 45^\circ, 90^\circ, -45^\circ\}$, the rotated \mathbf{C}'_i of all layers shall belong to the set \mathcal{C}_M , which gives rise to the unified local transfer matrix $\mathbf{T}_{6 \times 6}^{l_i}$ between all layers according to the Section 4.2.1. Here, we take a typical angle $\theta = 30^\circ$ to present the process of determining the coupled type of Lamb and SH waves as illustrated in Figure 4.11(b). For the coupled case, Algorithm 2 should be adopted to compute the dispersion solutions according to the result provided by Algorithm 1. After computation, the dispersion curves of the coupled Lamb and SH waves are depicted in Figure 4.12(b) for the current angle $\theta = 30^\circ$.

Note that the experimental data points in Figure 4.12 are extracted from [8], and they are used in Figure 4.12 for the comparison purpose from the experimental perspective. The good agreement between the theoretically computed curves and the experimental data points shown in Figure 4.12, as a consequence, validates the feasibility and effectiveness of the combined TMM and HMS methodology.

To intuitively observe all the singular angles of the quasi-isotropic laminate, the polar plot of wave velocities are created in Figure 4.13 for $fd = 0.1 \text{ MHz} \cdot \text{mm}$ and $fd = 0.4 \text{ MHz} \cdot \text{mm}$, where fd represents the product of frequency f and plate's total thickness d . In this figure, the eight singular angles are indicated, they are $\theta \in \{0^\circ, 45^\circ, 90^\circ, 135^\circ, 180^\circ, 225^\circ, 270^\circ, 315^\circ\}$.

4.7. NUMERICAL EXAMPLE ON A QUASI-ISOTROPIC LAMINATE

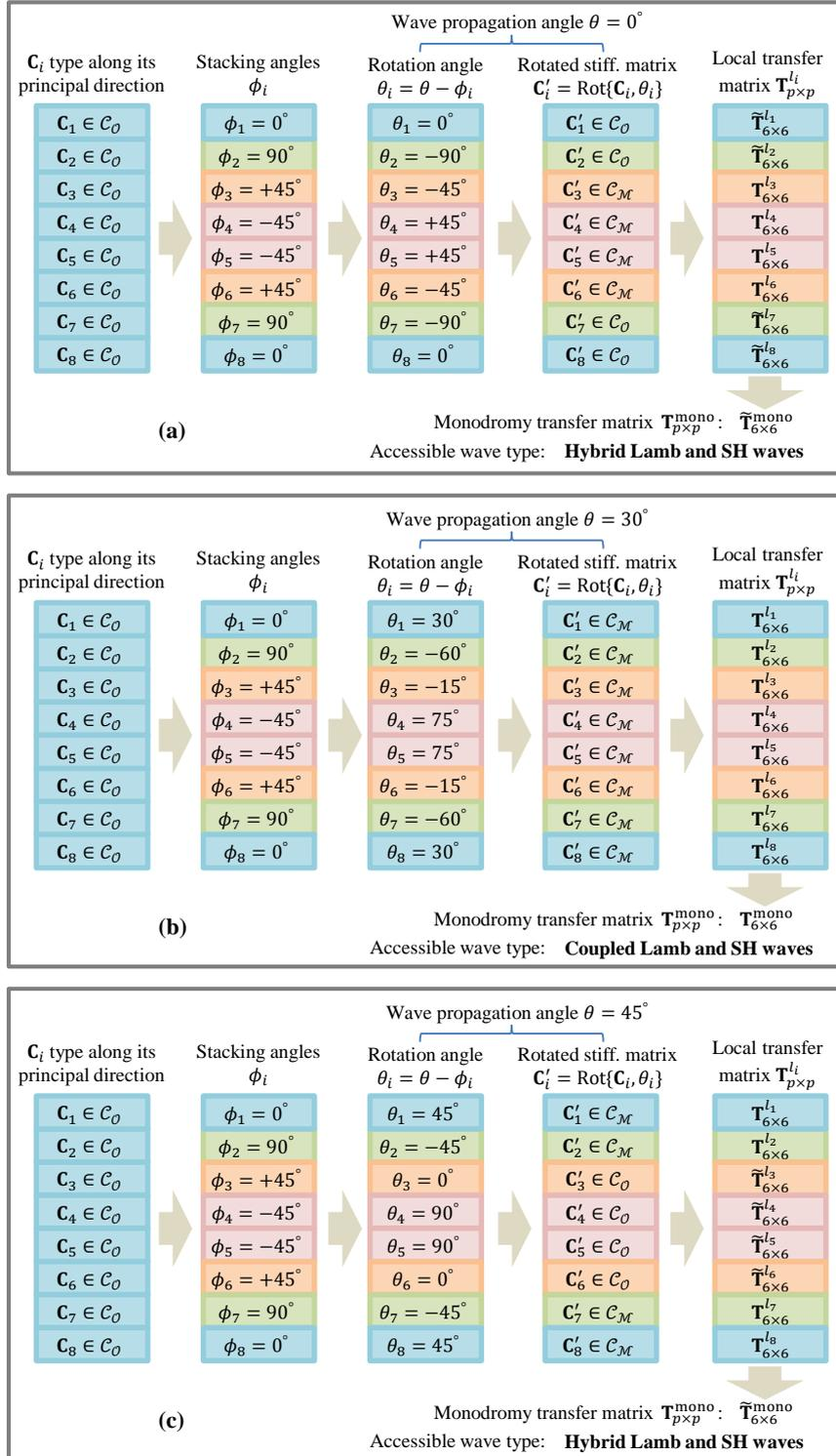


Figure 4.11 – Conceptual diagram of determining the wave type existing in the quasi-isotropic laminate $[0/90/+45/-45]_s$ at the wave propagation angle (a) $\theta = 0^\circ$, (b) $\theta = 30^\circ$, (c) $\theta = 45^\circ$.

4.7. NUMERICAL EXAMPLE ON A QUASI-ISOTROPIC LAMINATE

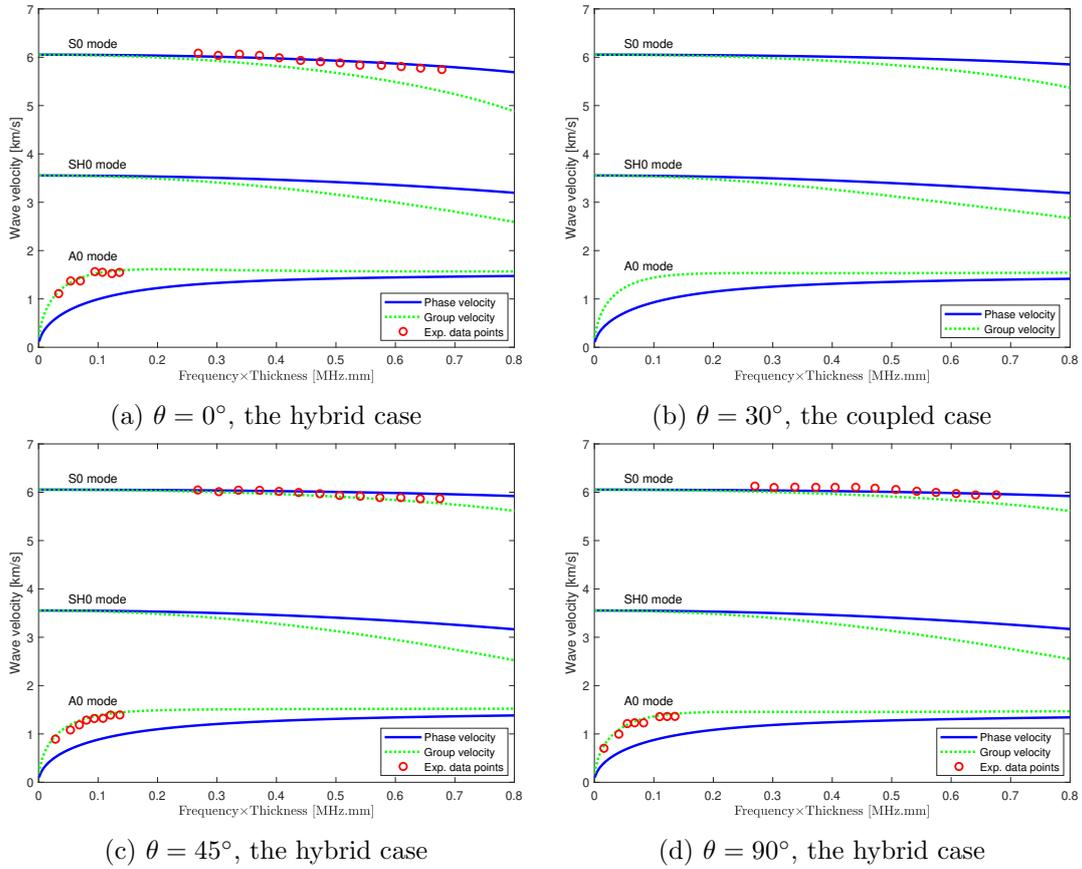


Figure 4.12 – Dispersion curves of the hybrid or coupled Lamb and SH waves of the quasi-isotropic laminate. The experimental data points are extracted from [8].

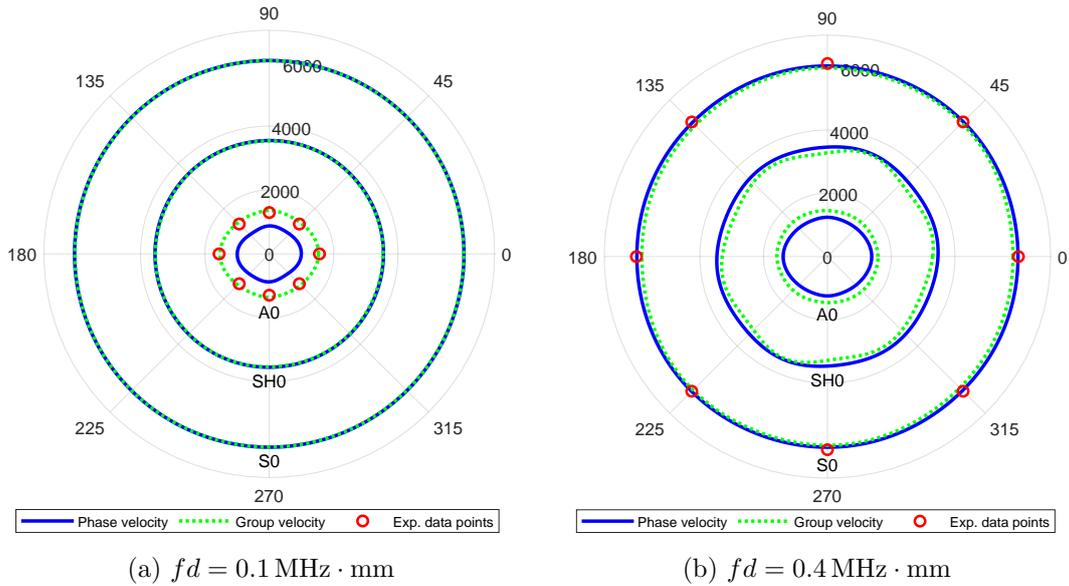


Figure 4.13 – Polar plot of wave velocities. The experimental data points are extracted from [8].

4.7.3 Illustration of Pant's pseudo correction measure

Pant's pseudo correction measure to alleviate the incompatibility issue is presented in Figure 4.3. This measure is conceptually illustrated in Figure 4.14 for the angle $\theta = 0^\circ$ which has been discussed in Figure 4.11(a). The core idea of this measure is detailed in the right-most two columns of Figure 4.14. By additionally rotating the $\mathbf{C}'_j \in \mathcal{C}_O$ ($j = 1, 2, 7, 8$) with a minor angle $\Delta\theta = -1^\circ$, all the rotated stiffness matrices now belong to the set \mathcal{C}_M that finally produces the coupled Lamb and SH waves.

As the additional angle is relatively small, this pseudo correction has very little effect on the overall stiffness of the laminate. Thus, it is doable for the quasi-isotropic laminate but not orthodox from the mathematical view. In the metallic-composite laminate, Pant's pseudo correction is invalid because the stiffness matrix of the metallic layer always remains the orthotropic type irrespective of the rotation angle. We will demonstrate this case in Section 4.8.3.

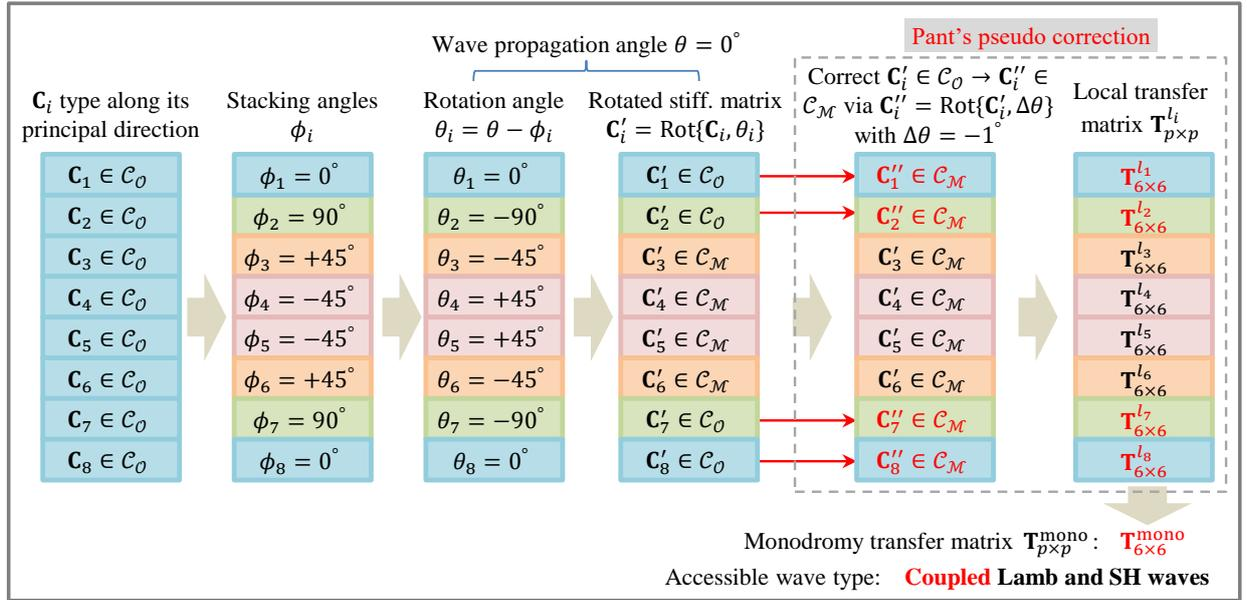


Figure 4.14 – Conceptual diagram of Pant's pseudo correction to deal with the incompatibility issue of the quasi-isotropic laminate $[0/90/+45/-45]_s$ when $\theta = 0^\circ$.

4.8 Numerical example on a metallic-composite laminate

In this section, the HMS is applied to a metallic-composite laminate composed by three aluminum layers and four glass fiber layers with stacking angles of layups $[Al/0/90/Al/90/0/Al]$. The material

properties of the two materials are cited from [8] and listed in Table 4.4 and 4.5 for convenience. The stiffness matrices of the two materials along their respective principal-axis direction can be computed based on Eqs. (2.14) and (2.12). Thanks to the isotropic property of aluminum material, there exists a common principle-axis direction between the aluminum and the glass fiber layers, 0° and 90° . Thus, for the metallic-composite plate, the incompatibility issue occurs at any angle other than $\theta = 0^\circ$ or 90° .

Table 4.4 – Material properties of aluminum

Density [kg/m^3]	E [GPa]	ν	Ply thickness [mm]
2780	73.1	0.33	0.33

Table 4.5 – Material properties of glass fiber

Density ($[\text{kg}/\text{m}^3]$)	E_1 [GPa]	E_2 [GPa]	G_{12} [GPa]	ν_{12}	ν_{23}	Ply thickness [mm]
1980	50.6	9.9	3.7	0.32	0.32	0.127

4.8.1 The pure Lamb and SH waves when $\theta = 0^\circ$ or 90°

Figure 4.15(a) illustrates the process of determining wave type when one principle-axis direction $\theta = 0^\circ$ is concerned. At this direction, the rotated stiffness matrices of aluminum layers remain the isotropic property $\mathbf{C}'_i \in \mathcal{C}_{\mathcal{I}}$ ($i = 1, 4, 7$), and the rotated stiffness matrices of glass fiber layers keep the orthotropic property $\mathbf{C}'_j \in \mathcal{C}_{\mathcal{O}}$ ($j = 2, 3, 5, 6$). According to the classification $\mathcal{C}_{\mathcal{I}} \subseteq \mathcal{C}_{\mathcal{O}}$ defined in the Characteristic 3 of Section 2.3.3, we can also classify the $\mathbf{C}'_i \in \mathcal{C}_{\mathcal{O}}$ ($i = 1, 4, 7$). As such, all the rotated stiffness matrices now belong to the orthotropic type that finally produces the pure Lamb and SH waves. For another principle-axis direction $\theta = 90^\circ$, the same outcome of the pure case is anticipated. The dispersion curves of the pure Lamb and SH waves at the two principle-axes directions are then retrieved by running Algorithm 3 and 4 and are depicted in Figure 4.16(a)(e). The good agreement between the computed curves and the experimental data points demonstrates the high accuracy of the TMM framework in processing the metallic-composite laminate.

4.8. NUMERICAL EXAMPLE ON A METALLIC-COMPOSITE LAMINATE

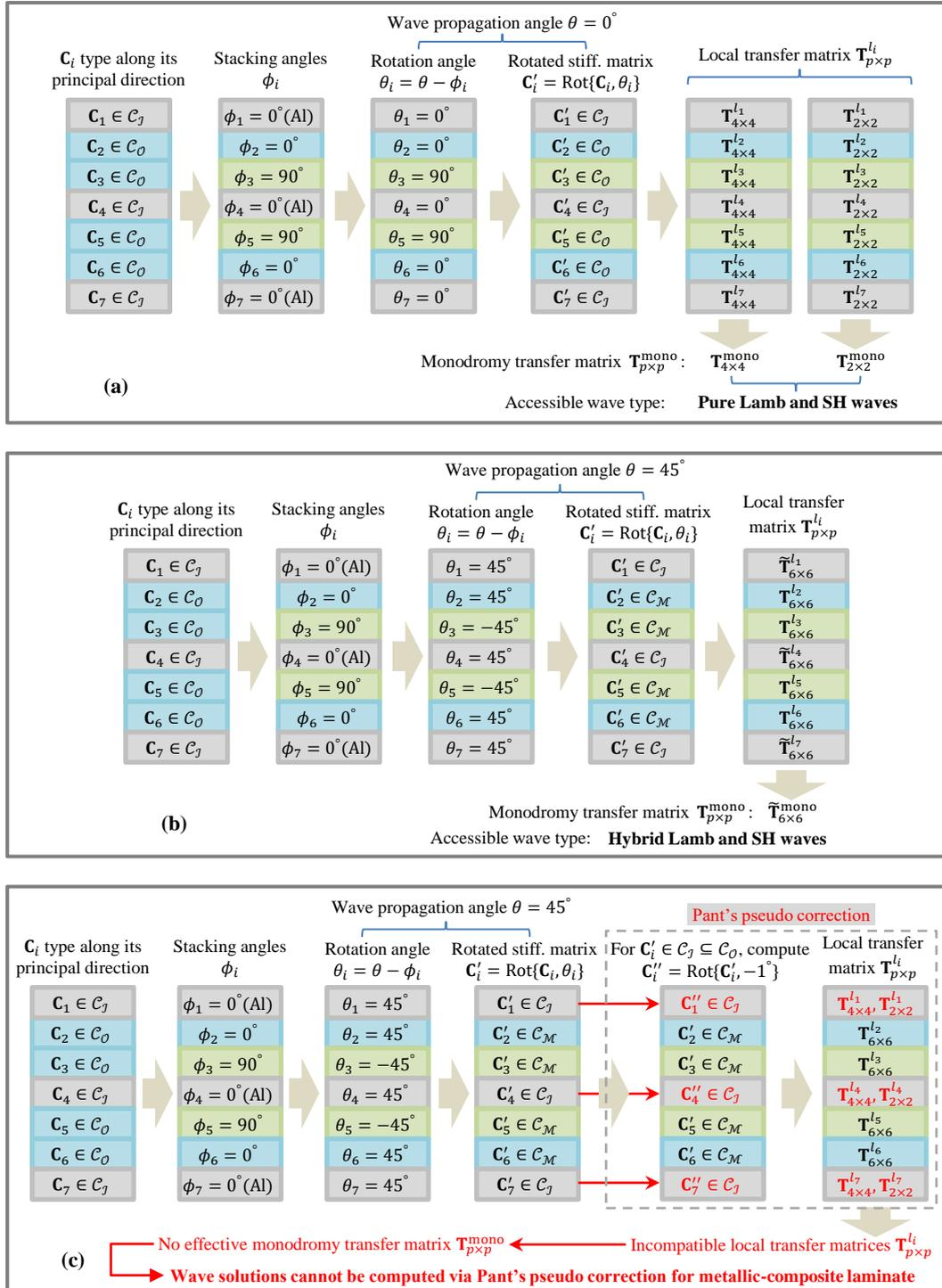


Figure 4.15 – Conceptual diagram of determining the wave type existing in the metallic-composite laminate [Al/0/90/Al/90/0/Al] at the wave propagation angle (a) $\theta = 0^\circ$, (b) $\theta = 45^\circ$ and (c) $\theta = 45^\circ$ for Pant's pseudo correction.

4.8. NUMERICAL EXAMPLE ON A METALLIC-COMPOSITE LAMINATE

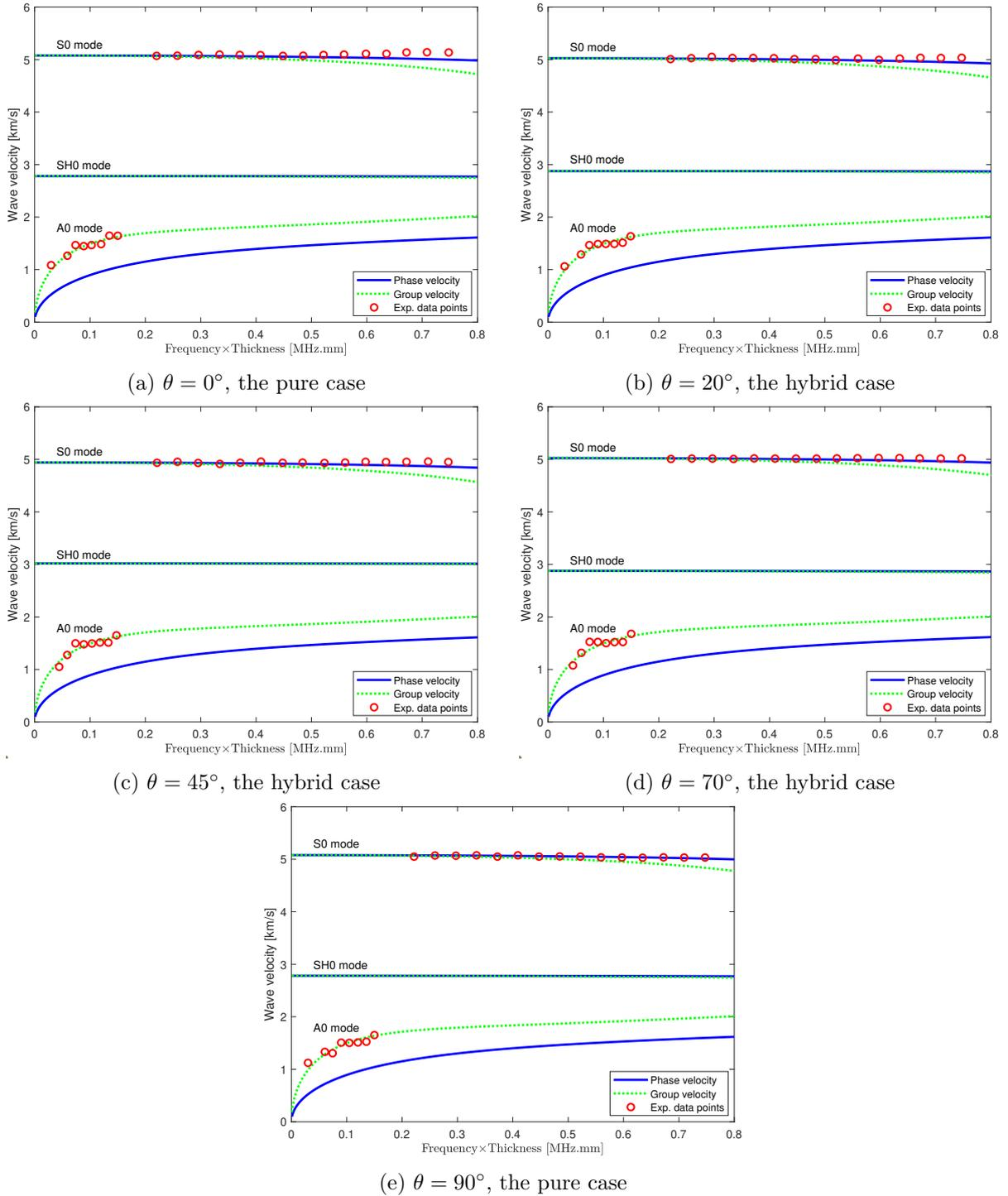


Figure 4.16 – Dispersion curves of the hybrid or pure Lamb and SH waves of the metallic-composite laminate. The experimental data points are extracted from [8].

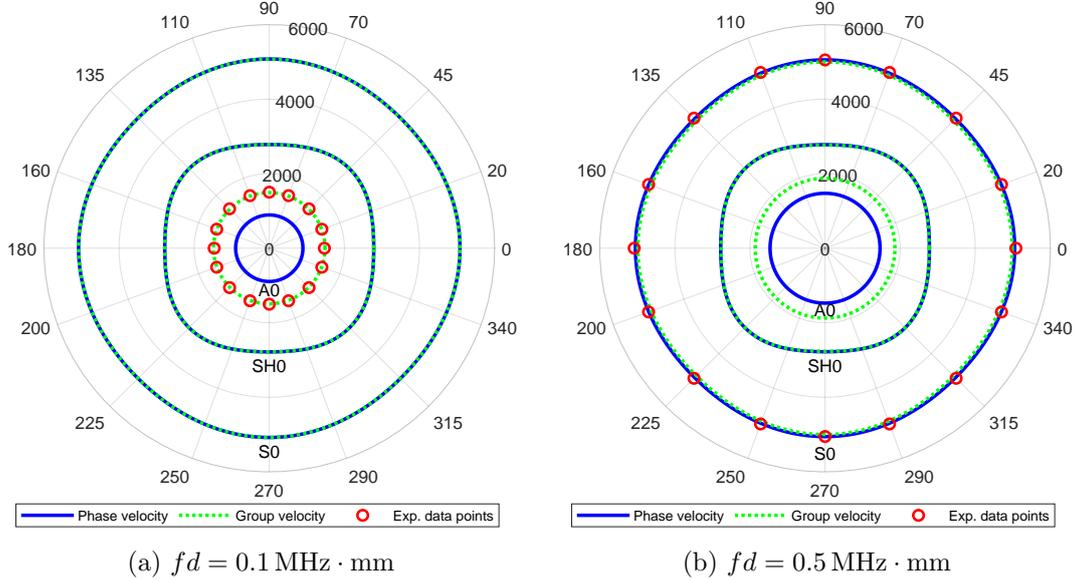


Figure 4.17 – Polar plot of wave velocities. The experimental data points are extracted from [8].

4.8.2 The hybrid Lamb and SH waves when $\theta = 20^\circ, 45^\circ$ or 70°

There are many singular angles that will invoke the incompatibility issue in the metallic-composite laminate. Figure 4.15(b) illustrates the process of determining wave type when $\theta = 45^\circ$. At this direction, the stiffness matrices of aluminum layers are rotated to $\mathbf{C}'_i \in \mathcal{C}_{\mathcal{I}} \subseteq \mathcal{C}_{\mathcal{O}}$ ($i = 1, 4, 7$) due to the rotation invariance property of isotropic material, and the stiffness matrices of the glass fiber layers are rotated to $\mathbf{C}'_j \in \mathcal{C}_{\mathcal{M}}$ ($j = 2, 3, 5, 6$). The inconformity of stiffness matrix classes between aluminum and glass fiber layers at the current angle $\theta = 45^\circ$ makes the requirement that only the hybrid local transfer matrices of the aluminum layers $\tilde{\mathbf{T}}_{6 \times 6}^{l_i}$ ($i = 1, 4, 7$) are compatible with the local transfer matrices of the glass fiber layers $\mathbf{T}_{6 \times 6}^{l_j}$ ($j = 2, 3, 5, 6$) as illustrated in Figure 4.15(b). Correspondingly, the hybrid type of Lamb and SH waves is determined. For another two angles $\theta = 20^\circ$ and 70° , the same hybrid wave type can be analyzed. After running Algorithm 5, the dispersion curves at the three angles $\theta = 20^\circ, 45^\circ, 70^\circ$ are retrieved in Figure 4.16(b), (c), (d), respectively. The reason of exhibiting the dispersion curves of $\theta = 20^\circ$ and 70° in Figure 4.16 is that the experimental data of the two angles are available from [8]. The good agreement between the computed curves and the experimental data points validates the feasibility of the HMS in processing the metallic-composite laminate.

In the quasi-isotropic laminate $[0/90/+45/-45]_s$, there are only eight singular angles $\theta \in \{0^\circ, 45^\circ, 90^\circ, 135^\circ, 180^\circ, 225^\circ, 270^\circ, 315^\circ\}$ as indicated in Figure 4.13. However, in the metallic-composite

laminate, any propagation angle is singular except $\theta \in \{0^\circ, 90^\circ, 180^\circ, 270^\circ\}$. This is the major difference between the polar plot of the quasi-isotropic laminate in Figure 4.13 and the polar plot of the metallic-composite laminate in Figure 4.17.

4.8.3 Superiority of HMS over Pant's pseudo correction measure

Figure 4.15(c) illustrates the ineffectiveness of Pant's pseudo correction measure during processing the incompatibility issue of metallic-composite laminate. It shows that the additionally rotated stiffness matrices of aluminum layers still remains isotropic property, $\mathbf{C}_i'' \in \mathcal{C}_{\mathcal{I}}$ ($i = 1, 4, 7$), due to the rotation invariance of isotropic material. In consequence, the two kinds of local transfer matrices of aluminum layers $(\mathbf{T}_{4 \times 4}^{l_i}, \mathbf{T}_{2 \times 2}^{l_i})$ ($i = 1, 4, 7$) are still incompatible with the local transfer matrices of glass fiber layers $\mathbf{T}_{6 \times 6}^{l_j}$ ($j = 2, 3, 5, 6$) if without using the hybrid ones $\tilde{\mathbf{T}}_{6 \times 6}^{l_i}$ ($i = 1, 4, 7$) employed in Figure 4.15(b). This illustration proves that Pant's pseudo correction measure fails to deal with the incompatibility issue of metallic-composite laminate but the HMS is the unique solution to address this issue if the matrix-based methodologies (TMM and GMM¹) are adopted to analyze wave propagation characteristics.

4.9 Conclusion

This chapter reviewed in detail the classical TMM framework for modelling guided waves propagation in anisotropic composite laminates. For an arbitrarily oriented plate, the Lamb modes and SH modes will couple to each other, or completely separate depending on the stacking angles of layups and the observed wave propagation direction. For the quasi-isotropic laminate, if the observation angle of interest is just along one layer's principle axis, the matrix incompatibility issue will appear. This issue is more severe in metallic-composite laminate because it occurs at any direction in the plate plane except along the common principal axes of composite laminae. To address this issue, the HMS is theoretically derived by following the PWSA. It is thus possible to deal with wave propagation problem in an arbitrarily oriented composite laminate.

Algorithm 1 is the quintessence of this chapter. It judges which wave type exists in the currently studied composite laminate at the interested propagation angle. The related variables, matrices and equations corresponding to each wave type have been programmatically interpreted in Algorithm 2,

1. GMM framework is studied in Chapter 5.

4.9. CONCLUSION

3, 4 and 5. These algorithms are controlled by Algorithm 1. With the smooth cooperation between Algorithm 1 and Algorithms 2-5, the correct wave characteristics can be computed including the dispersion relation (phase and group velocities), wave mode shapes and polar plots of these quantities.

Numerical examples on three commonly used composite laminates validates the effectiveness of the standard TMM and the HMS. TMM framework is accurate enough when comparing to experimental data. The HMS is also superior than Pant's pseudo correction measure for dealing with the wave propagation problem in metallic-composite plate.

Chapter 5

Guided wave propagation in a multi-layered plate: global matrix method

Although the effectiveness of TMM has been sufficiently validated in Chapter 4, one fatal flaw of TMM is the notorious *large fd problem* which states that at the large product value of frequency f and layer thickness d , the dispersion curves obtained from the solutions of the dispersion equation built with TMM become unstable. The usual way to address this issue is to adopt the global matrix method (GMM). But one side effect of GMM is its low efficiency when using it to cope with a multi-layered plate that has many layers.

In this chapter, three advanced techniques are jointly applied to the traditional GMM to improve the computational inefficiency issue. They are sparse matrix technique, parallel computing technique and the matrix order reduction technique inspired by the symmetry condition. The thoroughly optimized GMM is applied to compute the dispersion curves of a 400-layered composite structure that is the prototype of the rocket booster pressure vessels of the future launcher Ariane 6. The success of this application proves the possibility that by introducing advanced computing techniques, GMM can be applied to the aerospace composites that usually have a large number of layers.

5.1 The standard global matrix method

Before starting to derive the equations of GMM, we make the assumption that all layers have the compatible field variables in terms of matrix order, i.e. $(\mathbf{u}_{\frac{p}{2} \times 1}, \boldsymbol{\sigma}_{\frac{p}{2} \times 1}, \mathbf{S}_{p \times 1})^{l_k}$ ($k = 1, \dots, n$), where n is the total number of layers and p is the number of partial waves in each layer ($p = 6$ for the

coupled or hybrid Lamb and SH waves, $p = 4$ for the pure Lamb waves and $p = 2$ for the pure SH waves). This assumption leads to that all layers have the compatible local lamina matrices as well, $(\mathbf{\Gamma}_{p \times p}, \mathbf{\Lambda}_{p \times p}(x_3), \mathbf{Z}_{p \times p}(x_3))^{l_k}$ ($k = 1, \dots, n$).

If not so, the HMS is employed to pre-process the incompatible layers such that the hybrid matrix $(\tilde{\mathbf{\Gamma}}_{6 \times 6}, \mathbf{\Lambda}_{6 \times 6}(x_3), \tilde{\mathbf{Z}}_{6 \times 6}(x_3))^{l_i}$ and the coupled matrix $(\mathbf{\Gamma}_{6 \times 6}, \mathbf{\Lambda}_{6 \times 6}(x_3), \mathbf{Z}_{6 \times 6}(x_3))^{l_j}$ are coexisting and compatible in terms of matrix order. In the sequel, the subscript indicating the matrix order $p \times p$ is suppressed for the sake of conciseness.

For a general layer l_k in Figure 4.2(b), its field variables (displacement and stress) can be uniformly rewritten as the following matrix multiplication form.

$$\mathbf{u}^{l_k} = \mathbf{U}^{l_k} \mathbf{\Lambda}^{l_k}(x_3) \boldsymbol{\eta}^{l_k} e^{i\xi(x_1 - vt)} \quad (5.1a)$$

$$\boldsymbol{\sigma}^{l_k} = \boldsymbol{\beta}^{l_k} \mathbf{\Lambda}^{l_k}(x_3) \boldsymbol{\eta}^{l_k} e^{i\xi(x_1 - vt)} \quad (5.1b)$$

$$\mathbf{S}^{l_k} = \mathbf{\Gamma}^{l_k} \mathbf{\Lambda}^{l_k}(x_3) \boldsymbol{\eta}^{l_k} e^{i\xi(x_1 - vt)} = \mathbf{Z}^{l_k}(x_3) \boldsymbol{\eta}^{l_k} e^{i\xi(x_1 - vt)} \quad (5.1c)$$

where, $\mathbf{\Gamma}^{l_k} = \begin{bmatrix} \mathbf{U}^{l_k} \\ \boldsymbol{\beta}^{l_k} \end{bmatrix} \in \mathbb{C}^{p \times p}$ and $\mathbf{Z}^{l_k}(x_3) = \mathbf{\Gamma}^{l_k} \mathbf{\Lambda}^{l_k}(x_3) \in \mathbb{C}^{p \times p}$.

In a laminate, we have the continuity condition (CC) at all interfaces of two adjacent layers and traction-free BC at the top and bottom surfaces of the laminate. Specifically, at a typical interface i_k as illustrated in Figure 4.2(b), the field variables of layer l_k at its bottom side should equal to the field variables of layer l_{k+1} at its top side as a result of rigid connection.

$$\mathbf{S}_{\text{bot}}^{l_k} = \mathbf{S}_{\text{top}}^{l_{k+1}} \quad (k = 1, \dots, n-1) \quad (5.2)$$

where, the subscript ‘bot’ and ‘top’ represents bottom and top side, respectively.

Substituting Eq. (5.1c) into Eq. (5.2) can lead to the following equation.

$$\mathbf{Z}_{\text{bot}}^{l_k} \boldsymbol{\eta}^{l_k} - \mathbf{Z}_{\text{top}}^{l_{k+1}} \boldsymbol{\eta}^{l_{k+1}} = \mathbf{0} \quad (k = 1, \dots, n-1) \quad (5.3)$$

where, $\mathbf{Z}_{\text{bot}}^{l_k} = \mathbf{Z}^{l_k}(d_k) \in \mathbb{C}^{p \times p}$, $\mathbf{Z}_{\text{top}}^{l_{k+1}} = \mathbf{Z}^{l_{k+1}}(0) \in \mathbb{C}^{p \times p}$.

For the traction-free BC at the top- and bottom-most surfaces as shown in Figure 4.2(b), it corresponds to the following equation.

$$\boldsymbol{\sigma}_{\text{top}}^{l_1} = \mathbf{0} \quad \text{and} \quad \boldsymbol{\sigma}_{\text{bot}}^{l_n} = \mathbf{0} \quad (5.4)$$

Substituting Eq. (5.1b) into Eq. (5.4) can lead to Eq. (5.5).

$$\mathbf{Z}_{\text{top}}^{\sigma, l_1} \boldsymbol{\eta}^{l_1} = \mathbf{0} \quad \text{and} \quad \mathbf{Z}_{\text{bot}}^{\sigma, l_n} \boldsymbol{\eta}^{l_n} = \mathbf{0} \quad (5.5)$$

where, $\mathbf{Z}_{\text{top}}^{\sigma, l_1} = \beta^{l_1} \boldsymbol{\Lambda}^{l_1}(0) \in \mathbb{C}^{\frac{p}{2} \times p}$, $\mathbf{Z}_{\text{bot}}^{\sigma, l_n} = \beta^{l_n} \boldsymbol{\Lambda}^{l_n}(d_n) \in \mathbb{C}^{\frac{p}{2} \times p}$.

Sequentially applying Eq. (5.3) from interface i_1 to i_{n-1} as illustrated in Figure 4.2(b) and combining Eq. (5.5), all the resulted equations can be regularly organized to a global linear homogeneous equation set, Eq. (5.6), which requires the vanished determinant of the coefficients matrix, $\mathbf{D}_G(v, \xi) \in \mathbb{C}^{np \times np}$, finally generating the implicit dispersion equation of guided waves propagating in a laminate as presented in Eq. (5.7).

$$\begin{array}{l} \text{BC at the top surface} \rightarrow \\ \text{CC at the interfaces} \left\{ \right. \\ \text{BC at the bot. surface} \rightarrow \end{array} \left[\begin{array}{cccc} -\mathbf{Z}_{\text{top}}^{\sigma, l_1} & & & \\ \mathbf{Z}_{\text{bot}}^{l_1} & -\mathbf{Z}_{\text{top}}^{l_2} & & \\ \vdots & \vdots & & \\ & \mathbf{Z}_{\text{bot}}^{l_k} & -\mathbf{Z}_{\text{top}}^{l_{k+1}} & \\ & \vdots & \vdots & \\ & & \mathbf{Z}_{\text{bot}}^{l_{n-1}} & -\mathbf{Z}_{\text{top}}^{l_n} \\ & & & \mathbf{Z}_{\text{bot}}^{\sigma, l_n} \end{array} \right] \begin{bmatrix} \boldsymbol{\eta}^{l_1} \\ \vdots \\ \boldsymbol{\eta}^{l_k} \\ \vdots \\ \boldsymbol{\eta}^{l_n} \end{bmatrix} = \mathbf{0} \quad (5.6)$$

$$\mathcal{D}_G(v, \xi) = \mathcal{D}_G^R(v, \xi) + i\mathcal{D}_G^I(v, \xi) \triangleq \det\{\mathbf{D}_G(v, \xi)\} = 0 \quad (5.7)$$

where, the subscript ‘G’ denotes that the dispersion equation is built with GMM.

If the studied structure is a single layer plate, the CC in Eq. (5.6) is diminished and only the two BC remain. In this case, Eq. (5.6) collapses to the following form, which has been systematically studied in Chapter 3.

$$\begin{bmatrix} \mathbf{Z}_{\text{top}}^{\sigma, l_1} \\ \mathbf{Z}_{\text{bot}}^{\sigma, l_1} \end{bmatrix} \boldsymbol{\eta}^{l_1} = \mathbf{0} \quad (5.8)$$

Until this stage, the derivation of the standard GMM has been completed. The whole process of solving the dispersion equation built with GMM is similar to the TMM and summarized in Algorithm 6 for the coupled Lamb and SH waves. For other wave type, the corresponding algorithm can be easily designed.

It should be noted that the computational burden of GMM is more salient than TMM for a laminate having many layers because the order of global matrix $\mathbf{D}_G(v, \xi) \in \mathbb{C}^{np \times np}$ increases with the increasing number of layers n . However, the order of the monodromy transfer matrix $\mathbf{T}^{\text{mono}} \in \mathbb{C}^{p \times p}$

5.2. BENCHMARK TEST OF GMM THROUGH THE DATASET OPEN GUIDED WAVES

in Eq. (4.34) remains unchanged regardless of the number of layers. But GMM is more robust than TMM at higher frequency range from the numerical analysis view. We will validate this point in the subsequent benchmark testing.

Algorithm 6 Process the coupled Lamb and SH waves via GMM

Input: Each layer's material properties $(\mathbf{C}_k, \rho_k, d_k, \phi_k)$ for $(k = 1, \dots, n)$;
The wave propagation angle of interest θ ;
The minimum and maximum wavenumber of interest (ξ_{\min}, ξ_{\max}) ;
The minimum, maximum and incremental velocity of interest $(v_{\min}, v_{\max}, \Delta v)$.

- 1: Compute $\mathbf{C}'_k = \text{Rot}\{\mathbf{C}_k, \theta - \phi_k\}$ for $(k = 1, \dots, n)$.
- 2: **if** Any $\mathbf{C}'_k \notin \mathcal{C}_{\mathcal{M}}$ **then**
- 3: Call Algorithm 1 to determine the correct wave type.
- 4: **end if**
- 5: **for** $v_0 = v_{\min} : \Delta v : v_{\max}$ **do** % Solve the dispersion equation at each fixed v_0 .
- 6: **for** $k = 1 : 1 : n$ **do** % Loop through each layer.
- 7: Compute $(\alpha_r, V_r, W_r, \beta_{1r}, \beta_{2r}, \beta_{3r})$ for $(r = 1, \dots, 6)$ via Eqs. (3.24)(3.27)(3.31) using the data $(\mathbf{C}'_k, \rho_k, v_0)$.
- 8: Compute the local lamina matrices $(\mathbf{\Gamma}_{6 \times 6}^{lk}, \mathbf{\Lambda}_{6 \times 6}^{lk}(d_k))$ via Eq. (4.11).
- 9: Compute $(\mathbf{Z}_{\text{bot}}^{lk}, \mathbf{Z}_{\text{top}}^{lk+1})$ via Eq. (5.3).
- 10: **end for**
- 11: Compute $(\mathbf{Z}_{\text{top}}^{\sigma, l_1}, \mathbf{Z}_{\text{bot}}^{\sigma, l_n})$ via Eq. (5.5).
- 12: Assemble the global matrix \mathbf{D}_G based on Eq. (5.6).
- 13: Solve $\mathcal{D}_G(v_0, \xi) = 0$ in Eq. (5.7) to get multiple roots $(\xi_1, \xi_2, \dots) \in [\xi_{\min}, \xi_{\max}]$.
- 14: **end for**

Output: All solution points (v_i, ξ_i) in the range $[v_{\min}, v_{\max}] \times [\xi_{\min}, \xi_{\max}]$.
Plot dispersion curves of the coupled Lamb and SH waves in (v, ξ) , (ω, ξ) , (ω, v) and (ω, c_g) domains where $\omega = \xi v$ and $c_g = \frac{\partial \omega}{\partial \xi}$ is the group velocity.

5.2 Benchmark test of GMM through the dataset Open Guided Waves

In this section, the dataset of Open Guided Waves (OGW) [62] is used to validate the standard GMM. We choose this composite structure because it is a benchmark platform for studying guided waves-based subjects including wave propagation simulation models, damage detection methods and structural health monitoring techniques. OGW is a 16-layered carbon fiber reinforced polymer (CFRP) plate with the dimensions of 500 mm \times 500 mm and a total thickness of 2 mm. The stacking angles of layups is [45/0/ - 45/90/ - 45/0/45/90]_s, indicating the quasi-isotropic property. The material properties of OGW laminae are listed in Table 5.1. The orthotropic type stiffness matrix of this material is presented in Eq. (5.9).

5.2. BENCHMARK TEST OF GMM THROUGH THE DATASET OPEN GUIDED WAVES

Table 5.1 – Material properties of composite laminate of Open Guided Waves

Density [kg/m ³]	Ply thickness [mm]	Stacking angles
1571	0.125	[45/0/ – 45/90/ – 45/0/45/90] _s

$$\mathbf{C}_O = \begin{bmatrix} 130 & 6.1 & 6.1 & 0 & 0 & 0 \\ & 11.2 & 5.2 & 0 & 0 & 0 \\ & & 11.2 & 0 & 0 & 0 \\ & & & 3.0 & 0 & 0 \\ \text{sym} & & & & 4.2 & 0 \\ & & & & & 4.2 \end{bmatrix} \text{ GPa} \quad (5.9)$$

5.2.1 Dispersion curves comparison between GMM and TMM

Both TMM and GMM are adopted to compute the dispersion curves of OGW at the propagation angle $\theta = 0^\circ$. The coarse dispersion curves computed via the two methods are generated in Figure 5.1 for comparison. It shows that in a whole both methods produce consistent results but TMM has unstable solutions in the higher frequency range. The unstable issue of TMM corresponds to the *large fd problem* [6]. We will investigate this issue in detail in Section 6.6.

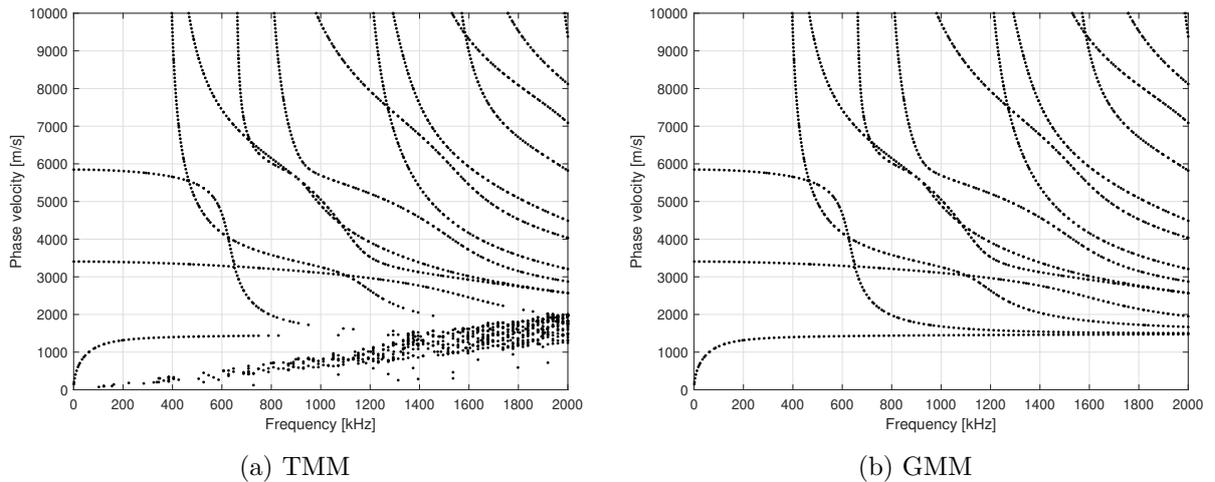


Figure 5.1 – Dispersion curves of Open Guided Waves at the propagation angle $\theta = 0^\circ$ computed via TMM and GMM.

5.2.2 Dispersion curves comparison between GMM and experimental data

The OGW project has reported the experimental wave field signals. We analyzed these signals to identify the wave velocities that can be used as a reference to compare with the numerically computed dispersion curves. The experimentally obtained wave velocity data at several excitation frequencies is presented in Figure 5.2(b) with the legend ‘EXP’. Besides, the polar plot of experimentally identified wave velocities are depicted in Figure 5.3 to explore the quasi-isotropic property of the OGW plate. The numerically computed dispersion curves via GMM are also presented in the two figures. Obviously, the GMM computation shows a good agreement with the experimental data, which proves the validity of GMM.

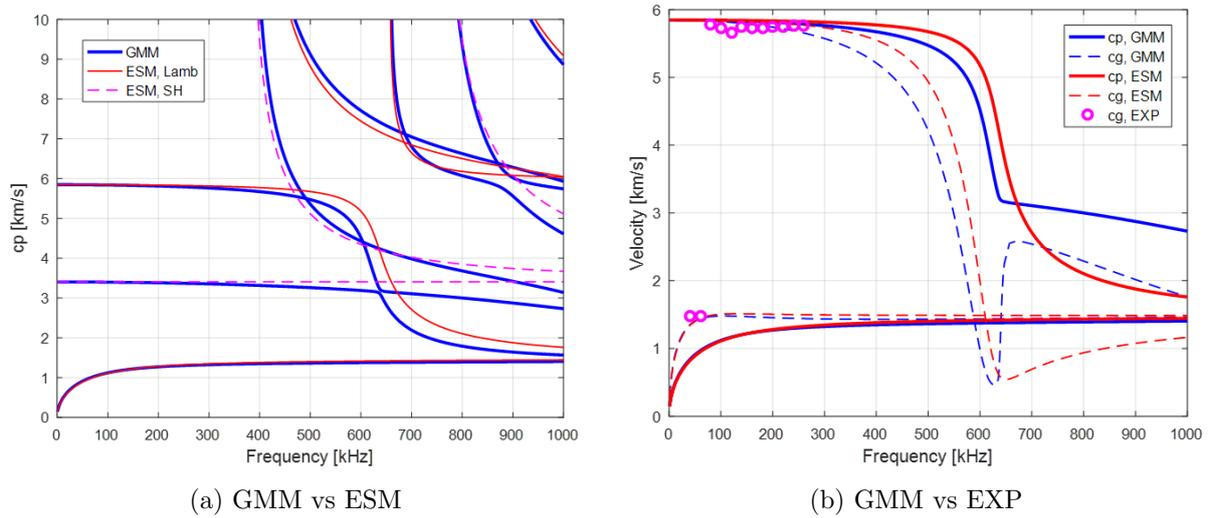


Figure 5.2 – Dispersion curves of Open Guided Waves at the propagation angle $\theta = 0^\circ$ computed via GMM and ESM.

5.2.3 Dispersion curves comparison between GMM and ESM

As stated previously, when dealing with a laminate having many layers, TMM has superiority of computational efficiency in comparison with GMM, but it usually suffers from the *large fd problem*. An alternative of TMM named the effective stiffness matrix method (ESM) is briefly introduced here to compute the dispersion curves of a multi-layered plate system.

ESM was originally studied in [10]. The core idea of ESM is the equivalence. It regards a multi-layered plate system as a single-layered homogeneous plate with the same thickness. But the material

5.2. BENCHMARK TEST OF GMM THROUGH THE DATASET OPEN GUIDED WAVES

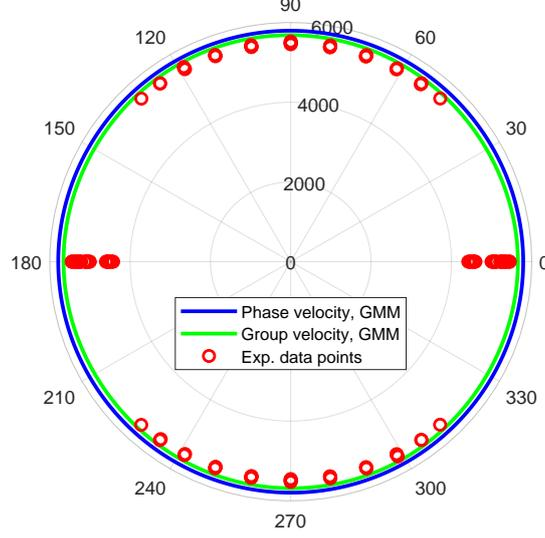


Figure 5.3 – Polar plot of Open Guided Waves plate at frequency=260 kHz.

$$\begin{aligned}
 \bar{C}_{11} &= \sum_{n=1}^N v_n C_{11}^{(n)} + \sum_{n=2}^N (C_{13}^{(n)} - \bar{C}_{13}) v_n (C_{13}^{(1)} - C_{13}^{(n)}) / C_{33}^{(n)} \\
 \bar{C}_{12} &= \sum_{n=1}^N v_n C_{12}^{(n)} + \sum_{n=2}^N (C_{13}^{(n)} - \bar{C}_{13}) v_n (C_{23}^{(1)} - C_{23}^{(n)}) / C_{33}^{(n)} \\
 \bar{C}_{13} &= \sum_{n=1}^N v_n C_{13}^{(n)} + \sum_{n=2}^N (C_{33}^{(n)} - \bar{C}_{33}) v_n (C_{13}^{(1)} - C_{13}^{(n)}) / C_{33}^{(n)} \\
 \bar{C}_{22} &= \sum_{n=1}^N v_n C_{22}^{(n)} + \sum_{n=2}^N (C_{23}^{(n)} - \bar{C}_{23}) v_n (C_{23}^{(1)} - C_{23}^{(n)}) / C_{33}^{(n)} \\
 \bar{C}_{23} &= \sum_{n=1}^N v_n C_{23}^{(n)} + \sum_{n=2}^N (C_{33}^{(n)} - \bar{C}_{33}) v_n (C_{23}^{(1)} - C_{23}^{(n)}) / C_{33}^{(n)} \\
 \bar{C}_{33} &= 1 / \left(\sum_{n=1}^N v_n / C_{33}^{(n)} \right) \\
 \bar{C}_{45} &= \left(\sum_{n=1}^N v_n C_{45}^{(n)} / \Delta_n \right) / \Delta \\
 \bar{C}_{55} &= \left(\sum_{n=1}^N v_n C_{55}^{(n)} / \Delta_n \right) / \Delta \\
 \Delta &= \left(\sum_{n=1}^N v_n C_{44}^{(n)} / \Delta_n \right) \left(\sum_{n=1}^N v_n C_{55}^{(n)} / \Delta_n \right) - \left(\sum_{n=1}^N v_n C_{45}^{(n)} / \Delta_n \right)^2 \\
 \Delta_n &= C_{44}^{(n)} C_{55}^{(n)} - \left(C_{45}^{(n)} \right)^2
 \end{aligned}$$

The elements of stiffness matrix in the n -th layer:

$$\bar{C}_{16} = \sum_{n=1}^N v_n C_{16}^{(n)} + \sum_{n=2}^N (C_{13}^{(n)} - \bar{C}_{13}) v_n (C_{36}^{(1)} - C_{36}^{(n)}) / C_{33}^{(n)}$$

$$\bar{C}_{26} = \sum_{n=1}^N v_n C_{26}^{(n)} + \sum_{n=2}^N (C_{23}^{(n)} - \bar{C}_{23}) v_n (C_{36}^{(1)} - C_{36}^{(n)}) / C_{33}^{(n)}$$

$$\bar{C}_{36} = \sum_{n=1}^N v_n C_{36}^{(n)} + \sum_{n=2}^N (C_{33}^{(n)} - \bar{C}_{33}) v_n (C_{36}^{(1)} - C_{36}^{(n)}) / C_{33}^{(n)}$$

$$\bar{C}_{66} = \sum_{n=1}^N v_n C_{66}^{(n)} + \sum_{n=2}^N (C_{36}^{(n)} - \bar{C}_{36}) v_n (C_{36}^{(1)} - C_{36}^{(n)}) / C_{33}^{(n)}$$

$$\bar{C}_{44} = \left(\sum_{n=1}^N v_n C_{44}^{(n)} / \Delta_n \right) / \Delta$$

$$\begin{Bmatrix} \sigma_{11} \\ \sigma_{22} \\ \sigma_{33} \\ \sigma_{23} \\ \sigma_{13} \\ \sigma_{12} \end{Bmatrix} = \begin{bmatrix} \bar{C}_{11} & \bar{C}_{12} & \bar{C}_{13} & 0 & 0 & \bar{C}_{16} \\ \bar{C}_{12} & \bar{C}_{22} & \bar{C}_{23} & 0 & 0 & \bar{C}_{26} \\ \bar{C}_{13} & \bar{C}_{23} & \bar{C}_{33} & 0 & 0 & \bar{C}_{36} \\ 0 & 0 & 0 & \bar{C}_{44} & \bar{C}_{45} & 0 \\ 0 & 0 & 0 & \bar{C}_{45} & \bar{C}_{55} & 0 \\ \bar{C}_{16} & \bar{C}_{26} & \bar{C}_{36} & 0 & 0 & \bar{C}_{66} \end{bmatrix} \begin{Bmatrix} \varepsilon_{11} \\ \varepsilon_{22} \\ \varepsilon_{33} \\ \gamma_{23} \\ \gamma_{13} \\ \gamma_{12} \end{Bmatrix}$$

The simplified effective stiffness matrix (monoclinic type)

Figure 5.4 – Equations of ESM to compute the effective stiffness matrix [10].

property of the equivalent plate is changed to the monoclinic class. The mass density of the equivalent plate is the weighted average of each layer's density on their respective layer thickness. The equivalent (effective) stiffness matrix is computed from each layer's stiffness matrix in the weighted average sense. The computation equations are concisely provided in Figure 5.4. These equations were obtained from the mechanical analysis for composite materials [63].

Figure 5.4 shows that the averaged effective stiffness matrix possesses the monoclinic property. Wave propagation equations on the single-layered monoclinic plate has been studied in detail in Section 3.3. Thus, we directly present the computed dispersion curves of OGW plate in Figure 5.2(a), accompanied by the GMM computation for comparison. One can see that ESM can produce consistent dispersion curves comparable with GMM for the three fundamental modes (S0, A0 and SH0 modes) especially at lower frequency range. The difference at higher frequency range may be caused by the inaccurate stiffness matrix that is computed by using the equations in Figure 5.4. Based on this demonstration, one can recognize that the validity of ESM is limited to the fundamental modes and lower frequency range.

5.3 The optimized global matrix method

It has long been recognized that GMM has lower computational efficiency than TMM when dealing with a laminate having large number of layers [6]. In this section, we demonstrate that by making three optimizations for the standard GMM, the optimized GMM can receive a great promotion on the computational efficiency even for a 400-layered laminate which has the largest number of layers reported so far in reference [11]. The three optimizations are outlined: (1) addition of symmetry condition to the global matrix, (2) applying the sparse matrix technique, (3) endowing the parallel computing attribute.

5.3.1 The symmetry condition in the global matrix

For the dispersion equation expressed in Eqs. (5.6) and (5.7), the symmetric and anti-symmetric modes are mutually coupled. On the other hand, the dimension of the global matrix $\mathbf{D}_G(v, \xi) \in \mathbb{C}^{6n \times 6n}$ is huge for a large number of layers n , which causes heavy computational burden. For most aerospace composite structures, symmetrically stacked plies are commonly applied in composite laminates, this

5.3. THE OPTIMIZED GLOBAL MATRIX METHOD

fact leads to that the guided waves can be always separated into symmetric and anti-symmetric modes, regardless of propagation direction. If the symmetry condition (SC) can be embedded into the global matrix ahead, the size of the global matrix $\mathbf{D}_G(v, \xi)$ can be halved to reduce computational burden. Specifically, the SC in Eqs. (3.3) and (3.4) now has to be evaluated at the midplane of a symmetric laminate, as follows.

$$\boldsymbol{\varsigma}_{\text{mp}}^{s,l_m} \triangleq \left\{ u_3, \sigma_{23}, \sigma_{13} \right\}_{x_3=\text{midplane}}^{l_m \text{T}} = \left\{ 0, 0, 0 \right\}^{\text{T}} \quad \text{for sym. modes} \quad (5.10)$$

$$\boldsymbol{\varsigma}_{\text{mp}}^{a,l_m} \triangleq \left\{ u_1, u_2, \sigma_{33} \right\}_{x_3=\text{midplane}}^{l_m \text{T}} = \left\{ 0, 0, 0 \right\}^{\text{T}} \quad \text{for anti. modes} \quad (5.11)$$

where, the superscript ' l_m ' represents the middle layer that embraces the midplane and the subscript 'mp' implies the location of the midplane, both which can be identified according to the odevity of a laminate [64] as illustrated in Figure 5.5.

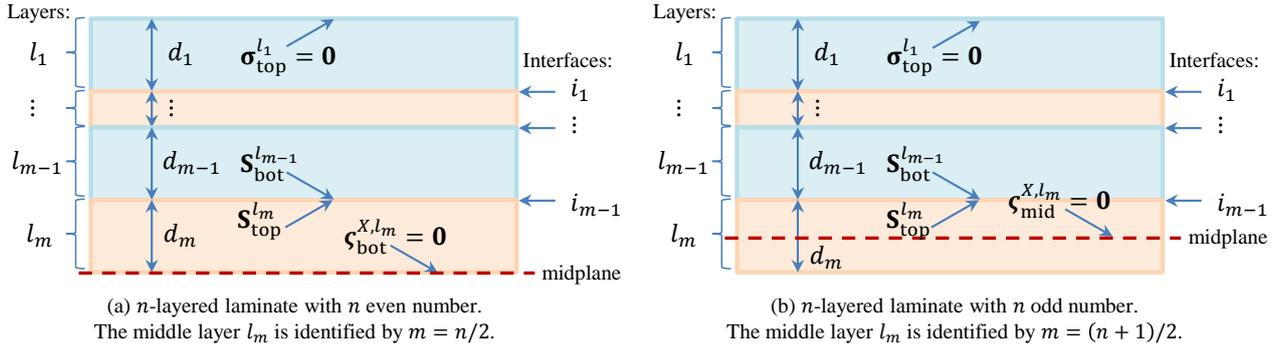


Figure 5.5 – A symmetric laminate showing only the upper half layers. In the SC $\boldsymbol{\varsigma}_{\text{bot}}^{X,l_m}$ and $\boldsymbol{\varsigma}_{\text{mid}}^{X,l_m}$, the superscript $X = s$ and a represent the symmetric and anti-symmetric condition, respectively.

In view of the odevity of a n -layered symmetric laminate, the midplane places at different locations for n being an even or odd number. Thus, the SC should be evaluated separately for the two types of laminate.

- The laminate has an even number of layers.

For this laminate type, its midplane locates at the bottom side of the middle layer l_m as illustrated in Figure 5.5(a). Substituting the specific terms from Eqs. (3.29) and (3.30) into Eqs. (5.10) and (5.11), meanwhile setting $x_3 = d_m$ and rearranging the resulted expressions to matrix form, the following compact form of SC can be obtained.

$$\mathbf{Z}_{\text{bot}}^{s,l_m} \boldsymbol{\eta}^{l_m} = \mathbf{0} \quad \text{and} \quad \mathbf{Z}_{\text{bot}}^{a,l_m} \boldsymbol{\eta}^{l_m} = \mathbf{0} \quad (5.12)$$

5.3. THE OPTIMIZED GLOBAL MATRIX METHOD

where, $\mathbf{Z}_{\text{bot}}^{s,l_m} = \boldsymbol{\chi}_s^{l_m} \boldsymbol{\Lambda}^{l_m}(d_m) \in \mathbb{C}^{3 \times 6}$, $\mathbf{Z}_{\text{bot}}^{a,l_m} = \boldsymbol{\chi}_a^{l_m} \boldsymbol{\Lambda}^{l_m}(d_m) \in \mathbb{C}^{3 \times 6}$. $\boldsymbol{\chi}_s^{l_m}$ and $\boldsymbol{\chi}_a^{l_m}$ are defined in Eq. (5.14). $\boldsymbol{\Lambda}^{l_m}(\cdot)$ is defined in Eq. (4.5). The superscripts ‘s’ and ‘a’ denote the symmetric and anti-symmetric condition, respectively. The subscript ‘bot’ implies the location of the midplane at the bottom side of layer l_m .

- The laminate has an odd number of layers.

For this laminate type, the midplane locates at the mid-height of the layer l_m as illustrated in Figure 5.5(b). In this case, $\boldsymbol{\Lambda}^{l_m}(d_m)$ in Eq. (5.12) should be replaced by $\boldsymbol{\Lambda}^{l_m}(d_m/2)$, leading to the following compact form of SC.

$$\mathbf{Z}_{\text{mid}}^{s,l_m} \boldsymbol{\eta}^{l_m} = \mathbf{0} \quad \text{and} \quad \mathbf{Z}_{\text{mid}}^{a,l_m} \boldsymbol{\eta}^{l_m} = \mathbf{0} \quad (5.13)$$

where, $\mathbf{Z}_{\text{mid}}^{s,l_m} = \boldsymbol{\chi}_s^{l_m} \boldsymbol{\Lambda}^{l_m}(d_m/2) \in \mathbb{C}^{3 \times 6}$, $\mathbf{Z}_{\text{mid}}^{a,l_m} = \boldsymbol{\chi}_a^{l_m} \boldsymbol{\Lambda}^{l_m}(d_m/2) \in \mathbb{C}^{3 \times 6}$. The subscript ‘mid’ implies the location of the midplane at the mid-height of layer l_m .

$$\boldsymbol{\chi}_s^{l_m} = \begin{bmatrix} W_1 & W_2 & W_3 & W_4 & W_5 & W_6 \\ \beta_{21} & \beta_{22} & \beta_{23} & \beta_{24} & \beta_{25} & \beta_{26} \\ \beta_{31} & \beta_{32} & \beta_{33} & \beta_{34} & \beta_{35} & \beta_{36} \end{bmatrix}^{l_m}, \quad \boldsymbol{\chi}_a^{l_m} = \begin{bmatrix} 1 & 1 & 1 & 1 & 1 & 1 \\ V_1 & V_2 & V_3 & V_4 & V_5 & V_6 \\ \beta_{11} & \beta_{12} & \beta_{13} & \beta_{14} & \beta_{15} & \beta_{16} \end{bmatrix}^{l_m} \quad (5.14)$$

Regardless of symmetry and odevity, Eqs. (5.12) and (5.13) can be abstractly written as follows by designating the symmetry script ‘X’ and the midplane location script ‘mp’.

$$\mathbf{Z}_{\text{mp}}^{X,l_m} \boldsymbol{\eta}^{l_m} = \mathbf{0} \quad (5.15)$$

Following the indication in Figure 5.5, the CC (see Eq. (5.3)) can be sequentially applied from interface i_1 to and only to i_{m-1} . Combining the BC (see Eq. (5.5)) and the SC (see Eq. (5.15)), the SC-induced global matrix $\mathbf{D}_G^X(v, \xi) \in \mathbb{C}^{6m \times 6m}$ can be generated into Eq. (5.16), which yields the implicit dispersion equation Eq. (5.17) in accordance with the superscript $X = s$ and a for the symmetric and anti-symmetric modes, respectively, and the subscript mp=bot and mid for the laminate having an even and odd number of layers, respectively.

$$\begin{array}{l} \text{BC at the top surface} \rightarrow \\ \text{CC at the interfaces} \left\{ \right. \\ \text{SC at the midplane} \rightarrow \end{array} \left[\begin{array}{cccccc} -\mathbf{Z}_{\text{top}}^{\sigma,l_1} & & & & & \\ \mathbf{Z}_{\text{bot}}^{l_1} & -\mathbf{Z}_{\text{top}}^{l_2} & & & & \\ & & \ddots & & & \\ & & & \mathbf{Z}_{\text{bot}}^{l_{m-1}} & -\mathbf{Z}_{\text{top}}^{l_m} & \\ & & & & \mathbf{Z}_{\text{mp}}^{X,l_m} & \end{array} \right] \begin{bmatrix} \boldsymbol{\eta}^{l_1} \\ \boldsymbol{\eta}^{l_2} \\ \vdots \\ \boldsymbol{\eta}^{l_{m-1}} \\ \boldsymbol{\eta}^{l_m} \end{bmatrix} = \mathbf{0} \quad (5.16)$$

$$\mathcal{D}_G^X(v, \xi) = \mathcal{D}_G^{X,R}(v, \xi) + i\mathcal{D}_G^{X,I}(v, \xi) \triangleq \det\{\mathbf{D}_G^X(v, \xi)\} = 0 \quad (5.17)$$

There are two merits of the SC-induced GMM. The first one is the halved size of the SC-induced global matrix comparing to the original one, turning out to reduce the computational burden. The second one is that the symmetric and anti-symmetric modes' solutions are separated beforehand. As a consequence, the post separation can be exempted and the mode jumping problem studied in [64] can be avoided.

5.3.2 Sparsity of global matrix

The global matrix has sparsity property. Observing Eqs. (5.6) and (5.16), the non-zero entries of the global matrices are regularly distributed along the diagonal band. This fact indicates that the sparse matrix technique can be applied to the GMM. Using sparse matrix can play an important role when dealing with a laminate having a large number of layers which causes a large sized global matrix. By transforming this matrix into its sparse counterpart, the storage space can be saved and the computational speed can be greatly accelerated during processing the large sized matrix. We use MATLAB built-in function *sparse* to achieve the sparse matrix technique.

5.3.3 Parallelization of GMM

Even if not so apparent, GMM can be perfectly parallelized. Mathematically, the dispersion equation $\mathcal{D}(v, \xi) = 0$ defined in Eq. (5.7) can be solved by fixing $v = v_0$ to sweep the roots of ξ ($\mathcal{D}(v_0, \xi) = 0$) or by fixing $\xi = \xi_0$ to sweep the roots of v ($\mathcal{D}(v, \xi_0) = 0$). The two sweeping schemes are mutually independent.

Moreover, in both sweeping schemes, the sweeping process between the different fixed variables are mutually independent as well. For the example of sweeping ξ , the two equations $\mathcal{D}(v_0^{(1)}, \xi) = 0$ and $\mathcal{D}(v_0^{(2)}, \xi) = 0$ can be solved concurrently as there is no any communication between the two equations. It is also true when sweeping v , the two equations $\mathcal{D}(v, \xi_0^{(1)}) = 0$ and $\mathcal{D}(v, \xi_0^{(2)}) = 0$ can be solved concurrently. This fact indicates that the two sweeping processes belongs to the classical *Perfectly Parallel Problem* [65]. Thus, execution of GMM can be parallelized during programming the algorithm to intentionally cope with the computational efficiency issue. Applying the parallel

5.4. APPLICATION OF THE OPTIMIZED GMM TO AN AEROSPACE COMPOSITE LAMINATE WITH 400 LAYERS

computing techniques for GMM can be easily achieved since there are many numerical computing toolboxes or packages available from widely used programming languages such as Matlab and Python.

By introducing the three advanced computing techniques to the standard GMM, the optimized GMM is now high efficiency and it is able to deal with aerospace composite laminate that usually has a large number of layers.

5.4 Application of the optimized GMM to an aerospace composite laminate with 400 layers

5.4.1 Dispersion curves

In this section, we apply the optimized GMM to a 400-layered aerospace composite laminate with layups $[0/90/45/-45]_{50s}$ which is the prototype of the booster pressure vessels of the rocket Ariane 6 under development [11]. The composing material of the laminate is CFRP. The stiffness matrix of this material along the fiber direction is provided in Eq. (5.18). The mass density is $\rho = 1550 \text{ kg/m}^3$. The plate total thickness is $d = 50 \text{ mm}$.

$$\mathbf{C} = \begin{bmatrix} 154 & 3.7 & 3.7 & 0 & 0 & 0 \\ & 9.5 & 5.2 & 0 & 0 & 0 \\ & & 9.5 & 0 & 0 & 0 \\ & & & 2.15 & 0 & 0 \\ \text{sym} & & & & 4.2 & 0 \\ & & & & & 4.2 \end{bmatrix} \text{ GPa} \quad (5.18)$$

Eq. (5.17) is adopted to compute the dispersion curves of this laminate in the frequency-phase velocity domain through the relation $\omega = \xi v$. It can be thought that if the original global matrix was used, the size of the matrix will be large to 2400 orders because there is 400 layers and each layer has six partial waves ($p = 6$). By using the SC-induced global matrix, the matrix size has been halved to 1200 orders. Given that the studied laminate has even number of layers, Figure 5.5(a) should be focused. Thus, Eq. (5.12) should be adopted to apply SC for the full sized global matrix.

The computed dispersion curves through the optimized GMM are depicted in Figure 5.6. It shows that in the ellipses, the curves belonging to the same symmetry kind can mutually close but never cross. This phenomenon is termed the veering effect [66], which will cause mode jumping problem in some computing software of dispersion curves [64]. In our computing program, we solve this problem by refining the solution points of the loci of one branch in the veering effect regions.

5.4. APPLICATION OF THE OPTIMIZED GMM TO AN AEROSPACE COMPOSITE LAMINATE WITH 400 LAYERS

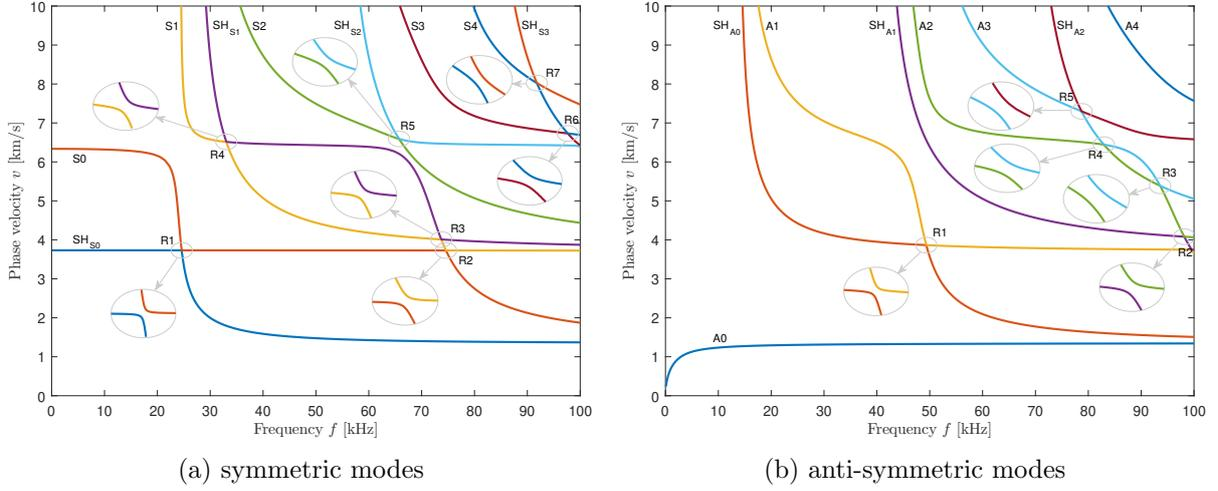


Figure 5.6 – Dispersion curves of the 400-layered aerospace laminate at $\theta = 0^\circ$ direction.

5.4.2 Study the veering effect to avoid mode jumping problem

The veering effect is also termed as the *repulsion behavior* of dispersion curves in some references [67, 68, 64] or the *osculation* of spectral lines in other reference [69]. It refers to the phenomenon that under certain coupling conditions two or more dispersion curves of different modes but belonging to the same symmetry kind close firstly and then veer away to finally diverge instead of crossing in the repulsion region. The extent of closing depends on the degree of coupling and anisotropy. This phenomenon happens constantly in Figure 5.6. The qualitative analysis has been made in some references [67, 68]. In the repulsion regions, the dispersion curves are usually accompanied by rapid exchanging of their mode shapes [66].

The frequent occurrence of veering effect complicates the generation of continuous dispersion curves especially for the extrapolation-based modal curve tracing technique [6, 70] and the correlation-based mode shape analysis [10] for which the mode jumping problem is a big trouble. For example, the crossed A_1 and SH_1 curves in Fig. 3(c) of [37], the crossed S_0 and S'_0 curves in Fig. 5 of [11], the crossed S_0 and SH_0 curves in Fig. 3(b) of [10], etc.

With the basic understanding to the veering effect, we get back to analyze Figure 5.6. Clearly, the dispersion curves of symmetric and anti-symmetric modes have seven and five repulsion regions, respectively. In order to clearly show the diverged points, the repulsion regions are zoomed in several times in the annotated ellipses. Specifically, repulsion regions R5 and R2 in the symmetric modes are

5.4. APPLICATION OF THE OPTIMIZED GMM TO AN AEROSPACE COMPOSITE LAMINATE WITH 400 LAYERS

zoomed in 21 and 2000 times, respectively; and repulsion regions R4 and R2 in the anti-symmetric modes are zoomed in 31 and 208 times, respectively. The mentioned numbers here are the minimum and maximum zoom factor among these annotated ellipses. Furthermore, the zoom factors reflect the degree of coupling and anisotropy for which a larger zoom corresponds to a heavier coupling or anisotropy. Two interesting points observed from Figure 5.6 are that (1) S0 mode is repulsed twice in regions R1 and R2; (2) S1 and SH_{S1} modes are mutually repulsed twice in regions R3 and R4. These unusual phenomena are rarely observed from simple composite structures.

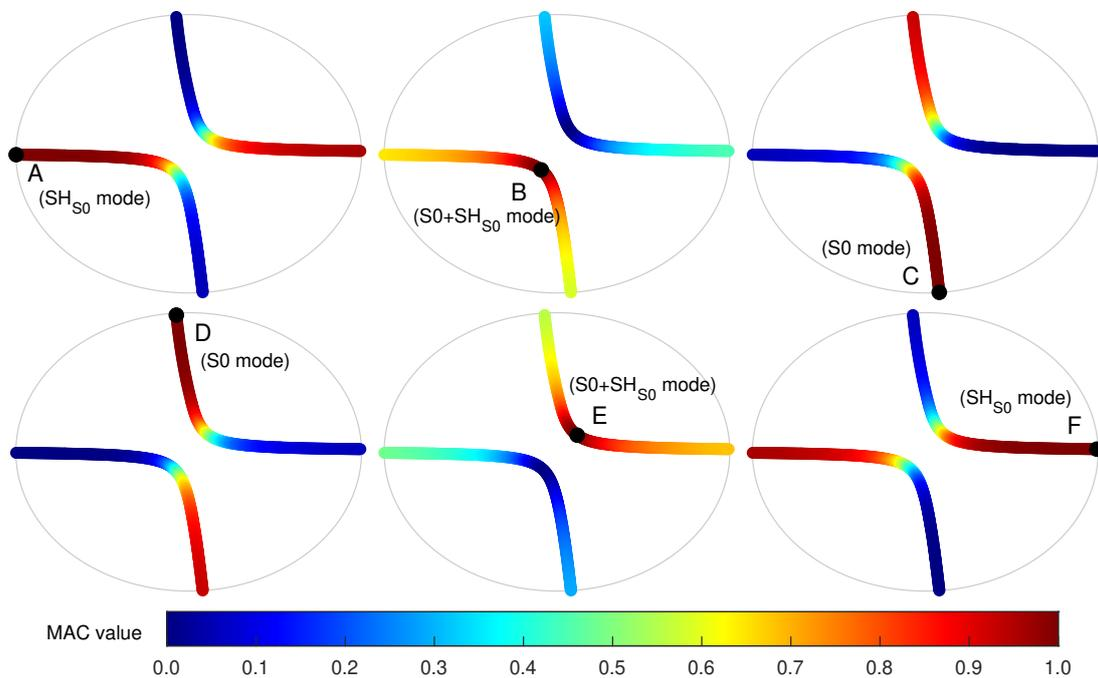


Figure 5.7 – MAC value tomography of displacement mode shapes in the region R1 of symmetric modes.

5.4.2.1 Displacement mode shape analysis

In the subsequent paragraphs, we quantitatively analyze the behavior of wave modes in the repulsion regions by taking region R1 in symmetric modes as the example. The two curves alongside their six master points are plotted in Figure 5.7, for which points A, B, C are the starting, turning, end points of the lower-left curve, respectively, and points D, E, F have the same meaning in the upper-right curve. The center of region R1 locates at (24.60 kHz, 3.731 km/s) in Figure 5.6(a), and the distance between points A and F is about 0.3 kHz, and the distance between C and D is about

5.4. APPLICATION OF THE OPTIMIZED GMM TO AN AEROSPACE COMPOSITE LAMINATE WITH 400 LAYERS

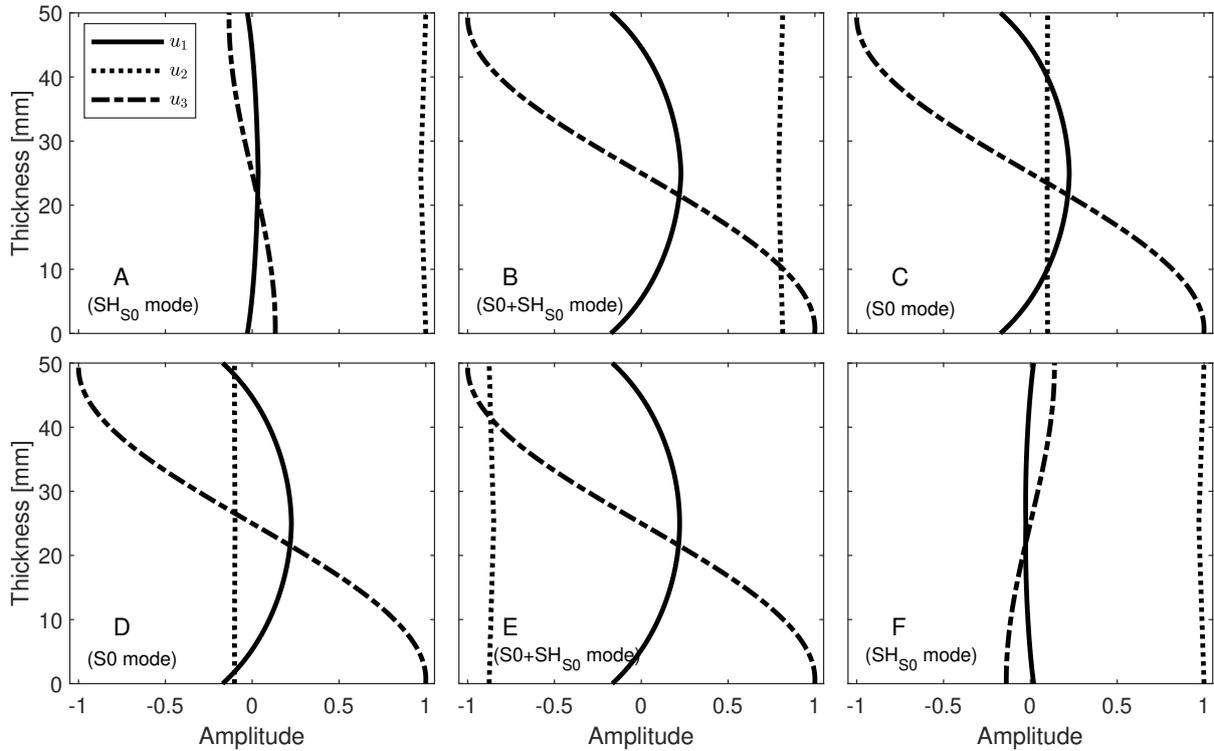


Figure 5.8 – Displacement mode shapes.

0.015 km/s, which manifest that R1 is a pretty small region and the veering effect in this region is considerably heavier. The displacement mode shapes corresponding to the six points are presented in Figure 5.8. Figures 5.8 and 5.7 contain fruitful information. We first analyze Figure 5.8 to determine the mode type of each master point. As for the color code in Figure 5.7, it will be discussed latter.

In Figure 5.8A, the shear horizontal displacement u_2 is predominates over u_1 and u_3 , indicating that point A should belong to the SH_{S0} mode, though not so pure. In Figure 5.8B, no displacement component is dominating among u_1 , u_2 , u_3 , thus S0 and SH_{S0} modes coexist in the turning point. In Figure 5.8C, u_1 and u_3 become larger components than u_2 , thus point C should belong to the S0 mode, though not so pure. The mode shape analysis based on the three subfigures reveals that although points A, B, C locate at the same curve they have different behaviors. For points D, E, F, a similar behaviors can be observed and mode shapes at those points belong to S0, $S0+SH_{S0}$ and SH_{S0} mode, respectively. In summary, after analyzing the veering effect in the small region R1, the two modal curves belong to the same symmetric modes and are very close but never cross. This is accompanied by a dramatically exchange of their displacement mode shapes.

Special attention should be paid to Figure 5.8CD, though the two points belong to the same S0 mode, their minor components u_2 have opposite phases, namely, positive and negative amplitudes of u_2 in Figure 5.8C and D, respectively. The same phenomenon also occurs in Figure 5.8AF and BE, for which the latter is more prominent. This phenomenon reveals that, during the exchange of the major component of mode shapes, the minor components have a rollover in its phase.

The mode shape analysis was also used to produce continuous dispersion curves in some references [9]. However, if the turning points are not identified in the repulsion regions, point A will mistakenly jump to F, so does for point C to D, thus causing the illusion that the two modal curves cross over in the repulsion region. This illusion occurred in the Fig. 3(b) of [10], causing the mode jumping problem in this reference.

5.4.2.2 MAC value tomography of displacement mode shapes

A thorough solution to this problem is to compute the modal assurance criteria (MAC) values [71] between the mode shapes of the consecutive dispersion solutions and the master points in the two modal curves. This has been achieved in Figure 5.7 in which the color code represents the MAC values of the loci points in one curve to the master point of the ellipse.

From these diagrams, it can be seen that the line segments near to the respective master points have larger MAC values. This is because the loci of the dispersion solutions is continuous, thus the closer to the master point, the more similar the mode shape will be, and causing a more larger MAC value. However, in Figure 5.7A, the line segment nearby point F possesses comparable MAC values with the counterpart, the line segment nearby point A. Likewise, in Figure 5.7D, the line segment nearby point C also possesses comparable MAC values with the line segment nearby point D. This is an intuitive illustration for the mode shapes exchanging phenomenon occurring in the repulsion regions. Besides, we observe the orthogonality of displacement mode shapes in Figure 5.7BE. Specifically, in Figure 5.7B, the MAC values of the upper-right curve to the turning point B are almost zero. Likewise, in Figure 5.7E, the MAC values of the lower-left curve to the turning point E are nearly zero as well. This phenomenon manifests that the turning point is a good indicator to distinguish mode branches in the repulsion regions to avoid mode jumping problem.

5.4.2.3 Stress mode shape analysis

For the six master points in the repulsion region R1 of symmetric modes, we also plot their stress mode shapes in Figure 5.10 and perform the MAC value tomography in Figure 5.9. It can be seen that the stress mode shapes of the six master points are mutually similar except points A and F. Moreover, Figure 5.9 demonstrates that the MAC value of stress mode shapes is not an ideal indicator to distinguish mode branches because the minimum MAC value is 0.96, indicating the non-orthogonality of stress mode shapes. In fact, among the three components of stresses ($\sigma_{33}, \sigma_{23}, \sigma_{13}$), the σ_{33} component is always the major one and the six points have the same σ_{33} mode shapes. In short, it is not recommended to use stress mode shapes for distinguishing mode branches of dispersion solutions, and the displacement mode shapes are the best choice.

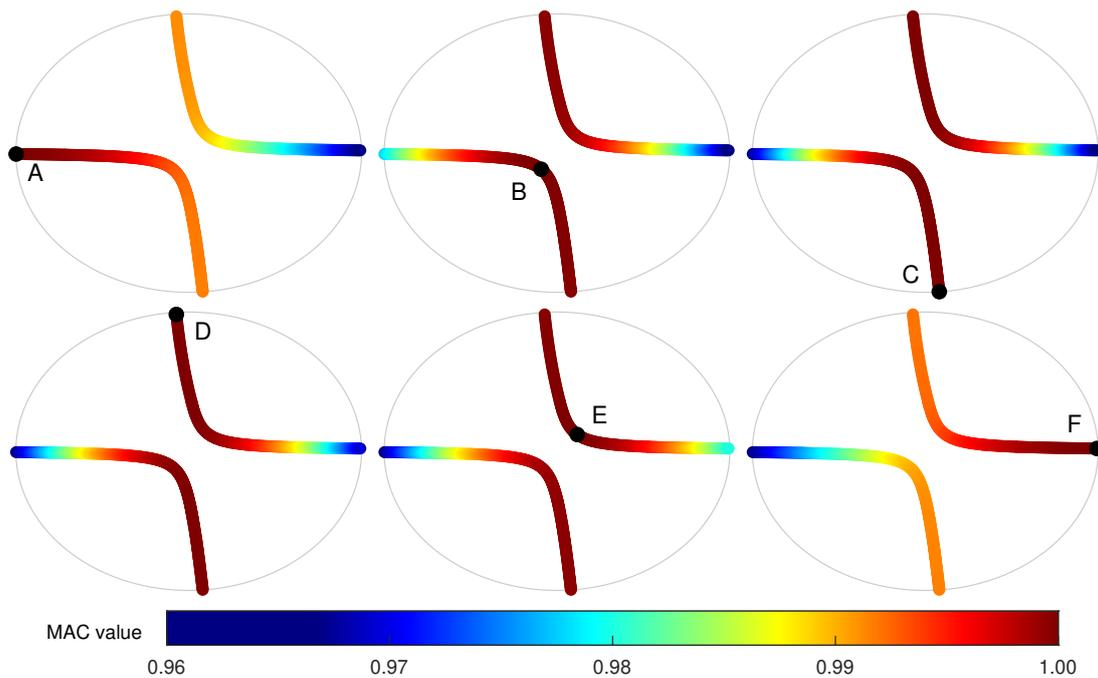


Figure 5.9 – MAC value tomography of stress mode shapes in the region R1 of symmetric modes.

5.4.3 Computational efficiency

The computational efficiency of the optimized GMM is reported in this subsection for the 400-layered laminate. The adopted solving methods to perform the test is bisection method and phase change method that will be introduced in Chapter 6. Computations were performed in MATLAB

5.4. APPLICATION OF THE OPTIMIZED GMM TO AN AEROSPACE COMPOSITE LAMINATE WITH 400 LAYERS

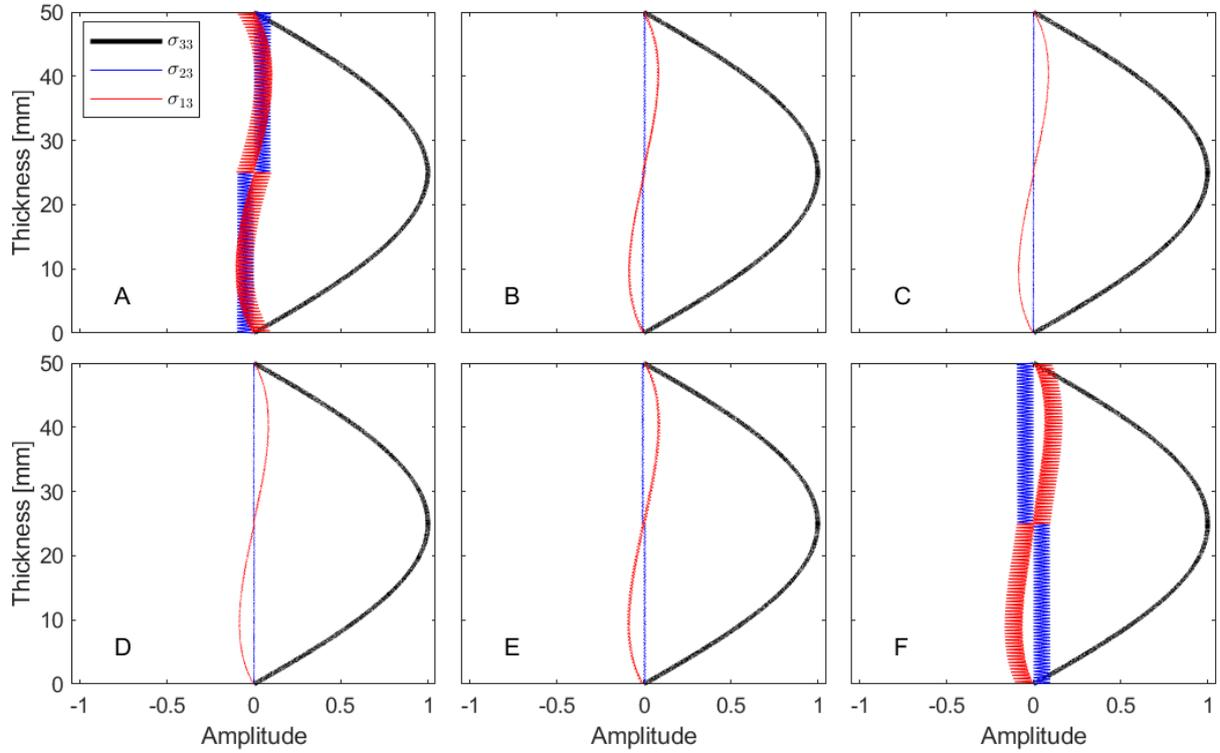


Figure 5.10 – Stress mode shapes.

R2016a hosted on a Dell Precision T3500 workstation with the processor Intel Xeon W3530@2.8GHz, 4 CPU cores, 18G RAM. Bi-directional sweeping scheme is used, namely, fixing $v = v_0$ to sweep the roots of f and fixing $f = f_0$ to sweep the roots of v . In each direction, the sweeping line is equally offsetted 100 times from the minimum to the maximum, and the precision of solutions is set to be the fifth decimal place. The sweeping step length of phase velocity and frequency is 10 m/s and 1 kHz, respectively. Each solving method runs 10 times and the averaged computational time of the symmetric and anti-symmetric modes is listed in Table 5.2.

Table 5.2 shows that sweeping v costs more time than sweeping f . The explanations to this phenomenon are given in Chapter 6. By using the optimized GMM, the computations for symmetric and anti-symmetric modes can be completed within half an hour, which is an encouraging result given that the studied laminate has the largest number of layers reported so far (400 layers). We also adopted the standard GMM to perform the computation with the same running parameters listed above. Within a reasonable duration (24 hours), computations did not complete even for once running of program. We had to cut the program down and thus no any computational time can be supplied in

5.5. CONCLUSION

Table 5.2 for the standard GMM. This fact proves that the thoroughly optimized GMM can greatly improve the computational efficiency when applying it to cope with a laminate having a large number of layers.

Table 5.2 – The computational time of the 400-layered laminate using the optimized GMM (unit: seconds)

Bisection method			Phase change method		
sweep v	sweep f	sum	sweep v	sweep f	sum
899 ^s	462 ^s	1361 ^s	871 ^s	469 ^s	1340 ^s
780 ^a	454 ^a	1234 ^a	752 ^a	453 ^a	1205 ^a

^s The computational time corresponds to the symmetric modes.

^a The computational time corresponds to the anti-symmetric modes.

5.5 Conclusion

This chapter reviews the standard GMM and derives the optimized GMM, and applying it to compute the dispersion curves of the Open Guided Waves plate and Ariane 6. The comparison between GMM computation and the experimental data validates the effectiveness of GMM framework. In the higher frequency range, GMM is more stable than TMM because the latter will suffer from the *large fd problem*. On the contrary, ESM is only valid at lower frequency range. To improve the computational efficiency of GMM, three optimizations are introduced including (1) addition of symmetry condition to the global matrix, (2) applying the sparse matrix technique, (3) endowing the parallel computing attribute. The numerical study on a 400-layered aerospace composite laminate validates the effectiveness of the optimized GMM.

5.5. CONCLUSION

Chapter 6

Dichotomy property of dispersion equation of guided waves propagating in anisotropic composite plates

The previous chapters mainly focus on the way to build complex-valued dispersion equations for guided waves propagating in a single-layered plate via PWSA [72] of Chapter 3 or a multi-layered plate via TMM [33, 38] of Chapter 4 and GMM [2, 4] of Chapter 5. Little attention is paid to develop efficient and stable numerical solving methods associated with the derived complex-valued dispersion equations. In this chapter, the conditions under which complex-valued dispersion equations are either real- or purely imaginary-valued equations (termed as dichotomy property) are derived for both single- and multi-layered composite plates. With such a property, the complex-valued dispersion equations can be efficiently numerically solved within the real number field via the standard bisection method or the corrected phase change method. It is thus now possible to overcome numerical issues frequently reported in literature. The proposed methodology of this chapter provides a new standard framework to solve the dispersion equations which is stable, multipurpose, and numerically efficient.

The works conducted in this chapter have been published in the journal *Mechanical Systems and Signal Processing*, see [73].

6.1 Problem statement

In Chapter 3, 4 and 5, dispersion equations are built with PWSA for the single layer plate and TMM and GMM for the multi-layered system, respectively. It can be recognized that even if significant

6.1. PROBLEM STATEMENT

efforts are carried out to find ways of building the dispersion equation via different methods, little work was conducted to study the property of the derived dispersion equation and to find efficient and stable associated numerical solving methods. In most references, once the derivation of dispersion equation is completed, one just says that *the solution to this equation usually requires the use of numerical methods* (see [37, 8, 38, 10, 12]), but little details are provided.

Mathematically, the derived dispersion equation belongs to the family of complex-valued equations, which is more difficult to solve than a real-valued equation, due to the existence of complex exponential terms $e^{i\xi\alpha_r x_3}$ presented in the related matrices. In general, the determinant in a certain dispersion equation, $\mathcal{D}(v, \xi)$, has real, $\mathcal{D}^R(v, \xi)$, and imaginary, $\mathcal{D}^I(v, \xi)$, parts. Thus, the intuitive way of solving the dispersion equation is to find the zero points of both parts and then take their intersections as the true solutions as presented in Eq. (6.1a), which is easy to implement because both $\mathcal{D}^R(v, \xi)$ and $\mathcal{D}^I(v, \xi)$ are real-valued functions such that many real variables-based root-finding algorithms can be used like the bisection method.

$$\mathcal{D}(v, \xi) \triangleq \mathcal{D}^R(v, \xi) + i\mathcal{D}^I(v, \xi) = 0 \Leftrightarrow \begin{cases} \mathcal{D}^R(v, \xi) = 0 \\ \mathcal{D}^I(v, \xi) = 0 \end{cases} \quad (6.1a)$$

$$\mathcal{D}(v, \xi) \triangleq \mathcal{D}^R(v, \xi) + i\mathcal{D}^I(v, \xi) = 0 \Leftrightarrow \text{abs}\{\mathcal{D}(v, \xi)\} = 0 \quad (6.1b)$$

However, the majority of methods mathematically transform the solving process to search the global minimal moduli of the dispersion function that should be zero in theory, see Eq. (6.1b). A representative example is the pioneering software *Disperse* which employed a path-dependent minimal moduli search strategy combined with the convergence criteria of checking the included phase angle of the complex-valued characteristic function that should be greater than 90° [74, 70]. The toolbox *ElasticMatrix* makes use of MATLAB built-in function *fminbnd* to achieve the minimal moduli searching purpose [41]. Another complex strategy adopted by the software *Dispersion Calculator* is to check, in a small interval, both the occurrence of minimum moduli and sign change of the dispersion function [11], see Figure 6.1. Recently, Zhu and Qian et al. developed an iterative method to solve the dispersion equation by also coping with the modulus of the dispersion function, which provides a strict convergence condition to distinguish the local and global minima [75].

In comparison with the multi-layered anisotropic system, the standard bisection method is widely used for the single-layered isotropic Rayleigh–Lamb equation. The solving process of the Rayleigh–Lamb equation is achieved by dividing the whole solution domain into three regions, i.e., region 1

6.1. PROBLEM STATEMENT

TABLE I. Boundary conditions used for the tracing of the six mode families.

Family	Situation	Boundary conditions
S		$\det \mathbf{K} = 0$, $\text{abs}(\det \mathbf{K}) = \min$, u_1^{++a}
A		$\det \mathbf{K} = 0$, $\text{abs}(\det \mathbf{K}) = \min$, u_1^{+-b}
B		$\det \mathbf{K} = 0$, $\text{abs}(\det \mathbf{K}) = \min$
S'	Single layer	$a_{21(m)}^c = 0$
	Single super layer	$\text{abs}(a_{21}^c) = \min$
	Periodic	$\text{abs}\left(\det \begin{bmatrix} a_{11}^c - 1 & a_{12}^c \\ a_{21}^c & a_{22}^c - 1 \end{bmatrix}\right) = \min$
A'	Single layer	$a_{21(m)}^c = 0$
	Else	$\det \mathbf{K} = 0$
B'	Single super layer	$a_{21}^c = 0$
	Per., $p/n = 1, 2, \dots$ Periodic	$a_{21}^c = 0$
	Per., $p/n \neq 1, 2, \dots$	$\det \begin{bmatrix} a_{11}^c - 1 & a_{12}^c \\ a_{21}^c & a_{22}^c + 1 \end{bmatrix} = 0$
S'_0, B'_0	Decoupled case	Non-dispersive, $v = \sqrt{C_{66}/\rho}$

^a u_1 at the plate's top and bottom have the same sign.

^b u_1 at the plate's top and bottom have the opposite sign.

Figure 6.1 – A summary of the solving strategy adopted by *Dispersion Calculator* [11].

of $v < c_T$, region 2 of $c_T < v < c_L$ and region 3 of $v > c_L$, where v is the phase velocity, and c_T and c_L are the velocities of transverse and longitudinal modes, respectively. Then in each region, the complex-valued Rayleigh-Lamb equation is derived to be a real one such that the standard bisection method can be adopted to solve it in an easy way [76, 12]. Figure 6.2 just explains this process.

In addition to the two strategies introduced above, another interesting method is by consecutively monitoring the phase change of the dispersion function, which is actually evolved from the convergence criteria of *Disperse*. However, this method suffers from numerical instability issues when applied to multiple layered plates having 50 layers, see Fig. 7(c) of [9].

Inspired by the strategy of solving the Rayleigh-Lamb equation introduced above, the same idea of converting the complex-valued equation to a real one, which can be easily solved via standard root-finding algorithms, has been applied here to the single-layered and multi-layered anisotropic dispersion equation built with PWSA, GMM and TMM. Finally an important property of dispersion equations, termed as dichotomy property in this chapter, is demonstrated: they are either real- or purely imaginary-valued equations. On the basis of this property, it is shown that some numerical issues can be overcome and as a consequence the obtained dispersion curves become very stable.

6.2. PROPERTIES OF CHRISTOFFEL EQUATION OF MONOCLINIC MATERIALS

6.3 Numerical Solution of the Rayleigh–Lamb Frequency Equations

Recall that the **Rayleigh–Lamb frequency equations** can be written as

$$\frac{\tan(qh)}{\tan(ph)} = -\frac{4k^2 pq}{(q^2 - k^2)^2} \quad \text{for symmetric modes.} \quad (6.31)$$

$$\frac{\tan(qh)}{\tan(ph)} = -\frac{(q^2 - k^2)^2}{4k^2 pq} \quad \text{for antisymmetric modes.} \quad (6.32)$$

Here p and q are given by

$$p^2 = \left(\frac{\omega}{c_L}\right)^2 - k^2 \quad \text{and} \quad q^2 = \left(\frac{\omega}{c_T}\right)^2 - k^2.$$

It is often useful to consider various regions of the Rayleigh–Lamb equations for k compared with ω/c_L or ω/c_T (see Graff 1991). Let **region 1** be $k > \omega/c_T$; **region 2**, $\omega/c_T > k > \omega/c_L$; and **region 3**, $k < \omega/c_L$. **In region 1**, where $c_p < c_T$, we therefore have

$$\frac{\tanh(q'h)}{\tanh(p'h)} = \left\{ \frac{4p'q'k^2}{(k^2 - q'^2)^2} \right\}^{\pm 1};$$

from (6.32), $p = ip'$, $q = iq'$, $p'^2 = -p^2$, and $q'^2 = -q^2$ (the exponent +1 is for symmetric and -1 for antisymmetric modes). **In region 2**, where $c_T < c_p < c_L$, we have

$$\frac{\tan(q'h)}{\tanh(p'h)} = \pm \left\{ \frac{4p'q'k^2}{(k^2 - q'^2)^2} \right\}^{\pm 1};$$

in region 3, where $c_p > c_L$, equations (6.31) and (6.32) are unaltered.

Figure 6.2 – The complex-to-real strategy for solving Rayleigh-Lamb equation [12].

6.2 Properties of Christoffel equation of monoclinic materials

The investigation starts with the Christoffel equation of monoclinic material $\mathbf{K}(\alpha)\mathbf{U} = \mathbf{0}$ that is presented in Eq. (3.22) with the detailed coefficients $K_{ij}(\alpha)$ in Eq. (3.23). For other material classes, specifically, orthotropic, transversely isotropic and isotropic materials, the investigation made in this section is naturally compatible with these materials. But for triclinic materials, we directly take advantage of numerical validation due to the complexity of the derived equations from the triclinic materials.

6.2.1 Property of the polynomial discriminant Δ

The third order polynomial equation in terms of α^2 corresponding to the Christoffel equation of monoclinic material is presented in Eq. (3.24) and we duplicate this equation into Eq. (6.2) for convenience.

$$\mathcal{A}(\alpha^2) \triangleq A_6\alpha^6 + A_4\alpha^4 + A_2\alpha^2 + A_0 = 0 \quad (6.2)$$

6.2. PROPERTIES OF CHRISTOFFEL EQUATION OF MONOCLINIC MATERIALS

where, the coefficients A_6, A_4, A_2, A_0 are presented in Eq. (3.25) which depends on the constant elastic coefficients C_{pq} and mass density ρ as well as phase velocity v .

$$\Delta = \frac{p^3}{27} + \frac{q^2}{4}, \quad p = \frac{3A_6A_2 - A_4^2}{3A_6^2}, \quad q = \frac{27A_6^2A_0 - 9A_6A_4A_2 + 2A_4^3}{27A_6^3} \quad (6.3)$$

Once the polynomial coefficients (A_6, A_4, A_2, A_0) are known, the three α^2 roots can be solved from Eq. (6.2) via Cardano's Formula or polynomial root-finding algorithm, for which their behavior is determined by the discriminant Δ defined in Eq. (6.3) according to the following three cases [9, 77].

$$\begin{cases} (1) & \Delta < 0, \text{ all } \alpha^2 \text{ roots are real and unique;} \\ (2) & \Delta = 0, \text{ all } \alpha^2 \text{ roots are real and at least two are equal;} \\ (3) & \Delta > 0, \text{ one } \alpha^2 \text{ root is real and the other two are complex conjugates.} \end{cases}$$

It is of great importance to state that the case $\Delta > 0$ will be automatically excluded for isotropic materials (see Ch. 5.6 of [33] for more information). Actually, the absence of $\Delta > 0$ is not limited to isotropic materials, after a number of numerical investigations on various composite materials including transversely isotropic, orthotropic and monoclinic materials studied in the next subsection, only a few materials will lead to $\Delta > 0$ in a small phase velocity range. That is to say, for most composite materials, the case $\Delta > 0$ will be also automatically excluded. One convincing evidence catering this perspective comes from the Fig. 2 of [9]. In the following numerical examples, the existence of $\Delta > 0$ will be checked firstly for the sake of strictness. For $\Delta \leq 0$, the three α^2 roots are all real numbers and can be sorted in Eq. (6.4a). The six α roots regardless of which case are obtained by satisfying the condition in Eq. (6.4b).

$$\alpha_1^2 \leq \alpha_3^2 \leq \alpha_5^2, \quad \text{if } \Delta \leq 0 \quad (6.4a)$$

$$\alpha_2 = -\alpha_1, \alpha_4 = -\alpha_3, \alpha_6 = -\alpha_5 \quad (6.4b)$$

6.2.2 Illustration of the property of polynomial discriminant Δ

The typical $\Delta - v$ relation, in two cases respectively representing the absence of $\Delta > 0$ and the presence of $\Delta > 0$, is plotted in Figure 6.3 based on Eqs. (3.25) and (6.3).

From Figure 6.3(b), it can be seen that the case $\Delta > 0$ only happens in a narrow phase velocity range for this particular composite material. Actually, most of composite materials reported in references will automatically exclude the case $\Delta > 0$ (similarly to Figure 6.3(a)). Only a few of

6.2. PROPERTIES OF CHRISTOFFEL EQUATION OF MONOCLINIC MATERIALS

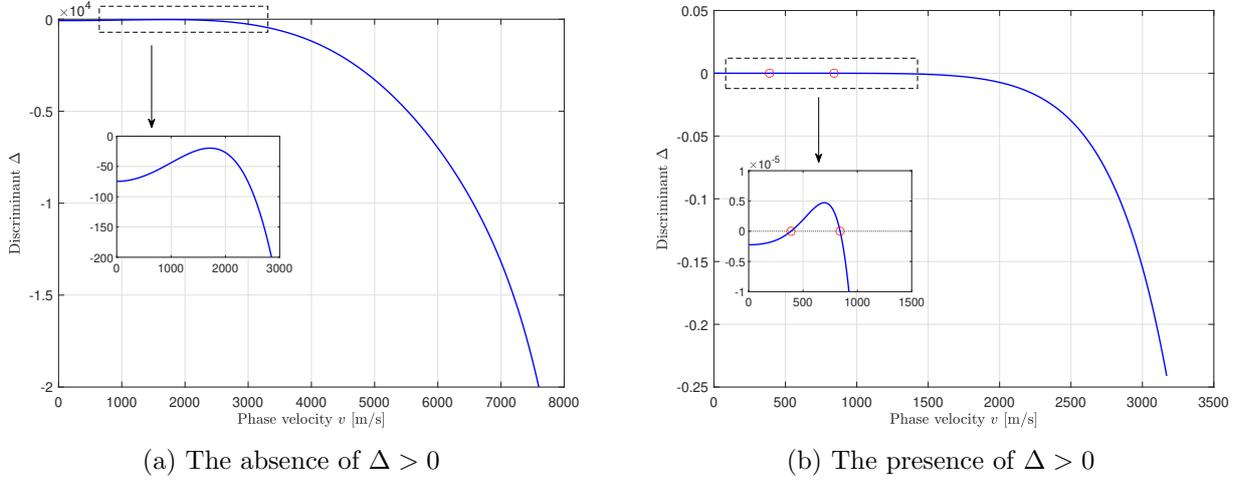


Figure 6.3 – The typical $\Delta - v$ relation showing (a) the absence of $\Delta > 0$ and (b) the presence of $\Delta > 0$ in a narrow phase velocity range.

composite materials can invoke the presence of $\Delta > 0$ in a limited phase velocity range (similarly to Figure 6.3(b)). After we performed a number of numerical investigations on various composite materials from references, a list denoting for various materials the absence or presence of $\Delta > 0$ is generated in Table 6.1 and 6.2, respectively. In the two tables, the listed materials have been rotated to the 45° direction to keep the monoclinic type of stiffness matrix, otherwise it is indicated in the table.

Based on the results of the numerical investigations in Table 6.1 and 6.2 achieved on various composite materials, the occurrence of $\Delta > 0$ is application-dependent (and occurs only for some special materials). For most composite materials, the case $\Delta > 0$ will be automatically excluded. For sake of strictness, in each numerical example of this chapter, we firstly check whether or not the case $\Delta > 0$ existed.

6.2.3 Properties of intermediate parameters

In this subsection, we only focus on the case $\Delta \leq 0$ to theoretically explore the property of some intermediate parameters that are used to generate dispersion equation. There are three reasons to exclude the case $\Delta > 0$ in this subsection: (1) the theoretical study on the case $\Delta \leq 0$ is enough to show the essence of dichotomy property; (2) the theoretical derivation on the case $\Delta > 0$ is untractable, thus numerical validation is necessary and will be conducted in Section 6.5.2; (3) the case $\Delta > 0$ is an

6.2. PROPERTIES OF CHRISTOFFEL EQUATION OF MONOCLINIC MATERIALS

Table 6.1 – The composite materials that automatically exclude the case $\Delta > 0$.

Reference number	Structure name (material type), data source in the cited reference
[77]	SC (orthotropic), Table I
[37]	AS4/3502 (transversely isotropic), Table 1 ¹
[45]	GRE plate (transversely isotropic), Eqs. (A11)(A12)
[72]	Unidirectional carbon-epoxy panel (orthotropic), Table 2.3
[62]	Hexply M21/34/UD134/T700/300 (transversely isotropic), Table 4
[8]	G40-800/5276-1 (transversely isotropic), Table 2
[8]	S2-FM94 (transversely isotropic), Table 2
[38]	A single-layered plate (orthotropic), section 3.1
[78]	Prepreg Carbon (transversely isotropic), Table 1
[11]	T800/913 (transversely isotropic), Eq. (81)
[9]	Unknown structure (isotropic), Eq. (19)
[9]	Unknown structure (transversely isotropic), Eq. (29)
[9]	Unknown structure (orthotropic), Eq. (32)
[9]	Unknown structure (monoclinic), Eq. (34), tested on 0° direction
[79]	Unknown structure (transversely isotropic), Eq. (23)
[80]	Unknown structure (orthotropic), Eqs. (A.7)(A.8)
[44]	Unknown structure (orthotropic), Eqs. (A1)(A2)
[44]	Unknown structure (transversely isotropic), Eqs. (A.9)(A.10)
[44]	Unknown structure (transversely isotropic), Eqs. (A.12)(A.13)
[44]	Unknown structure (isotropic), Eqs. (A.16)(A.17)
[7]	T800/924 lamina (transversely isotropic), Table 3

¹ This item is used to generate Figure 6.3(a).

Table 6.2 – The composite materials that invoke the case $\Delta > 0$ in a limited phase velocity range.

Reference number	Structure name (material type), data source in the cited reference
[77]	AL (cubic), Table I, tested on 30° direction
[77]	WA (orthotropic), Table I
[77]	SA (orthotropic), Table I
[77]	SB (orthotropic), Table I
[45]	Unknown structure (orthotropic), Eqs. (A1)(A2) ¹
[45]	Unknown structure (orthotropic), Eqs. (A3)(A4)
[12]	IM7/977–3 composite lamina (transversely isotropic), Table 15.1
[42]	Unidirectional fiber composite (transversely isotropic), Eq. (26)

¹ This item is used to generate Figure 6.3(b).

6.3. DICHOTOMY PROPERTY OF DISPERSION EQUATION OF A SINGLE LAYER PLATE

extremely rare phenomenon for composite materials according to the explanation in Section 6.2.2.

For the case $\Delta \leq 0$, all three α^2 roots are real numbers. Based on this, if $\alpha_r^2 \geq 0$ then $\alpha_r (= \pm\sqrt{\alpha_r^2})$ is a real number regardless of being positive or negative, while if $\alpha_r^2 < 0$ then α_r is a purely imaginary number. In order to investigate the dichotomy property of dispersion equations, three properties of the intermediate parameters $V_r, W_r, \beta_{1r}, \beta_{2r}, \beta_{3r}, B_5$, which are the intermediate parameters to generate dispersion equation, depending on α_r are listed below and the proof is provided in Appendix A.

Property 1: $\alpha_r \in \mathbb{R} \implies (V_r, W_r, \beta_{1r}, \beta_{2r}, \beta_{3r}) \in \mathbb{R}^5$.
Property 2: $\alpha_r \in i\mathbb{R} \implies (V_r, \beta_{1r}) \in \mathbb{R}^2$ and $(W_r, \beta_{2r}, \beta_{3r}) \in i\mathbb{R}^3$.
Property 3: $\forall \alpha_r, B_5 \in i\mathbb{R}$.

When the six roots of Eq. (6.2) are obtained for a specific monoclinic material and v_0 , one can sort them to satisfy the condition in Eq. (6.4a) ($\alpha_1^2 \leq \alpha_3^2 \leq \alpha_5^2$). This leads to the following four cases:

$$\left\{ \begin{array}{l} (1) \text{ all } \alpha_1, \alpha_3, \alpha_5 \text{ are real numbers } (0 \leq \alpha_1^2 \leq \alpha_3^2 \leq \alpha_5^2); \\ (2) \text{ only } \alpha_1 \text{ is a purely imaginary number } (\alpha_1^2 < 0 \leq \alpha_3^2 \leq \alpha_5^2); \\ (3) \text{ only } \alpha_1, \alpha_3 \text{ are purely imaginary numbers } (\alpha_1^2 \leq \alpha_3^2 < 0 \leq \alpha_5^2); \\ (4) \text{ all } \alpha_1, \alpha_3, \alpha_5 \text{ are purely imaginary numbers } (\alpha_1^2 \leq \alpha_3^2 \leq \alpha_5^2 < 0). \end{array} \right.$$

It is obvious that the boundary of the four cases is $\alpha_1 = 0, \alpha_3 = 0, \alpha_5 = 0$, respectively, which can be reached by letting $A_0 = 0$ in Eq. (6.2). Keeping in mind the expression of A_0 in Eq. (3.25), this further leads to the definition of three critical velocities, which characterize the three bulk wave velocities (longitudinal, shear horizontal and shear vertical modes) propagating along the lamina plane. Note that dispersion equation has a singularity at the bulk wave velocity, thus, some outliers in the dispersion solutions will occur. For example, the constant phase velocities appearing in Fig. 3 of [40] and produced by the software *Disperse* can be interpreted as one of these outliers.

$$v_{\text{I}} = \sqrt{\frac{A + \sqrt{B}}{2\rho}}, \quad v_{\text{II}} = \sqrt{\frac{A - \sqrt{B}}{2\rho}}, \quad v_{\text{III}} = \sqrt{\frac{C_{55}}{\rho}} \quad (6.5)$$

where, $A = C_{11} + C_{66}$ and $B = (C_{11} - C_{66})^2 + 4C_{16}^2$.

6.3 Dichotomy property of dispersion equation of a single layer plate

In this section, the single-layered paradigm will be concerned. The dispersion equation of anti-symmetric modes derived in Section 3.3.3 will be adopted to study the dichotomy property. The

6.3. DICHOTOMY PROPERTY OF DISPERSION EQUATION OF A SINGLE LAYER PLATE

tools used for anti-symmetric modes are readily applicable to symmetric modes. For convenience, the related equations are duplicated here.

$$\mathbf{D}_a(v, \xi) = \begin{bmatrix} 1 & 1 & 1 & 1 & 1 & 1 \\ V_1 & V_1 & V_3 & V_3 & V_5 & V_5 \\ \beta_{11} & \beta_{11} & \beta_{13} & \beta_{13} & \beta_{15} & \beta_{15} \\ \beta_{11}e^{i\xi\alpha_1 h} & \beta_{11}e^{-i\xi\alpha_1 h} & \beta_{13}e^{i\xi\alpha_3 h} & \beta_{13}e^{-i\xi\alpha_3 h} & \beta_{15}e^{i\xi\alpha_5 h} & \beta_{15}e^{-i\xi\alpha_5 h} \\ \beta_{21}e^{i\xi\alpha_1 h} & -\beta_{21}e^{-i\xi\alpha_1 h} & \beta_{23}e^{i\xi\alpha_3 h} & -\beta_{23}e^{-i\xi\alpha_3 h} & \beta_{25}e^{i\xi\alpha_5 h} & -\beta_{25}e^{-i\xi\alpha_5 h} \\ \beta_{31}e^{i\xi\alpha_1 h} & -\beta_{31}e^{-i\xi\alpha_1 h} & \beta_{33}e^{i\xi\alpha_3 h} & -\beta_{33}e^{-i\xi\alpha_3 h} & \beta_{35}e^{i\xi\alpha_5 h} & -\beta_{35}e^{-i\xi\alpha_5 h} \end{bmatrix} \quad (6.6)$$

$$\mathcal{D}_a(v, \xi) = \mathcal{D}_a^R(v, \xi) + i\mathcal{D}_a^I(v, \xi) \triangleq \det\{\mathbf{D}_a(v, \xi)\} = 0 \quad \text{implicit form} \quad (6.7)$$

where, the subscript ‘a’ denotes the anti-symmetric modes.

$$\begin{aligned} \mathcal{D}_a(v, \xi) = & [B_1 \sin(\xi\alpha_1 h) \cos(\xi\alpha_3 h) \cos(\xi\alpha_5 h) + B_2 \cos(\xi\alpha_1 h) \sin(\xi\alpha_3 h) \cos(\xi\alpha_5 h) \\ & + B_3 \cos(\xi\alpha_1 h) \cos(\xi\alpha_3 h) \sin(\xi\alpha_5 h)]B_5 = 0 \quad \text{explicit form} \end{aligned} \quad (6.8)$$

where,

$$\begin{aligned} B_1 &= \beta_{11}(\beta_{25}\beta_{33} - \beta_{23}\beta_{35}), \quad B_2 = \beta_{13}(\beta_{21}\beta_{35} - \beta_{25}\beta_{31}), \quad B_3 = \beta_{15}(\beta_{23}\beta_{31} - \beta_{21}\beta_{33}) \\ B_5 &= 8i [V_1(\beta_{15} - \beta_{13}) + V_3(\beta_{11} - \beta_{15}) + V_5(\beta_{13} - \beta_{11})] \end{aligned} \quad (6.9)$$

6.3.1 Dichotomy property of dispersion equation when sweeping ξ

6.3.1.1 Case 1: all $\alpha_1, \alpha_3, \alpha_5$ are real numbers.

For case 1, according to Property 1, all $\beta_{1r}, \beta_{2r}, \beta_{3r}$ ($r = 1, 3, 5$) are real numbers. The three coefficients B_1, B_2, B_3 defined in Eq. (6.9) are real numbers as well. Besides, set $B_5 = iP_5$ where P_5 is a real number according to the Property 3. Thus, the dispersion function $\mathcal{D}_a(v, \xi)$ defined in Eq. (6.8) can be written as follows.

$$\begin{aligned} \mathcal{D}_a(v, \xi) = & i[B_1 \sin(\xi\alpha_1 h) \cos(\xi\alpha_3 h) \cos(\xi\alpha_5 h) + B_2 \cos(\xi\alpha_1 h) \sin(\xi\alpha_3 h) \cos(\xi\alpha_5 h) \\ & + B_3 \cos(\xi\alpha_1 h) \cos(\xi\alpha_3 h) \sin(\xi\alpha_5 h)]P_5 = i\mathcal{D}_a^I(v, \xi) \Rightarrow \text{a purely imag. quantity} \end{aligned} \quad (6.10)$$

It is evident from Eq. (6.10) that $\mathcal{D}_a(v, \xi)$ should be a purely imaginary-valued function in case 1 given that all the terms in this function are real numbers other than the imaginary number unit. This is equivalent to say that its real part is identically vanishing, $\mathcal{D}_a^R(v, \xi) \equiv 0$. Thus, the original complex-valued equation $\mathcal{D}_a(v, \xi) = 0$ now has been transformed to $\mathcal{D}_a^I(v, \xi) = 0$, which is a real-valued

6.3. DICHOTOMY PROPERTY OF DISPERSION EQUATION OF A SINGLE LAYER PLATE

equation easy to be solved via bisection method. This phenomenon casts the essence of dichotomy property.

6.3.1.2 Case 2: only α_1 is a purely imaginary number.

In this case, set $\alpha_1 = ia_1$. According to the Property 2 and 3, $\beta_{21}, \beta_{31}, B_5$ become purely imaginary numbers, so one can set them as $\beta_{21} = ip_{21}, \beta_{31} = ip_{31}, B_5 = iP_5$, here a_1, p_{21}, p_{31}, P_5 are real numbers. In that way, B_1, B_2, B_3 in Eq. (6.9) can be deduced as follows.

$$\begin{aligned} B_1 &= \beta_{11}(\beta_{25}\beta_{33} - \beta_{23}\beta_{35}) \Rightarrow \text{a real number} \\ B_2 &= \beta_{13}(ip_{21}\beta_{35} - \beta_{25}ip_{31}) = i\beta_{13}(p_{21}\beta_{35} - \beta_{25}p_{31}) = iP_2 \Rightarrow \text{an imag. number} \\ B_3 &= \beta_{15}(\beta_{23}ip_{31} - ip_{21}\beta_{33}) = i\beta_{15}(\beta_{23}p_{31} - p_{21}\beta_{33}) = iP_3 \Rightarrow \text{an imag. number} \end{aligned} \quad (6.11)$$

where, P_2, P_3 are definitely real numbers.

With the new definitions, keeping in mind that $\sin(i\xi a_1 h) = i \sinh(\xi a_1 h)$, $\cos(i\xi a_1 h) = \cosh(\xi a_1 h)$, where $\sinh(\cdot)$ and $\cosh(\cdot)$ is the hyperbolic sine and cosine function, respectively, $\mathcal{D}_a(v, \xi)$ defined in Eq. (6.8) can be deduced as follows.

$$\begin{aligned} \mathcal{D}_a(v, \xi) &= - [B_1 \sinh(\xi a_1 h) \cos(\xi \alpha_3 h) \cos(\xi \alpha_5 h) + P_2 \cosh(\xi a_1 h) \sin(\xi \alpha_3 h) \cos(\xi \alpha_5 h) \\ &\quad + P_3 \cosh(\xi a_1 h) \cos(\xi \alpha_3 h) \sin(\xi \alpha_5 h)] P_5 \Rightarrow \text{a real quantity} \end{aligned} \quad (6.12)$$

This result reveals that in case 2, the imaginary part is identically vanishing, $\mathcal{D}_a^I(v, \xi) \equiv 0$. Thus, the original complex-valued equation $\mathcal{D}_a(v, \xi) = 0$ now has been converted to $\mathcal{D}_a^R(v, \xi) = 0$, which is a real-valued equation easy to be solved via bisection method.

6.3.1.3 Case 3: only α_1, α_3 are purely imaginary numbers.

In this case, set $\alpha_1 = ia_1, \alpha_3 = ia_3$, meanwhile according to the Property 2 and 3, set $\beta_{21} = ip_{21}, \beta_{31} = ip_{31}, \beta_{23} = ip_{23}, \beta_{33} = ip_{33}, B_5 = iP_5$, where $a_1, a_3, p_{21}, p_{31}, p_{23}, p_{33}, P_5$ are real numbers. With the new substitutions, B_1, B_2, B_3 in Eq. (6.9) can be deduced as follows.

$$\begin{aligned} B_1 &= \beta_{11}(\beta_{25}ip_{33} - ip_{23}\beta_{35}) = i\beta_{11}(\beta_{25}p_{33} - p_{23}\beta_{35}) = iP_1 \Rightarrow \text{an imag. number} \\ B_2 &= \beta_{13}(ip_{21}\beta_{35} - \beta_{25}ip_{31}) = i\beta_{13}(p_{21}\beta_{35} - \beta_{25}p_{31}) = iP_2 \Rightarrow \text{an imag. number} \\ B_3 &= \beta_{15}(ip_{23}ip_{31} - ip_{21}ip_{33}) = \beta_{15}(-p_{23}p_{31} + p_{21}p_{33}) \Rightarrow \text{a real number} \end{aligned} \quad (6.13)$$

where, P_1, P_2 are definitely real numbers.

6.3. DICHOTOMY PROPERTY OF DISPERSION EQUATION OF A SINGLE LAYER PLATE

Substitute Eq. (6.13) into Eq. (6.8) to lead to the following form. Obviously, as with case 1, the solving process should be focused on the imaginary part in case 3, $\mathcal{D}_a^I(v, \xi) = 0$.

$$\begin{aligned} \mathcal{D}_a(v, \xi) = & i[-P_1 \sinh(\xi a_1 h) \cosh(\xi a_3 h) \cos(\xi \alpha_5 h) - P_2 \cosh(\xi a_1 h) \sinh(\xi a_3 h) \cos(\xi \alpha_5 h) \\ & + B_3 \cosh(\xi a_1 h) \cosh(\xi a_3 h) \sin(\xi \alpha_5 h)]P_5 \Rightarrow \text{a purely imag. quantity} \end{aligned} \quad (6.14)$$

6.3.1.4 Case 4: all $\alpha_1, \alpha_3, \alpha_5$ are purely imaginary numbers.

In this case, set $\alpha_1 = ia_1, \alpha_3 = ia_3, \alpha_5 = ia_5$, according to the Property 2 and 3, continuously set $\beta_{21} = ip_{21}, \beta_{31} = ip_{31}, \beta_{23} = ip_{23}, \beta_{33} = ip_{33}, \beta_{25} = ip_{25}, \beta_{35} = ip_{35}, B_5 = iP_5$, where, $a_1, a_3, a_5, p_{21}, p_{31}, p_{23}, p_{33}, p_{25}, p_{35}, P_5$ are real numbers. Substitute these new settings into Eq. (6.9) to deduce as follows.

$$\begin{aligned} B_1 &= \beta_{11}(ip_{25}ip_{33} - ip_{23}ip_{35}) = \beta_{11}(-p_{25}p_{33} + p_{23}p_{35}) \Rightarrow \text{a real number} \\ B_2 &= \beta_{13}(ip_{21}ip_{35} - ip_{25}ip_{31}) = \beta_{13}(-p_{21}p_{35} + p_{25}p_{31}) \Rightarrow \text{a real number} \\ B_3 &= \beta_{15}(ip_{23}ip_{31} - ip_{21}ip_{33}) = \beta_{15}(-p_{23}p_{31} + p_{21}p_{33}) \Rightarrow \text{a real number} \end{aligned} \quad (6.15)$$

Under the new settings, Eq. (6.8) can be further deduced to Eq. (6.16). Hence, case 4 has the same dichotomy property as with case 2, i.e., the solving process should be focused on the real part, $\mathcal{D}_a^R(v, \xi) = 0$.

$$\begin{aligned} \mathcal{D}_a(v, \xi) = & -[B_1 \sinh(\xi a_1 h) \cosh(\xi a_3 h) \cosh(\xi a_5 h) + B_2 \cosh(\xi a_1 h) \sinh(\xi a_3 h) \cosh(\xi a_5 h) \\ & + B_3 \cosh(\xi a_1 h) \cosh(\xi a_3 h) \sinh(\xi a_5 h)]P_5 \Rightarrow \text{a real quantity} \end{aligned} \quad (6.16)$$

6.3.1.5 Numerical validation of the dichotomy property when sweeping ξ

The chosen structure is a single layer plate with monoclinic type stiffness matrix shown in Eq. (6.17). The mass density is $\rho = 1500 \text{ kg/m}^3$ and the plate thickness is $d = 1 \text{ mm}$. These material properties are cited from [9].

$$\mathbf{C} = \begin{bmatrix} 102.6 & 24.1 & 6.3 & 0 & 0 & 40 \\ & 18.7 & 6.4 & 0 & 0 & 10 \\ & & 13.3 & 0 & 0 & -0.1 \\ & & & 3.8 & 0.9 & 0 \\ \text{sym} & & & & 5.3 & 0 \\ & & & & & 23.6 \end{bmatrix} \text{GPa} \quad (6.17)$$

The absence of $\Delta > 0$ has been checked in the Fig. 2(d) of [9] that shows the three real-valued α^2 roots. With the provided material properties, the three critical velocities can be computed based

6.3. DICHOTOMY PROPERTY OF DISPERSION EQUATION OF A SINGLE LAYER PLATE

on Eq. (6.5), which, therefore, divide the whole domain of phase velocity v into four ranges that correspond to the four cases presented in Table 6.3.

Table 6.3 – The ranges of phase velocity v [m/s] that correspond to the four cases.

Case 1	Case 2	Case 3	Case 4
$0 \leq \alpha_1^2 \leq \alpha_3^2 \leq \alpha_5^2$	$\alpha_1^2 < 0 \leq \alpha_3^2 \leq \alpha_5^2$	$\alpha_1^2 \leq \alpha_3^2 < 0 \leq \alpha_5^2$	$\alpha_1^2 \leq \alpha_3^2 \leq \alpha_5^2 < 0$
[8918.75, $+\infty$)	[2142.25, 8918.75)	[1879.72, 2142.25)	(0, 1879.72)

Analysis of Case 1:

Firstly, we assign a typical phase velocity $v_0 = 9000$ m/s according to Table 6.3, and substitute the specified material parameters into Eq. (3.25) to calculate the polynomial coefficients of Eq. (6.2). Then, the three α^2 roots of the bi-cubic equation, $\mathcal{A}(\alpha^2) = 0$, can be solved via Cardano's Formula, from which the six α roots are finally obtained with the three predominant ones being $\alpha_1 = 0.5667$, $\alpha_3 = 3.2007$, $\alpha_5 = 5.8644$. All the three terms are real numbers, which is in agreement with the precondition of case 1.

Once α_1 , α_3 , α_5 are obtained, all the intermediate parameters can be calculated. Then, the implicit dispersion equation for anti-symmetric modes defined in Eq. (6.7) can be generated, which is a complex-valued equation with respect to ξ at $v_0 = 9000$ m/s due to the existence of the complex exponential terms in matrix $\mathbf{D}_a(v, \xi)$. Thus, the standard solving procedures should handle both real and imaginary parts, represented in Eq. (6.1a). We plot its function curves of real and imaginary parts in Figure 6.4 to intuitively study the distribution of solutions of the equation $\mathcal{D}_a(v_0 = 9000, \xi) = 0$ before solving it via bisection method.

Let us focus on the implicit curve firstly in both subfigures of Figure 6.4. For the real part, its curve is oscillating and chaotic, superficially indicating '*many spurious roots*' in the presented x -axis range. For the imaginary part, its curve is continuous and smooth and the seven zero-points can be clearly recognized as marked by red circles. Comparing the order of magnitude for both curves, the one of real part (10^{-8}) is largely smaller than the one of imaginary part (10^7).

Then, we superimpose the explicit curves to make deep comparison with the implicit curves, where the explicit curves are plotted based on the explicit expression, Eq. (6.10). In the subfigure of imaginary part both curves are totally overlapped because the explicit expression just succeeds from the implicit one. In the subfigure of real part the zero-valued explicit curve reflects the inference of Eq. (6.10) in a

6.3. DICHOTOMY PROPERTY OF DISPERSION EQUATION OF A SINGLE LAYER PLATE

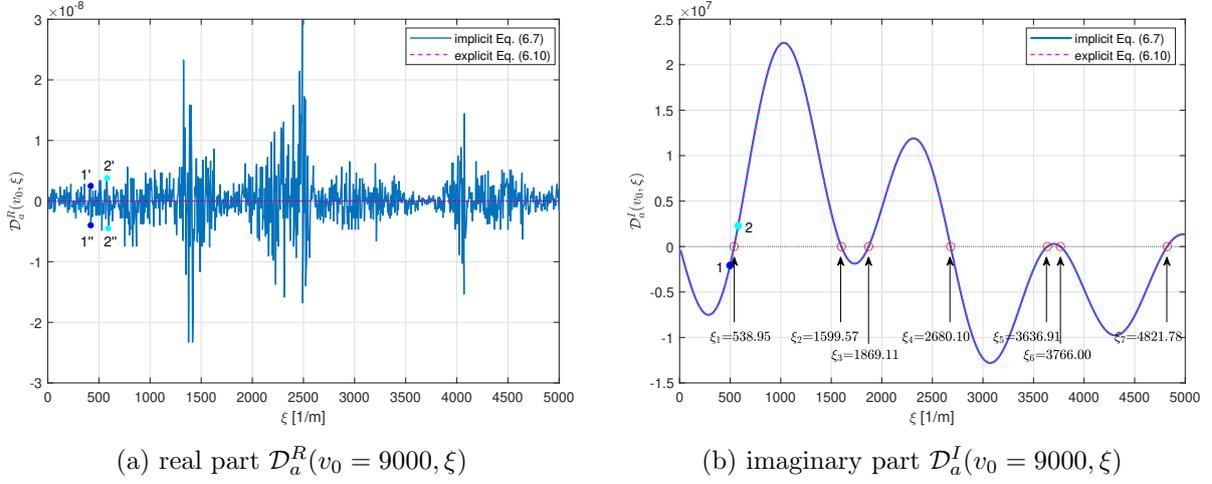


Figure 6.4 – Using bisection method to solve the equation $\mathcal{D}_a(v_0 = 9000, \xi) = 0$.

numerical way. As for the chaotic implicit curve, which should have been totally zero-valued in theory like the explicit curve, the reason lies in the numerical errors, e.g. round-off error or machine epsilon, that is inevitable when performing numerical analysis.

Anyway, the solving process should be focused on the effective part (imaginary part in this case). By sweeping ξ with a small enough step within an interested range, the accurate solutions of ξ can be solved via bisection method as shown in Figure 6.4(b). These solutions correspond to the points of dispersion curves, v versus ξ , of the anti-symmetric modes at $v_0 = 9000$ m/s. The conventional dispersion curves v versus ω can be transformed from v versus ξ through $\omega = \xi v$.

One positive effect of dichotomy property is the ability to overcome the numerical instability issue encountered in [9], which adopts a phase change method¹ to solve the dispersion equation. In the thesis, we exemplify the solution of $\xi_1 = 538.95$ to illustrate our improvement to the phase change method adapted to dichotomy property.

In the implicit curve of Figure 6.4(b), there are two points 1 and 2 around the solution $\xi_1 = 538.95$. We map the two points on the complex plane as schematically shown in Figure 6.5(a). It can be seen that each point may appear at any one of two positions in the complex plane due to the existence of tiny real part, see Figure 6.4(a), caused by numerical error which can be regarded as a random disturbance to the theoretic positions locating on the y -axis in Figure 6.5(a). In practice, no matter

1. In the author's opinion, the phase change method is evolved from the convergence criteria of *Disperse* that checks the included phase angle of the complex-valued dispersion function being greater than 90° for real solutions of dispersion equation [74].

6.3. DICHOTOMY PROPERTY OF DISPERSION EQUATION OF A SINGLE LAYER PLATE

which $1'$ or $1''$ is identified, the phase angle of point 1 is approximately equal to -90° , and the phase angle of point 2 is approximately equal to 90° . In Figure 6.4(b), if moving point 1 to 2 along the curve, there should have a sudden 180° phase change in Figure 6.5(a) when crossing the accurate solution $\xi_1 = 538.95$. Thus, like the bisection method, one can consecutively monitor the occurrence of 180° phase change to search ξ solutions.

Figure 6.5(b) intuitively shows the continuous curves of phase angle changing with ξ . Employing the phase change method, all the ξ solutions can be obtained as shown in this figure, which are the same as the solutions via bisection method marked in Figure 6.4(b).

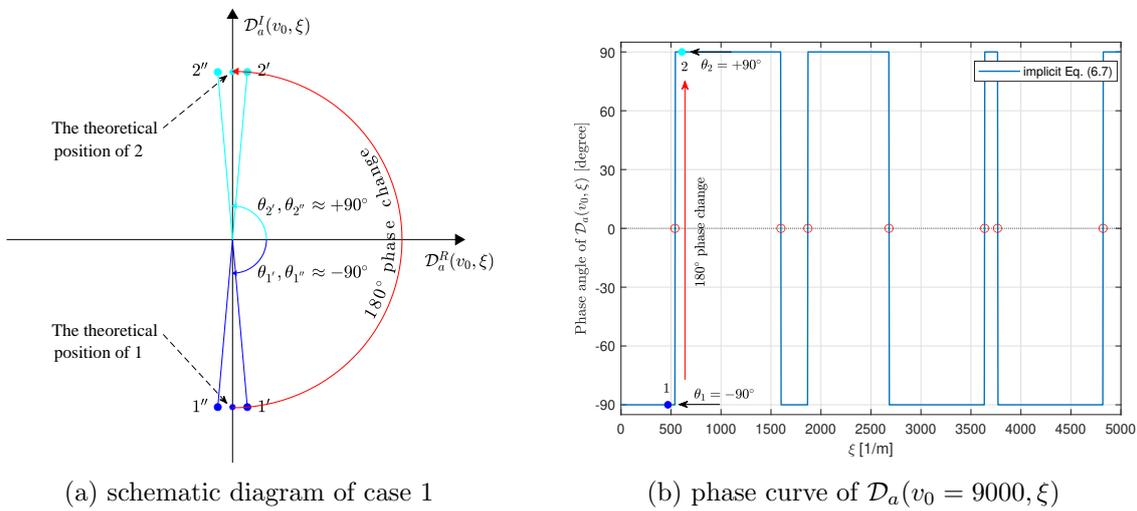


Figure 6.5 – Using phase change method to solve the equation $\mathcal{D}_a(v_0 = 9000, \xi) = 0$.

6.3. DICHOTOMY PROPERTY OF DISPERSION EQUATION OF A SINGLE LAYER PLATE

Analysis of Case 2:

Adopting the previously introduced material properties and assigning a typical phase velocity $v_0 = 5000$ m/s according to Table 6.3, the three predominant α solutions can be easily obtained as $\alpha_1 = 3.6014i$, $\alpha_3 = 1.5933$, $\alpha_5 = 3.0868$. Apparently, only α_1 is a purely imaginary number, which is in agreement with the precondition of case 2. With the solved α_1 , α_3 , α_5 , the implicit Eq. (6.7) and explicit Eq. (6.12) can be illustrated in Figure 6.6, with the real and imaginary part respectively, to intuitively study the distribution of its solutions. As predicted in Eq. (6.12), for case 2, the real part becomes effective whereas due to the existence of numerical error the imaginary part becomes chaotic. Finally, the three solutions of ξ at $v_0 = 5000$ m/s can be solved using bisection method as marked in Figure 6.6(a).

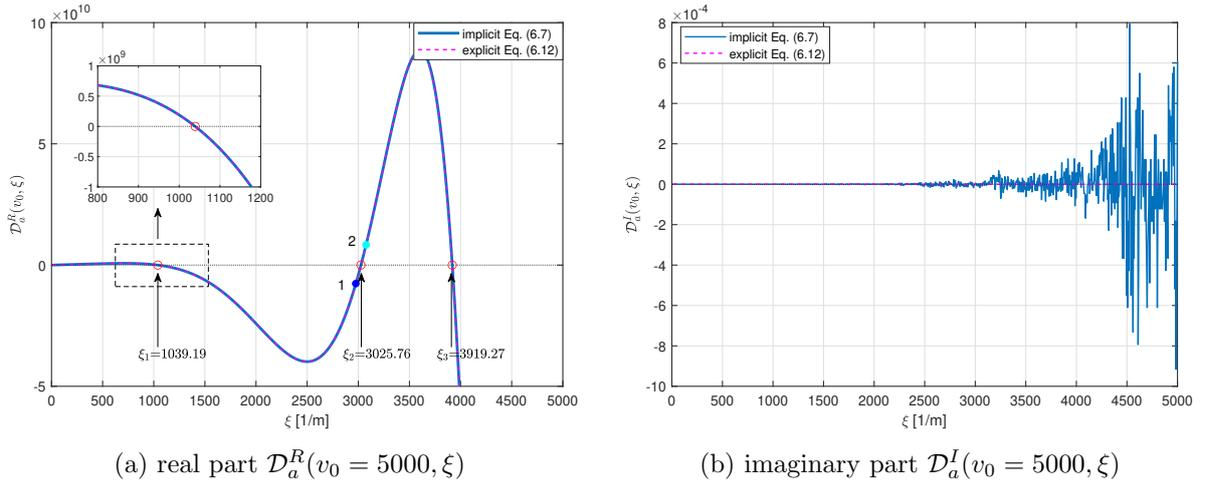


Figure 6.6 – Using bisection method to solve the equation $\mathcal{D}_a(v_0 = 5000, \xi) = 0$.

In case 2, particular attention should be paid to the phase change method due to the existence of tiny imaginary part which will give rise to disorder in the phase angle. We take the solution of $\xi_2 = 3025.76$ as the example to illustrate this issue. Map the two points 1 and 2 in Figure 6.6(a) on the complex plane as schematically shown in Figure 6.7. Like in case 1, each point may appear at any one of two points in the complex plane due to the disturbance of tiny imaginary part. Thus, point 1' and 1'' will be identified as two different phase angles respectively approaching to 180° and -180° , which will further give rise to oscillating in the phase angle curve as illustrated in Figure 6.8(a). If directly applying phase change method to such an disordered curve, instability issue like spurious or loss roots will be faced [9]. Thus, when sweeping ξ to monitor phase change, the spurious phase angle of -180°

6.3. DICHOTOMY PROPERTY OF DISPERSION EQUATION OF A SINGLE LAYER PLATE

should be corrected as 180° firstly, as displayed in Figure 6.8(b). Eventually, with the corrected phase angle curve, the ξ solutions can be obtained via phase change method as indicated in Figure 6.8(b), which are the same as by using bisection method in Figure 6.6(a).

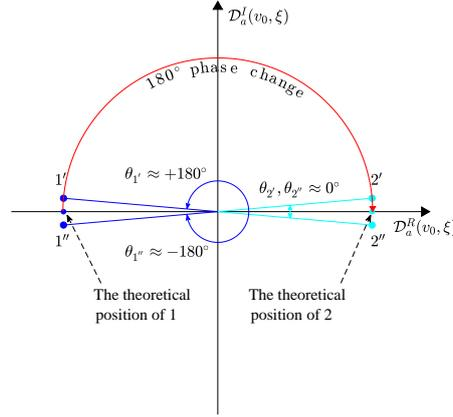


Figure 6.7 – The schematic diagram of phase change method for case 2.

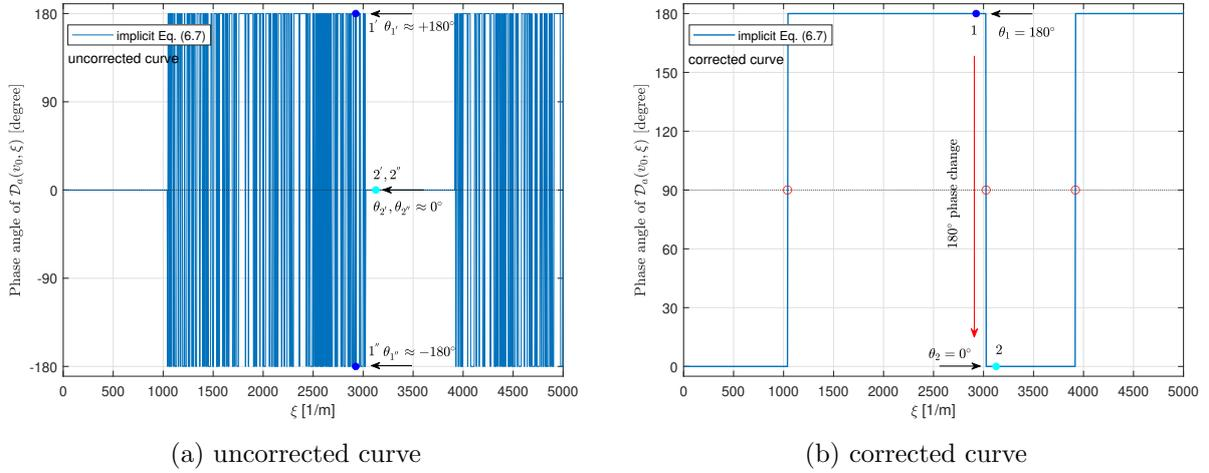


Figure 6.8 – Using phase change method to solve the equation $\mathcal{D}_a(v_0 = 5000, \xi) = 0$.

6.3.2 Dichotomy property of dispersion equation when sweeping v

The efforts made above are related with the dichotomy property when sweeping wavenumber ξ . Alternatively, this property is also owned when sweeping phase velocity v at a fixed ξ_0 but with more complexity, since at a fixed ξ_0 , the process of sweeping v will cross all the four cases of $\alpha_1, \alpha_3, \alpha_5$. However, when sweeping ξ , a single v_0 only leads to an unitary case among the four possible ones. Thanks to the theoretical derivations previously carried out, it is possible to automatically adapt when

6.3. DICHOTOMY PROPERTY OF DISPERSION EQUATION OF A SINGLE LAYER PLATE

sweeping phase velocity. We only take here a numerical example to illustrate the solving process of the dispersion equation $\mathcal{D}_a(v, \xi_0) = 0$ via both bisection and phase change methods which considers the dichotomy property when sweeping phase velocity.

It should be noted that the intermediate parameters, $\alpha_r, V_r, W_r, \beta_{ir}$ ($r = 1, 3, 5; i = 1, 2, 3$) only depend on phase velocity v for the given material parameters. Thus, when sweeping ξ at a fixed v_0 , all evaluations of $\mathcal{D}_a(v_0, \xi)$ at all stagnation steps of ξ share the same intermediate parameters. However, when sweeping v at a fixed ξ_0 , these intermediate parameters should be computed repeatedly at different stagnation steps of v , thus decelerating the sweeping speed. This point will be assessed in Section 6.7.1 by comparing the computational time of the two sweeping schemes.

Figure 6.9 shows the typical function curves of implicit $\mathcal{D}_a(v, \xi_0)$ at $\xi_0 = 1750$ [1/m] in the format of real and imaginary parts as well as phase angle curves. It can be seen that the whole range of v interested is large enough to span all the four cases related with $\alpha_1, \alpha_3, \alpha_5$. Within each case, only the effective part is plotted, and at the boundary of two different cases, there exists a switch between real and imaginary parts, this occurrence is accompanied by a 90° phase change in the phase angle curve. It should be noted that the phase angle curve in case 2 and 4 has been corrected in Figure 6.9, and in case 3 there is no roots. In any case, the curves of real and imaginary parts should be fed to bisection method, or the corrected phase curve should be fed to phase change method, to get the solutions of v as indicated in Figure 6.9.

After comprehensively studying the dichotomy property of dispersion equation for the anti-symmetric modes, we computed its complete dispersion curves as shown in Figure 6.10(a), in which the horizontal and vertical dotted lines highlight the sweeping lines used in the previous paragraphs to exemplify the dichotomy property of different cases. The dichotomy property of symmetric modes, though not presented in this thesis, can be also investigated by following the methodology used for anti-symmetric modes, thus its dispersion curves have been depicted in Figure 6.10(b).

Comparing the two schemes of sweeping ξ and v from Figure 6.10, sweeping ξ will lose many data points in a mode's non-dispersive ranges, like A0 mode in higher wavenumber, S0 mode in lower wavenumber and SH0 mode in the whole range of wavenumber. However, sweeping v will lose data points near to a mode's cutoff wavenumber, like A1 mode near to 500 [1/m]. Therefore, in order to generate the complete dispersion curves, sweeping ξ and v simultaneously then combining both solution sets are necessary. In reference [9], an interpolation method is adopted to reconstruct the

6.3. DICHOTOMY PROPERTY OF DISPERSION EQUATION OF A SINGLE LAYER PLATE

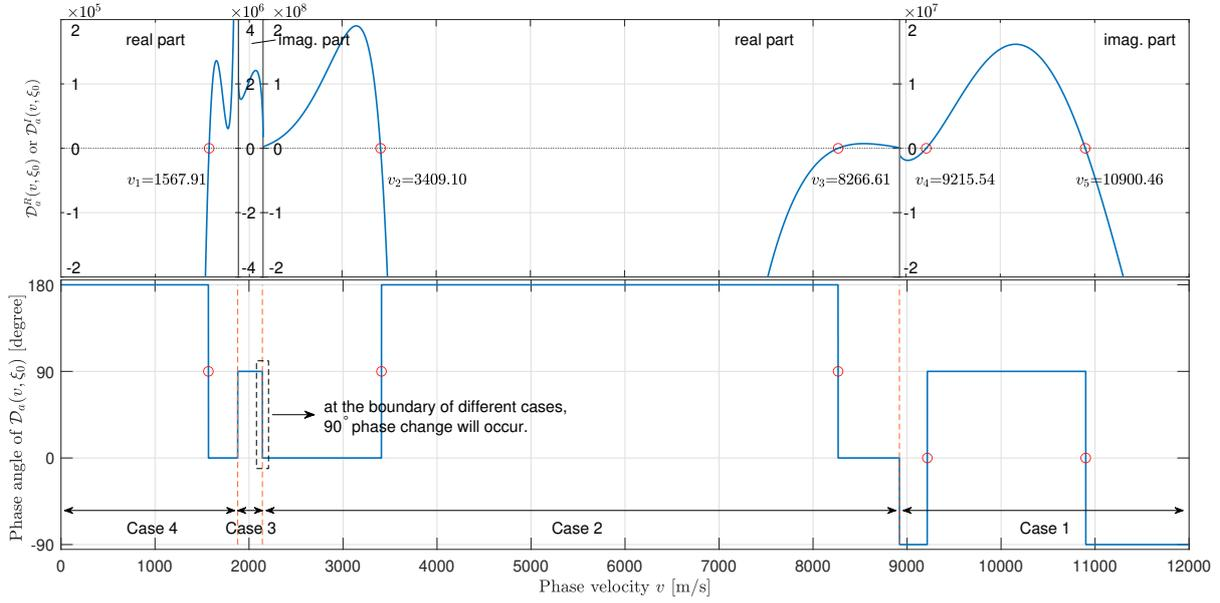


Figure 6.9 – Using bisection and phase change methods to solve the equation $D_a(v, \xi_0 = 1750) = 0$. The small width of case 3 is caused by the degree of anisotropy.

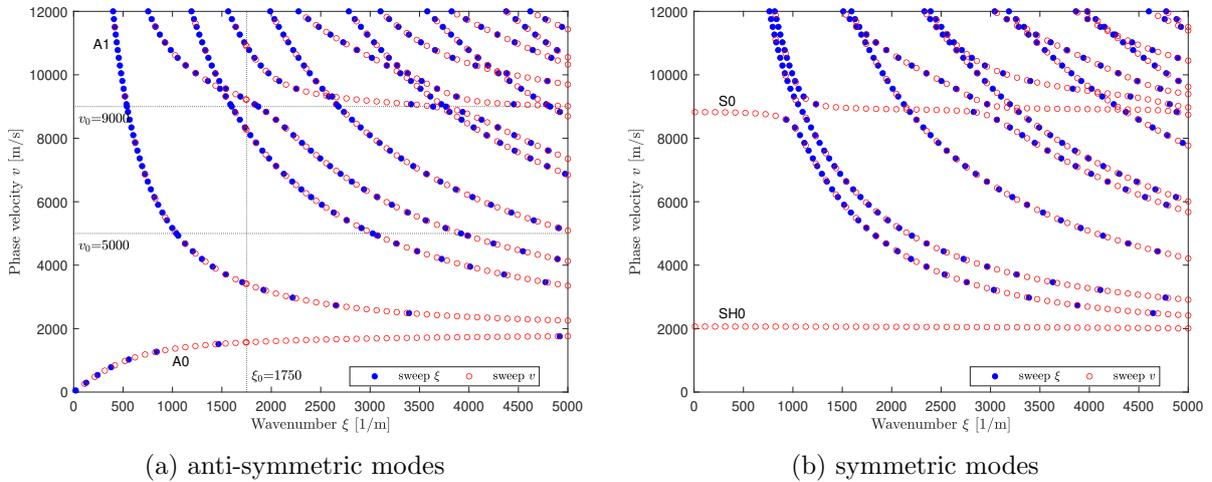


Figure 6.10 – Dispersion curves of the monoclinic lamina.

missing points in the discrete dispersion solutions. This is only valid for lower modes.

6.3.3 Dichotomy property of dispersion equation in $f - \xi$ and $f - v$ domains

The dispersion curves v versus ξ retrieved from the symmetry-ignored dispersion equation $D(v, \xi) = 0$ belong to actually the wavenumber-phase velocity domain. The conventional dispersion curves f versus ξ and v versus f can be retrieved from Eq. (6.18a) and Eq. (6.18b), respectively, through the

6.3. DICHOTOMY PROPERTY OF DISPERSION EQUATION OF A SINGLE LAYER PLATE

relation $f = \xi v / (2\pi)$.

$$\mathfrak{D}(f, \xi) \triangleq \mathcal{D}(2\pi f / \xi, \xi) = 0 \quad \text{frequency-wavenumber domain} \quad (6.18a)$$

$$\mathfrak{d}(v, f) \triangleq \mathcal{D}(v, 2\pi f / v) = 0 \quad \text{frequency-phase velocity domain} \quad (6.18b)$$

The newly generated two dispersion equations $\mathfrak{D}(f, \xi) = 0$ and $\mathfrak{d}(v, f) = 0$ still hold the dichotomy property because they naturally succeed from the equation $\mathcal{D}(v, \xi) = 0$. Thus, bisection and phase change methods can be used to be the solver for the two equations, but the effective part should be identified firstly, and if the real part is the effective one, phase correction measure should be taken to avoid numerical instability issue.

6.3.4 Dichotomy property of evanescent waves

When it comes to evanescent waves, the wavenumber becomes purely imaginary $\xi = i\zeta$ wherein ζ is a real number. In contrast to propagating waves, the energy of evanescent waves is quickly dissipated, as a result, its range of propagation is limited to the near field of source. The evanescent waves have received increasing attention in the recent years due to its high sensitivity to minor defects of composite structures [81, 82].

In this subsection, we prove the dichotomy property of evanescent waves propagating in a single layer plate with monoclinic property, under the condition $\Delta \leq 0$. The derivation directly starts from Eqs. (6.10)(6.12)(6.14)(6.16) which are the explicit expressions showing the dichotomy properties of the propagating waves for the four cases.

Substitution of $\xi = i\zeta$ into Eqs. (6.10)(6.12)(6.14)(6.16) and upon simplification via the identical relations $\sinh(ix) = i\sin(x)$ and $\cosh(ix) = \cos(x)$, the dichotomy property of evanescent waves for the four cases are concluded as follows.

For case 1, all $\alpha_1, \alpha_3, \alpha_5$ are real numbers.

$$\begin{aligned} \mathcal{D}_a(v, i\zeta) = & - [B_1 \sinh(\zeta\alpha_1 h) \cosh(\zeta\alpha_3 h) \cosh(\zeta\alpha_5 h) + B_2 \cosh(\zeta\alpha_1 h) \sinh(\zeta\alpha_3 h) \cosh(\zeta\alpha_5 h) \\ & + B_3 \cosh(\zeta\alpha_1 h) \cosh(\zeta\alpha_3 h) \sinh(\zeta\alpha_5 h)] P_5 = \mathcal{D}_a^R(v, \zeta) \Rightarrow \mathcal{D}_a^I(v, \zeta) \equiv 0 \end{aligned} \quad (6.19)$$

For case 2, only α_1 is a purely imaginary number.

$$\begin{aligned} \mathcal{D}_a(v, i\zeta) = & - i [B_1 \sin(\zeta\alpha_1 h) \cosh(\zeta\alpha_3 h) \cosh(\zeta\alpha_5 h) + P_2 \cos(\zeta\alpha_1 h) \sinh(\zeta\alpha_3 h) \cosh(\zeta\alpha_5 h) \\ & + P_3 \cos(\zeta\alpha_1 h) \cosh(\zeta\alpha_3 h) \sinh(\zeta\alpha_5 h)] P_5 = i\mathcal{D}_a^I(v, \zeta) \Rightarrow \mathcal{D}_a^R(v, \zeta) \equiv 0 \end{aligned} \quad (6.20)$$

6.4. DICHOTOMY PROPERTY OF DISPERSION EQUATION OF A MULTI-LAYERED PLATE

For case 3, only α_1, α_3 are purely imaginary numbers.

$$\begin{aligned} \mathcal{D}_a(v, i\zeta) = & [P_1 \sin(\zeta a_1 h) \cos(\zeta a_3 h) \cosh(\zeta \alpha_5 h) + P_2 \cos(\zeta a_1 h) \sin(\zeta a_3 h) \cosh(\zeta \alpha_5 h) \\ & - B_3 \cos(\zeta a_1 h) \cos(\zeta a_3 h) \sinh(\zeta \alpha_5 h)] P_5 = \mathcal{D}_a^R(v, \zeta) \Rightarrow \mathcal{D}_a^I(v, \zeta) \equiv 0 \end{aligned} \quad (6.21)$$

For case 4, all $\alpha_1, \alpha_3, \alpha_5$ are purely imaginary numbers.

$$\begin{aligned} \mathcal{D}_a(v, i\zeta) = & -i[B_1 \sin(\zeta a_1 h) \cos(\zeta a_3 h) \cos(\zeta a_5 h) + B_2 \cos(\zeta a_1 h) \sin(\zeta a_3 h) \cos(\zeta a_5 h) \\ & + B_3 \cos(\zeta a_1 h) \cos(\zeta a_3 h) \sin(\zeta a_5 h)] P_5 = i\mathcal{D}_a^I(v, \zeta) \Rightarrow \mathcal{D}_a^R(v, \zeta) \equiv 0 \end{aligned} \quad (6.22)$$

6.4 Dichotomy property of dispersion equation of a multi-layered plate

Chapter 4 and 5 have presented the dispersion equation $\mathcal{D}_X(v, \xi) = 0$ in the context of a multi-layered plate system, where the subscript ‘X’ represents T and G for TMM and GMM, respectively. In the context of a single monoclinic lamina, we have also observed the dichotomy property of $\mathcal{D}_X(v, \xi)$, that is to say, in some ranges of v the real part is identically vanishing, $\mathcal{D}_X^R(v_0, \xi) \equiv 0$, while in other ranges of v , $\mathcal{D}_X^I(v_0, \xi) \equiv 0$. Strictly proving this property for an arbitrary n -layered laminate is not reachable since the explicit expression of $\mathcal{D}_X(v, \xi)$ is no longer available. Furthermore, in extreme conditions, the total number of cases in a general n -layered laminate will be as large as $3n + 1$ given that each layer has three critical velocities according to Eq. (6.5) such that the case by case deduction is no more realizable.

In order not to stuck in intractable mathematical pitfall, we propose a sampling strategy to investigate the dichotomy property of dispersion equation in a numerical way through making qualitative analysis. Inspired by the investigation on the single monoclinic lamina, the dichotomy property of dispersion equation in the context of laminate stems from the property of the intermediate parameters of each layer, which is actually controlled by the common phase velocity v once each layer’s material properties are given. Thus, no matter what value the fixed v_0 is, the implicit function $\mathcal{D}_X(v_0, \xi)$ defined in Eq. (4.39) for TMM and Eq. (5.7) for GMM with ξ being the argument can be divided into real part $\mathcal{D}_X^R(v_0, \xi)$ and imaginary part $\mathcal{D}_X^I(v_0, \xi)$, no matter which part being the vanished one, it will not be totally zero in practice due to numerical error. However, we can uniformly sample m points for the two functions within the interested range $[\xi_{\min}, \xi_{\max}]$, and find the maximum absolute function value from these sampling points for each part.

$$M^R = \max_{1 \leq i \leq m} |\mathcal{D}_X^R(v_0, \xi_i)|, \quad M^I = \max_{1 \leq i \leq m} |\mathcal{D}_X^I(v_0, \xi_i)| \quad \text{for } \xi_i \in [\xi_{\min}, \xi_{\max}] \quad (6.23)$$

6.5 Overcoming common numerical issues using dichotomy property

After studying the dichotomy property, some numerical issues frequently reported in literature can be overcome with the help of dichotomy property. Two typical issues are the instability of the phase change method and the instability of TMM.

6.5.1 Overcoming numerical instability of the phase change method

In [9] numerical instabilities were encountered when generating the dispersion curves of a 50-layered orthotropic laminate via GMM, see Figure 6.12(b). This laminate has a special layup $[0]_{50}$, i.e. each layer orients at the same fiber direction. The authors of [9] alleged that the numerical instabilities were caused by the large number of layers under study, and the maximum ability of their method to compute a laminate must be no more than 13 layers in order to obtain satisfying results for GMM.

In this section, we recompute the dispersion curves of this laminate by using the same GMM but corrected phase change method (CPCM), as shown in Figure 6.12(a). The adopted material properties can be referred from [9, 73]. Figure 6.12(a) shows that our results do not suffer from instability issue anymore. The reason is that when solving dispersion equation built with GMM via phase change method, at the region of missing roots in Figure 6.12(b), phase correction measure should be taken. The comparison between the original phase change method and the corrected phase change method is conducted in Figure 6.13. It shows that the chaos uncorrected phase curve leads to the missing roots in Figure 6.12(b). In contrast, the corrected phase curve clearly shows the locations of solutions at each step of the corrected phase curve. Thus, by applying phase correction measure, the instability issue is just addressed.

6.5.2 Overcoming numerical instability of TMM

TMM usually suffers from instability issue known as the so-called *large fd problem* which refers to the unstable solutions at a large product value of frequency f and plate thickness d . One typical example citing from [42] is plotted on Figure 6.14(b) for illustration, in the frequency-wavenumber domain. In this graph, the red curve divides the graph into two parts, with the left part of solutions via TMM and right part via SMM, because either method suffered from instability in its opposite part as explained in [42].

6.5. OVERCOMING COMMON NUMERICAL ISSUES USING DICHOTOMY PROPERTY

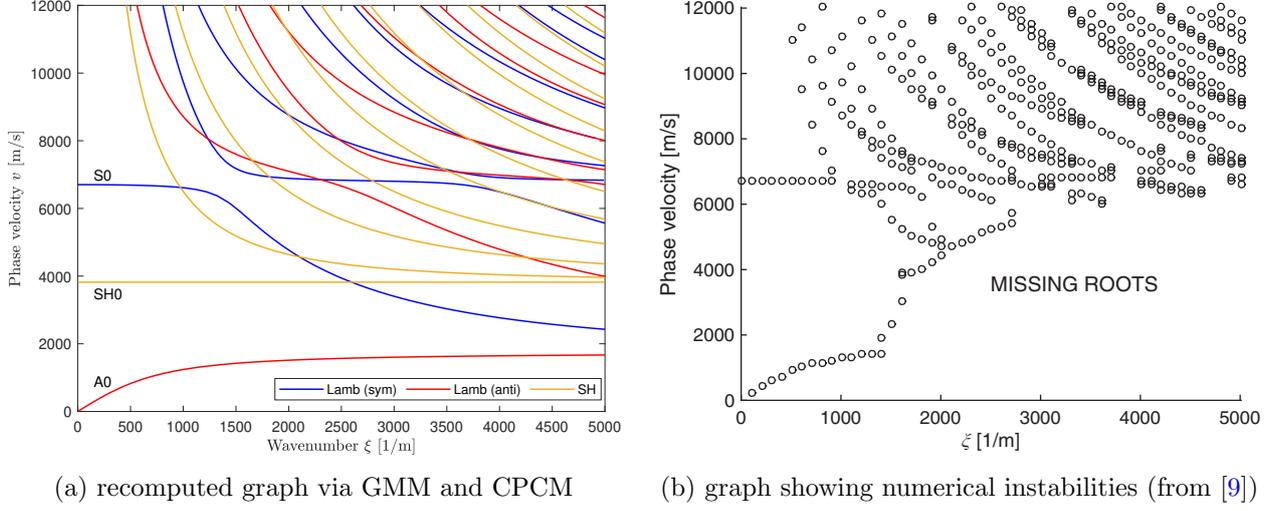


Figure 6.12 – Dispersion curves propagating at 0° for the $[0]_{50}$ unidirectional laminate.

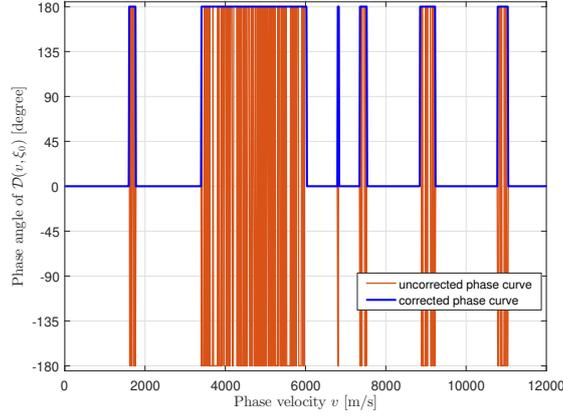


Figure 6.13 – Phase angle curve of $\mathcal{D}_G(v, \xi_0) = 0$ for the $[0]_{50}$ unidirectional laminate.

The presence of $\Delta > 0$ is checked for this material by making the curve of Δ with respect to v as shown in Figure 6.15(a), as long as substituting the corresponding material parameters in [42, 73] into Eq. (3.25) and Eq. (6.3). Figure 6.15(a) shows the presence of $\Delta > 0$ when $v \in (0, v_\Delta)$ where $v_\Delta = 1648.05$ such that $\Delta(v_\Delta) = 0$. For this special case, there is a need to explore whether or not the dichotomy property still holds. Nonetheless, the complexity of this case hinders the theoretical manner on dichotomy property that is used in the enumeration strategy. Thus, making numerical validation is the sensible way. For this purpose, we arbitrarily assign $v_0 = 1000$ that consequently leads to $\Delta = 24.05$ and $\alpha_1^2 = -11.89$, $\alpha_3^2 = -0.69 - 0.20i$, $\alpha_5^2 = -0.69 + 0.20i$. Clearly, α_1^2 is a real number and α_3^2 and α_5^2 are mutually complex-conjugated. Then, the function curve of $\mathcal{D}_a(v_0 = 1000, \xi)$

6.5. OVERCOMING COMMON NUMERICAL ISSUES USING DICHOTOMY PROPERTY

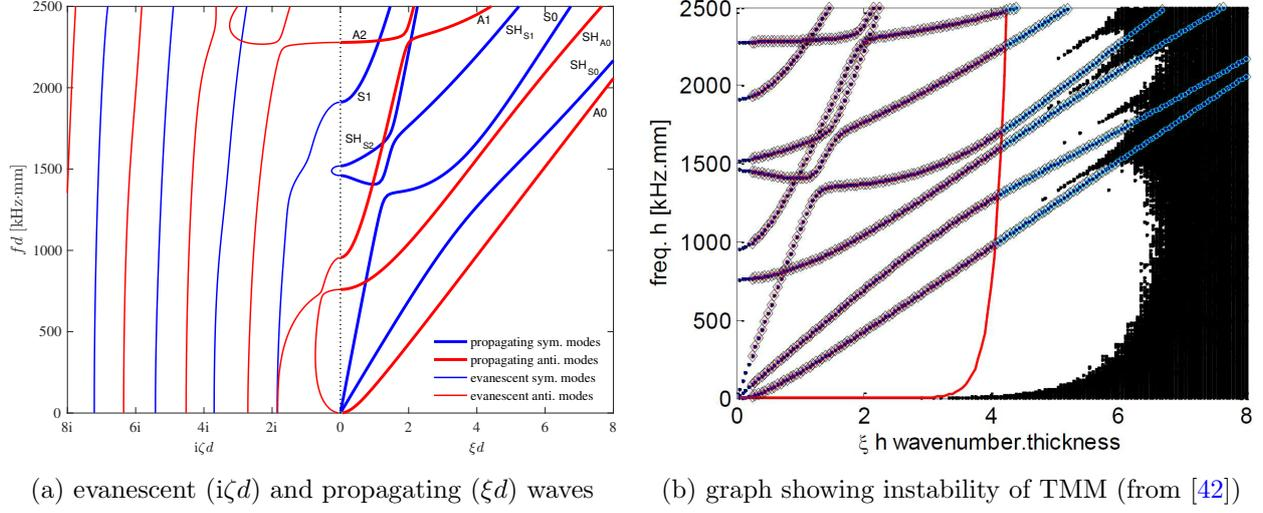


Figure 6.14 – Dispersion curves in frequency-wavenumber domain propagating at 45° of the single-layered unidirectional composite plate.

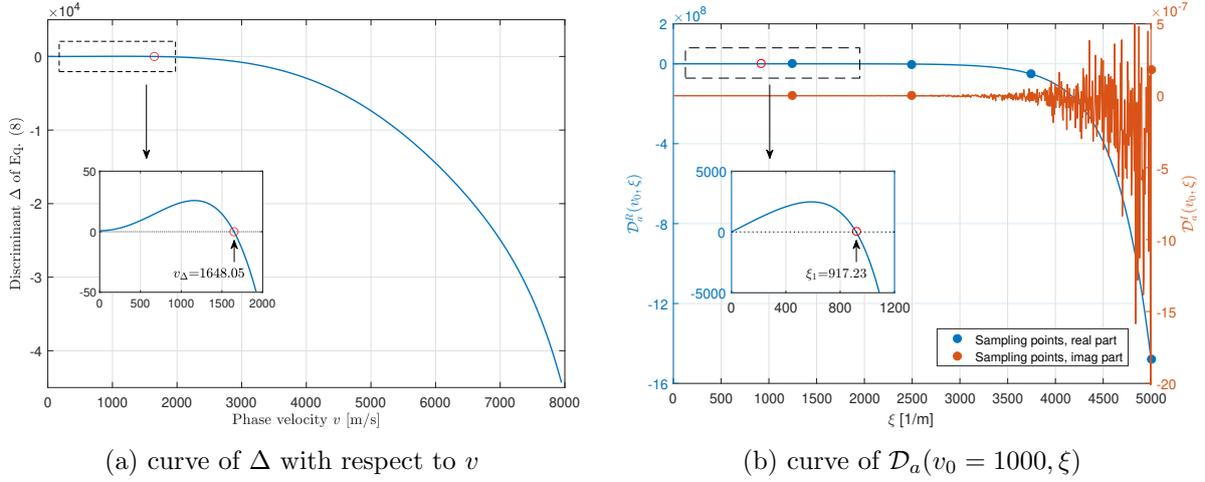


Figure 6.15 – Dichotomy property of dispersion equation at $v_0 = 1000$ m/s that invokes $\Delta > 0$.

can be generated in Figure 6.15(b) as real and imaginary part, respectively. This subfigure clearly shows the preservation of dichotomy property in the special case $\Delta > 0$, with the real part effective that is identified automatically through the sampling strategy formalized in Eq. (6.23).

The frequency-wavenumber domain dispersion equation, Eq. (6.18a), is employed to recompute the dispersion curves of this plate as delineated in Figure 6.14(a) lying in the right part being the propagating waves. It can be seen that the instability issue does not occur in our computation, thus proving the stability and robustness of our method that accounts for the dichotomy property.

The curves of evanescent waves shown in Figure 6.14(a) lying in the left part are retrieved by considering the dichotomy property of evanescent waves which has been proved in Section 6.3.4. It can be seen that the evanescent waves connect with the propagating waves at zero wavenumber. Furthermore, some evanescent modes connect two different propagating modes possessing the same symmetry. For example, the first anti-symmetric evanescent mode connects the propagating A0 and SH_{A0} modes, and the first symmetric evanescent mode connect the propagating SH_{S1} and SH_{S2} modes. This phenomenon has also been observed in [82] but via semi-analytical finite element (SAFE) method for most of non-isotropic materials. Our theoretical analysis on the unidirectional composite plate contribute a plus to the theory of guided waves propagation in composite materials.

Finally, the emphasis should be placed on the multi-layered composite laminate in terms of the dispersion equation of evanescent waves built by GMM, which possesses the dichotomy property as well. Thus, as the analysis for propagating waves in a laminate, the sampling strategy should be a simple and efficient tool to retrieve the dispersion curves of the evanescent waves.

6.6 Exploring the *large fd problem* of TMM using dichotomy property

In Figure 5.1(a), TMM suffers from the *large fd problem*. In this section, we adopt the methodology of studying dichotomy property to investigate this problem. The function curve of $\mathcal{D}_X(v_0, \xi) = 0$ at $v_0 = 1000$ m/s are presented in Figure 6.16 for both TMM and GMM. From Figure 6.16(a)(b), both the real and imaginary parts of TMM become disordered and heavily oscillating in the high frequency range, which produces many spurious roots in the high frequency range of Figure 5.1(a). In other words, there is no effective part for TMM at $v_0 = 1000$ m/s. However, for GMM, the effective part (imaginary part in this case) is still observable. The unique root can be obtained from the effective part of GMM via bisection method.

The true reason of causing the *large fd problem* of TMM lies in the fact that the monodromy transfer matrix, \mathbf{T}^{mono} defined in Eq. (4.34), has a poor condition number. To illustrate this, the condition number of the monodromy transfer matrix and global matrix are presented in Figure 6.17. It can be seen that for GMM, poor condition occurs only at the unique root location, but for TMM, poor condition occurs in high frequency range. Thus, TMM usually suffers from the *large fd problem* at higher frequency range.

6.6. EXPLORING THE *LARGE FD PROBLEM* OF TMM USING DICHOTOMY PROPERTY

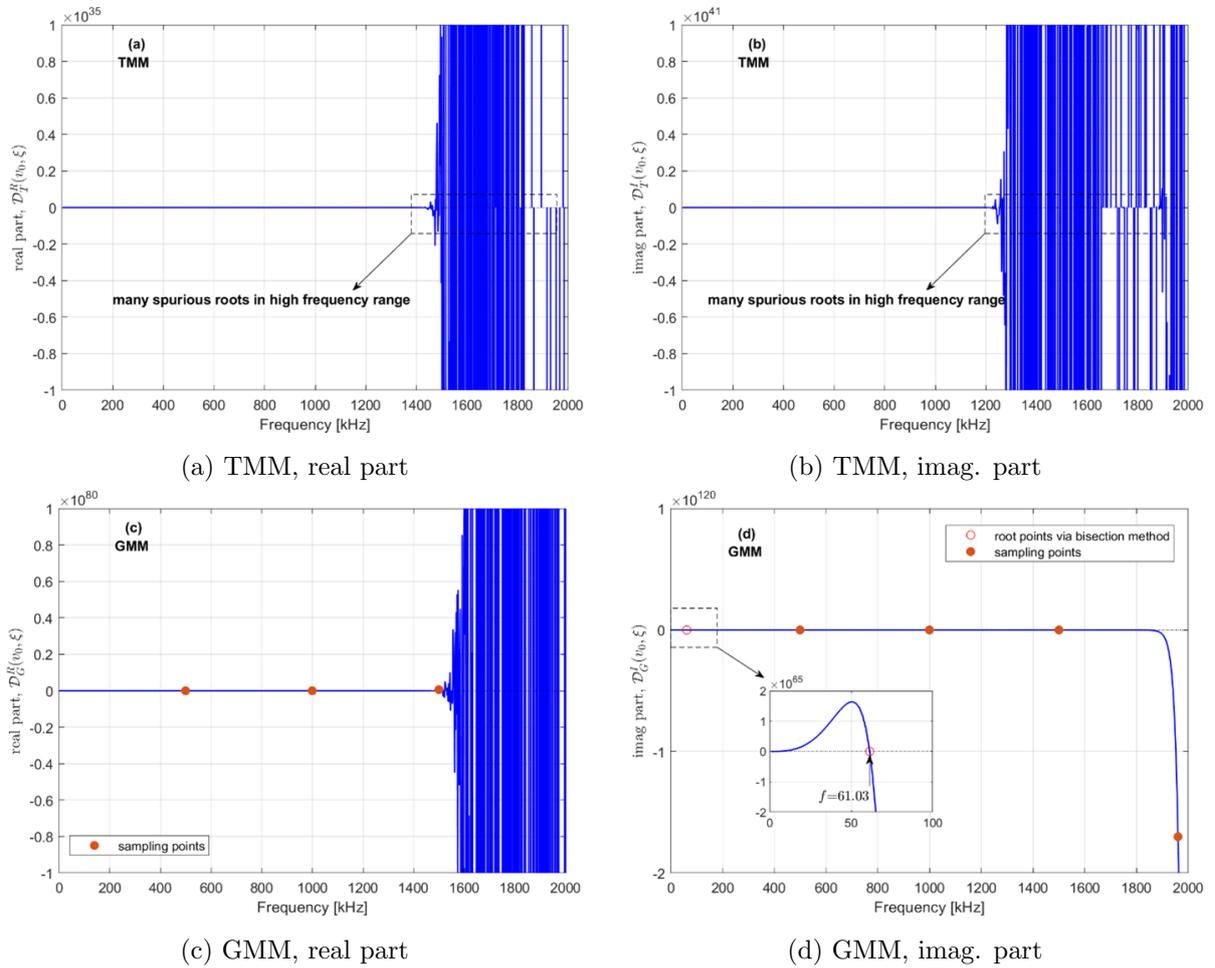


Figure 6.16 – Function curves of $\mathcal{D}_X(v_0, \xi) = 0$ at $v_0 = 1000$ m/s of the Open Guided Waves.

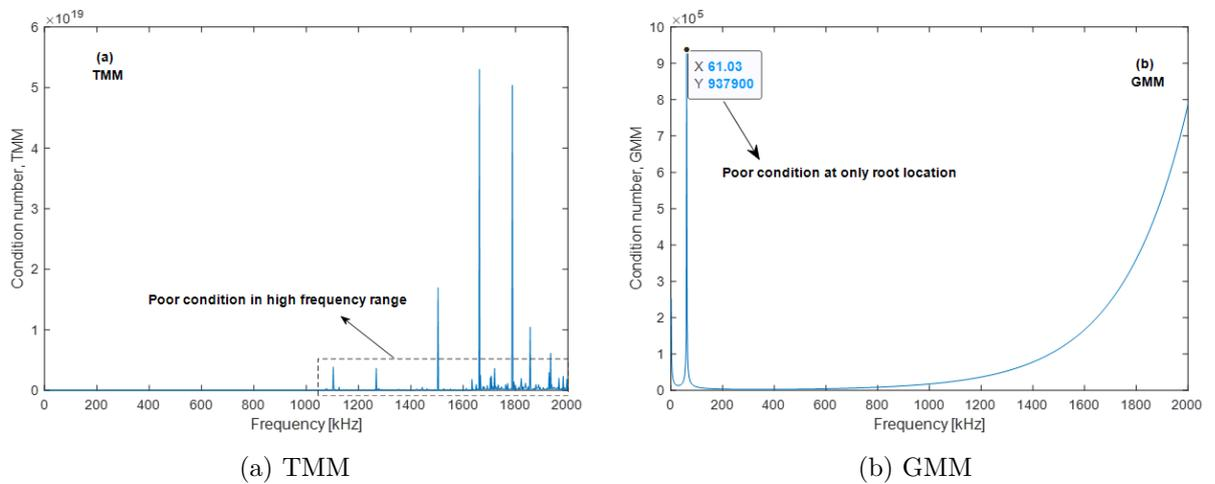


Figure 6.17 – The condition number of matrices of the Open Guided Waves at $v_0 = 1000$ m/s for (a) the monodromy transfer matrix \mathbf{T}^{mono} and (b) the global matrix \mathbf{D}_G .

6.7. DISCUSSION

After we recomputed the dispersion curves of composite structures in some classical references, which pertained to studying various computational models of dispersion curves of composite materials, a list that summarizes the presence or absence of *large fd problem* of TMM has been made in Table 6.4. This table demonstrates that TMM does not always encounter the *large fd problem*. It is application dependent.

Table 6.4 – The presence or absence of *large fd problem* of TMM in classical references.

Reference number	Structure name, stacking angles, data source in the cited reference, with (+) or without (-) <i>large fd problem</i>
[12]	Cross ply laminate, $[(0/90)_s]_2$, Table 15.1, (+)
[12]	Quasi-isotropic laminate, $[(0/45/90/-45)_s]_2$, Table 15.1, (+)
[62]	SHM plate, $[45/0/-45/90/-45/0/45/90]_s$, Table 4, (+) ¹
[37]	Specimen I, $[+45_6/-45_6]_s$, Table 1, (+)
[37]	Specimen II, $[+45/-45/0/90]_s$, Table 1, (-)
[8]	Carbon-fiber epoxy composite, $[0/90/+45/-45]_s$, Table 2, (+)
[8]	GLARE 3-3/4, $[Al/0/90/Al/90/0/Al]$, Table 2, (-)
[38]	Composite-metal plate, $[0/Al]$, Section 3.1, (+)
[78]	Sandwich plate with HD PVC foam core, $[90/PVC/90]$, Table 1, (-)
[9]	Quasi-isotropic laminate, $[+45/-45/0/90]_s$, Eq. (32), (-)
[9]	Fiber metal laminate, $[0/0]_s$, Eqs. (19)(29), (-)

¹ This item is used to generate Figures 6.16 and 6.17.

Note: the tested frequency range is up to 2000 kHz that is the highest frequency commonly used for guided waves-based structural health monitoring techniques.

6.7 Discussion

6.7.1 Comparison of computational efficiencies of two sweeping schemes

In this section, we compare the computational efficiencies of the two sweeping schemes for solving dispersion equation, i.e. fixing $v = v_0$ to sweep ξ roots and fixing $\xi = \xi_0$ to sweep v roots by using two solving methods (bisection and phase change methods). The tested structure is the 50-layered plate in Section 6.5.1. Both serial and parallel³ computing techniques are applied to the standard GMM. Computations were performed in MATLAB R2016a hosted on a Dell Precision T3500 workstation with the processor Intel Xeon W3530@2.8GHz, 4 CPU cores, 18G RAM. Computing range is shown

3. Parallel computing technique is introduced in Section 5.3.3.

in Figure 6.12. Bi-directional sweeping scheme is used. In each direction, the sweeping line is equally offsetted 100 times from the minimum to the maximum, and the precision of solutions is set to be the fifth decimal place. The sweeping step length of phase velocity and wavenumber is 10 m/s and 10 [1/m], respectively. Each solving method runs 10 times and the averaged computational time is listed in Table 6.5.

Table 6.5 – The computational time of the 50-layered plate (unit: seconds).

Bisection method			Phase change method		
sweep v	sweep ξ	sum	sweep v	sweep ξ	sum
6437 ^s	3052 ^s	9489 ^s	6729 ^s	3071 ^s	9800 ^s
2284 ^P	1058 ^P	3342 ^P	2338 ^P	1052 ^P	3390 ^P

^s Serial computing technique is applied.

^P Parallel computing technique is applied.

Table 6.5 shows that sweeping v costs more time than sweeping ξ irrespective of the serial or parallel computing technique. The explanations to them are given in Section 6.3.2. Additionally, the speed-up ratio of the computational time between parallel and serial computing technique is as large as 2.8 for a computer with four CPU cores, which is desired. Finally, the computational time of CPCM is slightly greater than the counterpart of bisection method, which is due to the phase correction operation. The comparison result of Table 6.5 validates Figure 6.11(b).

6.7.2 Generalization of dichotomy property in other material classes

The methodology developed in this chapter can be also applied to other material classes like triclinic material, which is full anisotropy having 21 independent stiffness coefficients, and piezoelectric material, whose dispersion equations are more complex than composite materials. After investigation for a certain material, if dichotomy property does not present in it, both the real and imaginary parts of dispersion function are effective in this case such that the true roots of the dispersion equation are the intersected roots of real and imaginary parts, i.e. Eq. (6.1a) should be applied. An example of this case for a triclinic material⁴ is illustrated in Figure 6.18(a).⁵ However, for this case, phase change method is still applicable without need to take phase correction measure because phase angle changes smoothly with searching variable as illustrated in Figure 6.18(b).

4. The dispersion equation of a single layer plate with triclinic material is presented in Section 3.2.

5. The used material properties can be referred from [73, 45].

6.8. CONCLUSION

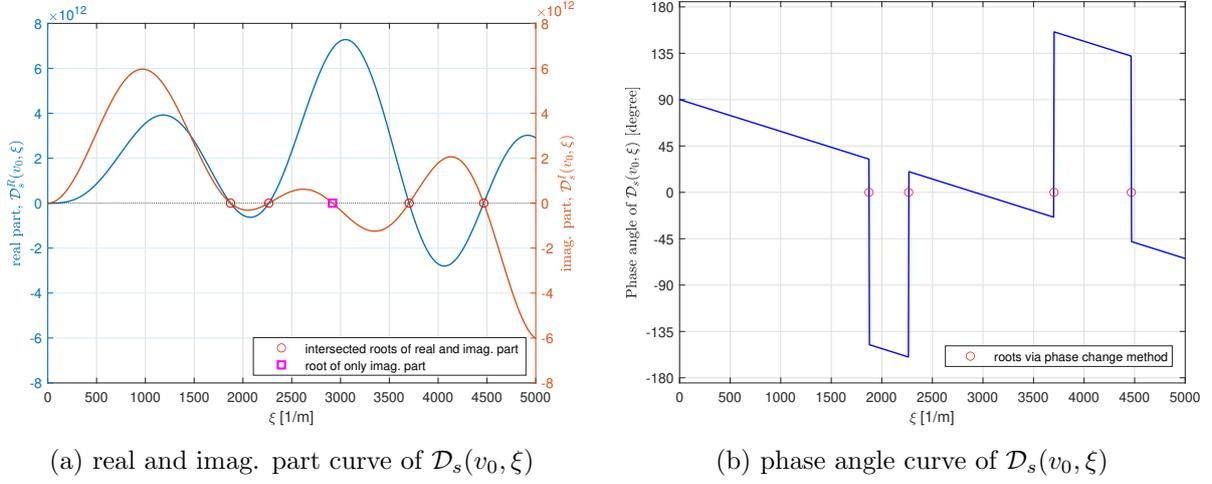


Figure 6.18 – Function curve of the symmetric modes of dispersion equation $\mathcal{D}_s(v_0, \xi)$ for a triclinic material at $v_0 = 4000$ m/s.

6.8 Conclusion

The dispersion equation of guided waves propagating in elastic composite plates are not a completely complex-valued equation, and it presents the dichotomy property of being either a real- or purely imaginary-valued equation. This property is strictly investigated firstly for a single-layered monoclinic lamina in the case $\Delta \leq 0$ by using the enumeration strategy, showing that there exists four cases for $\alpha_1, \alpha_3, \alpha_5$ depending on their properties of being real or purely imaginary number. The three parameters will lead to two mutually-exclusive effective parts, real and imaginary parts of the dispersion equation. Bisection and phase change methods are two efficient ways to solve the dispersion equations, but if the real part becomes to be effective one, phase correction measure should be taken toward to the phase change method in order to overcome some numerical instability issues.

The dichotomy property is further extended to a general multi-layered composite laminate through the proposed sampling strategy under the framework of GMM and TMM, but it is still applicable to SMM. The enumeration strategy and sampling strategy reflect the know-why and know-how aspects of the dichotomy property, respectively. Although this chapter comprehensively studies the dichotomy property of dispersion equation in wavenumber-phase velocity domain, the counterparts in frequency-wavenumber and frequency-phase velocity domain still hold this property, as well as in the case of evanescent wave modes. Thus, this property has formed a closure characteristic on itself in mathematical sense as long as the damping effect is not involved.

6.8. CONCLUSION

Chapter 7

Prediction of frequency and spatially dependent attenuation of guided waves propagating in anisotropic viscoelastic composite laminates

The industrial application of guided waves-based structural health monitoring techniques is highly tributary of the number and placement of the active sensor elements. Yet, the optimal sensorization of a structure relies on the decrease in amplitude of guided waves over propagation distance. A reliable prediction of amplitude attenuation of guided waves is still a challenge especially for anisotropic viscoelastic composite materials which exhibits complex changes of attenuation with propagation direction, and thus a spatial dependency of attenuation. In Chapter 5, GMM is applied to the pure elastic case. In this chapter, the damped global matrix method (dGMM), having stable and efficient merits, is developed to predict the frequency and spatially dependent attenuation of waves propagating in anisotropic viscoelastic composite materials. dGMM integrates three damping models (Hysteretic, Kelvin-Voigt and Biot models) into the conventional undamped GMM of Chapter 5 to consider viscoelasticity of composite laminates. The proposed dGMM is presented and then validated by numerical comparison with the semi-analytical finite element method. Besides, two industrial case studies, parts of an A380 nacelle at scale one, are employed to experimentally validate the proposed attenuation prediction method. The first one is a fan cowl structure and the second one an inner fixed structure, both either unmounted or mounted on an actual instrumented A380 plane. This makes the validation works extremely valuable for both the scientific and industrial communities. The proposed attenua-

tion prediction method thus paves the way to optimally deploy sensor network for SHM of anisotropic viscoelastic composite structures.

A manuscript related to this chapter has been submitted to the journal *Structural Health Monitoring* for peer review.

7.1 Background of guided waves attenuation

When adopting guided waves as an inspection tool for composite structures, the attenuation property of these waves is an essential aspect that should be considered carefully in addition to dispersion property [21]. This is especially true for carbon fiber reinforced composites as such materials possess inherent viscoelasticity that causes attenuation and thus impacts significantly the sensor network deployment in terms of sensor geometry, installation, number, and position [83, 84]. In comparison with the network used for lightly damped structures, a larger sensor network (i.e. having a larger number of sensors) is required to cover highly damped structures with enough wave amplitudes [85, 86]. Furthermore, attenuation property plays an important role in amplitude-based damage identification methods [87] and machine learning tools for modeling guided waves [88].

Over the past decades, studies related to attenuation are mainly focused on numerical computations and experimental measurements. In composite structures, materials viscoelastic damping, usually characterized by Hysteretic (HR) or Kelvin-Voigt (KV) damping models, is the primary factor that causes attenuation [89, 90]. The Rayleigh damping model is also adopted to investigate the damping effect on wave attenuation [91, 92]. Theoretically, attenuation coefficients of guided waves can be computed from the corresponding dispersion equations (DEs). Thus, considerable efforts have been made to derive accurate or approximated DEs, being complex-valued in the viscoelastic media, and to develop efficient numerical algorithms to solve them. The simplest one is the classical Rayleigh-Lamb equation which represents waves propagation in a homogeneous isotropic viscoelastic plate [75, 93]. The partial wave superposition approach (PWSA) is generally employed to derive the DEs of the single layer anisotropic viscoelastic plate [72, 94]. For the multi-layered system, PWSA is extended to a class of matrix-based methods, e.g. transfer matrix method (TMM) [95] and global matrix method (GMM) [96], which are based on the linear 3D elasticity theory and thus become the standard manner to derive the analytical DEs of this system. However, solving these equations is not

an easy task and it usually requires Lowe's dual-variable root-finding method [6] or Zhu-Qian's 2D Module Ratio Convergence Method (2D MRCM) [75]. Some alternative approaches turn to establish the approximated DEs but are solved by efficient root-searching algorithms such as the Newton-Raphson method and eigenvalue decomposition method. The representatives are the approaches based on Legendre polynomials [97, 98, 99] and higher-order plate theory [100, 101, 102]. Furthermore, discrete numerical methods are widely applied as well to solve the problem of complex wave in multi-layered viscoelastic plates due to their easy implementation. For instance, one can cite the wave finite element method (WFEM) using the Floquet periodicity condition [103, 66], the spectral collocation method (SCM) based on Chebyshev polynomials [44, 80], and the semi-analytical finite element method (SAFE) suitable for arbitrary cross-section waveguides [7, 104, 79]. The common characteristic of these methods lies in that discretization only takes place in the thickness direction of the plate, thus increasing computational efficiency compared to the traditional 3D finite element modeling.

In addition to the numerical approach, attenuation coefficients can be also measured experimentally, but the related works are scarce compared to the abundant theoretical advancements. The simplest approach consists in computing the attenuation rate of wave amplitudes between two sensors in an A-scan experiment [85, 91]. A comprehensive method is to use a curve fitting technique which estimates attenuation by fitting the experimental data of wave amplitudes versus propagation distances, having the merit of considering both geometric spreading and structural damping [89, 105]. Besides, two advanced identification methods are also used, including the matrix pencil method [93] and the estimation of signal parameters via rotational invariance techniques (ESPRIT) [78]. The common characteristic of both methods lies in that they can identify not only the attenuation coefficient but also the propagating wavenumber.

In the aforementioned works, much effort was put to obtain the 3D dispersion curves depending on frequency at a fixed propagation direction [94, 99, 80]. Scarce work was devoted to study the directional property of attenuation especially for practical engineering structures, which has a great significance for sensors network operational deployment in anisotropic composite plates. To this end, this chapter proposes a new method to predict the frequency and spatially dependent attenuation of guided waves propagating in anisotropic viscoelastic composite laminates. Here frequency and spatially means that wave attenuation depends not only on frequency but also on the propagation direction. The proposed method extends the conventional damping free GMM, see Chapter 5, to

7.2. WAVE PROPAGATION THEORY IN THE VISCOELASTIC COMPOSITE LAMINATE

the damping case by incorporating viscoelastic damping models. This method is termed “dGMM” for damped global matrix method. It is supported by a two-step numerical root-solving algorithm, having stable and efficient merits. The proposed dGMM is first validated theoretically by numerical comparison with the SAFE method. Then, through experimentation on two aeronautic composite parts (at scale one) of an Airbus A380 nacelle as shown in Figure 7.1. For each structure, two cases were considered, unmounted and mounted parts on the plane. The two structures are rather different as one is made up of a multi-layered carbon epoxy composite plate with many stiffeners, fan cowl structure (FCS) as shown in Figure 7.1(a), which is 2.20 m high and 5.80 m in half-circumference; and the other one is a sandwich type structure, inner fixed structure (IFS) shown in Figure 7.1(b), with an aluminum alloy honeycomb core and two multi-ply carbon epoxy outer skins, which has a dimension of 2.75 m in height and 3.80 m in half-circumference [3]. It should be emphasized here, that unlike the experiments on small-scale plates [83, 84, 85, 91, 79], the results reported in this chapter are the unique work so far concerning attenuation prediction for practical aeronautic structures, and the most important contribution to the state-of-the-art is that in-service data of the mounted cases of both structures are used to validate the proposed method.

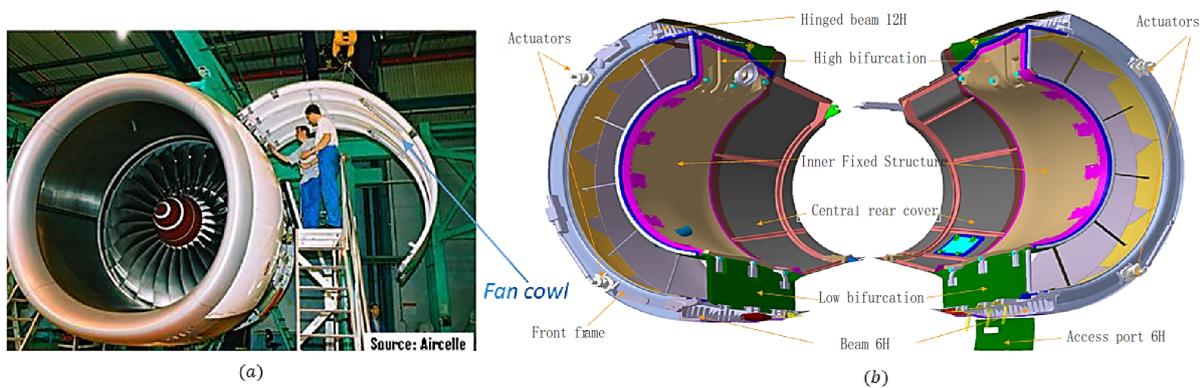


Figure 7.1 – The studied aircraft nacelles of an A380 plane for (a) fan cowl structure and (b) inner fixed structure.

7.2 Wave propagation theory in the viscoelastic composite laminate

The composite laminate model introduced in Chapter 4 are directly duplicated in Figure 7.2 for problem statement. The intrinsic viscoelastic damping properties of composite materials are taken into account in this chapter that cause attenuation of guided waves during propagation. The damping

models adopted in this chapter are first introduced in order to integrate them into the standard GMM for predicting attenuation coefficients.

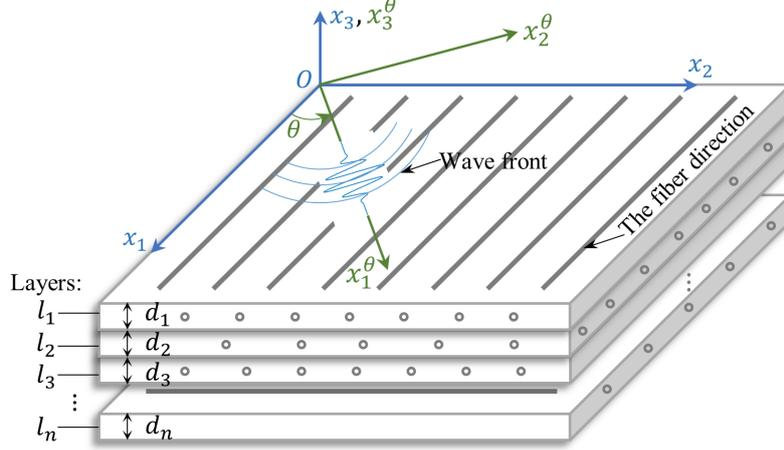


Figure 7.2 – Schematic diagram of a n -layered aeronautic composite laminate.

7.2.1 Viscoelastic damping models of composite materials

The HR and KV models are two common damping models able to describe the viscoelasticity of composite materials [12] as presented in Eqs. (7.1) and (7.2), respectively. For both models, the elastic modulus is considered as a complex number E^* , in which the real part E is the storage modulus and the imaginary part is associated with two factors γ_{HR} and γ_{KV} that are defined as the respective loss factors of the two models. Besides, a less common damping model named Biot (BT) model is presented in Eq. (7.3), which is mainly applied to highly damped aerospace structures [106]. Amongst the three models, HR model generates a complex modulus E^* independent of frequency ω , whereas KV and BT models produce a frequency dependent complex modulus. Thus, the dependency property on ω is attached to E^* for the two models, i.e. $E^*(\omega)$.

$$E^* = E(1 - i\gamma_{HR}) \quad \text{HR model} \quad (7.1)$$

$$E^*(\omega) = E \left(1 - i\gamma_{KV} \frac{\omega}{\omega_0} \right) \quad \text{KV model} \quad (7.2)$$

$$E^*(\omega) = E \left[1 + \frac{2}{\pi} \gamma_{BT} \ln \sqrt{1 + \left(\frac{\omega}{\epsilon} \right)^2} - i \frac{2}{\pi} \gamma_{BT} \arctan \left(\frac{\omega}{\epsilon} \right) \right] \quad \text{BT model} \quad (7.3)$$

7.2. WAVE PROPAGATION THEORY IN THE VISCOELASTIC COMPOSITE LAMINATE

where, i is the unit of the imaginary number, and the superscript ‘*’ denotes that the associated term belongs to the complex number family; ω_c is the characteristic frequency of the KV model characterizing that γ_{KV} is measured at ω_c ; γ_{BT} and ϵ are the loss factor and scaling factor of the BT model, respectively.

For a general layer composing the laminate, e.g. layer l_1 in Figure 7.2, the stiffness matrix of this layer has been introduced in Eq. (2.10) for the pure elastic case, which is characterized by nine independent elastic constants, i.e. three longitudinal moduli E_1 , E_2 , E_3 , and three shear moduli G_{23} , G_{31} , G_{12} , as well as three Poisson’s ratios ν_{12} , ν_{13} , ν_{23} . Since the viscoelastic property of composite materials is considered in this chapter, a given damping model selected among Eqs. (7.1), (7.2) or (7.3) can be applied to the six elastic moduli, thus producing frequency dependent complex moduli [103] $E_1^*(\omega)$, $E_2^*(\omega)$, $E_3^*(\omega)$, $G_{23}^*(\omega)$, $G_{31}^*(\omega)$, $G_{12}^*(\omega)$.¹ In view of this, the usual stiffness matrix \mathbf{C} becomes correspondingly a frequency dependent complex matrix $\mathbf{C}^*(\omega)$ as presented in Eq. (7.4), which shows the orthotropic anisotropy of composite materials.

$$\mathbf{C}^*(\omega) = \begin{bmatrix} 1/E_1^*(\omega) & -\nu_{12}/E_1^*(\omega) & -\nu_{13}/E_1^*(\omega) & 0 & 0 & 0 \\ & 1/E_2^*(\omega) & -\nu_{23}/E_2^*(\omega) & 0 & 0 & 0 \\ & & 1/E_3^*(\omega) & 0 & 0 & 0 \\ & & & 1/G_{23}^*(\omega) & 0 & 0 \\ & \text{sym} & & & 1/G_{31}^*(\omega) & 0 \\ & & & & & 1/G_{12}^*(\omega) \end{bmatrix}^{-1} \quad (7.4)$$

where, the six Poisson’s ratios are real numbers and ν_{21} , ν_{31} , ν_{32} are not independent due to the symmetry of the stiffness matrix.

The stiffness matrix $\mathbf{C}^*(\omega)$ corresponds to each layer’s fiber direction, for instance, the x_1 axis direction in the layer l_1 of Figure 7.2. It should be rotated to the currently focused wave propagation direction that is along the x_1^θ axis as shown in Figure 7.2, which has been introduced in Section 2.3. The rotated stiffness matrix is presented in Eq. (7.5) showing the monoclinic anisotropy of composite

1. For notation homogeneity and for readability purposes, the frequency dependency is also shown for the HR model even if it is by definition frequency-independent.

materials.

$$\mathbf{C}^*(\omega, \theta) = \begin{bmatrix} C_{11}^* & C_{12}^* & C_{13}^* & 0 & 0 & C_{16}^* \\ & C_{22}^* & C_{23}^* & 0 & 0 & C_{26}^* \\ & & C_{33}^* & 0 & 0 & C_{36}^* \\ & & & C_{44}^* & C_{45}^* & 0 \\ & \text{sym} & & & C_{55}^* & 0 \\ & & & & & C_{66}^* \end{bmatrix} \quad (7.5)$$

7.2.2 Damped global matrix method

With the viscoelastic stiffness matrix $\mathbf{C}^*(\omega, \theta)$ in a general layer l_i , the damped global matrix method (dGMM) will be briefly derived by following the steps of the standard GMM to keep the completeness of dGMM. The displacement and stress vectors in a general layer l_i are expressed in compact form in Eqs. (7.6) and (7.7) that represent the superposition of six partial waves derived from 3D elasticity theory in Chapter 3.

$$\mathbf{u}^{l_i} = [u_1, u_2, u_3]^T = \mathbf{U}^{l_i} \mathbf{\Lambda}^{l_i}(x_3) \boldsymbol{\eta}^{l_i} e^{ik(x_1 - vt)} \quad (7.6)$$

$$\boldsymbol{\sigma}^{l_i} = [\sigma_{33}, \sigma_{23}, \sigma_{13}]^T = \boldsymbol{\beta}^{l_i} \mathbf{\Lambda}^{l_i}(x_3) \boldsymbol{\eta}^{l_i} e^{ik(x_1 - vt)} \quad (7.7)$$

where, the superscript " l_i " implies that the associated term belongs to the layer l_i . k is the (complex) wavenumber instead of ξ used in the previous chapters. \mathbf{U}^{l_i} and $\boldsymbol{\beta}^{l_i}$ are the amplitude matrix of displacement and stress, respectively. $\mathbf{\Lambda}^{l_i}(x_3)$ is a diagonal matrix depending on the thickness direction coordinate x_3 . $\boldsymbol{\eta}^{l_i}$ is the partial wave participation vector. They are uniformly defined in Eqs. (7.8)(7.9)(7.10)(7.11).

$$\mathbf{U}^{l_i} = \begin{bmatrix} 1 & 1 & 1 & 1 & 1 & 1 \\ V_1 & V_2 & V_3 & V_4 & V_5 & V_6 \\ W_1 & W_2 & W_3 & W_4 & W_5 & W_6 \end{bmatrix} \quad (7.8)$$

$$\boldsymbol{\beta}^{l_i} = \begin{bmatrix} \beta_{11} & \beta_{12} & \beta_{13} & \beta_{14} & \beta_{15} & \beta_{16} \\ \beta_{21} & \beta_{22} & \beta_{23} & \beta_{24} & \beta_{25} & \beta_{26} \\ \beta_{31} & \beta_{32} & \beta_{33} & \beta_{34} & \beta_{35} & \beta_{36} \end{bmatrix} \quad (7.9)$$

$$\mathbf{\Lambda}^{l_i}(x_3) = \begin{bmatrix} e^{ik\alpha_1 x_3} & & & & & \\ & \ddots & & & & \\ & & & & & \\ & & & & & e^{ik\alpha_6 x_3} \end{bmatrix} \quad (7.10)$$

$$\boldsymbol{\eta}^{l_i} = [\eta_1, \eta_2, \eta_3, \eta_4, \eta_5, \eta_6]^T \quad (7.11)$$

7.2. WAVE PROPAGATION THEORY IN THE VISCOELASTIC COMPOSITE LAMINATE

In Eqs. (7.8)(7.9)(7.10)(7.11), α_j , V_j and W_j with ($j = 1, \dots, 6$) are computed from the (complex) Christoffel equation, Eq. (7.12), i.e. the non-trivial vector $[U, V, W]^T$ requires the singularity of the coefficient matrix in Eq. (7.12), which further leads to a cubic equation in terms of α^2 as presented in Eq. (7.13).

$$\begin{bmatrix} C_{11}^* - \rho v^2 + C_{55}^* \alpha^2 & C_{16}^* + C_{45}^* \alpha^2 & (C_{13}^* + C_{55}^*) \alpha \\ C_{16}^* + C_{45}^* \alpha^2 & C_{66}^* - \rho v^2 + C_{44}^* \alpha^2 & (C_{36}^* + C_{45}^*) \alpha \\ (C_{13}^* + C_{55}^*) \alpha & (C_{36}^* + C_{45}^*) \alpha & C_{55}^* - \rho v^2 + C_{33}^* \alpha^2 \end{bmatrix} \begin{bmatrix} U \\ V \\ W \end{bmatrix} = \begin{bmatrix} 0 \\ 0 \\ 0 \end{bmatrix} \quad (7.12)$$

$$A_6 \alpha^6 + A_4 \alpha^4 + A_2 \alpha^2 + A_0 = 0 \quad (7.13)$$

where, the four polynomial coefficients are presented in Eq. (3.25).

For each solution of α_j in Eq. (7.13), corresponds a pair of solution of V_j , W_j , β_{1j} , β_{2j} , β_{3j} as presented in Eqs. (7.14) and (7.15):

$$\begin{cases} V_j = \frac{(C_{11}^* - \rho v^2 + C_{55}^* \alpha_j^2)(C_{36}^* + C_{45}^*) - (C_{16}^* + C_{45}^* \alpha_j^2)(C_{13}^* + C_{55}^*)}{(C_{13}^* + C_{55}^*)(C_{66}^* - \rho v^2 + C_{44}^* \alpha_j^2) - (C_{16}^* + C_{45}^* \alpha_j^2)(C_{36}^* + C_{45}^*)} \\ W_j = \frac{(C_{11}^* - \rho v^2 + C_{55}^* \alpha_j^2)(C_{36}^* + C_{45}^*) \alpha_j - (C_{16}^* + C_{45}^* \alpha_j^2)(C_{13}^* + C_{55}^*) \alpha_j}{(C_{16}^* + C_{45}^* \alpha_j^2)(C_{55}^* - \rho v^2 + C_{33}^* \alpha_j^2) - (C_{13}^* + C_{55}^*)(C_{36}^* + C_{45}^* \alpha_j^2)} \end{cases} \quad (j = 1, \dots, 6) \quad (7.14)$$

$$\begin{cases} \beta_{1j} = C_{13}^* + C_{36}^* V_j + C_{33}^* \alpha_j W_j \\ \beta_{2j} = C_{45}^* \alpha_j + C_{44}^* \alpha_j V_j + C_{45}^* W_j \\ \beta_{3j} = C_{55}^* \alpha_j + C_{45}^* \alpha_j V_j + C_{55}^* W_j \end{cases} \quad (j = 1, \dots, 6) \quad (7.15)$$

To this step, the displacement and stress vectors in Eqs. (7.6) and (7.7) can be combined to ease the application of the continuity condition at the interface of interlamination. We then have,

$$\mathbf{S}^{l_i} = \begin{bmatrix} \mathbf{u}^{l_i} \\ \boldsymbol{\sigma}^{l_i} \end{bmatrix} = \begin{bmatrix} \mathbf{U}^{l_i} \\ \boldsymbol{\beta}^{l_i} \end{bmatrix} \boldsymbol{\Lambda}^{l_i}(x_3) \boldsymbol{\eta}^{l_i} e^{ik(x_1 - vt)} = \mathbf{Z}^{l_i}(x_3) \boldsymbol{\eta}^{l_i} e^{ik(x_1 - vt)} \quad (7.16)$$

where $\mathbf{Z}^{l_i}(x_3) = \begin{bmatrix} \mathbf{U}^{l_i} \\ \boldsymbol{\beta}^{l_i} \end{bmatrix} \boldsymbol{\Lambda}^{l_i}(x_3)$. At the interface between layers l_i and l_{i+1} , the continuity condition requires that the displacement and stress fields should be continuous, as stated in Eq. (7.17). Besides, the traction-free boundary condition at the two outer surfaces should be satisfied due to the free surface of the plate, as expressed in Eq. (7.18).

$$\mathbf{S}^{l_i}|_{x_3=d_i} = \mathbf{S}^{l_{i+1}}|_{x_3=0} \quad (i = 1, \dots, n-1) \quad (7.17)$$

correlated eigenvectors of the global matrix $\mathbf{G}(\omega, k^*, \theta)$. Finally, the displacement and stress mode shapes of the laminate can be portrayed along the plate thickness direction through Eqs. (7.6) and (7.7).

With the solved dispersion relation between ω and k^* at a specified θ_0 , phase velocity c_p is computed from Eq. (7.21). If the damping effect is slight, i.e. $|k_i| \ll |k_r|$, group velocity c_g can be computed through Eq. (7.22). But for heavily damped structures, the energy velocity c_e defined in Eq. (7.23) should be adopted because in this case, the imaginary part k_i is large enough such that the group velocity computed through Eq. (7.22) is physically meaningless [72, 107].

$$c_p = \frac{\omega}{k_r} \quad (7.21)$$

$$c_g = \frac{\partial \omega}{\partial k_r} \quad (7.22)$$

$$c_e = \frac{\int_0^H \langle P_1 \rangle dx_3}{\int_0^H (\langle E_k \rangle + \langle E_p \rangle) dx_3} \quad (7.23)$$

where, H is the plate's total thickness, $\langle P_1 \rangle$ is the time-averaged Poynting vector along the wave propagation direction, i.e. x_1^θ in Figure 7.2, $\langle E_k \rangle$ and $\langle E_p \rangle$ are the time-averaged kinetic and potential energy density stored in the wave guide. The three terms are defined in Eq. (7.24), in which, the Einstein summation convention is implied for repeated index.

$$\langle P_i \rangle = -\frac{1}{2} \text{Re}\{\sigma_{ij} \bar{u}_j\} \quad (i = 1, 2, 3), \quad \langle E_k \rangle = \frac{1}{4} \text{Re}\{\rho \dot{u}_i \bar{u}_i\}, \quad \langle E_p \rangle = \frac{1}{4} \text{Re}\{\sigma_{ij} \bar{\epsilon}_{ij}\} \quad (7.24)$$

where, $\text{Re}\{\cdot\}$ is the real part operator, \dot{u}_i is the particle velocity of the waveguide along direction x_i^θ ; the overbar “ $\bar{\cdot}$ ” denotes the complex conjugate.

7.2.3 Numerical algorithm of solving the complex DE

The task of solving the complex DE, Eq. (7.20) is extremely complex from mathematical view. Indeed, it is a multivariate transcendental equation given that, at a specified propagation angle θ_0 , for a solution pair (ω, k^*) there are actually three real variables (ω, k_r, k_i) to be identified because of $k^* = k_r + ik_i$. Thus, a certain dimensionality reduction is necessary in order to solve the ternary-variable equation. Note that the complex stiffness matrix $\mathbf{C}^*(\omega)$ is frequency dependent as implied by Eq. (7.4), thus, ω should be considered as another independent variable in addition to θ during

the solving process. Specifically, at a specified propagation angle θ_0 , ω is independently fixed as a constant ω_0 , by doing so, the original quaternary-variable equation $\mathcal{D}(\omega, k_r, k_i, \theta) = 0$ is now transited to a dual-variable equation $\mathcal{D}(k_r, k_i; \omega_0, \theta_0) = 0$. This equation can be solved by applying a dual variable searching method [6]. In the thesis, a recently developed method named 2D MRCM [75] is employed which mathematically transforms the dual-variable root-finding process to search the global minimal modulus of the characteristic function $|\mathcal{D}(k_r, k_i)|$ by checking the module ratio convergence. The interested readers can refer to Zhu's works [75, 94] for more information. To get the full-frequency spectrum of k_r and k_i , the above solving process is repeated by changing ω_0 , which reveals the dispersion property of both quantities. Alternatively, by changing θ_0 , the resulted diagrams are the polar plot of k_r and k_i , which just shows the anisotropic property of guided waves propagating in anisotropic composite laminates, viz. the spatial effect.

It is well known that there are multiple solutions (k_r, k_i) at a stationary pair (ω_0, θ_0) , which represents multiple guided wave modes propagation at the specified frequency ω_0 . 2D MRCM can search all the solutions by scanning the structured grids as long as the step length of scanning element is small enough. Scanning the whole space of interest is required to generate the multi-modal 3D dispersion curves (k_r, k_i, ω) , known as the forward procedure, but is time-consuming. If only a single mode's dispersion curve is desired, e.g. S0 or A0 mode, a single curve tracing technique can accelerate the searching efficiency since tracing the trajectory of a single mode's solution is just a fractional workload of searching the full 3D spectral lines. Besides, in the following inverse procedure of model updating process, the traced single mode's dispersion curve can be immediately contrasted to the counterpart that is experimentally measured, thereof avoiding the branch identification and mode matching problem [52]. To this end, a quadratic extrapolation-based single mode curve tracing technique is developed, as schematically illustrated in Figure 7.3. It is detailed in the following paragraph.

Specifically, for the n th ($n \geq 4$) solution k_n^* of a certain mode to be solved at the specified ω_n , once the previous three solution points $(\omega_{n-1}, k_{n-1}^*)$, $(\omega_{n-2}, k_{n-2}^*)$ and $(\omega_{n-3}, k_{n-3}^*)$ in the curve are known, the initial guess $k_n'^*$ is calculated by extrapolating the three points to ω_n . Then, the accurate solution k_n^* is searched via 2D MRCM in the vicinity of the guess $k_n'^*$. For the first three solution points (ω_1, k_1^*) , (ω_2, k_2^*) and (ω_3, k_3^*) , they are searched via 2D MRCM in the vicinity of the guesses $k_1 + i0$, $k_2 + i0$ and $k_3 + i0$, where k_1 , k_2 , k_3 are the solutions of the real case DE, i.e. undamped case studied in Chapter 6, at frequencies ω_1 , ω_2 , ω_3 , which is an easy task. This strategy is particularly

effective for tracing fundamental modes' curves, i.e. S0, A0 and SH0 modes, since the proximity of the complex case curve to the real case one in $\omega - k_r$ plane guarantees the success of the tracing process, as illustrated in Figure 7.3. It is worth noting that the extrapolation equation $k'_{r,n}$ in Figure 7.3, which is the real part of k_n^* , can be applied to non-constant frequency increment given that the frequency increment obtained from the real case solution may not be equal to the one of complex case.

The above elaboration is now implemented to be a two-step dGMM algorithm of solving the complex DE as presented in Figure 7.4. Step 1 is trivial because it works out the real case DEs through the undamped GMM of Chapter 5. Step 2 is just the realization of the combined dGMM, curve tracing technique and 2D MRCM.

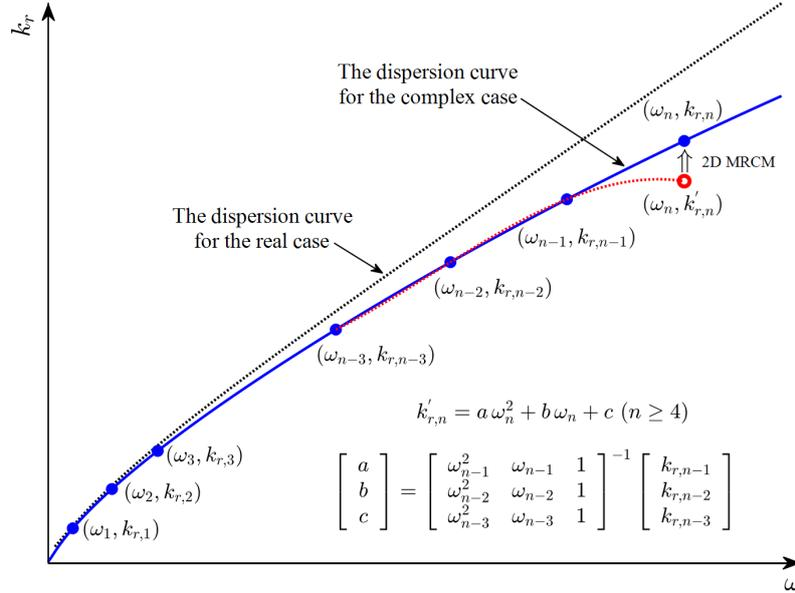


Figure 7.3 – The schematic diagram of the curve tracing technique.

7.3 Data-driven structural parameters estimation

The key to success of predicting attenuation using the developed algorithm in Figure 7.4 relies on the accuracy of the viscoelastic loss factors that are involved in the damping models in Eqs. (7.1), (7.2) and (7.3). These parameters can be obtained from the material manufacturer or from standard mechanical test data [108, 109]. However, in most cases, both ways are not available, especially for in-situ structures which are under service. On the other hand, the acquired guided wave signals from

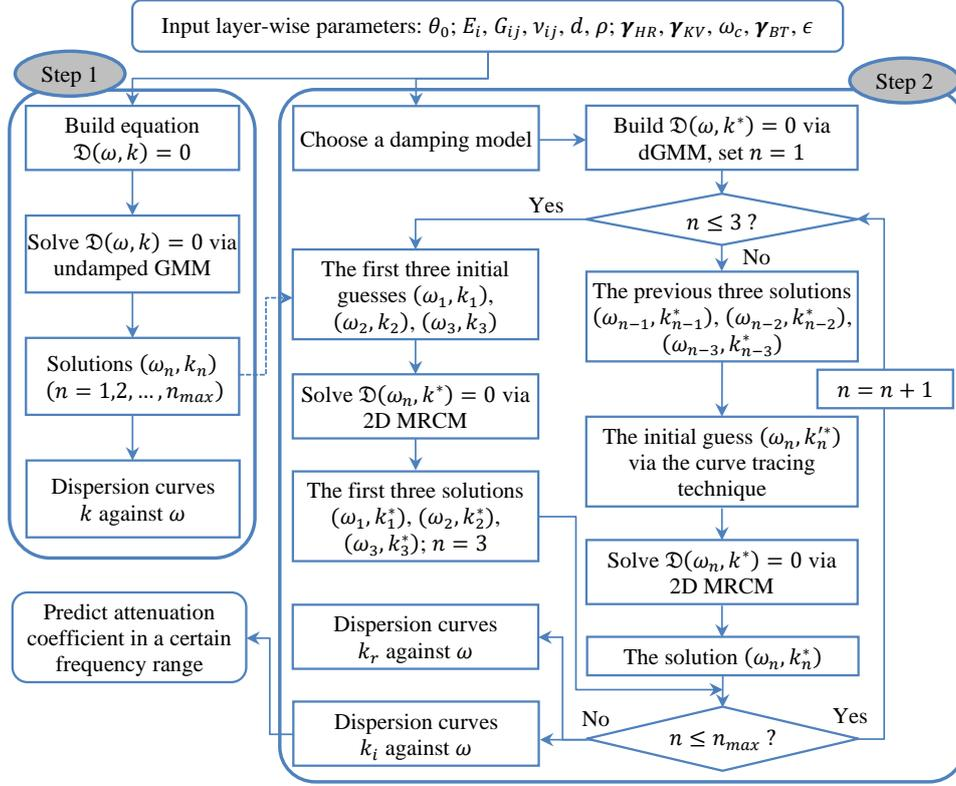


Figure 7.4 – The flowchart of the two-step dGMM algorithm for solving the complex DE.

the installed sensor network contain fruitful information of the monitored structures, including the materials properties of interest. In this chapter, an original model updating procedure is proposed to estimate the material loss factors of damping models, which is an inverse process in contrast with the forward dispersion curves computations based on known material parameters [94, 97].

7.3.1 Identification of attenuation coefficient

For circular-like crested guided waves propagating in composite plates, geometric spreading and material damping are two main factors of wave amplitude attenuation [89]. The former is responsible for the near-field propagation (usually less than three wavelengths) and the latter mainly for far field propagation [89, 110]. In Eq. (7.6), the effect of geometric spreading is not accounted since it is a solution of the plate's free vibration [73], in other words, far field condition is fulfilled. As such, the displacement field of Eq. (7.6) for a general layer l_i can be extended to the whole laminate system, as

expressed in Eq. (7.25).

$$u_i(x_1, x_3, t) = \hat{u}_i(x_3)e^{i(k^*x_1 - \omega t)} \quad (i = 1, 2, 3) \quad (7.25)$$

where, $\hat{u}_i(x_3)$ is the through thickness wave amplitude at the excitation source. Substituting $k^* = k_r + ik_i$ into Eq. (7.25) leads to Eq. (7.26).

$$u_i(x_1, x_3, t) = \hat{u}_i(x_3)e^{-k_ix_1}e^{i(k_rx_1 - \omega t)} \quad (i = 1, 2, 3) \quad (7.26)$$

Comparing the two equations, the wave amplitude decays exponentially over propagation distance x_1 with decaying ratio k_i , which allows to interpret the physical essence of the imaginary part of the complex wavenumber, i.e. being the attenuation coefficient. Besides, Eq. (7.26) also demonstrates that all layers share the same attenuation coefficient³ since the decaying term $e^{-k_ix_1}$ is independent of the thickness direction coordinate x_3 , and it can be measured by the piezoelectric transducers (PZTs) surface mounted on the laminate. Explicitly, making $x_3 = 0$ and taking logarithm for both sides of Eq. (7.26) but omitting the phase term $e^{i(k_rx_1 - \omega t)}$, a linear formulation is yielded in Eq. (7.27).

$$\text{Log}[u_i(x_1, 0)] = -k_ix_1 + \text{Log}[\hat{u}_i(0)] \quad (i = 1, 2, 3) \quad (7.27)$$

where, $u_i(x_1, 0)$ represents the wave packet amplitude recorded by PZT that is surface mounted at distance x_1 from the excitation source located at 0. Based on Eq. (7.27), the attenuation coefficient k_i can be identified from recorded wave signals by linearly regressing logarithmic amplitude of wave packets versus propagation distance x_1 , from which the negative of the slope of the regressed line is just the attenuation coefficient.

The linear regression (LR) method is also used to identify energy velocity from the recorded wave signals since, at a specified frequency and along a fixed direction, a certain mode's wave packet propagates with constant velocity value. The detailed manipulation will be presented in the case study sections.

7.3.2 Estimation of viscoelastic loss factors

The experimentally identified attenuation coefficients can be used to estimate the viscoelastic loss factors which are not available in most cases. To this end, the attenuation coefficient k_i is expressed

3. This property conforms with the Snell's law [2] which requires that all the partial waves keep the same (complex) wavenumber in the interface between adjacent laminae along the wave propagation direction.

as the function of frequency ω with undetermined loss factors γ .

$$k_i = \mathcal{K}(\gamma, \omega) \quad (7.28)$$

where, $\gamma = [\gamma_1, \gamma_2, \gamma_3, \gamma_{23}, \gamma_{31}, \gamma_{12}]$ in which the six elements are the loss factors of E_1^* , E_2^* , E_3^* , G_{23}^* , G_{31}^* , G_{12}^* , respectively, as defined in Eq. (7.4). When computing, γ is specialized to a certain damping model, as defined in Eqs. (7.1), (7.2) and (7.3), γ_{HR} , γ_{KV} and γ_{BT} . The loss factors γ is then determined in the least square sense by inverting the experimentally identified attenuation coefficients, also known as model updating process (we use here the *lsqcurvefit.m* MATLAB function):

$$\hat{\gamma} = \arg \min_{\gamma} \sum_{l=1}^m [\mathcal{K}(\gamma, \omega_l) - \hat{k}_{i,l}]^2 \quad (7.29)$$

where, the series pair $(\omega_l, \hat{k}_{i,l})_{l=1, \dots, m}$ is the experimentally identified attenuation coefficients at various frequencies, and $\hat{\gamma}$ is the estimated loss factors for a certain damping model.

It is worth noting that the function $k_i = \mathcal{K}(\gamma, \omega)$ in Eq. (7.28) should represent the same branch of dispersion curves as the experimentally identified one, which is achieved through the single mode curve tracing technique illustrated in Figure 7.3. In some cases, due to the inaccurate elastic moduli or the existence of uncertainties, the computed energy velocities do not match well with the identified ones. To solve this issue, the same updating process is applied to the experimentally identified energy velocities to calibrate the inaccurate elastic moduli. For brevity, detailed formulation is not presented here but an example is provided in the IFS case study.

7.3.3 Overview of the attenuation prediction method

Once all the required material parameters are available, the numerical dGMM algorithm in Figure 7.4 is driven to predict various spectra of attenuation including dispersion curves and spatial attenuation distribution. Figure 7.5 just outlines the overview of the proposed attenuation prediction method in which the three purple boxes summarize the theoretical works established in the previous sections.

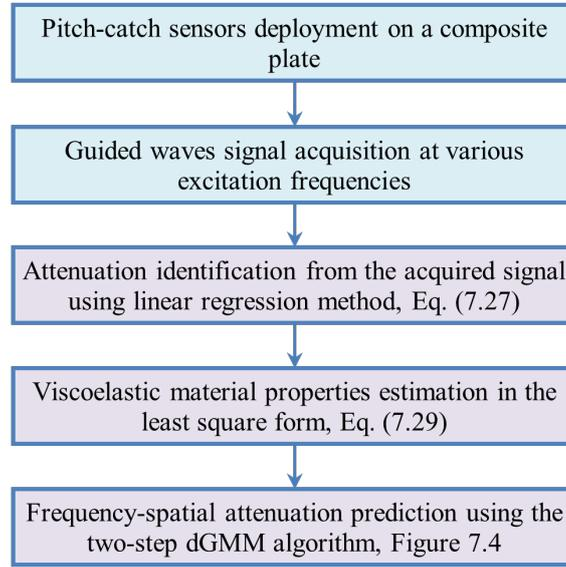


Figure 7.5 – Overview of the proposed method to predict guided waves attenuation.

7.4 Case study on an unmounted and mounted FCS of A380 plane

7.4.1 Experimental setup

In this section, two cases of fan cowl structure (FCS), either unmounted or mounted on an instrumented A380 plane, are employed to validate the proposed guided wave attenuation prediction method. The actual FCS is shown in Figure 7.1(a). This structure is made up of a four-layered carbon epoxy composite plate with stacking sequence [0/-45/+45/0]. Its elastic material properties of each layer can be obtained from Fendzi’s PhD thesis [3] and listed in Table 7.1 for convenience, but the viscoelastic properties are not available. Thus, the model updating process introduced previously will be adopted to estimate them. Obtained results are listed in Table 7.1 for HR and KV models beforehand.

Table 7.1 – Elastic and viscoelastic material properties of composite lamina of the unmounted FCS.

(E_1, E_2, E_3) [GPa]	(G_{23}, G_{31}, G_{12}) [GPa]	$(\nu_{12}, \nu_{13}, \nu_{23})$	ρ [kg/m ³]	Ply thickness [mm]	Stacking sequence
(60,40,8.1)	(4.8,4.8,4.8)	(0.03,0.3,0.3)	1554	0.28	[0/-45/+45/0]
HR model	$\gamma_1=1.74\%$, $\gamma_2=0.01\%$, $\gamma_3=0.01\%$, $\gamma_{23}, \gamma_{31}, \gamma_{12}=0.01\%$				
KV model	$\gamma_1=3.47\%$, $\gamma_2=0.01\%$, $\gamma_3=0.012\%$, $\gamma_{23}, \gamma_{31}, \gamma_{12}=0.01\%$, $f_c = 250$ kHz				

The PZT deployments for both cases are shown in Figure 7.6. There are in total 13 and 43

7.4. CASE STUDY ON AN UNMOUNTED AND MOUNTED FCS OF A380 PLANE

sensors surface installed on the unmounted and mounted FCS, respectively. Due to the presence of stiffeners, the 43 sensors in the mounted FCS are partitioned to six regions, marked from R1 to R6, according to their geometrical characteristics, as shown in Figure 7.6(b). By doing so, each region can be considered at once and signals are processed with great convenience. The 13 sensors in the unmounted FCS constitute only one region and are thus not marked for brevity. Furthermore, sensors of each region in both cases are intentionally divided into three groups during signal processing according to their alignment pattern, i.e. according to their direction with respect to the ply sequence. The group information of the unmounted FCS is illustrated in Figure 7.6(a). For the mounted FCS, in each region, Group 1 includes all sensors and Group 2 and 3 contain sensors roughly aligned along the upper and lower horizontal line, respectively. For example, in R1, Group 1 includes sensors from 1 to 9, and Group 2 and 3 includes sensors 1,2,4,6,8 and 3,5,7,9, respectively. The accurate fiber orientation of each layer in the plate is not available but the horizontal direction of the plate is assumed to be the fiber orientation of the 0° layer because this direction leads to the best match between theoretical predictions and experimental measurements for both energy velocity and attenuation coefficient as will be shown later.

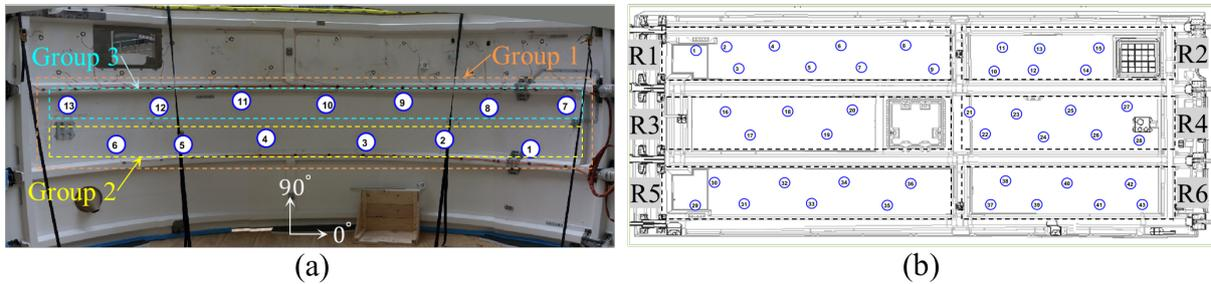


Figure 7.6 – The PZT deployments of FCS for (a) the unmounted case and (b) the mounted case on an instrumented A380 plane.

The experimental setup of the unmounted FCS is shown in Figure 7.7. During testing, the signal generator produced a five-cycle sinusoid tone burst signal modulated by Hanning window given that this kind of exciting signal becomes a standard in SHM of composite structures [2]. The central frequency of the excitation signal was swept from 50 kHz to 150 kHz with 5 kHz increment for the unmounted FCS experiment whereas for the mounted FCS experiment only measurements performed at 100 kHz are available. The sampling frequency was set as 1 MHz which meets the requirement of Nyquist sampling theorem. Among these PZT sensors, each one was used as an actuator in a round

7.4. CASE STUDY ON AN UNMOUNTED AND MOUNTED FCS OF A380 PLANE

robin fashion and the remaining others were receivers, i.e. a sequential pitch-catch testing scheme was conducted. The acquired wave signals were processed with time averaging and wavelet denoising to enhance signal to noise ratio [111]. Note that the frequency sweep testing is required for understanding the mechanism of wave attenuation within an interested frequency range and it is different from a single sweet spot frequency testing which is desired for damage detection [112].

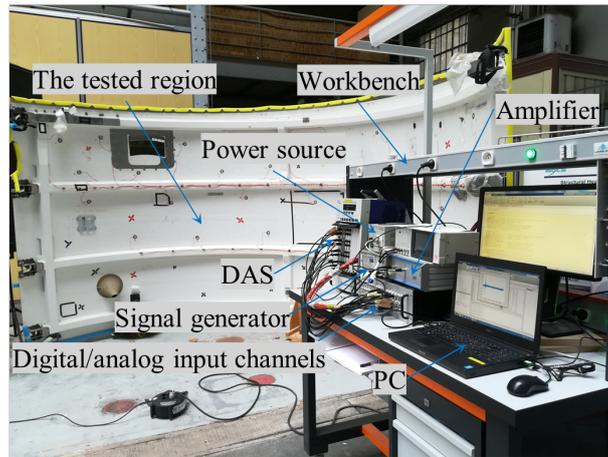


Figure 7.7 – The experimental setup of the unmounted FCS.

Figure 7.8 shows several typical guided wave signals in Group 2 of the unmounted FCS in which PZT 1 serves as the actuator and its signal is normalized to the same order of magnitude with the receivers. Evidently, the signal amplitude decreases with the increasing of propagation distance. Besides, only the S0 mode wave packet is discernible that makes the subsequent identification of energy velocity and attenuation coefficient only focus on S0 mode.

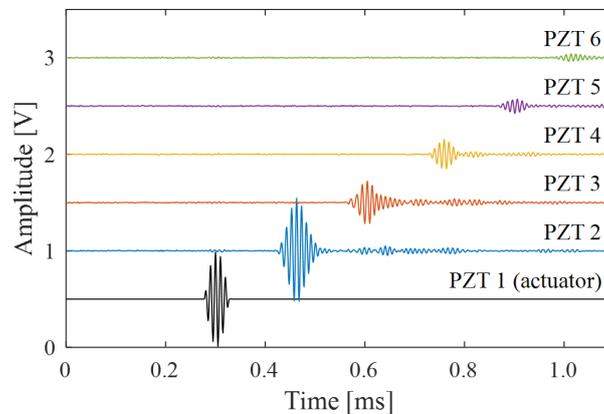


Figure 7.8 – Typical guided wave signals of the unmounted FCS at 100 kHz.

7.4.2 Dispersion curve identification for energy velocity and attenuation coefficient

7.4.2.1 Energy velocity and attenuation coefficient identification at 100 kHz

The LR method introduced previously is used to identify energy velocity at a given frequency 100 kHz in the unmounted FCS experiments, as illustrated in Figure 7.9(a). The regressed lines for the three groups are plotted based on the scatter points representing the time of arrival (ToA) of S0 mode's wave packet versus sensing distance, from which energy velocity is identified from the inverse of the slope of the regressed line. The regression results are listed in Table 7.2, which shows the consistent energy velocities identified amongst the three sensor groups and meanwhile the higher correlation coefficients R^2 (0.99).

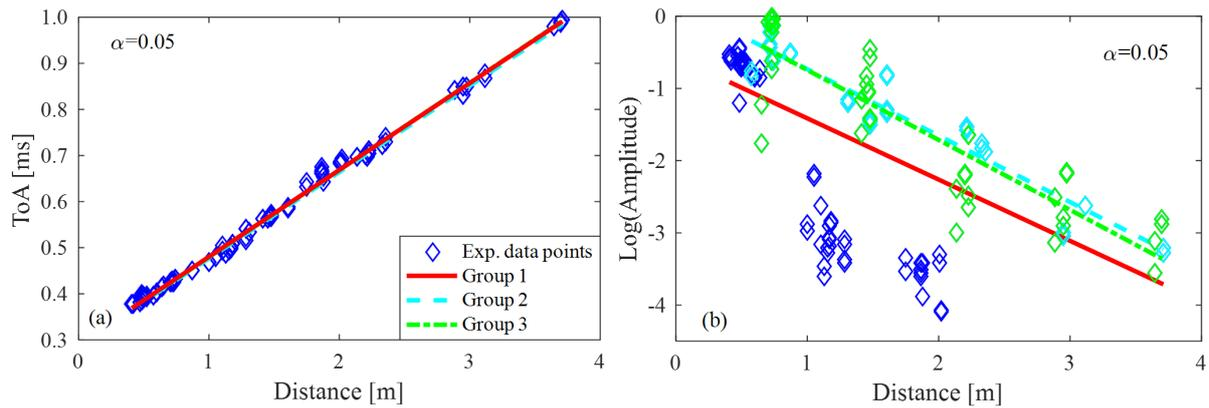


Figure 7.9 – Example of identifying (a) energy velocity and (b) attenuation coefficient via LR method at 100 kHz for the unmounted FCS. Both figures share the same legend and α is used to give the confidence level with $100(1 - \alpha)\%$.

Attenuation coefficient can also be identified by using LR method based on Eq. (7.27), as illustrated in Figure 7.9(b), in which some points of Group 1 are overlapped by the points of Group 2 and 3 because the sensors in Group 2 and 3 are contained in Group 1. The results extracted from Figure 7.9(b) are listed in Table 7.3, from which the R^2 in Group 1 (0.39) is greatly lower than the one of Group 2 (0.92) and Group 3 (0.79). This result is consistent with the dispersed scatter points of Group 1 in Figure 7.9(b). More fundamentally, the lower R^2 in Group 1 is caused by the anisotropic effect of composite materials since the sensors in Group 1 yield multiple directions of propagation paths whereas Group 2 and 3 only orient at the horizontal direction, thus a larger R^2 value is guaranteed respectively for the two groups.

7.4. CASE STUDY ON AN UNMOUNTED AND MOUNTED FCS OF A380 PLANE

Table 7.2 – Identified energy velocities from Figure 7.9(a). R^2 is the correlation coefficient.

Group 1			Group 2			Group 3		
c_e [m/s]	c_e bound [m/s]	R^2	c_e [m/s]	c_e bound [m/s]	R^2	c_e [m/s]	c_e bound [m/s]	R^2
5308	[5258, 5359]	0.99	5340	[5279, 5402]	0.99	5291	[5257, 5325]	0.99

Table 7.3 – Identified attenuation coefficient from Figure 7.9(b). R^2 is the correlation coefficient.

Group 1			Group 2			Group 3		
k_i [Np/m]	k_i bound [Np/m]	R^2	k_i [Np/m]	k_i bound [Np/m]	R^2	k_i [Np/m]	k_i bound [Np/m]	R^2
0.85	[0.66, 1.04]	0.39	0.92	[0.81, 1.03]	0.92	0.97	[0.80, 1.13]	0.79

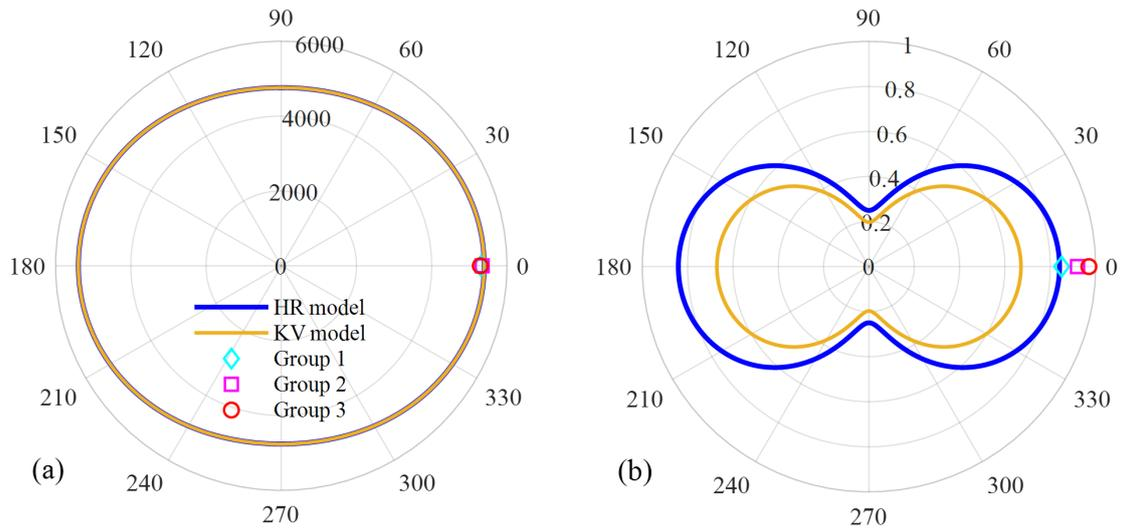


Figure 7.10 – Polar plot of S0 mode of (a) energy velocity [m/s] and (b) attenuation coefficient [Np/m] at 100 kHz for the unmounted FCS. Both subfigures share the same legend.

7.4. CASE STUDY ON AN UNMOUNTED AND MOUNTED FCS OF A380 PLANE

To further illustrate the anisotropic effect of energy velocity and attenuation coefficient, their polar plots of S0 mode are generated in Figure 7.10(a) and (b) based on the viscoelastic material properties of HR and KV models listed in Table 7.1. In both figures, the experimentally identified values of the three groups are depicted as well for comparison, but the data point of Group 1 along 0° direction only plays the reference role given that the propagation paths in Group 1 are actually multi-directional. Observing Figure 7.10(a), at 0° direction, the model predicted energy velocity is comparable to the experimentally identified ones. For Figure 7.10(b), HR model predicts a more accurate value of attenuation coefficient than KV model. One interesting point from both figures is that unlike the quasi-isotropic property of energy velocity, wave attenuation is heavily influenced by the anisotropic effect of composite materials, which shows that the 0° and 90° directions present the largest and smallest value of attenuation coefficient, respectively. The anisotropic phenomenon of wave attenuation physically explains the dispersed experimental data points in Group 1 of Figure 7.9(b). In view of the inapplicable LR method to Group 1, only Group 2 and 3 of the unmounted FCS are employed to identify the attenuation coefficient dispersion curves in the next subsection (see Figure 7.12(b)).

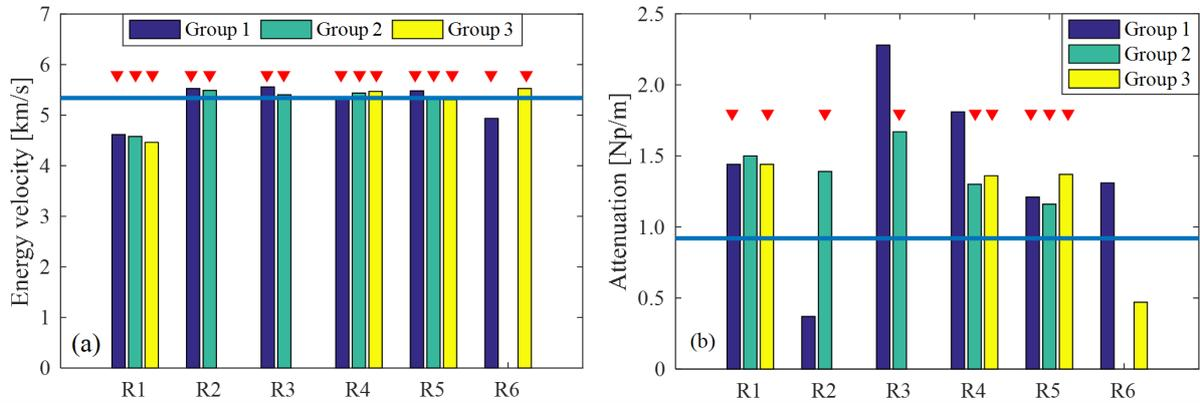


Figure 7.11 – Bar chart to display regression results of (a) energy velocity and (b) attenuation coefficient via LR method for the mounted FCS at 100 kHz. The horizontal line represents the reference value of the unmounted FCS, and the triangles denote that the marked bars correspond to a R^2 larger than 0.7.

For the mounted FCS, there is only one frequency testing data, 100 kHz, available from measurements performed by C. Fendzi (cf. Fendzi’s PhD thesis [3]). The identified values of the six regions are displayed in Figure 7.11 in the form of bar chart, in which the horizontal lines represent the reference values that are obtained from the unmounted FCS counterpart, i.e. for energy velocity 5340 m/s and for attenuation coefficient 0.92 Np/m as listed in Group 2 of Table 7.2 and 7.3, respectively. The tri-

7.4. CASE STUDY ON AN UNMOUNTED AND MOUNTED FCS OF A380 PLANE

angles in Figure 7.11 denote that the marked bars correspond to a R^2 larger than 0.7 which suggests a strong linear correlation. From Figure 7.11, these findings can be obtained: 1) all the R^2 values of energy velocity in the six regions are larger than 0.7 whereas only nine out of fifteen for attenuation coefficient; 2) energy velocities tend to be consistent but the distribution of attenuation coefficients are more variable; 3) the identified energy velocities in different groups of the six regions agree well with the reference value. However there exists more discrepancy between the identified attenuation coefficients and the reference one but the same order of magnitude remained. In a word, the quality of energy velocity identification is much better than the quality of the attenuation coefficient which may be interpreted that the attenuation coefficient is much smaller than the propagating wavenumber ($|k_i| \ll |k_r|$) and thus much more sensitive to experimental noise. Note that in Figure 7.11 several bars are not shown because of their unphysical meanings such as too large or too small energy velocity or negative attenuation coefficient, which may be attributed to the superposed S0 mode's wave packet by other modes, e.g. A0 or the reflected modes.

7.4.2.2 Identified dispersion curves of energy velocity and attenuation coefficient

By applying the LR method to each frequency tested for the unmounted FCS, the dispersion curves of energy velocity and attenuation coefficient are formed in Figure 7.12(a) and (b), respectively. Note that in Figure 7.12(a) only the identified curve of Group 1 is presented due to the closing curves amongst the three groups, whereas in Figure 7.12(b) only the identified curves of Group 2 and 3 are shown thanks to the anisotropic effect in Group 1 which has been declared in the previous subsection. Additionally, the curves of correlation coefficients R^2 corresponding to Figure 7.12(a) and (b) are presented in Figure 7.12(c) to assess the quality of the identified dispersion curves. Obviously, the identified S0 mode's energy velocity curve is accurate because of its greater correlation coefficients (all larger than 0.95). Although the identified attenuation curves (Figure 7.12(b)) are not as good as the energy velocity curve (Figure 7.12(a)), we can still get some meaningful findings: 1) in the frequency range 75-150 kHz, the identified attenuation coefficients are reliable enough given that the corresponding R^2 values are larger than 0.7 except the initial points (50-70 kHz); 2) both curves present the same trend, i.e. attenuation increases with frequency firstly and then decreases; 3) the identified attenuation coefficients for both groups are equal at approximately 95 kHz, and the lower and upper bounds of the two groups are intersected in the vicinity of 95 kHz.

7.4. CASE STUDY ON AN UNMOUNTED AND MOUNTED FCS OF A380 PLANE

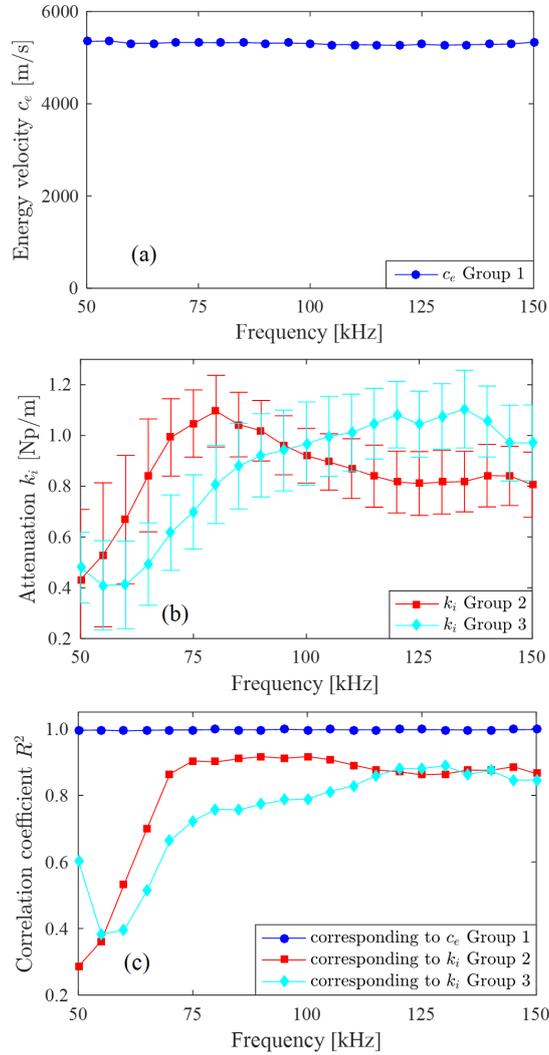


Figure 7.12 – The identified dispersion curves of (a) energy velocity, (b) attenuation coefficient and (c) correlation coefficient. These subfigures relate to the S0 mode propagating at 0° direction of the unmounted FCS.

7.4.3 Estimation of viscoelastic material properties of the unmounted FCS

The experimentally identified S0 mode attenuation coefficients in Figure 7.12(b) are further employed to estimate viscoelastic material properties via the least square method formulized in Eq. (7.29). When specifying damping models, only HR and KV models are used considering that BT model is mainly used for highly damped structures whereas FCS is slightly damped because attenuation coefficient is no more than 2 Np/m in the interested frequency range according to Figure 7.12(b). The estimated viscoelastic properties of the two models are listed in posterior in Table 7.1. From this table,

7.4. CASE STUDY ON AN UNMOUNTED AND MOUNTED FCS OF A380 PLANE

for both models γ_1 is greatly larger than the remaining five parameters, meaning that the damping effect is predominated in the principal fiber direction of composite lamina. Besides, the loss factors of KV model are the relative values to the ones at the characterization frequency $f_c = 250$ kHz. If f_c changes to a different value, the loss factors of KV model will change correspondingly (but the ratio γ_{KV}/f_c keeps unchanged) [12].

Once all the required material parameters in Table 7.1 have been obtained, they are used as inputs to the developed algorithm exhibited in Figure 7.4. After computing, the dispersion curves of energy velocity and attenuation coefficient for the two damping models are depicted in Figure 7.13(a) and (b), respectively, in which the experimentally identified data points in Figure 7.12(a) and (b) are also presented for comparison. Figure 7.13(a) shows that the computed S0 mode energy velocity curve agrees well with the experimental points, among which the diamond point is the mean value of the bars in Figure 7.11(a), representing the mounted FCS. Besides, the two damping models produce the mutually overlapped energy velocity curves for the three basic modes in the shown frequency range, denoting that viscoelastic damping effect does not change the property of energy velocity for the slightly damped FCS.

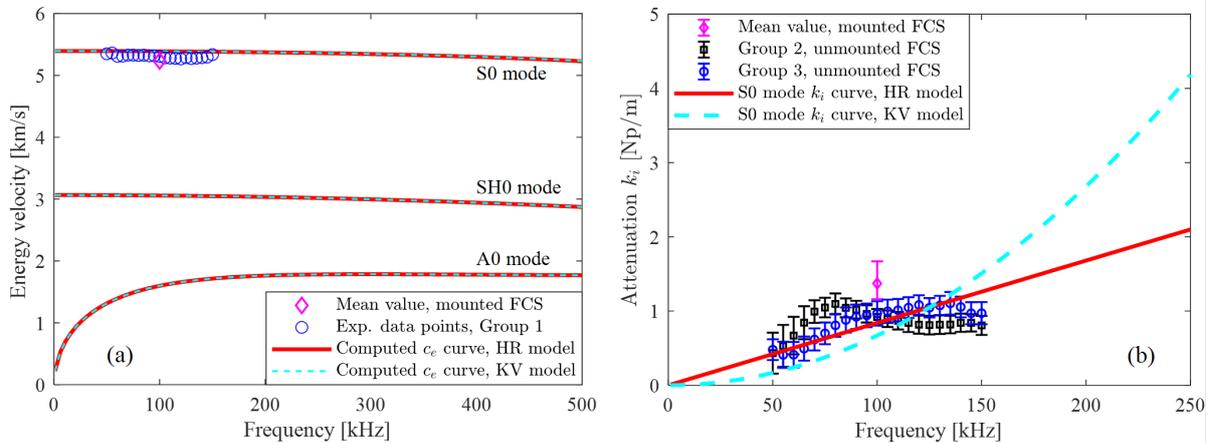


Figure 7.13 – Comparison between the computed and experimentally identified dispersion curves of (a) energy velocity and (b) attenuation coefficient for the unmounted FCS at $\theta = 0^\circ$.

Figure 7.13(b) shows that the curve of HR model presents the linear trend whereas the curve of KV model expresses the parabola trend, which results in overestimated attenuation prediction in higher frequency range. Furthermore, the upward concavity of the curve of KV model is contrary to the upward convexity of the experimental data points, thus, HR model fits better with the experimental

data than KV model, and thanks to this reason, HR model will be adopted to predict attenuation coefficient in the next subsection. Note that the diamond point in Figure 7.13(b) is the mean value of the marked bars in Figure 7.11(b), representing the mounted FCS, and its lower and upper bounds are the minimum and maximum values of the marked bars in Figure 7.11(b).

7.4.4 Attenuation coefficient prediction for the unmounted FCS

By using the elastic and viscoelastic parameters of HR model in Table 7.1, the attenuation coefficient can be predicted in two ways. One is the traditional dispersion curve in a wide frequency range at a fixed propagation direction as depicted in Figure 7.14(b), and another one is the polar plot representing the distribution of attenuation coefficient for all propagation direction at a fixed frequency as illustrated in Figure 7.14(d). Besides, the two displaying ways are also applied to phase velocity in Figure 7.14(a)(c), in which the color code on the curves are the attenuation coefficient superimposed from Figure 7.14(b)(d). With the colored diagrams, the dispersion property of phase velocity and attenuation can be explored in the same Figure 7.14(a), and the anisotropic degree of both quantities can be simultaneously compared in Figure 7.14(c).

Comparing Figure 7.14(a)(b), phase velocity presents slight dispersion property in most of the frequency range, whereas attenuation coefficient increases in the same frequency range except for the S0 mode after 820 kHz, which shows a sudden drop (see Figure 7.14(a)(b)). Besides, A0 mode attenuation is larger than the one of the S0 mode in the tested frequency range of 50-150 kHz. This explains why only the S0 mode wave packet is discernible in the recorded wave signals (see Figure 7.8) since A0 mode wave packet has been rapidly attenuated. Comparing Figure 7.14(c)(d), phase velocities of the three basic modes present a consistent quasi-isotropic behavior, whereas attenuation coefficients are anisotropic for the three considered modes. Figure 7.14(d) clearly shows that S0 and A0 modes possess larger and smaller attenuation in the principal (0° and 180°) and minor (90° and 270°) directions, respectively. Attenuation of the SH0 mode is less variable, the smallest value appearing at 30° in the first quadrant. Note that the open circles in Figure 7.14 are the solutions of SAFE method [7, 79] that is used here for comparison and validation with the proposed dGMM approach. For SAFE computation in this instance, five 1D quadratic elements per layer are used to mesh the through thickness section of the four-layered [0/-45/+45/0] composite laminate, which guarantees its convergence as proved in Figure 7.14.

7.4. CASE STUDY ON AN UNMOUNTED AND MOUNTED FCS OF A380 PLANE

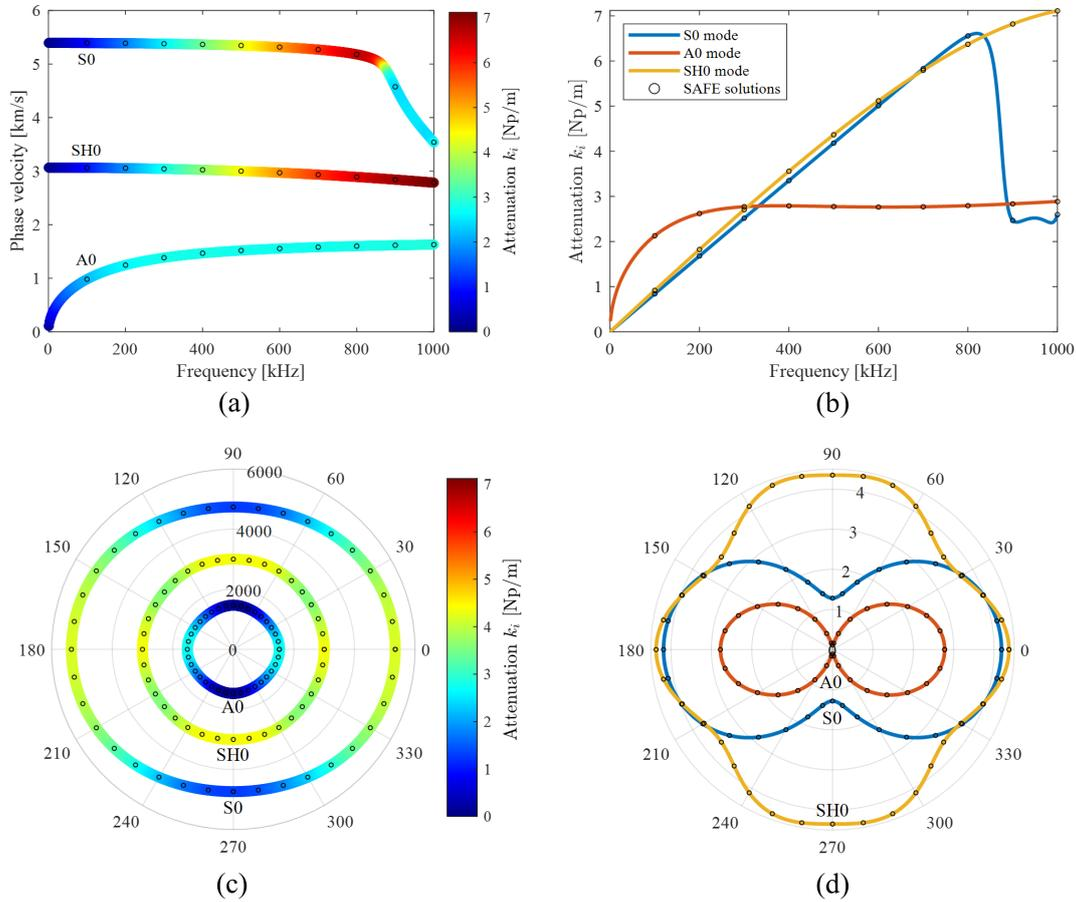


Figure 7.14 – For the unmounted FCS, HR model’s prediction of (a) dispersion curve of phase velocity at $\theta = 180^\circ$, (b) dispersion curve of attenuation coefficient at $\theta = 180^\circ$, (c) polar plot of phase velocity [m/s] at $f = 500$ kHz, (d) polar plot of attenuation coefficient [Np/m] at $f = 500$ kHz. The open circles in the four subfigures are the solutions computed by SAFE method.

The 3D surface diagrams for the three basic modes are shown in Figure 7.15 to unveil the relation between frequency, propagation angle, and phase velocity or attenuation coefficient. In another sense, the frequency-spatial spectrum of the two quantities is plotted here. The surface plots can be generated in two ways that are derived from Figure 7.14. Consider the example in Figure 7.15(a): one way is to ‘spin’ the phase velocity curve of the S0 mode in Figure 7.14(a) with propagation angle, and another one is to ‘extrude’ the phase velocity contour of the S0 mode in Figure 7.14(c) along the frequency axis. Due to the quasi-isotropic property of phase velocity, its surface plot presents a cylindrical shape for each considered mode, whereas the shape of the attenuation coefficient is multifarious for different modes. This phenomenon reveals again that in the frequency-spatial spectrum, attenuation coefficient

7.5. CASE STUDY ON AN UNMOUNTED AND MOUNTED IFS OF A380 PLANE

behaves in an anisotropic manner even if the current composite laminate of FCS is quasi-isotropic from the phase velocity point of view. As a consequence, obtaining a precise characterization of attenuation is in practice more complex than for phase velocity. Note that in Figure 7.15(a)(c)(e), only HR model's predictions are presented since KV model produces very similar diagrams. In Figure 7.15(b)(d)(f), both HR and KV models' diagrams are depicted with the inner and outer surfaces belonging to HR and KV models, respectively.

7.5 Case study on an unmounted and mounted IFS of A380 plane

7.5.1 Experimental setup

To further demonstrate the effectiveness of the proposed wave attenuation prediction method, two cases of IFS either unmounted or mounted on an instrumented A380 plane are investigated in this section. The sketch picture of this structure is shown in Figure 7.1(b), along with its geometrical dimensions given in Section 7.1, and its actual profile is presented in Figure 7.16(a). The IFS is a sandwich type structure consisting of an aluminum alloy honeycomb core and two four-ply carbon epoxy outer skins with stacking sequence [0/-45/+45/0/Al/0/+45/-45/0]. The total thickness of the sandwich plate is 3.44 mm. The elastic material properties of the composing laminae can be obtained from Fendzi's PhD thesis [3] and are listed in Table 7.4 and 7.5 for convenience. Table 7.6 lists the viscoelastic properties of the two materials corresponding to the specific damping models, which are obtained through model updating process (see Section 7.5.3) since the viscoelastic information is not available from this reference.

Table 7.4 – Elastic material properties of the carbon epoxy ply in the unmounted IFS.

(E_1, E_2, E_3) [GPa]	(G_{23}, G_{31}, G_{12}) [GPa]	$(\nu_{12}, \nu_{13}, \nu_{23})$	ρ kg/m ³	Ply thickness [mm]
$(51.0, 65.7, 8.1)$ ¹	$(5.2, 5.2, 5.2)$	$(0.02, 0.3, 0.3)$	1554	0.28
$(40.0, 55.0, 8.1)$ ²				

¹ The original values from [3] that lead to a great agreement to the experimental data of the unmounted IFS.

² The updated values that result in the best match with the experimental data of the mounted IFS.

Table 7.5 – Elastic material properties of the aluminum core layer in the unmounted IFS.

E [MPa]	G [MPa]	ν	ρ [kg/m ³]	Layer thickness [mm]
866	354	0.2232	67	1.2

There are in total 10 PZTs surface installed on the unmounted and mounted IFS, which are

7.5. CASE STUDY ON AN UNMOUNTED AND MOUNTED IFS OF A380 PLANE

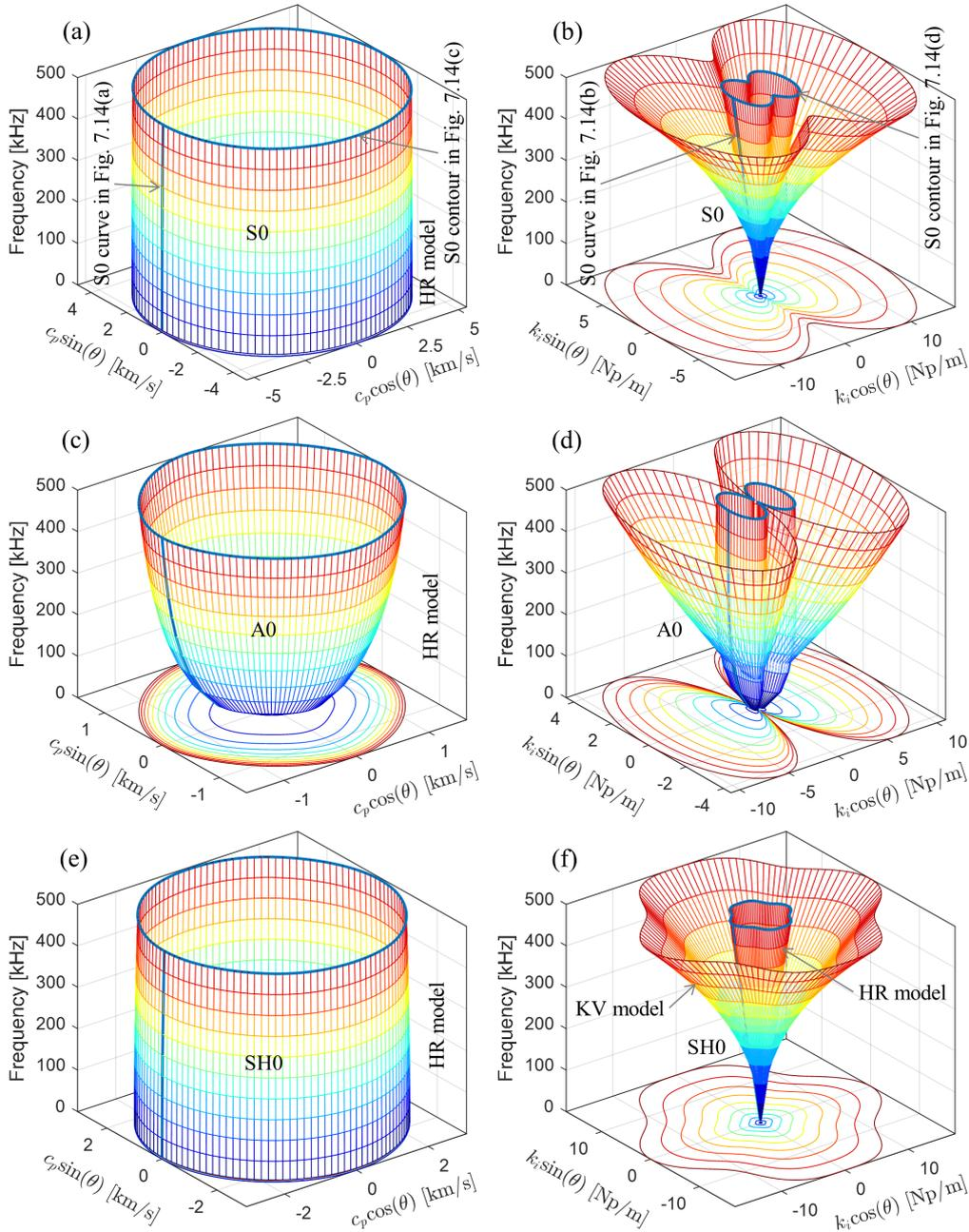


Figure 7.15 – For the unmounted FCS, surface plot of phase velocity (left) and attenuation coefficient (right): (a) and (b) S0 mode, (c) and (d) A0 mode, (e) and (f) SH0 mode. The inner and outer surfaces in subfigures (b)(d)(f) correspond to HR and KV models, respectively.

arranged into three groups for each case as illustrated in Figure 7.16. The orientation of the 0° layer of carbon epoxy lamina in the plate is unknown but assumed to be along the alignment direction of the sensors in Group 2 or 3 of Figure 7.16(a) considering that this direction can result in best

7.5. CASE STUDY ON AN UNMOUNTED AND MOUNTED IFS OF A380 PLANE

Table 7.6 – Viscoelastic material properties of the carbon epoxy ply and aluminum core in the unmounted IFS.

Combination of models	Carbon epoxy ply (HR or KV)							Aluminum (BT)		
	γ_1	γ_2	γ_3	γ_{23}	γ_{31}	γ_{12}	f_c [kHz]	γ_E	γ_G	ϵ
HR+BT model ¹	13.9%	0.04%	0.02%	5.60%	5.60%	5.60%	–	19.9%	19.9%	10
KV+BT model ²	27.4%	0.01%	0.01%	0.01%	0.01%	0.01%	250	30.0%	30.0%	10

¹ HR model is used for carbon epoxy plies and BT model is applied for aluminum core.

² KV model is used for carbon epoxy plies and BT model is applied for aluminum core.

match between the theoretical predictions and experimental measurements for both energy velocity and attenuation coefficient. The signal acquisition process was similar to the experiments on FCS and thus the detailed experimental setup is not shown for brevity. The frequency series in the unmounted IFS experiment were swept from 50 kHz to 150 kHz at 5 kHz increment but there was only 100 kHz available for the mounted IFS experiment. Time averaging and wavelet denoising strategies were also adopted for signal processing.

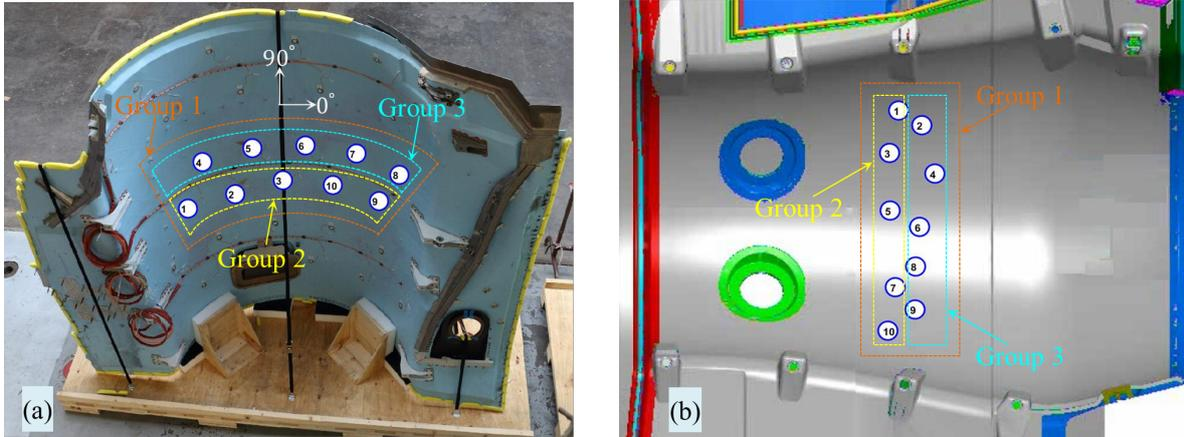


Figure 7.16 – The transducers layout of IFS for (a) the unmounted case and (b) the mounted case on an instrumented A380 plane.

7.5.2 Dispersion curve identification for energy velocity and attenuation coefficient

7.5.2.1 Comparison of energy velocity and attenuation coefficient at 100 kHz between the mounted and unmounted IFS

Figure 7.17(a) presents the comparison of the identified energy velocity via LR method between the mounted and unmounted IFS at 100 kHz as this frequency is unique for the mounted case. This subfigure shows that both cases produce close energy velocities and simultaneously the higher R^2

7.5. CASE STUDY ON AN UNMOUNTED AND MOUNTED IFS OF A380 PLANE

values larger than 0.8 are obtained except the Group 1 of the unmounted IFS. Thus, Group 2 and 3 of the unmounted IFS will be adopted to identify the dispersion curves of energy velocity in the next subsection.

A similar comparison of the identified attenuation coefficient is illustrated in Figure 7.17(b). It shows that overall, the mounted IFS returns about half the attenuation of its unmounted counterpart. This could be attributed to different environmental conditions in both cases, and especially to the fact that when IFS is mounted on an A380 plane the structure is stressed which can influence guided waves propagation properties [113]. Moreover, the attenuation coefficient of Group 2 is not equal to the one of Group 3 for both cases and the discrepancy in the mounted IFS is more salient, even though Group 2 and 3 have the same propagation direction. This phenomenon can be explained by the fact that the imaginary part of the wavenumber, i.e. the attenuation coefficient, is much smaller than the real part and thus much more prone to noise error. Since the correlation coefficients of Group 2 and 3 of the unmounted IFS are larger than 0.8, the two groups will be selected to identify dispersion curves of attenuation coefficient in the next subsection.

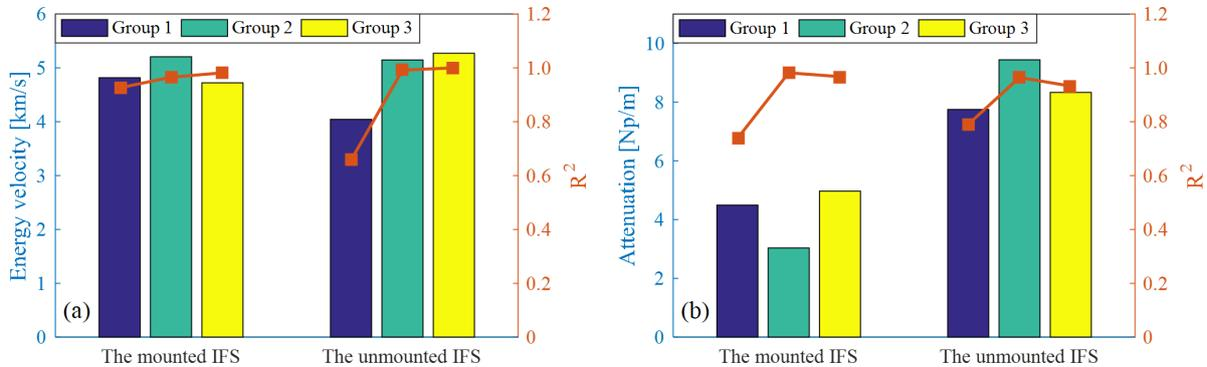


Figure 7.17 – Comparison between the mounted and unmounted IFS for (a) energy velocity and (b) attenuation coefficient at 100 kHz. In the two subfigures, the bars relate to the left y-axis and the lines correlate to the right y-axis.

To further explore directional dependence of the S0 mode energy velocity, the guided wave signals in Group 1 of the mounted IFS were processed to generate a polar plot of energy velocity, as depicted in Figure 7.18, since this group possess multiple wave propagation directions. Besides, the theoretical curves predicted via the developed dGMM method are also presented in Figure 7.18 for comparison purpose. The curves of dGMM prediction 1 and dGMM prediction 2 are created by using the (E_1, E_2, E_3) values 1 and 2 listed in Table 7.4, respectively. The other material properties listed

7.5. CASE STUDY ON AN UNMOUNTED AND MOUNTED IFS OF A380 PLANE

in Table 7.4 and 7.5 are the same. Figure 7.18 shows that the original (E_1, E_2, E_3) values 1 yield to an overestimated prediction (the curve of dGMM prediction 1). When these values are updated to values 2, the predicted curve of dGMM prediction 2 matches well with the experimental data points of the mounted IFS, which is the same structure as the unmounted counterpart but undergoing different environmental conditions, i.e. existing stress in the mounted case thus modifying wave propagation properties [113]. Figure 7.18 shows that the IFS structure holds quasi-isotropic property in terms of S0 mode energy velocity that is consistent with the symmetric stacking sequence of laminae $[0/-45/+45/0/A1/0/+45/-45/0]$.

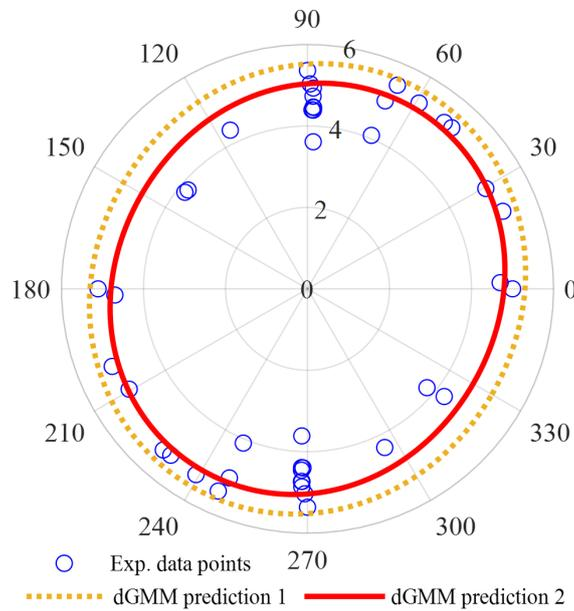


Figure 7.18 – Polar plot of S0 mode energy velocity [km/s] in the mounted IFS at 100 kHz. The contour of dGMM prediction 1 and dGMM prediction 2 are computed by using the (E_1, E_2, E_3) values 1 and 2 in Table 7.4, respectively.

7.5.2.2 Identified dispersion curves of energy velocity and attenuation coefficient

The identified dispersion curves of energy velocity and attenuation coefficient of the unmounted IFS are generated in Figure 7.19(a) and (b), respectively. Note that the corresponding correlation coefficient curves are not presented here because all values are larger than 0.8 which demonstrates reliable results of dispersion curves identification. Observing Figure 7.19(a), the energy velocity curves of both groups basically overlap to each other, whereas in Figure 7.19(b), Group 3 brings a lower attenuation than Group 2, but both curves keep the same tendency as the unmounted FCS, as seen

7.5. CASE STUDY ON AN UNMOUNTED AND MOUNTED IFS OF A380 PLANE

in Figure 7.12(b). Figure 7.19(b) reveals that for practical aeronautic composite structures, the attenuation mechanism induced by material damping is more complex than for a unidirectional CFRP composite plate [79]. The lower and upper bounds in Figure 7.19(b) represent the confidence intervals which are extracted from LR method under 95% confidence level.

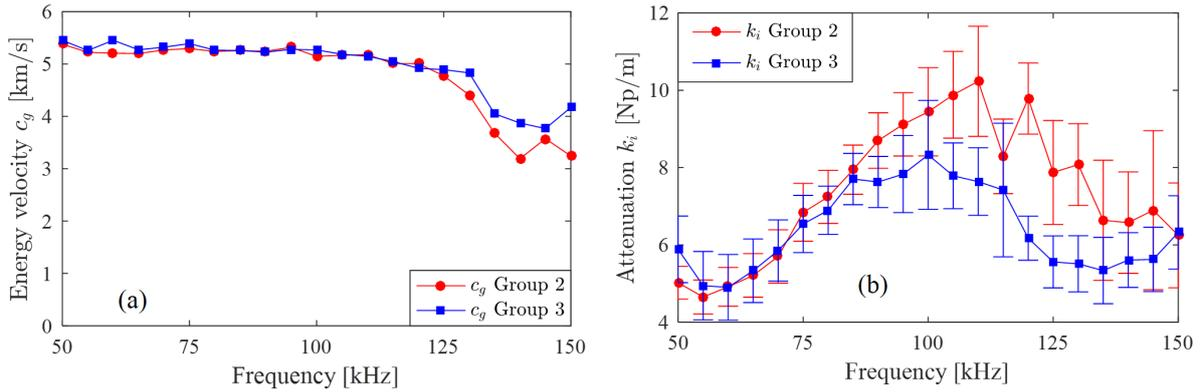


Figure 7.19 – The identified S0 mode dispersion curves of (a) energy velocity and (b) attenuation coefficient for the unmounted IFS.

7.5.3 Estimation of viscoelastic material properties of the unmounted IFS

With the experimentally identified attenuation coefficients in Figure 7.19(b), the viscoelastic material properties of the unmounted IFS can be estimated according to the model updating process formulized in Eq. (7.29). Before performing this process, one has to note that the attenuation of the unmounted IFS is larger than the one of FCS according to Figure 7.19(b), thus BT model should be applied to IFS in a certain form considering that BT model is mainly used for highly damped structures [106], and the unmounted IFS exactly belongs to this case. Furthermore, the IFS is a sandwich type structure composed by two inhomogeneous materials with the aluminum alloy honeycomb core and the carbon epoxy skin layers. Therefore, the core layer and the skin layers can be modeled by different damping models. By following the convention in FCS, the carbon epoxy layers in IFS are modeled by HR or KV models, thus BT model is naturally applied to the aluminum alloy core layer, which finally results in two combinations of damping models, HR+BT and KV+BT models.

By taking the identified attenuation coefficients in Figure 7.19(b) as the training data to the model updating process, the estimated viscoelastic material properties of the two combinations of damping models are obtained in Table 7.6. It shows that the parameters of BT model in the aluminum alloy core

7.5. CASE STUDY ON AN UNMOUNTED AND MOUNTED IFS OF A380 PLANE

layer are larger than the parameters of HR or KV model in the carbon epoxy layers, thus manifesting that the large attenuation of IFS is controlled by the highly damped aluminum alloy honeycomb core layer.

With the obtained viscoelastic material properties of the two combinations of damping models in Table 7.6, the energy velocity and attenuation curves are theoretically computed via the developed dGMM as depicted in Figure 7.20(a) and (b), respectively, in which the experimentally identified data points in Figure 7.19(a) and (b) are also presented for comparison, along with the diamond points in Figure 7.20(a) and (b) being the mean values of the mounted IFS in Figure 7.17(a) and (b), respectively.

We firstly analyze Figure 7.20(b). It shows that the linear trend curve of HR+BT model in the frequency range 0-150 kHz fits better with the experimental data than the parabola trend curve of KV+BT model in 0-200 kHz. Since the concavity of KV+BT model's curve is reversed to the trend of the experimental data points, KV+BT model predicts underestimated and overestimated attenuation in the lower and higher frequency range, respectively. For HR+BT model, its linear kind prediction represents the average effect to the experimental data in the least square sense.

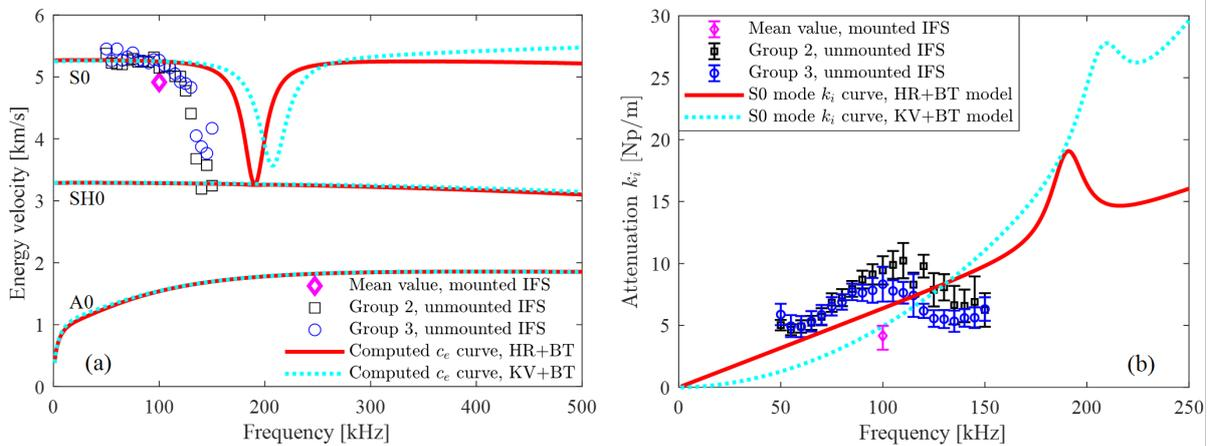


Figure 7.20 – Comparison between the computed and experimentally identified dispersion curves of (a) energy velocity and (b) attenuation coefficient for the unmounted IFS at $\theta = 0^\circ$.

Then, we analyze Figure 7.20(a). It shows that, for the two combinations of damping models, the computed S0 mode energy velocity curves do not agree well with the experimental data, and KV+BT model produces more deviations than HR+BT model in the frequency range 100-150 kHz. However, when we compute the group velocity via Eq. (7.22) by using the pure elastic material properties listed

7.5. CASE STUDY ON AN UNMOUNTED AND MOUNTED IFS OF A380 PLANE

in Table 7.4 and 7.5, i.e. performing the undamped GMM of Chapter 5, one interesting phenomenon that the computed S0 mode group velocity curve matches very well with the experimental data is observed in Figure 7.21. This phenomenon reveals the fact that, for the sandwich type structure made of inhomogeneous materials, the damping mechanism adopted has a great influence on wave propagation speed. And the model parameters (both the elastic constants and the loss factors) should be updated in order to get a better fit to both experimental energy velocity and attenuation data which could be one of the future works.

Back to Figure 7.20(a), from the point of computation, HR+BT and KV+BT models produce a mutually overlapped energy velocity curves for SH0 and A0 modes in the shown frequency range, which is different from the discrepant S0 curves computed with the two models.

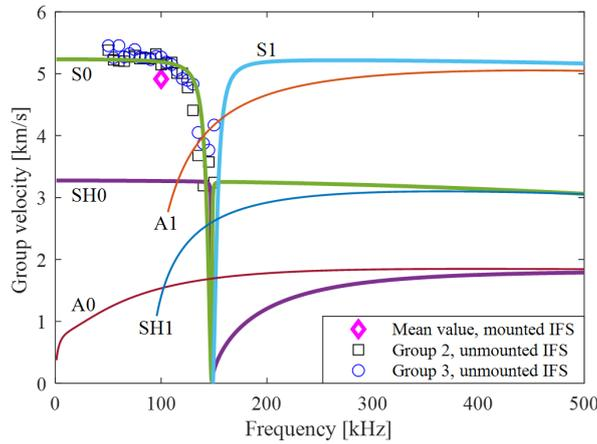


Figure 7.21 – The computed group velocity via the pure elastic GMM for the unmounted IFS at $\theta = 0^\circ$.

7.5.4 Prediction of dispersion curves in various forms for the unmounted IFS

The two combinations of damping models are further employed to predict the dispersion curves in the 3D space (f, k_r, k_i) at the fixed propagation angle $\theta = 90^\circ$ as depicted in Figure 7.22(a) and (b) for HR+BT and KV+BT models, respectively. These modal curves are classified into symmetric and anti-symmetric modes by checking the symmetry conditions of the displacement mode shapes, which are not presented in this chapter for the sake of brevity. For a certain combination of damping model, the 3D curves in Figure 7.22(a) or (b) are projected onto the (f, k_r) plane and the (f, k_i) plane to make a comparison of the two combinations of damping models. According to Figure 7.22(c) and (d), HR+BT and KV+BT models predict identical propagating wavenumbers for the six modes in the

7.5. CASE STUDY ON AN UNMOUNTED AND MOUNTED IFS OF A380 PLANE

shown frequency range, whereas the two combinations of damping models predict different attenuation coefficients, especially for SH0 and A0 modes, according to Figure 7.22(e) and (f). Thus, choosing the proper damping model (or their combinations) is the key to accurately predict wave attenuation here. Figure 7.22(c) and (d) also indicate that there is no cutoff frequency for S1, A1 and SH1 modes, which is accompanied by a large attenuation in the lower frequency range as shown in Figure 7.22(e) and (f). This behavior is a unique property of the damped wave guide [72].

To study the influence of attenuation on phase velocity, the attenuation curves of S0, A0 and SH0 modes in Figure 7.22(e) are separately drawn in Figure 7.23(b), then superimposed on the phase velocity curves in color code as illustrated in Figure 7.23(a). This subfigure shows that there is a step in the S0 mode phase velocity curve around 200 kHz, which is caused by the fluctuation of the S0 mode attenuation curve around 200 kHz in Figure 7.23(b). Besides, S0 mode holds a slight attenuation in comparison with SH0 and A0 modes. This could be the reason that only S0 mode information has been identified experimentally (see Figure 7.19) as SH0 and A0 modes have been rapidly attenuated. In short, Figure 7.23(a)(b) manifest that the phase velocity of guided waves in damped sandwich structure is characterized simultaneously by frequency (dispersion property) and attenuation (viscoelastic damping).

To study the anisotropic effect of phase velocity and attenuation, the polar plots of both quantities are depicted in Figure 7.23(c) and (d) at the same frequency $f = 200$ kHz. Figure 7.23(c) displays the quasi-isotropic property of phase velocity of the three basic modes. Nevertheless, pure anisotropic behavior of attenuation is observed in Figure 7.23(d) for S0 and A0 modes, both of which hold the largest and smallest attenuation in the principal (0° and 180°) and minor (90° and 270°) directions, respectively. As for SH0 mode's attenuation, its anisotropic degree is slight along the omnidirectional propagation angles. In a word, Figure 7.23(c)(d) give the evidence that despite the quasi-isotropic property, attenuation of guided waves in damped sandwich structure still possesses anisotropic effect.

Finally, the 3D surface diagrams of the three basic modes are predicted in Figure 7.24 to represent the frequency-spatial spectra of phase velocity and attenuation. In Figure 7.24(a)(c)(e), the cylindrical surfaces of S0 and A0 modes and the paraboloid of revolution of A0 mode signify the quasi-isotropic property of phase velocity. However, the manifold shapes of attenuation in Figure 7.24(b)(d)(f) again indicate the anisotropic property of attenuation in the frequency-spatial spectrum. Note that in Figure 7.24(a)(c)(e), KV+BT model's predictions are not presented since it yields almost the same

7.5. CASE STUDY ON AN UNMOUNTED AND MOUNTED IFS OF A380 PLANE

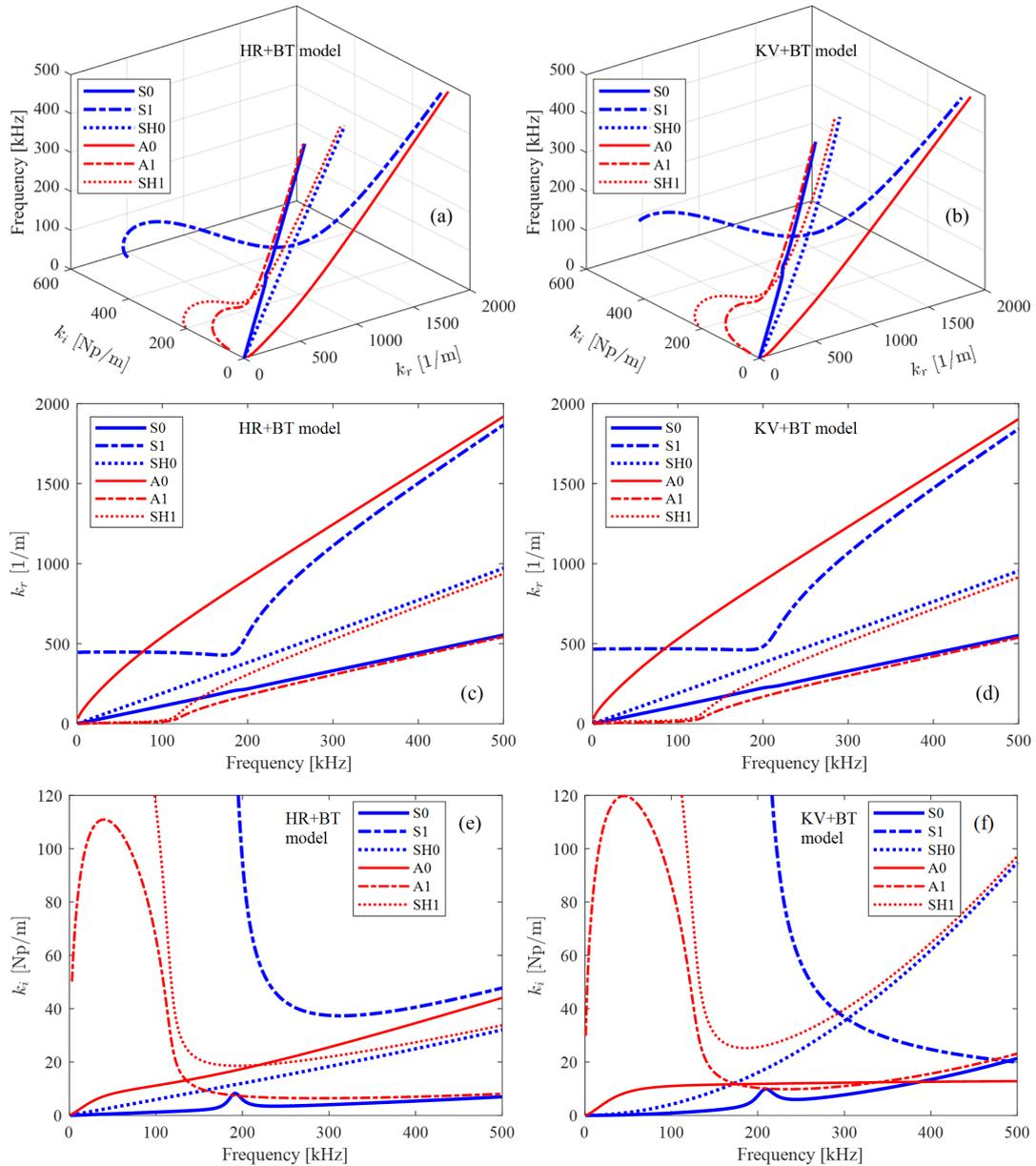


Figure 7.22 – For the unmounted IFS, the predicted dispersion curves at $\theta = 90^\circ$ for HR+BT model (left) and KV+BT model (right): (a) and (b) 3D space of (f, k_r, k_i) , (c) and (d) projection onto (f, k_r) plane, (e) and (f) projection onto (f, k_i) plane.

diagrams as HR+BT model. According to Figure 7.24(b)(f), HR+BT model predicts the attenuation of S0 and SH0 modes less than the one of KV+BT model, which is different from A0 mode in Figure 7.24(d).

The traditional curve in Figure 7.23 can be reconstructed from Figure 7.24. For instance, the S0

7.5. CASE STUDY ON AN UNMOUNTED AND MOUNTED IFS OF A380 PLANE

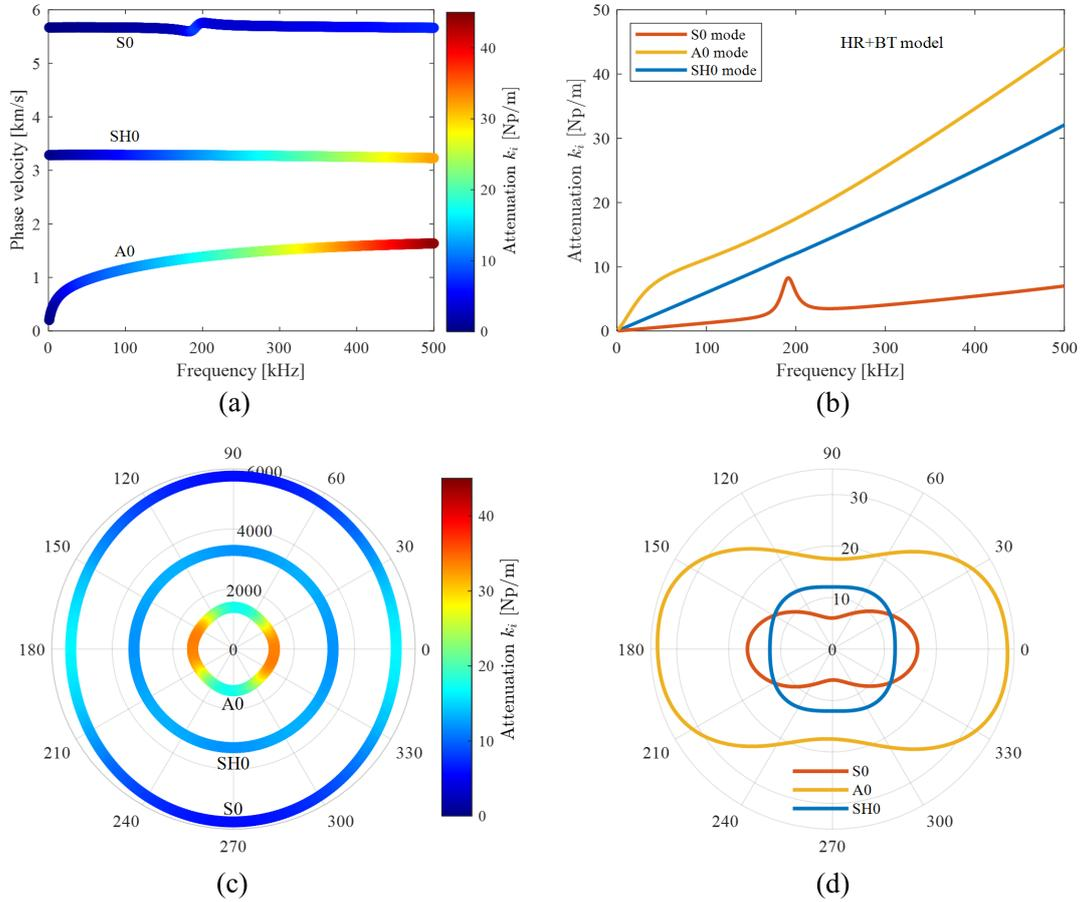


Figure 7.23 – For the unmounted IFS, HR+BT model's prediction of (a) dispersion curve of phase velocity at $\theta = 90^\circ$, (b) dispersion curve of attenuation coefficient at $\theta = 90^\circ$, (c) polar plot of phase velocity [m/s] at $f = 200$ kHz, (d) polar plot of attenuation coefficient [Np/m] at $f = 200$ kHz.

curve in Figure 7.23(b) is just the intersecting line of the plane $\theta = 90^\circ$ (in the cylindrical coordinate system) to the surface of HR+BT model in Figure 7.24(b), and the SH0 contour in Figure 7.23(d) is the intersecting line of the plane $f = 200$ kHz to the surface of HR+BT model in Figure 7.24(f). For brevity, these intersecting lines are not depicted in Figure 7.24. Thus, the frequency-spatial spectra of guided waves will convey more information than the traditional dispersion curves, and it will play a more important role in guided waves based SHM, especially for anisotropic viscoelastic materials.

7.5. CASE STUDY ON AN UNMOUNTED AND MOUNTED IFS OF A380 PLANE

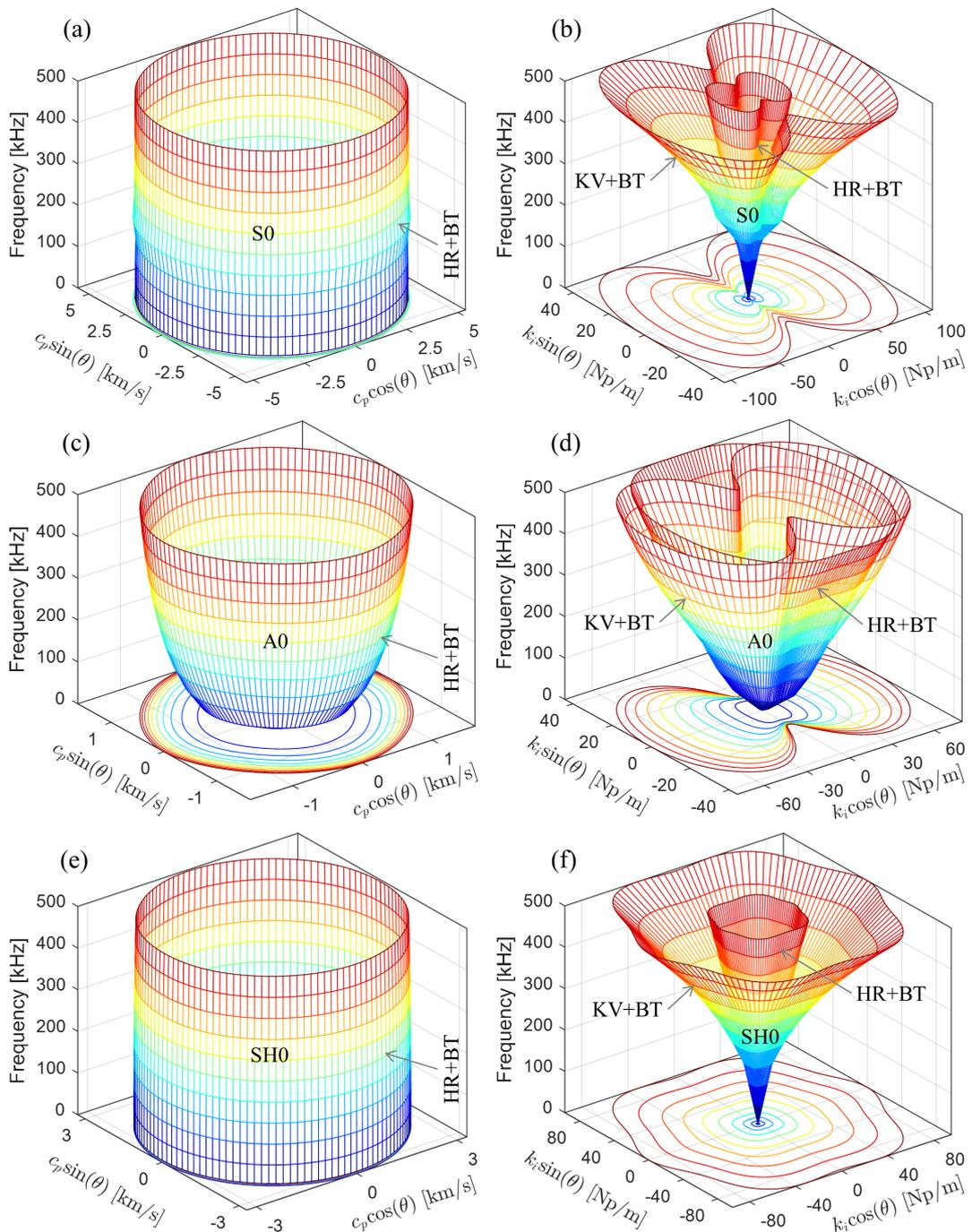


Figure 7.24 – For the unmounted IFS, surface plot of phase velocity (left) and attenuation coefficient (right): (a) and (b) S0 mode, (c) and (d) A0 mode, (e) and (f) SH0 mode.

7.6 Discussion

Although this chapter only presents the comparison results of S0 mode between the experimental and predicted data, the developed dGMM method can be generalized to other guided wave modes such as A0 and SH0 modes if these modes' information is experimentally identifiable such that the identified data can be integrated to update the viscoelastic material properties. However, simultaneously identifying S0 and A0 modes usually requires special setup of transducers from the hardware viewpoint that have flexible polarity directions, dual PZT for example [105], to sufficiently excite both fundamental modes. Besides, from the software viewpoint, any efficient decomposition algorithms are required that can separate coupled S0 and A0 wave packets in the signal processing level [93]. To acquire the SH0 wave signal, special SH wave transducers need to be utilized [20].

This chapter takes the damping effect of the elastic moduli into consideration. In some references [79, 114], the complex stiffness tensor is employed, i.e. $C_{ij}^*(\omega) = C'_{ij}(\omega) - iC''_{ij}(\omega)$, to represent the viscoelasticity of composite materials by specifying a certain damping model for the imaginary part $C''_{ij}(\omega)$. However, this utilization increases the number of variables for the model updating process, thus demanding advanced optimization algorithms [115].

In literature, KV model is increasingly adopted to compute the 3D dispersion curves in (f, k_r, k_i) domain no matter which numerical method is used [98, 79]. In contrast with this tendency, the two case studies in this chapter demonstrate that the HR involved models predict more accurate attenuation than the KV involved models in comparison with the experimental data. This fact reveals that choosing a damping model to represent the viscoelasticity of composite materials is application dependent.

7.7 Conclusion

This chapter puts forward a dGMM method to predict the frequency-spatial attenuation of guided waves in anisotropic viscoelastic composite laminates by integrating the damping models (HR, KV and BT) into the conventional pure elastic GMM. To efficiently solve the nonlinear transcendental DE, a two-step numerical algorithm is developed that combines dGMM method, 2D MRCM and the curve tracing technique. The proposed attenuation prediction approach is theoretically validated by comparing it with the SAFE method.

The energy velocities and attenuation coefficients at various frequencies are identified from recorded wave signals via LR method which can not only process multiple sensing pairs necessarily for monitoring a practical aeronautic structure but also output statistical information such as the confidence interval and correlation coefficient R^2 to assess the quality of the identified parameters. With the experimental attenuation data, the unknown viscoelastic material properties are nondestructively estimated in the least square sense to achieve the best agreement of prediction to experimental data.

Experiments on two physically different structures, the homogeneous FCS and the inhomogeneous IFS with each one unmounted or mounted on an instrumented A380 plane, were carried out to experimentally validate the proposed dGMM approach. FCS is a slightly damped structure and IFS is highly damped. The existence of stress in the mounted case can greatly change the property of attenuation as compared to the unmounted case. To consider the inhomogeneous characteristic of IFS, its core layer and skin layers are modeled by different damping models, thus two combinations of damping models (HR+BT and KV+BT) come into being. Both case studies demonstrate that the HR involved models predict more accurate attenuation than the KV involved models, and the spatial distribution of attenuation holds anisotropic property despite the quasi-isotropic stacking layups. In both structures, A0 mode undergoes much attenuation than S0 mode, thus selecting S0 mode for SHM of similar aeronautic structures is desired if the dispersion aspect is not the determining factor.

In summary, using the actual and in-service data of the practical aeronautic structures to validate the proposed attenuation prediction method is not an easy task but makes it extremely valuable for the scientific and industrial communities. In this sense, this chapter escorts the initiative of closing the gap between research and industrial deployment for SHM [54].

Chapter 8

General conclusions and perspectives

8.1 General conclusions

The thesis has presented the properties of guided waves propagating in elastic and viscoelastic composite laminates through theoretical derivation, numerical illustration and experimental validation. The focus of the thesis is placed on how to establish dispersion equations via matrix-based methods, and efficiently and stably solve dispersion equations in pure elastic and viscoelastic cases. The following conclusions and original findings are outlined.

The PWSA introduced in Chapter 3 is extended to the TMM to study the property of guided waves propagating in a multi-layered composite laminate. It combines the traction free boundary condition and perfect continuity condition. The later is formed using the transferring rule to link the field variables between adjacent layers and yields the monodromy transfer matrix of the whole plate system for applying the boundary condition. In accordance with different material types in each layer of the composite laminate, there exists three cases of guided waves, namely, the coupled Lamb and SH waves, the separated Lamb and SH waves, and the hybrid case which means that in some layers of the laminate the two wave types are coupled to each other but in another layers decoupled. The hybrid case is generally existing in a quasi-isotropic composite plate and metallic-composite plate for which metallic layers are isotropic but composite laminae are anisotropic. The standard TMM can deal with the coupled and decoupled cases, but for the hybrid case, an original HMS is proposed to address the local transfer matrix incompatibility issue. Three numerical examples are used to illustrate the three cases of guided waves coupling issues. Each example corresponds to a class of composite plates, i.e. cross-ply laminate, quasi-isotropic laminate and metallic-composite laminate.

8.1. GENERAL CONCLUSIONS

For the examples of quasi-isotropic and metallic-composite laminates, the computed dispersion curves via HMS are compared to experimental data points extracted from a classical reference, thus validating the effectiveness of HMS.

To solve the lower computational efficiency issue of the standard GMM, the optimized GMM is proposed, which simultaneously takes advantage of the symmetry condition induced global matrix, parallel computing and sparse matrix techniques. The GMM framework has proved its stability in a benchmark test based on the dataset of Open Guided Waves. This test shows the *large fd problem* of TMM. Thus, when the dispersion curves of a composite laminate at larger frequency values are interested, adopting GMM for computation is necessary. The good agreement between GMM computation and the experimental data of Open Guided Waves validates the effectiveness and feasibility of GMM.

The optimized GMM is successfully applied to an aerospace composite plate having 400 layers, which has the largest number of layers reported so far, to compute its phase velocity dispersion curves. This structure is a component of the booster pressure vessels of the rocket Ariane 6 under development. Due to the complexity of this structure, the dispersion curves experience heavy veering effect in a small region that will cause trouble when tracing the correct loci of dispersion solutions. To study this effect, the mode shape and MAC value tomography of displacement and stress are analyzed in the regions of veering effect. Analysis results show that within these regions, the dispersion solutions loci belonging to the same symmetry kind can be arbitrarily close but never cross, and this process is accompanied by a rapid exchange of their mode shapes. In comparison with stress mode shapes, displacement mode shapes are a desired indicator to distinguish the branches of dispersion diagram in the veering effect regions. An encouraging result is reported that the optimized GMM can complete computations of the 400-layered plate within half an hour in a standard workstation. This fact breaks down the common sense that GMM framework cannot be applied to laminates having a large number of layers and proves the ability of the optimized GMM in application of aerospace composite materials which usually possess many laminae.

It is furthermore demonstrated that dispersion equations built with PWSA for a single layer plate and with TMM and GMM for a multi-layered plate system hold the dichotomy property in the case of pure elastic materials. This property states that these a priori complex-valued equations collapse to pure real or imaginary valued equations, depending on the behavior of some intermediate param-

eters. This property is present in composite materials (excluding triclinic ones of few specific case) of propagating and evanescent waves, in wavenumber-phase velocity domain, frequency-wavenumber domain and frequency-phase velocity domain. For the single layer plate, dichotomy property can be analyzed through enumeration strategy that strictly follows the evolution of intermediate parameters' properties. For the multi-layered plate system, a simple sampling strategy is proposed to numerically evaluate dichotomy property. This property is extremely helpful for overcoming numerical instabilities encountered during the equation solving process. The *large fd problem* of TMM is quantitatively explored by using the methodology of studying dichotomy property. Analysis shows that the *large fd problem* of TMM is caused by the vanishing of effective part between real and imaginary parts of dispersion equation built with TMM due to the poor conditioning of the monodromy transfer matrix.

Considering the inherent viscoelasticity of composite materials, the damping effect of dispersion curves are investigated. Three damping models (Hysteretic, Kelvin-Voigt and Biot models) are integrated into the standard GMM to form an extended version, the damped GMM (dGMM). In viscoelastic case, the complex-valued dispersion equations built with dGMM have the solution pair of real frequency and complex wavenumber, and the attenuation coefficients of guided waves can be extracted from the imaginary part of the complex wavenumber. Due to the complexity of the viscoelastic case, solving the multivariate transcendental dispersion equation is mathematically intractable. To address this issue, a two-step root-finding approach is originally proposed that integrates the undamped GMM, 2D Module Ratio Convergence Method (2D MRCM) and curve tracing technique. With this approach, the 3D dispersion curves in real frequency-complex wavenumber domain can be computed. The classical SAFE method is adopted to validate the effectiveness of the proposed methodology.

In addition to the numerical computation approach, an identification method of attenuation coefficients is originally proposed that utilizes linear regression technique and is based on the propagation nature of wave displacement fields. With this method, attenuation coefficients can be experimentally identified from wave signals acquired in a pitch-catch sensor network. Considering that viscoelastic parameters of damping models are generally not available in practice, the model updating process is adopted to estimate these parameters in the least square sense that fits the experimentally identified attenuation coefficients with the dGMM such that there is a good agreement between theoretical computation and experimental identification.

The entire framework developed in the thesis is applied to two engineering structures, both are

components of A380 plane but physically different. For each structure, the dataset of mounted and unmounted cases are analyzed. The first one is a fan cowl structure (FCS) having quasi-isotropic property and the second one an inner fixed structure (IFS) being sandwich type. Analysis shows that FCS is a slightly damped structure and IFS is highly damped. The existence of stress in the mounted case can greatly change the property of attenuation as compared to the unmounted case. Two combinations of damping models (HR+BT and KV+BT) are used to consider the inhomogeneous characteristic of IFS in the first time, for which the aluminum core layer and carbon epoxy skin layers are modeled by different damping models. Both case studies demonstrate that attenuation coefficients holds anisotropic property despite the quasi-isotropic stacking layups, and A0 mode undergoes much attenuation than S0 mode. Thus, in the later deployment of SHM for similar structures, selecting S0 mode is desired in order to secure enough coverage of wave amplitudes.

In summary, using the actual and in-service data of the practical aeronautic structures to validate the proposed attenuation prediction method is not an easy task but makes it extremely valuable for the scientific and industrial communities. In this sense, this paper escorts the initiative of closing the gap between research and industrial deployment for SHM [54].

8.2 Perspectives

There are considerable works to be done in the future to achieve the application value of the thesis in engineering practice.

As an evolved version of TMM and GMM, the stiffness matrix method (SMM) [36, 11] will be implemented to complete the family of matrix-based methods for modelling guided waves propagation in composite laminates. The incompatibility issue in SMM will be checked and how to address this issue will be studied. Benchmark tests can be performed to validate the stability of SMM. Extending it to the viscoelastic case is worthwhile to do and comparing its performance with dGMM shall provide further recommendations for improvement.

More profound viscoelastic damping models should be integrated into dGMM to exactly predict attenuation of complex structures, e.g. the rational model [116] described in Eq. (8.1). Implementation of this model has the following two fatal issues:

- There is not a unique principle to determine the number of parameters n in Eq. (8.1).

- Even if n is given, it is still difficult to estimate the coefficients α_i and β_i from experimental attenuation data through the model updating process, unless these coefficients are directly provided.

$$E^*(\omega) = E \left[\frac{1 + \sum_{i=1}^n \beta_i (i\omega)^i}{1 + \sum_{i=1}^n \alpha_i (i\omega)^i} \right] \quad (8.1)$$

To implement the rational model for attenuation prediction, the mechanism of it should be studied firstly. As an alternative, implementing the standard linear solid (SLS) model [117, 118] expressed in Eq. (8.2) is achievable.

$$E^*(\omega) = E \frac{1 - i\omega\tau_\epsilon}{1 - i\omega\tau_\sigma} \quad (8.2)$$

where, τ_ϵ and τ_σ are the creep time and the stress relaxation time, respectively.

Extending the matrix-based methods to release an open source dispersion tool is a promising work. This tool should include the pre-processing module for easily defining model information (material and structure properties), high efficiency computation module, and user-friendly post-processing module for visualization of results (modal curve tracing and classification, animation of wave mode shapes, etc.). Some basic functionalities have been achieved in the thesis such as displaying dispersion diagram in $\xi - v$, $f - \xi$, $f - v$, $f - c_g$, $f - c_e$, $f - k_r - k_i$ domains, as well as in polar plot format $\theta - v$ and $\theta - k_i$ domains. Other extension of functionalities can be anticipated, for instance, computing the steering angle between phase velocity and group velocity directions which is a special concept existing in anisotropic composite plates [37]. A comprehensive comparison between the released dispersion tool with discrete methods, e.g. SAFE, should be conducted for validation purpose.

Some advanced signal processing methods will be adopted to replace the linear regression based attenuation identification method. The advanced methods are good candidates for experimentally identifying attenuation coefficients, for example, the matrix pencil method [93] and the estimation of signal parameters via rotational invariance techniques (ESPRIT) [119, 78]. These methods can simultaneously identify attenuation coefficient and propagating wavenumber. With more information identified, the model parameters can be estimated more precisely through model updating process, and thus producing more accurate predictions.

Due to the existence of uncertainties, the predicted energy velocity and attenuation coefficient do

not always match well simultaneously with the respective experimental data (see Figure 7.20). In this situation, the model updating process should yet involve in the identified energy velocity and the elastic constants. That finally leads to the multiple objective optimization problem as presented in Eq. (8.3). To conduct this work, some advanced optimization algorithms will be utilized [115, 120].

$$\hat{\gamma} = \arg \min_{\gamma, E_i, G_{ij}, \nu_{ij}} \left\{ \begin{array}{l} \sum_{l=1}^m [\mathcal{K}(\gamma, \omega_l) - \hat{k}_{i,l}]^2 \\ \sum_{l=1}^m [\mathcal{C}_e(\gamma, \omega_l) - \hat{c}_{e,l}]^2 \end{array} \right\} \quad (8.3)$$

Figures 7.14(d) and 7.23(d) shows that even if many aeronautic composite plates are designed and manufactured as quasi-isotropic property, attenuation of guided waves presents anisotropy in terms of spatial distribution. This property can affect the layout of sensors on distance, orientation, number and so on. Indeed, when designing a sensor network, one faces two practical issues: the first one is to get sure that all the structure under study will be covered by guided waves and thus that any potential damage position can be inspected [18]; the second one is to get sure that guided waves with enough amplitude will be reflected from the damage toward piezoelectric elements [19]. When designing sensor networks, the distance between sensors can be appropriately larger along the orientations of lower attenuation; but along the orientations of larger attenuation, sensors should be placed densely as much as possible to guarantee enough coverage of wave fields, thus increasing the number of sensors. The future work on optimal sensor network deployment procedures will take these factors into account. The attenuation prediction method developed in the thesis paves the way to perform this work. A preliminary idea is stated here. The maximum coverage of wave fields in a composite plate can be designed as the objective function [121], with the optimization variables of sensor locations and number [122]. The predicted spatially dependent attenuation will be designed as restriction conditions of the optimization problem which restricts that at each sensing path of interest, the attenuated wave amplitude should be higher than a preset threshold value in order to keep a sufficient signal to noise ratio (SNR).

Last but not least, improving the traditional damage localization methods such as delay-and-sum [123], RAPID [87] and Excitelet [124] by taking the viscoelasticity of composite materials into consideration is always of prime importance. Among these methods, temporal or frequency information is necessary, for instance, time of flight (ToF) for delay-and-sum [125] and wavenumber analysis for Excitelet [126]. The temporal information can be obtained from the prediction of phase velocity and group velocity dispersion diagrams [127], and the frequency information required for wavenumber

analysis is the output of the dispersion solutions in frequency-wavenumber domain [128]. In anisotropic viscoelastic plates, the existence of wave attenuation can change properties of temporal and frequency-related quantities. Thus, improvement can be made by bridging the gap between the temporal- or frequency-based damage localization methods and the viscoelastic wave propagation models studied in the thesis. This leaves the ongoing works.

8.3 Publications related to the thesis

This section groups together the various publications that are related to the thesis presented here.

Journal papers

- S. Guo, M. Rébillat, N. Mechbal, “Dichotomy property of dispersion equation of guided waves propagating in anisotropic composite plates”, *Mechanical Systems and Signal Processing*, 2022, 164: 108212.
- S. Guo, M. Rébillat and N. Mechbal, “Prediction of frequency and spatially dependent attenuation of guided waves propagating in mounted and unmounted A380 parts made up of anisotropic viscoelastic composite laminates”, Submitted to *Structural Health Monitoring*, under review.

Conference paper

- S. Guo, M. Rébillat, N. Mechbal, “Spatial attenuation prediction of Lamb waves in composite materials”, *The 9th ECCOMAS Thematic Conference on Smart Structures and Materials*, Paris, France, July 8-12, 2019.

8.3. PUBLICATIONS RELATED TO THE THESIS

Bibliography

- [1] F.-G. Yuan, *Structural health monitoring (SHM) in aerospace structures*. Woodhead Publishing, 2016.
- [2] V. Giurgiutiu, *Structural health monitoring of aerospace composites*. Academic Press, 2015.
- [3] C. Fendzi, “Structural health monitoring of composite structures: application to the monitoring of aeronautical nacelles,” Thèse de doctorat, ENSAM, 2015.
- [4] R. Lammering *et al.*, *Lamb-wave based structural health monitoring in polymer composites*. Springer, 2017.
- [5] Z. Su et L. Ye, *Identification of damage using Lamb waves: from fundamentals to applications*. Springer Science & Business Media, 2009, vol. 48.
- [6] M. J. Lowe, “Matrix techniques for modeling ultrasonic waves in multilayered media,” *IEEE transactions on ultrasonics, ferroelectrics, and frequency control*, vol. 42, n°. 4, p. 525–542, 1995.
- [7] I. Bartoli *et al.*, “Modeling wave propagation in damped waveguides of arbitrary cross-section,” *Journal of sound and vibration*, vol. 295, n°. 3-5, p. 685–707, 2006.
- [8] S. Pant *et al.*, “Derivation and experimental validation of lamb wave equations for an n-layered anisotropic composite laminate,” *Composite Structures*, vol. 111, p. 566–579, 2014.
- [9] D. Barazanchy et V. Giurgiutiu, “A unified formulation for predictive modeling of guided-ultrasonic wave dispersion curves in metallic and composite materials,” *Journal of Intelligent Material Systems and Structures*, vol. 28, n°. 10, p. 1272–1286, 2017.
- [10] A. R. Nandyala, A. K. Darpe et S. P. Singh, “Effective stiffness matrix method for predicting the dispersion curves in general anisotropic composites,” *Archive of Applied Mechanics*, vol. 89, n°. 9, p. 1923–1938, 2019.

BIBLIOGRAPHY

- [11] A. M. Huber et M. G. Sause, “Classification of solutions for guided waves in anisotropic composites with large numbers of layers,” *The Journal of the Acoustical Society of America*, vol. 144, n^o. 6, p. 3236–3251, 2018.
- [12] J. L. Rose, *Ultrasonic guided waves in solid media*. Cambridge university press, 2014.
- [13] C. R. Farrar et K. Worden, “An introduction to structural health monitoring,” *New Trends in Vibration Based Structural Health Monitoring*, p. 1–17, 2010.
- [14] D. L. Balageas, “Structural health monitoring r&d at the “european research establishments in aeronautics”(erea),” *Aerospace science and technology*, vol. 6, n^o. 3, p. 159–170, 2002.
- [15] J. Gray et G.-R. Tillack, “X-ray imaging methods over the last 25 years—new advances and capabilities,” dans *AIP Conference Proceedings*, vol. 557, n^o. 1. American Institute of Physics, 2001, p. 16–32.
- [16] H. Sohn *et al.*, “A review of structural health monitoring literature: 1996–2001,” *Los Alamos National Laboratory, USA*, vol. 1, 2003.
- [17] B. A. Auld, *Acoustic fields and waves in solids*. John Wiley and Sons, 1973.
- [18] M. Mitra et S. Gopalakrishnan, “Guided wave based structural health monitoring: A review,” *Smart Materials and Structures*, vol. 25, n^o. 5, p. 053001, 2016.
- [19] Z. Su, L. Ye et Y. Lu, “Guided lamb waves for identification of damage in composite structures: A review,” *Journal of sound and vibration*, vol. 295, n^o. 3-5, p. 753–780, 2006.
- [20] H. Miao et F. Li, “Shear horizontal wave transducers for structural health monitoring and non-destructive testing: A review,” *Ultrasonics*, p. 106355, 2021.
- [21] P. Wilcox, M. Lowe et P. Cawley, “The effect of dispersion on long-range inspection using ultrasonic guided waves,” *NDT & E International*, vol. 34, n^o. 1, p. 1–9, 2001.
- [22] K. Luangvilai, *Attenuation of ultrasonic Lamb waves with applications to material characterization and condition monitoring*. Georgia Institute of Technology, 2007.
- [23] L. Rayleigh, “On waves propagated along the plane surface of an elastic solid,” *Proceedings of the London mathematical Society*, vol. 1, n^o. 1, p. 4–11, 1885.
- [24] R. Lord, *The theory of sound*. Dover, New York, 1945.
- [25] A. E. H. Love, *Some Problems of Geodynamics: Being an Essay to which the Adams Prize in the University of Cambridge was Adjudged in 1911*. University Press, 1911, vol. 911.

BIBLIOGRAPHY

- [26] H. Lamb, “On waves in an elastic plate,” *Proceedings of the Royal Society of London. Series A, Containing papers of a mathematical and physical character*, vol. 93, n^o. 648, p. 114–128, 1917.
- [27] R. Stoneley, “Elastic waves at the surface of separation of two solids,” *Proceedings of the Royal Society of London. Series A, Containing Papers of a Mathematical and Physical Character*, vol. 106, n^o. 738, p. 416–428, 1924.
- [28] W. L. Pilant, *Elastic waves in the earth*. Elsevier, 2012, vol. 11.
- [29] H. Zhu, “Elastic wavefield separation based on the helmholtz decomposition,” *Geophysics*, vol. 82, n^o. 2, p. S173–S183, 2017.
- [30] E. Lizé *et al.*, “Optimal dual-pzt sizing and network design for baseline-free shm of complex anisotropic composite structures,” *Smart Materials and Structures*, vol. 27, n^o. 11, p. 115018, 2018.
- [31] A. Raghavan et C. E. Cesnik, “Finite-dimensional piezoelectric transducer modeling for guided wave based structural health monitoring,” *Smart materials and structures*, vol. 14, n^o. 6, p. 1448, 2005.
- [32] N. A. Haskell, “The dispersion of surface waves on multilayered media,” *Bulletin of the seismological Society of America*, vol. 43, n^o. 1, p. 17–34, 1953.
- [33] A. H. Nayfeh, *Wave propagation in layered anisotropic media: With application to composites*. Elsevier, 1995.
- [34] L. Knopoff, “A matrix method for elastic wave problems,” *Bulletin of the Seismological Society of America*, vol. 54, n^o. 1, p. 431–438, 1964.
- [35] L. Wang et S. Rokhlin, “Stable reformulation of transfer matrix method for wave propagation in layered anisotropic media,” *Ultrasonics*, vol. 39, n^o. 6, p. 413–424, 2001.
- [36] S. Rokhlin et L. Wang, “Stable recursive algorithm for elastic wave propagation in layered anisotropic media: Stiffness matrix method,” *The Journal of the Acoustical Society of America*, vol. 112, n^o. 3, p. 822–834, 2002.
- [37] L. Wang et F. Yuan, “Group velocity and characteristic wave curves of lamb waves in composites: Modeling and experiments,” *Composites science and technology*, vol. 67, n^o. 7-8, p. 1370–1384, 2007.

BIBLIOGRAPHY

- [38] A. Maghsoodi, A. Ohadi et M. Sadighi, “Calculation of wave dispersion curves in multilayered composite-metal plates,” *Shock and Vibration*, vol. 2014, 2014.
- [39] B. Pavlakovic et M. Lowe, “Disperse: User’s manual version 2.0. 11, imperial college, university of london,” *Non-Destructive Testing Laboratory*, vol. 3, 2001.
- [40] D. Barazanchy et V. Giurgiutiu, “A comparative convergence and accuracy study of composite guided-ultrasonic wave solution methods: Comparing the unified analytic method, safe method and disperse,” *Proceedings of the Institution of Mechanical Engineers, Part C: Journal of Mechanical Engineering Science*, vol. 231, n^o. 16, p. 2961–2973, 2017.
- [41] D. R. Ramasawmy, B. T. Cox et B. E. Treeby, “Elasticmatrix: A matlab toolbox for anisotropic elastic wave propagation in layered media,” *SoftwareX*, vol. 11, p. 100397, 2020.
- [42] A. Kamal et V. Giurgiutiu, “Stiffness transfer matrix method (stmm) for stable dispersion curves solution in anisotropic composites,” dans *Health Monitoring of Structural and Biological Systems 2014*, vol. 9064. International Society for Optics and Photonics, 2014, p. 906410.
- [43] P. Bocchini, A. Marzani et E. Viola, “Graphical user interface for guided acoustic waves,” *Journal of Computing in Civil Engineering*, vol. 25, n^o. 3, p. 202–210, 2011.
- [44] F. H. Quintanilla *et al.*, “Guided waves’ dispersion curves in anisotropic viscoelastic single-and multi-layered media,” *Proceedings of the Royal Society A: Mathematical, Physical and Engineering Sciences*, vol. 471, n^o. 2183, p. 20150268, 2015.
- [45] F. H. Quintanilla, M. Lowe et R. Craster, “Modeling guided elastic waves in generally anisotropic media using a spectral collocation method,” *The Journal of the Acoustical Society of America*, vol. 137, n^o. 3, p. 1180–1194, 2015.
- [46] B. R. Mace et E. Manconi, “Modelling wave propagation in two-dimensional structures using finite element analysis,” *Journal of Sound and Vibration*, vol. 318, n^o. 4-5, p. 884–902, 2008.
- [47] Ş. Soroğan *et al.*, “Extraction of dispersion curves for waves propagating in free complex waveguides by standard finite element codes,” *Ultrasonics*, vol. 51, n^o. 4, p. 503–515, 2011.
- [48] L. Wang et F. Yuan, “Lamb wave propagation in composite laminates using a higher-order plate theory,” dans *Nondestructive Characterization for Composite Materials, Aerospace Engineering, Civil Infrastructure, and Homeland Security 2007*, vol. 6531. International Society for Optics and Photonics, 2007, p. 65310I.

- [49] J. Zhao, H. Ji et J. Qiu, “Modeling of lamb waves in composites using new third-order plate theories,” *Smart materials and structures*, vol. 23, n^o. 4, p. 045017, 2014.
- [50] P. Stoklasová *et al.*, “Forward and inverse problems for surface acoustic waves in anisotropic media: A ritz–rayleigh method based approach,” *Ultrasonics*, vol. 56, p. 381–389, 2015.
- [51] T. Grabec, P. Sedlák et H. Seiner, “Application of the ritz–rayleigh method for lamb waves in extremely anisotropic media,” *Wave Motion*, vol. 96, p. 102567, 2020.
- [52] V. K. Tewary, “Green’s-function method for modeling surface acoustic wave dispersion in anisotropic material systems and determination of material parameters,” *Wave Motion*, vol. 40, n^o. 4, p. 399–412, 2004.
- [53] A. Karmazin *et al.*, “Investigation of lamb elastic waves in anisotropic multilayered composites applying the green’s matrix,” *Ultrasonics*, vol. 51, n^o. 1, p. 17–28, 2011.
- [54] P. Cawley, “Structural health monitoring: Closing the gap between research and industrial deployment,” *Structural Health Monitoring*, vol. 17, n^o. 5, p. 1225–1244, 2018.
- [55] R. F. Gibson, *Principles of composite material mechanics*. CRC press, 2016.
- [56] A. Jeffrey, *Matrix operations for engineers and scientists: an essential guide in linear algebra*. Springer Science & Business Media, 2010.
- [57] K. S. Nadella, K. I. Salas et C. E. Cesnik, “Characterization of guided-wave propagation in composite plates,” dans *Health Monitoring of Structural and Biological Systems 2010*, vol. 7650. International Society for Optics and Photonics, 2010, p. 76502H.
- [58] A. H. Nayfeh et D. E. Chimenti, “Free wave propagation in plates of general anisotropic media,” *Journal of applied mechanics*, vol. 56, p. 881–886, 1989.
- [59] D. E. Muller, “A method for solving algebraic equations using an automatic computer,” *Mathematical tables and other aids to computation*, vol. 10, n^o. 56, p. 208–215, 1956.
- [60] X.-M. Niu et T. Sakurai, “A method for finding the zeros of polynomials using a companion matrix,” *Japan journal of industrial and applied mathematics*, vol. 20, n^o. 2, p. 239–256, 2003.
- [61] F. Zhu *et al.*, “Waves in a generally anisotropic viscoelastic composite laminated bilayer: Impact of the imperfect interface from perfect to complete delamination,” *International Journal of Solids and Structures*, vol. 202, p. 262–277, 2020.

BIBLIOGRAPHY

- [62] J. Moll *et al.*, “Open guided waves: online platform for ultrasonic guided wave measurements,” *Structural Health Monitoring*, vol. 18, n^o. 5-6, p. 1903–1914, 2019.
- [63] C. T. Sun et S. Li, “Three-dimensional effective elastic constants for thick laminates,” *Journal of Composite Materials*, vol. 22, n^o. 7, p. 629–639, 1988.
- [64] F. Hernando Quintanilla, M. Lowe et R. Craster, “The symmetry and coupling properties of solutions in general anisotropic multilayer waveguides,” *The Journal of the Acoustical Society of America*, vol. 141, n^o. 1, p. 406–418, 2017.
- [65] M. Herlihy *et al.*, *The art of multiprocessor programming*. Newnes, 2020.
- [66] E. Manconi et S. Sorokin, “On the effect of damping on dispersion curves in plates,” *International Journal of Solids and Structures*, vol. 50, n^o. 11-12, p. 1966–1973, 2013.
- [67] H. Überall *et al.*, “Repulsion of phase-velocity dispersion curves and the nature of plate vibrations,” *The Journal of the Acoustical Society of America*, vol. 96, n^o. 2, p. 908–917, 1994.
- [68] T. Zharnikov et D. Syresin, “Repulsion of dispersion curves of quasidipole modes of anisotropic waveguides studied by finite element method,” *The Journal of the Acoustical Society of America*, vol. 137, n^o. 6, p. EL396–EL402, 2015.
- [69] E. Kausel, P. Malischewsky et J. Barbosa, “Osculations of spectral lines in a layered medium,” *Wave Motion*, vol. 56, p. 22–42, 2015.
- [70] M. Lowe et B. Pavlakovic, *Disperse User’s Manual Version 2.0.20a*. Imperial College London, London, 2013.
- [71] D. J. Ewins, *Modal testing: theory, practice and application*. John Wiley & Sons, 2009.
- [72] G. Neau, “Lamb waves in anisotropic viscoelastic plates. study of the wave fronts and attenuation,” Thèse de doctorat, L’Universite de Bordeaux, 2003.
- [73] S. Guo, M. Rébillat et N. Mechbal, “Dichotomy property of dispersion equation of guided waves propagating in anisotropic composite plates,” *Mechanical Systems and Signal Processing*, vol. 164, p. 108212, 2022.
- [74] M. J. Lowe, “Plate waves for the ntd of diffusion bonded titanium,” Thèse de doctorat, Imperial College London, 1992.

BIBLIOGRAPHY

- [75] F. Zhu, B. Wang et Z.-h. Qian, “A numerical algorithm to solve multivariate transcendental equation sets in complex domain and its application in wave dispersion curve characterization,” *Acta Mechanica*, vol. 230, n^o. 4, p. 1303–1321, 2019.
- [76] C. Hakoda et C. J. Lissenden, “Using the partial wave method for wave structure calculation and the conceptual interpretation of elastodynamic guided waves,” *Applied Sciences*, vol. 8, n^o. 6, p. 966, 2018.
- [77] Y. Li et R. B. Thompson, “Influence of anisotropy on the dispersion characteristics of guided ultrasonic plate modes,” *The Journal of the Acoustical Society of America*, vol. 87, n^o. 5, p. 1911–1931, 1990.
- [78] P. Margerit *et al.*, “The high-resolution wavevector analysis for the characterization of the dynamic response of composite plates,” *Journal of Sound and Vibration*, vol. 458, p. 177–196, 2019.
- [79] H. Mei et V. Giurgiutiu, “Guided wave excitation and propagation in damped composite plates,” *Structural Health Monitoring*, vol. 18, n^o. 3, p. 690–714, 2019.
- [80] F. H. Quintanilla, M. Lowe et R. Craster, “Full 3d dispersion curve solutions for guided waves in generally anisotropic media,” *Journal of Sound and Vibration*, vol. 363, p. 545–559, 2016.
- [81] X. Yan et F.-G. Yuan, “Conversion of evanescent lamb waves into propagating waves via a narrow aperture edge,” *The Journal of the Acoustical Society of America*, vol. 137, n^o. 6, p. 3523–3533, 2015.
- [82] V. Giurgiutiu et M. F. Haider, “Propagating, evanescent, and complex wavenumber guided waves in high-performance composites,” *Materials*, vol. 12, n^o. 2, p. 269, 2019.
- [83] K. J. Schubert et A. S. Herrmann, “On attenuation and measurement of lamb waves in viscoelastic composites,” *Composite Structures*, vol. 94, n^o. 1, p. 177–185, 2011.
- [84] K. Asamene, L. Hudson et M. Sundaresan, “Influence of attenuation on acoustic emission signals in carbon fiber reinforced polymer panels,” *Ultrasonics*, vol. 59, p. 86–93, 2015.
- [85] P. Sreekumar *et al.*, “Attenuation of ao lamb mode in hybrid structural composites with nanofillers,” *Composite Structures*, vol. 132, p. 198–204, 2015.

- [86] P. Wilcox, M. Lowe et P. Cawley, “Mode and transducer selection for long range lamb wave inspection,” *Journal of intelligent material systems and structures*, vol. 12, n^o. 8, p. 553–565, 2001.
- [87] M. Rébillat et N. Mechbal, “Damage localization in geometrically complex aeronautic structures using canonical polyadic decomposition of lamb wave difference signal tensors,” *Structural Health Monitoring*, vol. 19, n^o. 1, p. 305–321, 2020.
- [88] M. Haywood-Alexander *et al.*, “Structured machine learning tools for modelling characteristics of guided waves,” *Mechanical Systems and Signal Processing*, vol. 156, p. 107628, 2021.
- [89] M. Gresil et V. Giurgiutiu, “Prediction of attenuated guided waves propagation in carbon fiber composites using rayleigh damping model,” *Journal of Intelligent Material Systems and Structures*, vol. 26, n^o. 16, p. 2151–2169, 2015.
- [90] A. Treviso *et al.*, “Damping in composite materials: Properties and models,” *Composites Part B: Engineering*, vol. 78, p. 144–152, 2015.
- [91] C. Ramadas *et al.*, “Modelling of attenuation of lamb waves using rayleigh damping: Numerical and experimental studies,” *Composite Structures*, vol. 93, n^o. 8, p. 2020–2025, 2011.
- [92] A. Mardanshahi, M. Shokrieh et S. Kazemirad, “Simulated lamb wave propagation method for nondestructive monitoring of matrix cracking in laminated composites,” *Structural Health Monitoring*, p. 14759217211008620, 2021.
- [93] X. Cao, L. Zeng et J. Lin, “Lamb wave mode decomposition and reconstruction based on the viscoelastic propagation model,” *Structural Health Monitoring*, vol. 20, n^o. 1, p. 25–45, 2021.
- [94] F. Zhu *et al.*, “Accurate characterization of 3d dispersion curves and mode shapes of waves propagating in generally anisotropic viscoelastic/elastic plates,” *International Journal of Solids and Structures*, vol. 150, p. 52–65, 2018.
- [95] M. Castaings et B. Hosten, “Guided waves propagating in sandwich structures made of anisotropic, viscoelastic, composite materials,” *The Journal of the Acoustical Society of America*, vol. 113, n^o. 5, p. 2622–2634, 2003.
- [96] P. T. Birgani, S. Sodagar et M. Shishesaz, “Generation of low-attenuation lamb wave modes in three-layer adhesive joints,” *International Journal of Acoustics and Vibrations*, vol. 22, p. 51–57, 2017.

BIBLIOGRAPHY

- [97] S. Dahmen, M. B. Amor et M. H. B. Ghozlen, “Investigation of the coupled lamb waves propagation in viscoelastic and anisotropic multilayer composites by legendre polynomial method,” *Composite Structures*, vol. 153, p. 557–568, 2016.
- [98] S. Dahmen et C. Glorieux, “Optimization of coupled lamb wave parameters for defect detection in anisotropic composite three-layer with kelvin-voigt viscoelasticity using legendre polynomial method,” *Composite Structures*, vol. 272, p. 114158, 2021.
- [99] X. Zhang *et al.*, “Full dispersion and characteristics of complex guided waves in functionally graded piezoelectric plates,” *Journal of Intelligent Material Systems and Structures*, vol. 30, n^o. 10, p. 1466–1480, 2019.
- [100] M. Calomfirescu et A. Herrmann, “On the propagation of lamb waves in viscoelastic composites for shm applications,” dans *Key Engineering Materials*, vol. 347. Trans Tech Publ, 2007, p. 543–548.
- [101] M. A. Torres-Arredondo et C.-P. Fritzen, “A viscoelastic plate theory for the fast modelling of lamb wave solutions in ndt/shm applications,” *Ultragarsas” Ultrasound*, vol. 66, n^o. 2, p. 7–13, 2011.
- [102] A. H. Orta *et al.*, “Modelling lamb wave propagation in visco-elastic composite plates using a fifth-order plate theory,” *Ultrasonics*, p. 106482, 2021.
- [103] E. Manconi et B. R. Mace, “Estimation of the loss factor of viscoelastic laminated panels from finite element analysis,” *Journal of Sound and Vibration*, vol. 329, n^o. 19, p. 3928–3939, 2010.
- [104] L. Taupin, A. Lhémy et G. Inquiété, “A detailed study of guided wave propagation in a viscoelastic multilayered anisotropic plate,” dans *Journal of Physics: Conference Series*, vol. 269, n^o. 1. IOP Publishing, 2011, p. 012002.
- [105] K. Ono et A. Gallego, “Attenuation of lamb waves in cfrp plates.” *Journal of Acoustic emission*, vol. 30, 2012.
- [106] F. Mastroddi *et al.*, “Time-and frequency-domain linear viscoelastic modeling of highly damped aerospace structures,” *Mechanical Systems and Signal Processing*, vol. 122, p. 42–55, 2019.
- [107] A. Bernard, M. Lowe et M. Deschamps, “Guided waves energy velocity in absorbing and non-absorbing plates,” *The Journal of the Acoustical Society of America*, vol. 110, n^o. 1, p. 186–196, 2001.

BIBLIOGRAPHY

- [108] A. V. Boiko *et al.*, “Measurement method of complex viscoelastic material properties,” *International Journal of Solids and Structures*, vol. 47, n^o. 3-4, p. 374–382, 2010.
- [109] D. Montalvão *et al.*, “Experimental measurement of the complex young’s modulus on a cfrp laminate considering the constant hysteretic damping model,” *Composite Structures*, vol. 97, p. 91–98, 2013.
- [110] C. Ramadas, “Three-dimensional modeling of lamb wave attenuation due to material and geometry in composite laminates,” *Journal of Reinforced Plastics and Composites*, vol. 33, n^o. 9, p. 824–835, 2014.
- [111] L. Yu et V. Giurgiutiu, “Advanced signal processing for enhanced damage detection with piezoelectric wafer active sensors,” *Smart Structures and Systems*, vol. 1, n^o. 2, p. 185–215, 2005.
- [112] J. K. Agrahari et S. Kapuria, “A refined lamb wave time-reversal method with enhanced sensitivity for damage detection in isotropic plates,” *Journal of Intelligent Material Systems and Structures*, vol. 27, n^o. 10, p. 1283–1305, 2016.
- [113] N. Gandhi, J. E. Michaels et S. J. Lee, “Acoustoelastic lamb wave propagation in biaxially stressed plates,” *The Journal of the Acoustical Society of America*, vol. 132, n^o. 3, p. 1284–1293, 2012.
- [114] K. S. Ledi *et al.*, “An identification method for frequency dependent material properties of viscoelastic sandwich structures,” *Journal of Sound and Vibration*, vol. 428, p. 13–25, 2018.
- [115] J. Zhao, J. Qiu et H. Ji, “Reconstruction of the nine stiffness coefficients of composites using a laser generation based imaging method,” *Composites Science and Technology*, vol. 126, p. 27–34, 2016.
- [116] B. E et L. JM, “Viscoelastic vibration toolbox for use with matlab, user’s guide version 1.0,” <http://www.sdtools.com> Retrieved October 27, 2021.
- [117] E. Pan *et al.*, “Mode selection of guided waves for ultrasonic inspection of gas pipelines with thick coating,” *Mechanics of Materials*, vol. 31, n^o. 3, p. 165–174, 1999.
- [118] J. M. Carcione, S. Picotti et J. Ba, “P-and s-wave simulation using a cole–cole model to incorporate thermoelastic attenuation and dispersion,” *The Journal of the Acoustical Society of America*, vol. 149, n^o. 3, p. 1946–1954, 2021.

- [119] P. Margerit *et al.*, “High resolution wavenumber analysis (hrwa) for the mechanical characterisation of viscoelastic beams,” *Journal of Sound and Vibration*, vol. 433, p. 198–211, 2018.
- [120] Q. Chen, K. Xu et D. Ta, “High-resolution lamb waves dispersion curves estimation and elastic property inversion,” *Ultrasonics*, vol. 115, p. 106427, 2021.
- [121] M. Ghyabi, H. Nemati et E. Dehghan-Niri, “A simplified framework for prediction of sensor network coverage in real-time structural health monitoring of plate-like structures,” *Structural Health Monitoring*, p. 14759217211033217, 2021.
- [122] C. Yang, “Sensor placement for structural health monitoring using hybrid optimization algorithm based on sensor distribution index and fe grids,” *Structural Control and Health Monitoring*, vol. 25, n^o. 6, p. e2160, 2018.
- [123] J. E. Michaels et T. E. Michaels, “Damage localization in inhomogeneous plates using a sparse array of ultrasonic transducers,” dans *AIP Conference Proceedings*, vol. 894, n^o. 1. American Institute of Physics, 2007, p. 846–853.
- [124] N. Quaegebeur *et al.*, “Dispersion-based imaging for structural health monitoring using sparse and compact arrays,” *Smart Materials and Structures*, vol. 20, n^o. 2, p. 025005, 2011.
- [125] J. E. Michaels, “Detection, localization and characterization of damage in plates with an in situ array of spatially distributed ultrasonic sensors,” *Smart Materials and Structures*, vol. 17, n^o. 3, p. 035035, 2008.
- [126] N. Quaegebeur, P. Ostiguy et P. Masson, “Correlation-based imaging technique for fatigue monitoring of riveted lap-joint structure,” *Smart Materials and Structures*, vol. 23, n^o. 5, p. 055007, 2014.
- [127] L. Zeng *et al.*, “Determination of lamb wave phase velocity dispersion using time–frequency analysis,” *Smart Materials and Structures*, vol. 28, n^o. 11, p. 115029, 2019.
- [128] H. Mei et V. Giurgiutiu, “Characterization of multilayer delaminations in composites using wavenumber analysis: numerical and experimental studies,” *Structural Health Monitoring*, vol. 20, n^o. 3, p. 1004–1029, 2021.

BIBLIOGRAPHY

Appendix A

Proof of the properties of the intermediate parameters in Section 6.2.3

Property 1 is trivial. One just needs to check Eq. (3.27) for calculating V_r , W_r and Eq. (3.31) for calculating β_{1r} , β_{2r} , β_{3r} , meanwhile keep in mind that all the algebraic manipulations in Eqs. (3.27) and (3.31) only involving in real numbers if α_r is a real number.

For the Property 2, set $\alpha_r = ia_r$, here a_r is a real number, and substitute it into Eq. (3.27) to make the following derivations.

$$\begin{aligned}
 V_r &= \frac{K_{11}(ia_r)K_{23}(ia_r) - K_{12}(ia_r)K_{13}(ia_r)}{K_{13}(ia_r)K_{22}(ia_r) - K_{12}(ia_r)K_{23}(ia_r)} \\
 &= \frac{(C_{11} - \rho v^2 - C_{55}a_r^2)(C_{36} + C_{45})ia_r - (C_{16} - C_{45}a_r^2)(C_{13} + C_{55})ia_r}{(C_{13} + C_{55})ia_r(C_{66} - \rho v^2 - C_{44}a_r^2) - (C_{16} - C_{45}a_r^2)(C_{36} + C_{45})ia_r} \\
 &= \frac{(C_{11} - \rho v^2 - C_{55}a_r^2)(C_{36} + C_{45}) - (C_{16} - C_{45}a_r^2)(C_{13} + C_{55})}{(C_{13} + C_{55})(C_{66} - \rho v^2 - C_{44}a_r^2) - (C_{16} - C_{45}a_r^2)(C_{36} + C_{45})} \\
 &\Rightarrow \text{a real number}
 \end{aligned}$$

$$\begin{aligned}
 W_r &= \frac{K_{11}(ia_r)K_{23}(ia_r) - K_{12}(ia_r)K_{13}(ia_r)}{K_{12}(ia_r)K_{33}(ia_r) - K_{13}(ia_r)K_{23}(ia_r)} \\
 &= \frac{(C_{11} - \rho v^2 - C_{55}a_r^2)(C_{36} + C_{45})ia_r - (C_{16} - C_{45}a_r^2)(C_{13} + C_{55})ia_r}{(C_{16} - C_{45}a_r^2)(C_{55} - \rho v^2 - C_{33}a_r^2) - (C_{13} + C_{55})ia_r(C_{36} + C_{45})ia_r} \\
 &= i \frac{(C_{11} - \rho v^2 - C_{55}a_r^2)(C_{36} + C_{45})a_r - (C_{16} - C_{45}a_r^2)(C_{13} + C_{55})a_r}{(C_{16} - C_{45}a_r^2)(C_{55} - \rho v^2 - C_{33}a_r^2) + (C_{13} + C_{55})(C_{36} + C_{45})a_r^2} \\
 &\Rightarrow \text{a purely imaginary number}
 \end{aligned}$$

In this case, set $W_r = iw_r$, here w_r is a real number, but keep V_r unchanged because it is already a real number. Substitute ia_r , V_r , iw_r into Eq. (3.31) to make further derivations.

$$\beta_{1r} = C_{13} + C_{36}V_r + C_{33}(ia_r)(iw_r) = C_{13} + C_{36}V_r - C_{33}a_rw_r \Rightarrow \text{a real number}$$

$$\beta_{2r} = C_{45}(ia_r) + C_{44}(ia_r)V_r + C_{45}(iw_r) = i(C_{45}a_r + C_{44}a_rV_r + C_{45}w_r) \Rightarrow \text{an imag. number}$$

$$\beta_{3r} = C_{55}(ia_r) + C_{45}(ia_r)V_r + C_{55}(iw_r) = i(C_{55}a_r + C_{45}a_rV_r + C_{55}w_r) \Rightarrow \text{an imag. number}$$

For the Property 3, according to the Property 1 and 2, no matter what α_r being a real or purely imaginary number, V_r, β_{1r} are always real numbers for $r = 1, 3, 5$. Thus, B_5 defined in Eq. (3.38) is always a purely imaginary number because of

$$B_5 = 8i [V_1(\beta_{15} - \beta_{13}) + V_3(\beta_{11} - \beta_{15}) + V_5(\beta_{13} - \beta_{11})] = iP_5 \Rightarrow \text{an imag. number}$$

where, P_5 is definitely a real number.

Q.E.D.

Appendix B

Introduction (Français/French)

B.1 Contexte général de la thèse

L'un des enjeux majeurs en ingénierie concerne actuellement la surveillance des dommages structurels en temps réel afin de prévenir les défaillances catastrophiques pouvant survenir à cause de ces dommages. Ce processus est appelé contrôle de la santé des structures (SHM pour “*Structural Health Monitoring*”) et sa mise en oeuvre réussie est susceptible d’apporter non seulement des améliorations considérables en termes de sécurité mais également en termes de coûts de maintenance. Une procédure de SHM classique est généralement composée de cinq étapes [1, 13]:

1. *Détection*: Existe t’il un dommage?
2. *Localisation*: Où est le dommage?
3. *Classification*: De quel type de dommage s’agit-il?
4. *Quantification*: Quelle est la taille du dommage?
5. *Pronostic*: Comment le dommage va t’il évoluer?

Cette thématique de recherche est à l’étude depuis le début des année 1970 et en un demi-siècle, les techniques de SHM ont progressé vers leur maturité en jouant un rôle important dans l’évaluation de l’intégrité et de la durabilité des structures [5]. Grâce à des techniques de SHM efficaces, continues et automatisées, il est en théorie possible d’identifier les dommages structurels à un stade précoce afin d’éviter de nouvelles défaillances, générant ainsi d’énormes avantages économiques et ainsi que la sauvegarde de vies humaines [16].

Parmi tous les types de techniques de SHM existantes, les stratégies basées sur les ondes ultra-

sonores guidées dans les structures minces sont particulièrement efficaces pour surveiller l'état de santé et l'intégrité des structures composites aéronautiques [18]. Ces ondes ultrasonores guidées dans des structures minces ont la particularité de pouvoir se propager sur de relativement grandes distances et peuvent donc couvrir une surface de contrôle importante avec peu d'éléments actifs et en un temps plutôt court. Cet avantage se traduit en pratique par une réduction de la main d'oeuvre et des équipements nécessaires pour effectuer la surveillance de ces structures [19].

Lors du choix des ondes guidées comme outil d'inspection des structures composites aéronautiques, il est en préambule nécessaire de souligner leur aspect multi-modal: à une fréquence d'excitation donnée plusieurs types d'ondes (aussi appelés "*modes*") peuvent se propager simultanément avec des longueurs d'ondes et des vitesses différentes. Trois caractéristiques de ces ondes doivent en particulier être considérées avec attention pour bien comprendre la façon dont elles se propagent dans les matériaux d'intérêt. La première caractéristique est leur comportement dispersif qui décrit l'évolution de la longueur d'onde et de la vitesse des ondes avec les modes de propagation et la fréquence [21]. La seconde caractéristique est due à l'anisotropie inhérente des matériaux composites aéronautiques qui entraîne une dépendance des propriétés des ondes guidées avec leur direction de propagation [4]. La troisième caractéristique est l'atténuation des ondes guidées qui est généralement causée par la viscoélasticité des matériaux composites [83, 84].

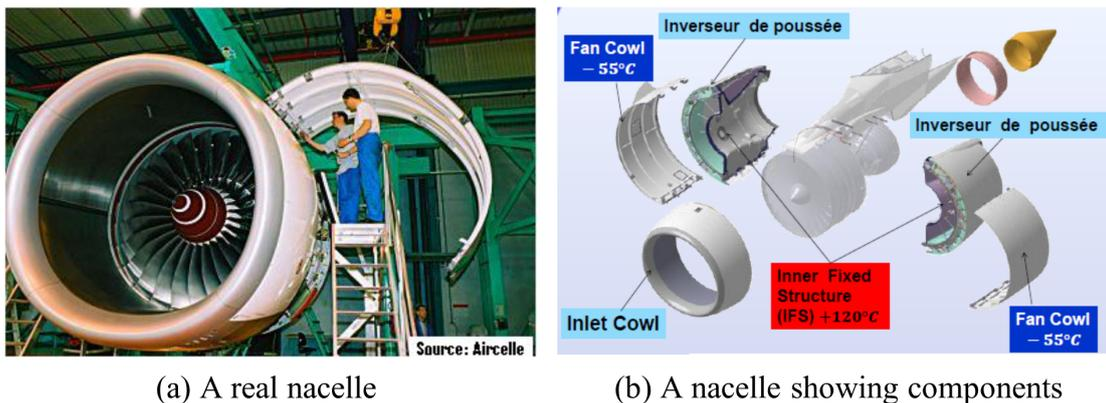


Figure B.1 – Image d'une nacelle d'Airbus A380 [3].

La nacelle d'un Airbus A380 est une structure complexe composée de plusieurs composants réalisés avec des matériaux différents. Les deux composants d'intérêt de la nacelle sont ici la capote de soufflante (FC pour "*Fan Cowl*") et la structure fixe interne (IFS pour "*Inner Fixed Structure*"), comme

indiqué sur la figure B.1(b). Le FC est fabriqué en matériaux composites multicouches (polymères renforcés de fibres de carbone) et est une pièce en contact direct avec l'environnement extérieur et qui est l'objet de nombreuses opérations de manutention. L'IFS est réalisé en matériaux sandwich (peaux composites et coeur en nid d'abeille fait d'alliage d'aluminium) et ses particularités opérationnelles font qu'il est très difficile d'accès et soumis à un fort gradient thermique entre ses faces internes et externes. Ces deux structures constituent donc un exemple applicatif concret pour l'étude des ondes de Lamb. Les matériaux qui composent ces structures présentent de plus un certain degré d'anisotropie et de viscoélasticité ce qui complique le suivi de l'état de santé des nacelles par le biais d'ondes guidées. En conséquence, l'objectif de cette thèse est de mieux comprendre la propagation des ondes guidées dans ces structures aéronautiques composites en étudiant en détail leurs trois caractéristiques majeures mentionnées précédemment: dispersion, atténuation et directivité.

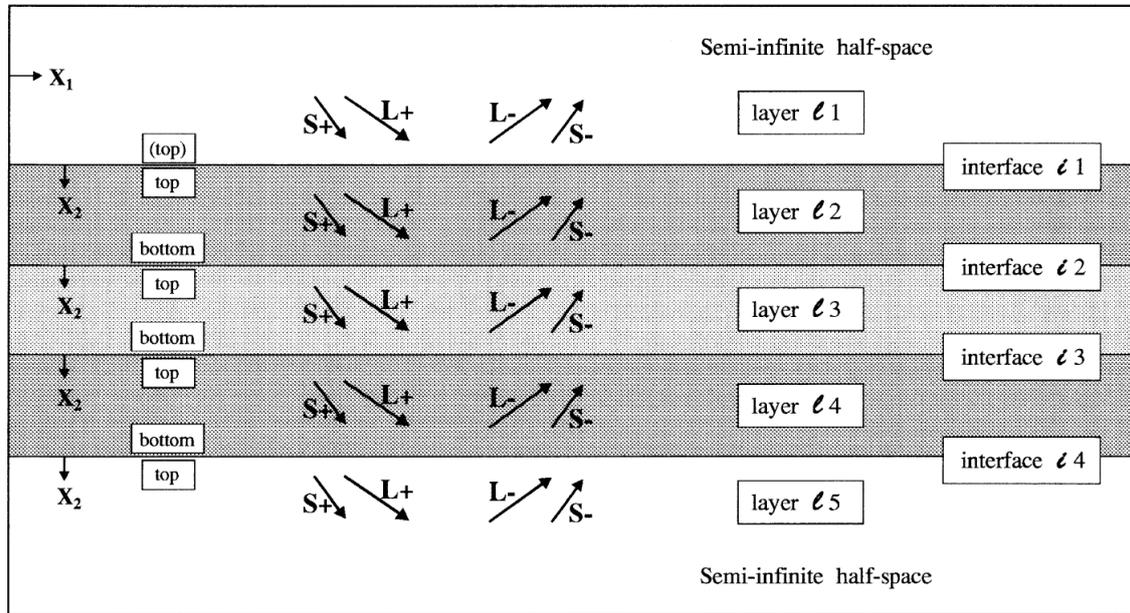
B.2 Etat de l'art

Le calcul précis et efficace des courbes de dispersion associées aux ondes ultrasonores guidées dans des structures minces est un prérequis obligatoire pour concevoir un système SHM de structures composites aéronautiques basé sur ces ondes. C'est en effet l'analyse de ces courbes qui est à la base de la sélection de la fréquence d'excitation appropriée pour l'interrogation et de la conception du réseau optimal de transducteurs piézoélectriques (PZT) (position et taille des éléments PZT) [30, 31]. Cependant, l'anisotropie et l'empilement de plusieurs couches de stratifiés composites compliquent la théorie de la propagation des ondes guidées dans ces structures. Ainsi le modèle isotrope monocouche conventionnel, c'est-à-dire l'équation de Rayleigh-Lamb [26], n'est plus applicable aux stratifiés composites. Au cours des deux dernières décennies, de multiples méthodes ont été développées pour être capable de prédire ces courbes de dispersion. Ces méthodes comprennent des méthodes matricielles, des méthodes d'éléments finis et d'autres méthodes et sont brièvement discutés dans la suite.

B.2.1 Les méthodes matricielles

Les méthodes matricielles sont principalement appliquées aux problèmes multicouches, et elles ont connu un grand développement depuis les années 1950, en allant des avancées théoriques aux applications d'ingénierie. Il existe trois méthodes spécifiques, notamment la méthode de la matrice de transfert (TMM pour "*Transfert Matrix Method*"), la méthode de la matrice globale (GMM pour

“Global Matrix Method”) et la méthode de la matrice de rigidité (SMM pour “Stiffness Matrix Method”).



Example, using three-layer plate with semi-infinite half-spaces.

Figure B.2 – Système d’étiquetage pour plaque multicouche [6].

B.2.1.1 Méthode de la matrice de transfert

Thomson a proposé la première version de la TMM en 1950 pour relier les variables de champ, c’est-à-dire les composantes de contrainte et de déplacement, aux surfaces supérieure et inférieure de la plaque à travers une série de matrices de transfert, qui tient compte simultanément de la continuité des variables de champ aux interfaces des couches adjacentes et les conditions aux limites sans traction aux deux faces extérieures de la plaque. Haskell a par la suite peaufiné la version de Thomson en corrigeant plusieurs petites erreurs [32]. La formulation de Thomson-Haskell a conceptualisé la simplicité de la TMM et a ensuite reçu un nombre important d’applications dans les domaines sismologique et ultrasonore [33]. Mais un défaut majeur de la TMM est le fameux “*problème pour les grands fd* ” qui signifie que pour des grandes valeurs du produit de la fréquence f et de l’épaisseur de la plaque d , les courbes de dispersion obtenues à partir des solutions de l’équation de dispersion construite via la TMM deviennent instables. Ce problème est du à un mauvais conditionnement des matrices de transfert lié à la coexistence de types d’ondes croissantes et décroissantes.

Wang et Yuan ont ajouté une condition de symétrie dans la TMM pour étudier les propriétés

anisotropes des stratifiés composites [37]. Magsoodi et al. ont appliqué la TMM pour prédire les courbes de dispersion de plaques en composite métallique [38]. Une lacune de cette tentative est qu'elle ne peut pas traiter le problème d'incompatibilité entre matrices lorsque la direction de propagation des ondes ne correspond pas à la direction principale des couches composites, mais correspond à la direction principale des couches métalliques en raison de l'isotropie du métal. Nandyala et al. ont proposé une méthode basée sur une matrice de rigidité équivalente (ESM pour "*Equivalent Stiffness Matrix*") pour calculer les courbes de dispersion en considérant un stratifié multicouche comme une seule couche équivalente de façon à améliorer l'efficacité de calcul de la TMM traditionnelle [10]. La méthode ESM est une méthode approximative et ne parvient pas à prédire les courbes de dispersion à des fréquences élevées et pour des modes d'ordre élevés [10].

B.2.1.2 Méthode matricielle globale

La méthode GMM a été proposée à l'origine par Knopoff en 1964 [34]. L'idée principale de la GMM est d'assembler toutes les sous-matrices représentant les conditions de continuité des variables de champ dans chaque couche dans une matrice globale, ainsi que les amplitudes d'onde de toutes les couches à déterminer par les conditions aux limites sans traction. Le principal mérite de la GMM repose sur sa stabilité numérique même pour les grands $f \times d$ mais au prix d'une charge de calcul croissante. Limitée par les faibles capacités de calcul au XXème siècle lorsque l'application était axée sur les composites ayant un nombre massif de couches, la matrice globale implique de travailler sur des matrices de très grandes tailles et donc le problème de la complexité de calcul est inévitable.

Lowe et al. (2003) ont développé le logiciel *Disperse* basé sur la GMM et qui est devenu le pionnier de ces deux dernières décennies [39]. Cependant, certains problèmes existent toujours dans *Disperse* tels que des racines manquantes ou bien la production de valeurs aberrantes pour un mode donné [40]. Pant et al. (2014) ont refondu la GMM conventionnelle basée sur l'élasticité 3D et l'approche de superposition d'ondes partielles [8] pour calculer les courbes de dispersion d'un matériau stratifié fibre-métal. Une lacune de leur méthode est qu'ils n'ont pas résolu techniquement le problème d'incompatibilité des matrices dans les plaques composites métalliques comme mentionné précédemment. Ramasawmy et al. (2020) ont développé une boîte à outils basée sur MATLAB appelées *ElasticMatrix* et basée sur la GMM pour calculer des courbes de dispersion [41]. Cette boîte à outils ne prend cependant en considération que les matériaux isotropes ou transversalement isotropes, et restreint également la

direction de propagation des ondes selon les axes principaux du matériau, ce qui n'est évidemment pas adapté aux matériaux composites aéronautiques anisotropes.

B.2.1.3 Méthode de la matrice de rigidité

Afin de résoudre le *problème des grands $f \times d$* de la TMM, Rokhlin et Wang (2001) ont développé la SMM en refondant la matrice de transfert de chaque couche pour former la matrice de rigidité qui relie le déplacement à la contrainte au haut et bas d'un pli [35, 36]. Ensuite, les conditions de continuité utilisées dans la TMM et la GMM sont transformées en procédure récursive allant de la première à la dernière couche pour produire une matrice de rigidité globale correspondant à la plaque entière. Enfin, la condition aux limites sans traction est appliquée à la matrice de rigidité globale générée précédemment pour obtenir l'équation de dispersion. Il a été prouvé que la SMM est inconditionnellement stable. Un inconvénient de la SMM est cependant sa dégénérescence de la simplicité conceptuelle en comparaison avec les méthodes TMM et GMM.

Kamal et Giurgiutiu (2014) ont combiné la SMM et la TMM pour former la méthode STMM [42]. Dans cette méthode, la SMM peut produire des solutions stables dans une région à nombre d'onde plus élevé et la TMM peut donner des solutions correctes dans une région à nombre d'onde inférieur. Huber et al. (2018) ont adopté la SMM pour calculer les courbes de dispersion de composites anisotropes avec 400 couches et étant un composant de la fusée Ariane 6 [11]. Ce travail a permis le développement d'un logiciel gratuit autonome nommé *Dispersion Calculator* et qui a reçu des mises à jour substantielles par Huber depuis sa création en 2018.

B.2.2 Méthodes basées sur les éléments finis

Une autre voie efficace permettant d'obtenir les équations de dispersion consiste à utiliser des méthodes basées sur les éléments finis (FEM), dont la principale est la méthode éléments finis semi-analytique (SAFE pour "*Semi-analytic Finite Elements*"), qui suppose que le champ de déplacement d'un stratifié peut s'écrire sous deux formes séparées : une section de guide d'onde 1D ou 2D est discrétisée par éléments finis et dans la direction de propagation une fonction harmonique analytique dépendant de la distance et du temps est appliquée [7]. Bénéficiant de la discrétisation flexible de la section, la méthode SAFE présente des avantages évidents pour modéliser la propagation des ondes dans des guides d'ondes de section arbitraire. La méthode de collocation spectrale (SCM) est basée

sur les polynômes de Chebyshev [44] qui allouent des points spectraux dans le sens de l'épaisseur de la plaque pour discrétiser chaque couche d'un stratifié, au lieu d'éléments finis comme proposé par la méthode SAFE. Afin de tirer pleinement parti des logiciels FEM commerciaux tels qu'ANSYS, une méthode d'éléments finis ondulatoires (WFEM pour "*Wave Finite Elements*") a été développée par Mace et Manconi (2008) [46] et Sorohan et al. (2011) [47]. Dans le sens de l'épaisseur, la WFEM discrétise le guide d'onde avec des éléments finis comme SAFE, mais dans le sens de la propagation, seule une longueur nominale, généralement une longueur d'onde, est discrétisée par un élément. Étant donné que la longueur d'onde change avec la fréquence, les éléments dans la direction de propagation doivent être remaillés pour différentes fréquences afin de conserver une précision constante [47], ainsi la WFEM n'est pas aussi flexible que SAFE et SCM.

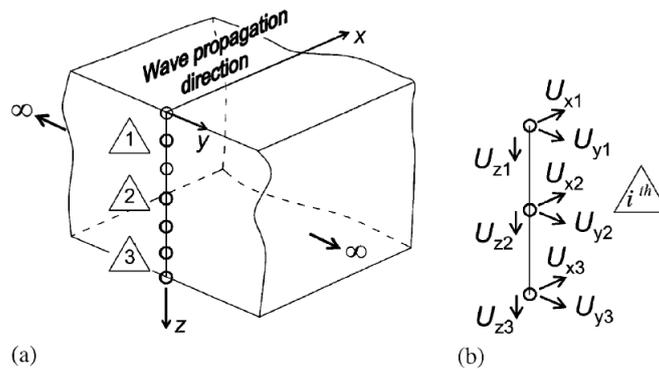


Figure B.3 – Modèle SAFE de propagation des ondes, (a) discrétisation dans le sens de l'épaisseur, (b) élément à trois nœuds et degrés de liberté de chaque nœud [7].

Il convient de préciser ici que l'objet de la thèse est les **méthodes basées sur les matrices** (en particulier les méthodes TMM et GMM) puisque ces méthodes sont basées sur la théorie de l'élasticité 3D linéaire et deviennent proposent ainsi un cadre standard permettant de dériver les équations de dispersion analytiques d'un système de plaques multicouches [40]. La méthode SAFE sera néanmoins adoptée pour la validation.

B.2.3 Autres méthodes

Les méthodes restantes disponibles pour obtenir les équations de dispersion d'un guide d'ondes constitué d'une plaque mince sont en partie basées sur la théorie des plaques d'ordre supérieur (HOPT pour "*High Order Plate Theory*") [48, 49], la méthode de Ritz-Rayleigh [50, 51], les fonctions de Green [52] et la matrice de Green [53]. Bien que la méthode basée sur la HOPT puisse prendre en

considération la déformation de cisaillement d'ordre supérieur des plaques, il s'agit toujours d'une méthode approximative. Le nombre de modes accessibles depuis les méthodes basées sur la HOPT ne peut pas être supérieur à six (trois modes symétriques et trois modes antisymétriques) en raison d'ordres matriciels limités [49]. En outre, concernant les modes d'ordre supérieur, par ex. S2 et A2, ou les fréquences plus élevées, la méthode HOPT peut s'avérer imprécise. Les méthodes basées sur les fonctions de Ritz-Rayleigh et de Green s'avèrent intéressantes concernant la caractérisation des paramètres des matériaux par des ondes acoustiques ultrasonores, et ont conduit à certaines applications pour les métaux austénitiques par exemple [50, 52], mais pas pour les matériaux composites, qui ont été abordés par les méthodes basées sur les fonctions de Green [53].

B.2.4 Atténuation des ondes guidées

Les études liées à l'atténuation sont principalement axées sur les calculs numériques et l'analyse de mesures expérimentales. Dans les structures composites, l'amortissement viscoélastique des matériaux, généralement caractérisé par des modèles d'amortissement hystérétique (HR) ou de Kelvin-Voigt (KV), est le principal facteur d'atténuation [89, 90]. Le modèle d'amortissement de Rayleigh est également adopté pour étudier l'atténuation des ondes [91, 92]. Théoriquement, les coefficients d'atténuation des ondes guidées peuvent être calculés à partir des équations de dispersion (ED) correspondantes. Ainsi, des efforts considérables ont été faits pour dériver des ED étant à valeurs complexes dans les milieux viscoélastiques et pour développer des algorithmes numériques efficaces pour les résoudre. La plus simple est l'équation classique de Rayleigh-Lamb qui représente la propagation des ondes dans une plaque viscoélastique isotrope homogène [75, 93]. L'approche de superposition d'ondes partielles (PWSA) est généralement utilisée pour dériver les ED d'une plaque viscoélastique anisotrope monocouche [72, 94]. Pour un système multicouche, la méthode PWSA est étendue à la TMM [95] et à la GMM [96], qui sont basées sur la théorie de l'élasticité 3D linéaire et deviennent ainsi la manière standard pour dériver les ED analytiques de ce système. Cependant, la résolution de ces équations n'est pas une tâche facile et nécessite d'utiliser la méthode de recherche de racine d'une fonction de deux variables de Lowe [6] ou la méthode de convergence du rapport de module 2D proposée par Zhu-Qian (2D MRCM) [75]. Certaines approches alternatives se basent sur des ED approximées et sont résolues par des algorithmes de recherche de racines efficaces tels que la méthode de Newton-Raphson et la méthode de décomposition des valeurs propres. Les représentants de ces

méthodes sont les approches basées sur les polynômes de Legendre [97, 98, 99] et la théorie des plaques d'ordre supérieur [100, 101, 102]. De plus, les méthodes numériques discrètes sont également largement appliquées pour résoudre le problème des ondes complexes dans les plaques viscoélastiques multicouches en raison de leur mise en œuvre facile. Par exemple, on peut citer la méthode des éléments finis d'ondes (WFEM) utilisant la condition de périodicité de Floquet [103, 66], la méthode de collocation spectrale (SCM) basée sur les polynômes de Chebyshev [44, 80], et la méthode semi-analytique des éléments finis (SAFE) adaptée aux guides d'ondes à section arbitraire [7, 104, 79]. La caractéristique commune de ces méthodes réside dans le fait que la discrétisation n'a lieu que dans le sens de l'épaisseur de la plaque, augmentant ainsi l'efficacité de calcul par rapport à la modélisation par éléments finis 3D traditionnelle.

En plus de l'approche numérique, les coefficients d'atténuation peuvent également être mesurés expérimentalement, mais les travaux expérimentaux sont assez rares par rapport aux avancées théoriques abondantes. L'approche la plus simple consiste à calculer le taux d'atténuation des amplitudes d'ondes entre deux capteurs dans une expérience A-scan [85, 91]. Une méthode plus complète consiste à estimer l'atténuation en ajustant les données expérimentales d'amplitudes d'ondes en fonction des distances de propagation. Cette méthode a le mérite de considérer à la fois l'étalement géométrique et l'amortissement structurel [89, 105]. En outre, deux méthodes d'identification avancées sont également utilisées dans ce contexte, notamment la méthode du crayon matriciel [93] et l'estimation des paramètres du signal via des techniques d'invariance par rotation (ESPRIT) [78]. La caractéristique commune des deux méthodes réside dans le fait qu'elles permettent d'identifier non seulement le coefficient d'atténuation mais également le nombre d'onde se propageant à partir de mesures expérimentales.

B.3 Apport de la thèse

Cette thèse a pour objectif de mieux comprendre les propriétés des ondes guidées se propageant dans les stratifiés composites élastiques et viscoélastiques à travers une dérivation théorique, des illustrations numériques, et une validation expérimentale. L'accent est mis en particulier sur une méthodologie permettant d'établir des équations de dispersion via des méthodes matricielles et sur la résolution efficace et de manière stable de ces équations dans des cas élastiques et viscoélastiques purs. Les contributions de chaque chapitre sont décrites plus précisément dans la suite.

B.3.1 Chapitre 2 - Aspects fondamentaux de la propagation des ondes dans les solides

Dans ce chapitre les équations fondamentales de l'élasticité 3D sont passées en revue, y compris la relation contrainte-déformation, la relation contrainte-déplacement et les équations élastodynamiques du mouvement. Cinq classes de matériaux composites largement utilisés sont présentées via les propriétés de leur matrice de rigidité respective: les matériaux tricliniques $\mathcal{C}_{\mathcal{T}}$, monocliniques $\mathcal{C}_{\mathcal{M}}$, orthotropes $\mathcal{C}_{\mathcal{O}}$, transversalement isotropes $\mathcal{C}_{\mathcal{TI}}$, et isotropes $\mathcal{C}_{\mathcal{I}}$. La rotation de la matrice de rigidité permettant de se placer dans la direction de propagation désirée est obtenue en utilisant la notation Voigt et la règle de rotation du tenseur. Cette rotation engendre un changement de classe de la matrice de rigidité et les caractéristiques de la matrice de rigidité après rotation sont indiquées dans le tableau B.1. Les équations de champs pour les matériaux tricliniques conduisent ensuite à des équations d'ondes de volume dans les solides. Dans ce chapitre, de nombreux concepts sont définis et certaines équations et caractéristiques fondamentales sont présentées. Il établit ainsi la base des chapitres suivants pour l'étude de la propagation des ondes guidées dans les plaques minces composites.

Table B.1 – Caractérisation des matrices de rigidité avant et après rotation

Forme matricielle dans la direction de l'axe principal	Nombre de coefficients indépendants	Forme matricielle hors axe principal
$\mathbf{C}_{\mathcal{T}} \in \mathcal{C}_{\mathcal{T}}$	21	$\mathbf{C}'_{\mathcal{T}} \in \mathcal{C}_{\mathcal{T}}$
$\mathbf{C}_{\mathcal{M}} \in \mathcal{C}_{\mathcal{M}}$	13	$\mathbf{C}'_{\mathcal{M}} \in \mathcal{C}_{\mathcal{M}}$
$\mathbf{C}_{\mathcal{O}} \in \mathcal{C}_{\mathcal{O}}$	9	$\mathbf{C}'_{\mathcal{O}} \in \mathcal{C}_{\mathcal{M}}$
$\mathbf{C}_{\mathcal{TI}} \in \mathcal{C}_{\mathcal{O}}$	5	$\mathbf{C}'_{\mathcal{TI}} \in \mathcal{C}_{\mathcal{M}}$
$\mathbf{C}_{\mathcal{I}} \in \mathcal{C}_{\mathcal{I}} \subseteq \mathcal{C}_{\mathcal{O}}$	2	$\mathbf{C}'_{\mathcal{I}} = \mathbf{C}_{\mathcal{I}} \in \mathcal{C}_{\mathcal{I}} \subseteq \mathcal{C}_{\mathcal{O}}$

B.3.2 Chapitre 3 - Propagation des ondes guidées dans une plaque monocouche

Dans ce chapitre, l'approche par superposition d'ondes partielles (PWSA) est introduite pour modéliser la propagation d'ondes guidées dans une plaque composite monocouche. La condition aux limites sans traction et la condition de symétrie sont utilisées pour dériver les équations de dispersion correspondantes. Dans les matériaux orthotropes, transversalement isotropes et isotropes, les ondes guidées sont découplées en ondes de Lamb et SH (qui désignent les ondes de cisaillement ou "*shear waves*" en anglais), alors que dans les matériaux tricliniques et monocliniques, les deux types d'ondes sont couplés l'un à l'autre. L'équation classique de Rayleigh-Lamb est également redémontrée en utilisant la PWSA qui sert d'alternative à la méthode de décomposition de Helmholtz.

B.3.3 Chapitre 4 - Propagation des ondes guidées dans une plaque multicouche : méthode de la matrice de transfert

La PWSA est ensuite étendue à la TMM pour étudier les propriétés des ondes guidées se propageant dans un stratifié composite multicouche. Cette approche combine la condition aux limites sans traction et la condition de continuité parfaite. La règle de transfert est utilisée pour relier les variables de champ entre les couches adjacentes du matériau stratifié et la matrice de transfert de monodromie de l'ensemble de la plaque est obtenue. En s'appuyant sur les résultats obtenus dans le cas monocouche, trois cas possibles pour les ondes guidées sont à envisager: soit les ondes Lamb et SH sont couplées dans toutes les couches, soit les ondes de Lamb et SH sont découplées dans chaque couche, ou alors il faut considérer le cas hybride où dans certaines couches du stratifié les deux types d'ondes sont couplés l'un à l'autre mais dans d'autres couches ils sont découplés. Le cas hybride existe généralement dans les plaques composites quasi-isotropes et les plaques composites métalliques pour lequel les couches métalliques sont isotropes mais les lames composites sont anisotropes comme indiqué dans le tableau B.2. La TMM standard peut traiter les cas couplés et découplés, mais pour le cas hybride, une méthode hybride originale (nommée HMS pour "*Hybrid Matrix Strategy*") est proposée pour résoudre le problème d'incompatibilité de la matrice de transfert locale entre deux couches ne présentant pas les mêmes propriétés de couplage entre les différents types d'ondes. Trois exemples numériques sont utilisés pour illustrer les trois types de couplage d'ondes guidées. Chaque exemple correspond à une classe de plaques composites usuelle, c'est-à-dire un stratifié croisé, un stratifié quasi-isotrope et un stratifié métal-composite. Pour les exemples de stratifiés quasi-isotropes et composites métalliques, les courbes de dispersion calculées via la HMS sont comparées à des points de données expérimentaux extraits d'une référence classique, validant ainsi l'efficacité de la HMS.

B.3.4 Chapitre 5 - Propagation des ondes guidées dans une plaque multicouche : méthode matricielle globale

Pour résoudre le problème d'efficacité de calcul de la GMM standard, une méthode GMM optimisée est proposée dans ce chapitre. Elle tire simultanément parti de la matrice globale induite par les conditions de symétrie, du calcul parallèle, et des techniques basées sur les matrices creuses. Cette GMM a prouvé sa stabilité dans un test de référence basé sur le jeu de données Open Guided Waves (voir Figure B.4(a)). Ce test illustre les problèmes rencontrés par la TMM pour les grandes valeurs du

B.3. APPORT DE LA THÈSE

Table B.2 – Classes de stratifiés composites et la dépendance du type d’onde à l’angle de propagation.

Classe de stratifié	Angles d’empilage	Angle de propagation θ	Cas couplé	Cas découplé	Cas hybride
Unidirectionnel ¹	$[0]_8$	$\theta \in \{0^\circ, 90^\circ\}$		✓	
		$\theta \notin \{0^\circ, 90^\circ\}$	✓		
Plis croisés	$[(0/90)_s]_2$	$\theta \in \{0^\circ, 90^\circ\}$		✓	
		$\theta \notin \{0^\circ, 90^\circ\}$	✓		
Quasi-isotrope	$[0/90/+45/-45]_s$	$\theta \in \{0^\circ, 45^\circ, 90^\circ, -45^\circ\}$			✓
		$\theta \notin \{0^\circ, 45^\circ, 90^\circ, -45^\circ\}$	✓		
Composite métallique	$[Al/0/90/Al/90/0/Al]_2$	$\theta \in \{0^\circ, 90^\circ\}$		✓	
		$\theta \notin \{0^\circ, 90^\circ\}$			✓

¹ Remarque relative à la classe des stratifiés unidirectionnels : étant donné que les variables de champ (déplacement et contrainte) sont considérées comme continues à travers l’interface des couches adjacentes (la condition d’interface parfaite est supposée), le stratifié unidirectionnel $[0]_8$ est mathématiquement équivalent à la plaque monocouche $[0]_1$ ayant la même épaisseur que la plaque $[0]_8$.

² Al désigne la couche d’aluminium qui est un matériau isotrope.

produit $f \times d$ (voir Figure B.4(b)). Ainsi, lorsque les courbes de dispersion d’un stratifié composite à des valeurs de fréquence plus élevées sont recherchées, l’utilisation de la GMM pour réaliser le calcul est nécessaire. Le bon accord entre les résultats produits par la GMM et les données expérimentales de la base de donnée Open Guided Waves valide l’efficacité et la faisabilité de la GMM optimisée proposée ici (voir Figure B.5).

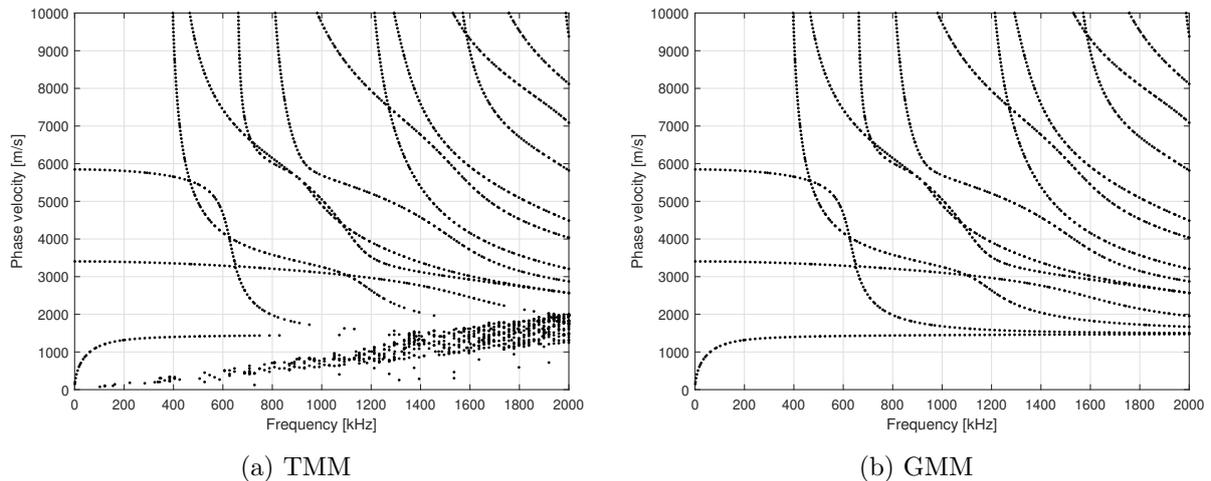


Figure B.4 – Courbes de dispersion pour le cas d’étude *Open Guided Waves* pour un angle de propagation $\theta = 0^\circ$ calculées via la TMM et la GMM.

La méthode GMM optimisée est ensuite appliquée avec succès à une plaque composite aéronautique ayant 400 couches, ce qui est le plus grand nombre de couches rapportées jusqu’à présent, pour calculer

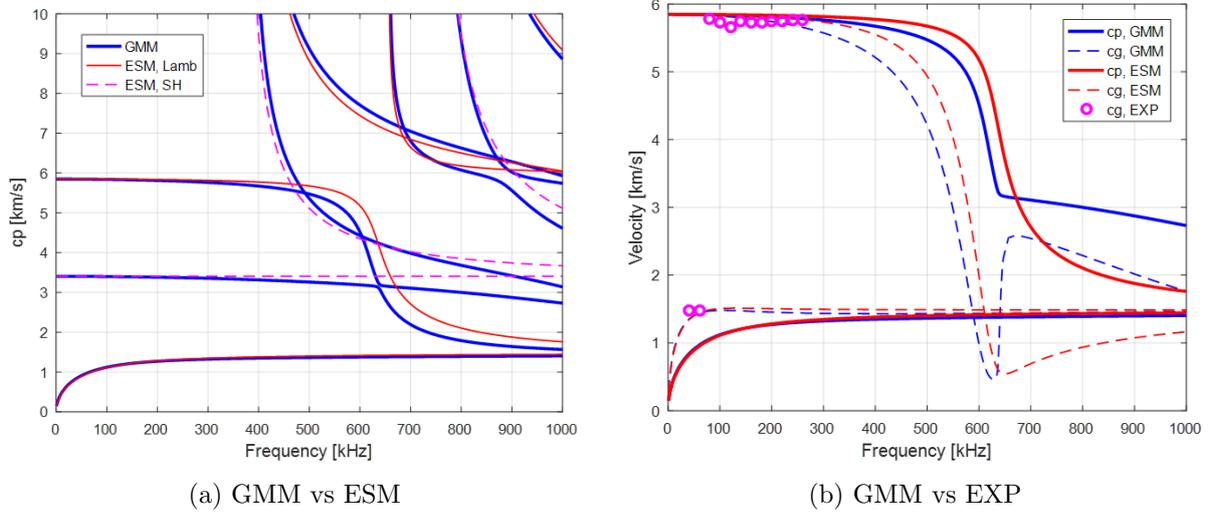


Figure B.5 – Courbes de dispersion des ondes guidées ouvertes à l’angle de propagation $\theta = 0^\circ$ calculées via GMM et ESM.

ses courbes de dispersion. Cette structure est un composant des enceintes de suppression de la fusée Ariane 6 en cours de développement. En raison de la complexité de cette structure, les courbes de dispersion subissent un fort effet de déviation dans une petite région ce qui génère des problèmes lors du tracé des courbes de dispersion (voir Figure B.6). Pour étudier cet effet, la forme modale et la valeur MAC (pour “*Modal Assurance Criterion*”) du déplacement et de la contrainte sont analysées dans les régions où se manifeste l’effet de déviation (voir la Figure B.7 pour la forme modale de déplacement et la Figure B.8 pour les valeurs MAC). Les résultats de ces analyses montrent qu’au sein de ces régions, les solutions de dispersion appartenant au même type de symétrie peuvent être arbitrairement proches mais ne jamais se croiser. Ce processus s’accompagne d’un échange rapide de leurs formes modales. En comparaison avec les formes de mode de contraintes, les formes de mode de déplacements constituent un indicateur plus fiable pour distinguer les branches du diagramme de dispersion dans les régions où cet effet de déviation est observé. La méthode GMM optimisée permet de terminer les calculs de la plaque à 400 couches en une demi-heure sur un poste de travail standard (voir Table B.3). Cela change une idée reçue selon laquelle la GMM ne peut pas être appliquée à des stratifiés ayant un grand nombre de couches et prouve la capacité de la GMM optimisée à être utilisée pour des matériaux composites aérospatiaux qui possèdent généralement de nombreuses couches.

B.3. APPORT DE LA THÈSE

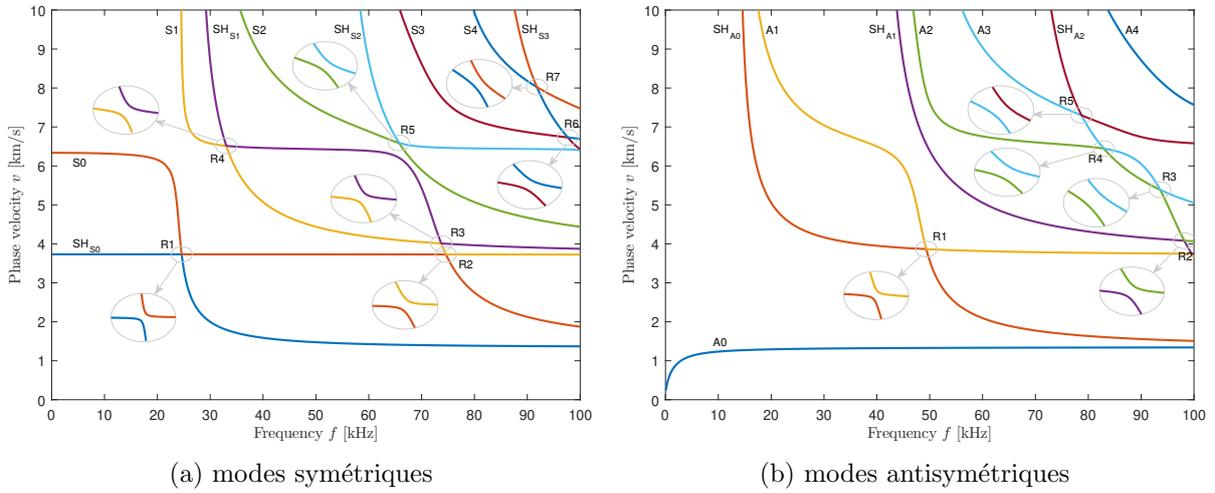


Figure B.6 – Courbes de dispersion du stratifié aérospatial à 400 couches dans la direction $\theta = 0^\circ$.

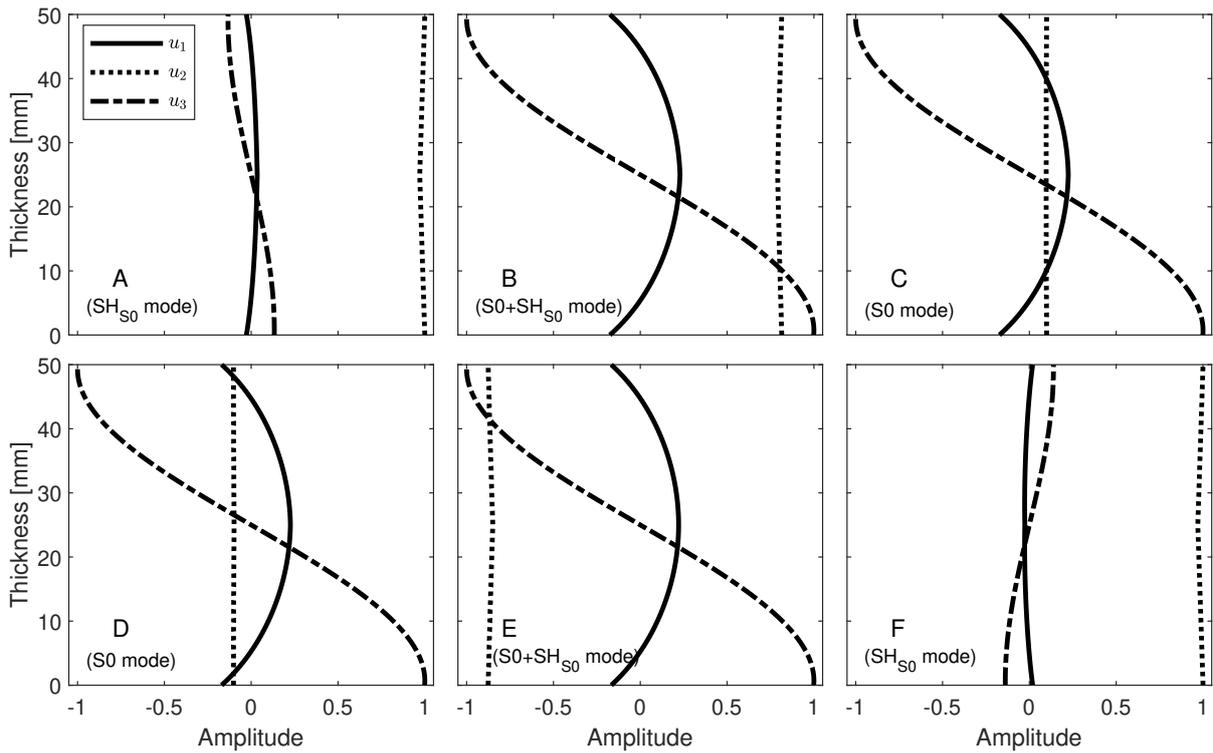


Figure B.7 – Formes de mode de déplacement.

B.3.5 Chapitre 6 - Propriété de dichotomie de l'équation de dispersion des ondes guidées se propageant dans des plaques composites anisotropes

Il est mathématiquement démontré dans ce chapitre que les équations de dispersion construites avec la PWSA pour une plaque monocouche et avec la TMM et la GMM pour un système de plaque

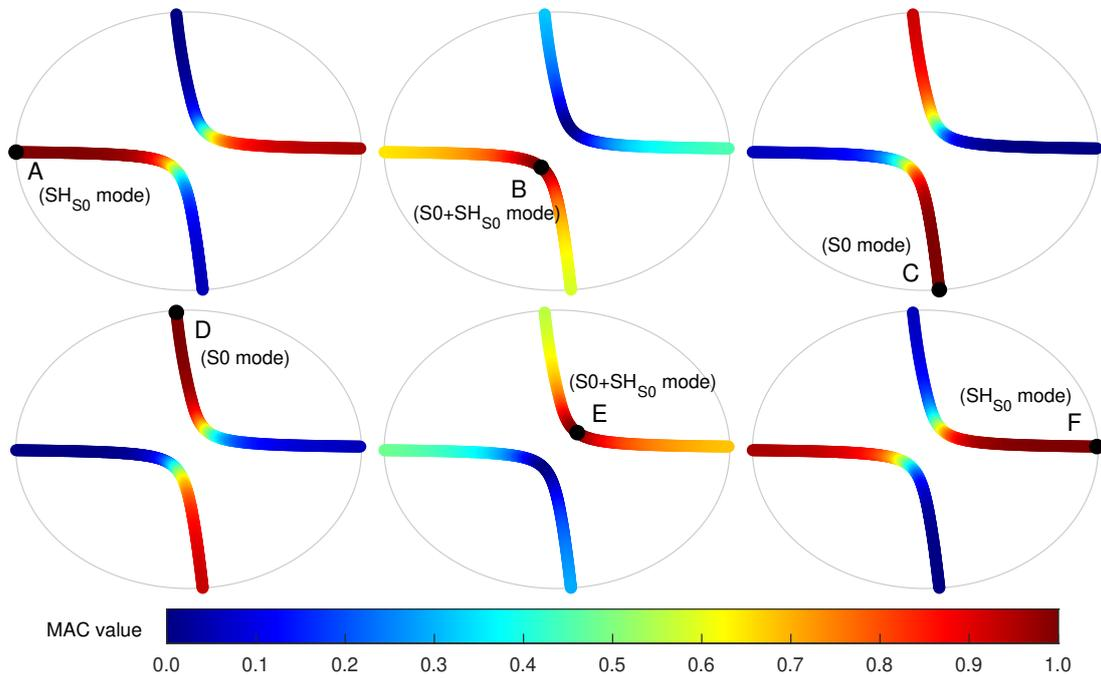


Figure B.8 – Tomographie à valeur MAC des formes de mode de déplacement dans la région R1 des modes symétriques.

Table B.3 – Le temps de calcul du stratifié à 400 couches en utilisant le GMM optimisé (unité : secondes)

Méthode de bisection			Méthode de changement de phase		
sweep v	sweep f	sum	sweep v	sweep f	sum
899 ^s	462 ^s	1361 ^s	871 ^s	469 ^s	1340 ^s
780 ^a	454 ^a	1234 ^a	752 ^a	453 ^a	1205 ^a

^s Le temps de calcul correspond aux modes symétriques.

^a Le temps de calcul correspond aux modes antisymétriques.

multicouches possèdent une propriété de dichotomie dans le cas de matériaux élastiques purs. Cette propriété induit que ces équations a priori à valeurs complexes se réduisent à des équations à valeurs réelles ou imaginaires pures, en fonction du comportement de certains paramètres intermédiaires. Cette propriété est vraie pour les matériaux composites (à l'exception de quelques cas particuliers) et pour les ondes propagatives et évanescentes. Pour une plaque monocouche, la propriété de dichotomie peut être analysée via une stratégie d'énumération qui suit l'évolution de certains paramètres intermédiaires. Pour le système de plaques multicouches, une stratégie d'échantillonnage simple est proposée pour évaluer numériquement la propriété de dichotomie. Les deux stratégies sont résumées dans la

B.3. APPORT DE LA THÈSE

Figure B.9.

Cette propriété est extrêmement utile pour surmonter les instabilités numériques rencontrées lors du processus d'obtention des équations de dispersion. Le cas des grands produits $f \times d$ rencontré par la TMM est exploré quantitativement en utilisant la propriété de dichotomie. L'analyse montre que le problème des grands produits $f \times d$ rencontré par la TMM est causé par un mauvais conditionnement de la matrice de transfert de monodromie (voir la Figure B.10).

	Cases	$\mathcal{D}_a(v, \xi) = 0$	$\mathcal{D}_s(v, \xi) = 0$	
A single-layered monoclinic lamina for $\mathcal{D}_a(v, \xi) = 0$ or $\mathcal{D}_s(v, \xi) = 0$ (enumeration strategy) ↓ know-why	case 1 and 3	$\begin{cases} \mathcal{D}_a^R(v, \xi) \equiv 0 \\ \mathcal{D}_a^I(v, \xi) = 0 \end{cases}$	$\begin{cases} \mathcal{D}_s^R(v, \xi) = 0 \\ \mathcal{D}_s^I(v, \xi) \equiv 0 \end{cases}$	
	case 2 and 4	$\begin{cases} \mathcal{D}_a^R(v, \xi) = 0 \\ \mathcal{D}_a^I(v, \xi) \equiv 0 \end{cases}$	$\begin{cases} \mathcal{D}_s^R(v, \xi) \equiv 0 \\ \mathcal{D}_s^I(v, \xi) = 0 \end{cases}$	
For any case, make sampling and comparison				
A single- or multi-layered laminate for $\mathcal{D}_X(v, \xi) = 0$ (sampling strategy) ↓ know-how	$M^R = \max_{1 \leq i \leq m} \mathcal{D}_X^R(v_0, \xi_i) $	If $M^R \ll M^I$, $\begin{cases} \mathcal{D}_X^R(v, \xi) \equiv 0 \\ \mathcal{D}_X^I(v, \xi) = 0 \end{cases}$		
	$M^I = \max_{1 \leq i \leq m} \mathcal{D}_X^I(v_0, \xi_i) $ for $\xi_i \in [\xi_{\min}, \xi_{\max}]$	If $M^R \gg M^I$, $\begin{cases} \mathcal{D}_X^R(v, \xi) = 0 \\ \mathcal{D}_X^I(v, \xi) \equiv 0 \end{cases}$		

	Effective part	Bisection method	Phase change method
Sweep ξ	$\mathcal{D}_X^I(v_0, \xi) = 0$	★★★ ⁽¹⁾	★★★ ⁽¹⁾
at $v = v_0$	$\mathcal{D}_X^R(v_0, \xi) = 0$	★★★ ⁽¹⁾	★★★ ^(1,3)
Sweep v	$\mathcal{D}_X^I(v, \xi_0) = 0$	★ ⁽²⁾	★ ⁽²⁾
at $\xi = \xi_0$	$\mathcal{D}_X^R(v, \xi_0) = 0$	★ ⁽²⁾	★ ^(2,3)

Comments on the numerical labels:

- (1) The intermediate parameters keep constants for a fixed v_0 , which maximizes the computational efficiency of both methods.
- (2) The intermediate parameters are computed repeatedly for different v , which slows down the computational efficiency of both methods.
- (3) Phase correction measure should be taken to avoid numerical instability.

(a)

(b)

Figure B.9 – (a) Stratégie à adopter pour déterminer la propriété de dichotomie de l'équation de dispersion. (b) Efficacité de calcul des méthodes de résolution basées sur la propriété de dichotomie.

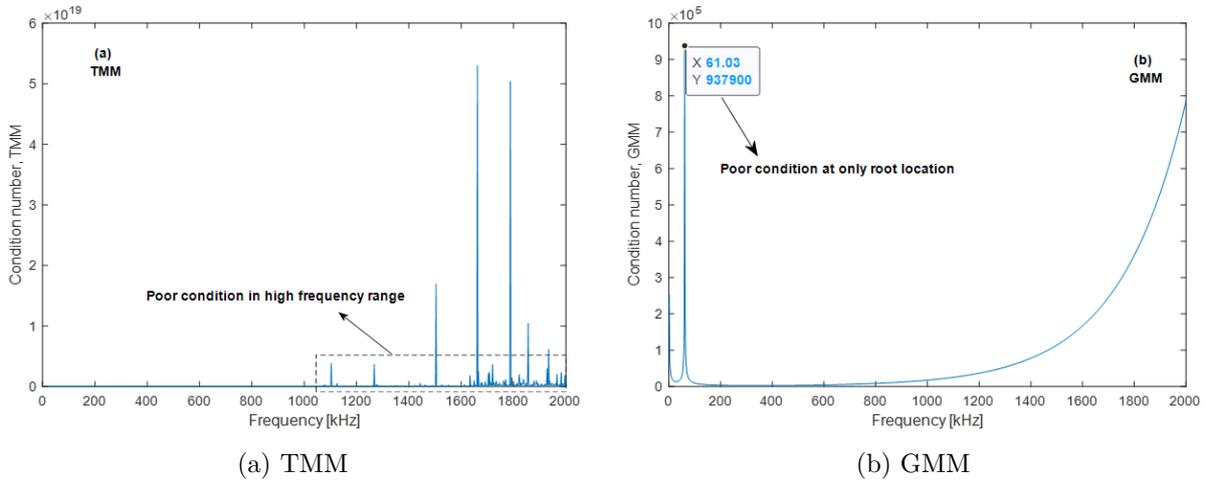


Figure B.10 – Le nombre de conditionnement des matrices pour le cas Open Guided Waves à $v_0 = 1000$ m/s pour (a) la matrice de transfert de monodromie \mathbf{T}^{mono} (méthode TMM) et (b) la matrice globale \mathbf{D}_G (méthode GMM).

B.3.6 Chapitre 7 - Prédiction de l'atténuation des ondes guidées se propageant dans les stratifiés composites viscoélastiques anisotropes en fonction de la fréquence et de la direction de propagation

Compte tenu de la viscoélasticité inhérente des matériaux composites, l'effet d'amortissement des ondes guidées est étudié dans ce chapitre en se basant sur les équations de dispersion. Trois modèles d'amortissement présentés dans les Eqs. B.1, B.2, et B.3 (modèles Hystérétique, de Kelvin-Voigt, et de Biot) sont intégrés au sein de la méthode GMM standard pour en former une version étendue: la GMM amortie (dGMM pour "*damped GMM*"). Dans le cas viscoélastique, les équations de dispersion à valeurs complexes construites avec la dGMM produisent des paires de solutions combinant une fréquence réelle et un nombre d'onde complexe. Les coefficients d'atténuation des ondes guidées peuvent être extraits de la partie imaginaire du nombre d'onde complexe. En raison de la complexité du cas viscoélastique, la résolution de l'équation de dispersion transcendantale multivariée est mathématiquement impossible à traiter. Pour résoudre ce problème, une approche de recherche de racine en deux étapes est proposée sur la base des solutions produites par la GMM non amortie, de la méthode de convergence du rapport de module 2D (MRCM 2D) et d'une technique de tracé de courbes (voir Figure B.11). Avec cette approche, les courbes de dispersion 3D dans le domaine des nombres d'onde complexes et en considérant des fréquences réelles peuvent être calculées. La méthode SAFE classique est adoptée pour valider l'efficacité de la méthodologie proposée.

$$E^* = E(1 - i\gamma_{HR}) \quad \text{HR model} \quad (\text{B.1})$$

$$E^*(\omega) = E \left(1 - i\gamma_{KV} \frac{\omega}{\omega_0} \right) \quad \text{KV model} \quad (\text{B.2})$$

$$E^*(\omega) = E \left[1 + \frac{2}{\pi} \gamma_{BT} \ln \sqrt{1 + \left(\frac{\omega}{\epsilon} \right)^2} - i \frac{2}{\pi} \gamma_{BT} \arctan \left(\frac{\omega}{\epsilon} \right) \right] \quad \text{BT model} \quad (\text{B.3})$$

En plus de l'approche numérique, une méthode d'identification expérimentale des coefficients d'atténuation est proposée en se basant sur une technique de régression linéaire. Avec cette méthode, les coefficients d'atténuation sont identifiés expérimentalement à partir de signaux mesurés sur l'IFS et le Fan Cowl. Considérant que les paramètres viscoélastiques des modèles d'amortissement ne sont généralement pas disponibles dans la pratique, un processus de recalage du modèle est adopté pour

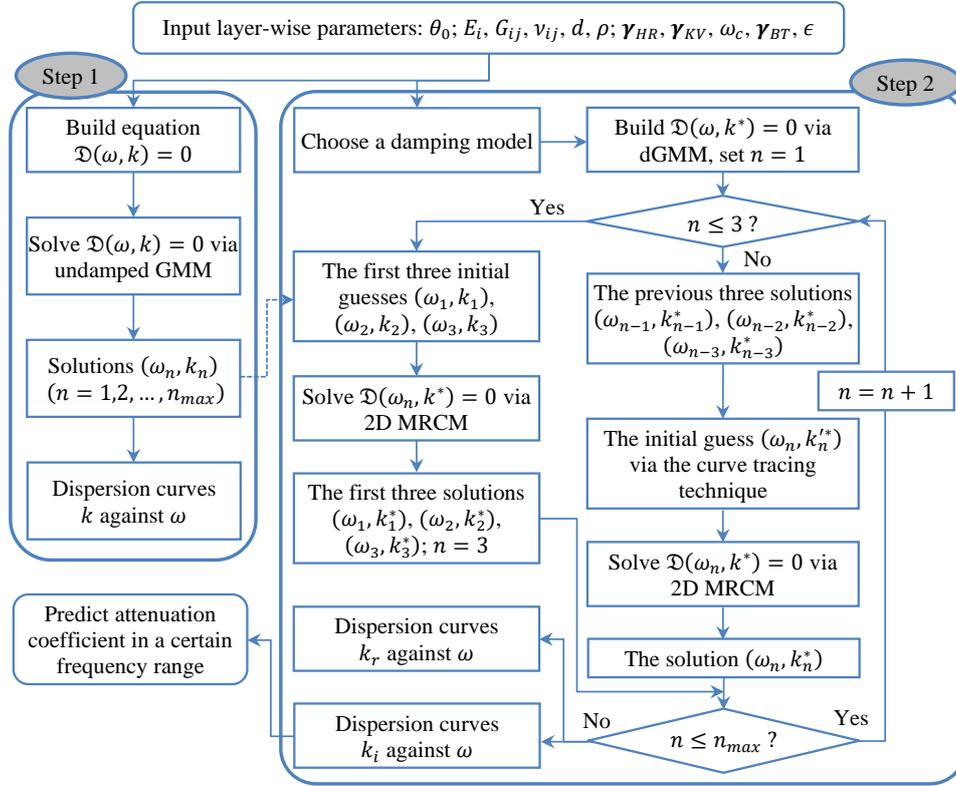


Figure B.11 – L’organigramme de l’algorithme dGMM en deux étapes pour résoudre le DE complexe.

estimer ces paramètres au sens des moindres carrés. Les coefficients d’atténuation identifiés expérimentalement avec la dGMM permettent d’obtenir un bon accord entre le calcul théorique et l’identification expérimentale (voir l’Eq. (B.4)).

$$\hat{\gamma} = \arg \min_{\gamma} \sum_{l=1}^m [\mathcal{K}(\gamma, \omega_l) - \hat{k}_{i,l}]^2 \quad (\text{B.4})$$

où, la paire de solutions $(\omega_l, \hat{k}_{i,l})_{l=1,\dots,m}$ correspond aux coefficients d’atténuation identifiés expérimentalement à différentes fréquences, et $\hat{\gamma}$ aux facteurs de perte estimés pour un certain modèle d’amortissement.

L’ensemble du cadre développé dans la thèse est enfin appliqué à deux structures issues de l’ingénierie aéronautique. Ces deux structures sont des composants de l’avion A380 qui sont physiquement assez différentes l’une de l’autre. Pour chaque structure, des données expérimentales correspondant à un cas où la structure est montée sur un A380 d’essai et à un cas où la structure n’est pas montée sont analysés. La première structure est le capot de soufflante (FCS pour “*Fan Cowl Structure*”) ayant des

propriétés quasi-isotropes (voir Figure B.12) et la seconde structure est une structure interne fixe (IFS pour “*Inner Fixed Structure*”) de type sandwich (voir Figure B.13).

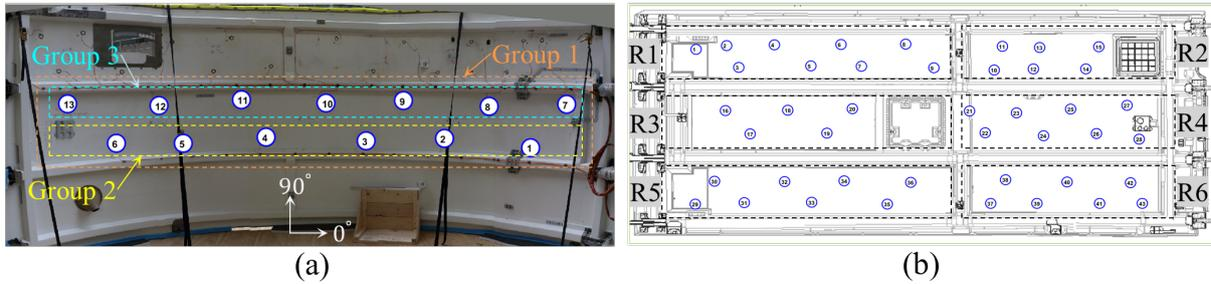


Figure B.12 – Le réseau de PZT pour le FCS: (a) le cas ou la structure n’est pas montée sur l’A380 et (b) le cas ou la structure est montée sur un A380 instrumenté.

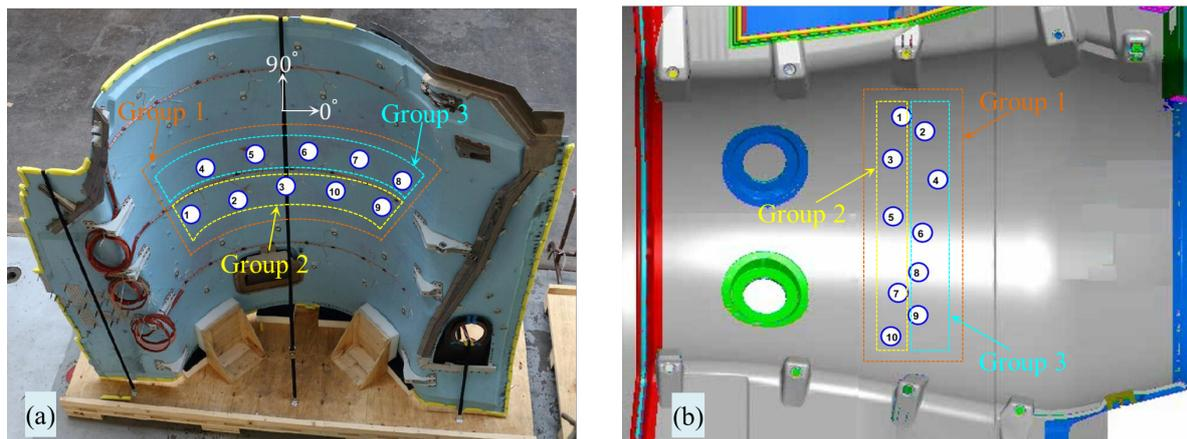


Figure B.13 – Le réseau de PZTs pour l’IFS: (a) le cas ou la structure n’est pas montée sur l’A380 et (b) le cas ou la structure est montée sur un A380 instrumenté.

L’analyse montre que le FCS est une structure légèrement amortie et que l’IFS est une structure beaucoup plus fortement amortie. Les cas ou les structures sont montées présentent des propriétés d’atténuation assez différentes des cas ou les structures ne sont pas montées. Deux combinaisons de modèles d’amortissement (HR + BT et KV + BT) sont utilisées pour considérer la caractéristique inhomogène de l’IFS. Avec cette approche, la couche centrale en aluminium et les couches de peau en carbone époxy sont modélisées par deux modèles d’amortissement différents. Ces deux études de cas démontrent également que les coefficients d’atténuation présentent un important degré d’anisotropie malgré les couches d’empilement quasi-isotropes et que le mode A0 subit beaucoup plus d’atténuation que le mode S0 (voir Figure B.14). Ainsi, dans l’optique du déploiement ultérieur de stratégies de

B.4. CONCLUSION

SHM pour des structures similaires, la sélection du mode S0 est souhaitée afin d'assurer une couverture spatiale suffisante de la structure à surveiller.

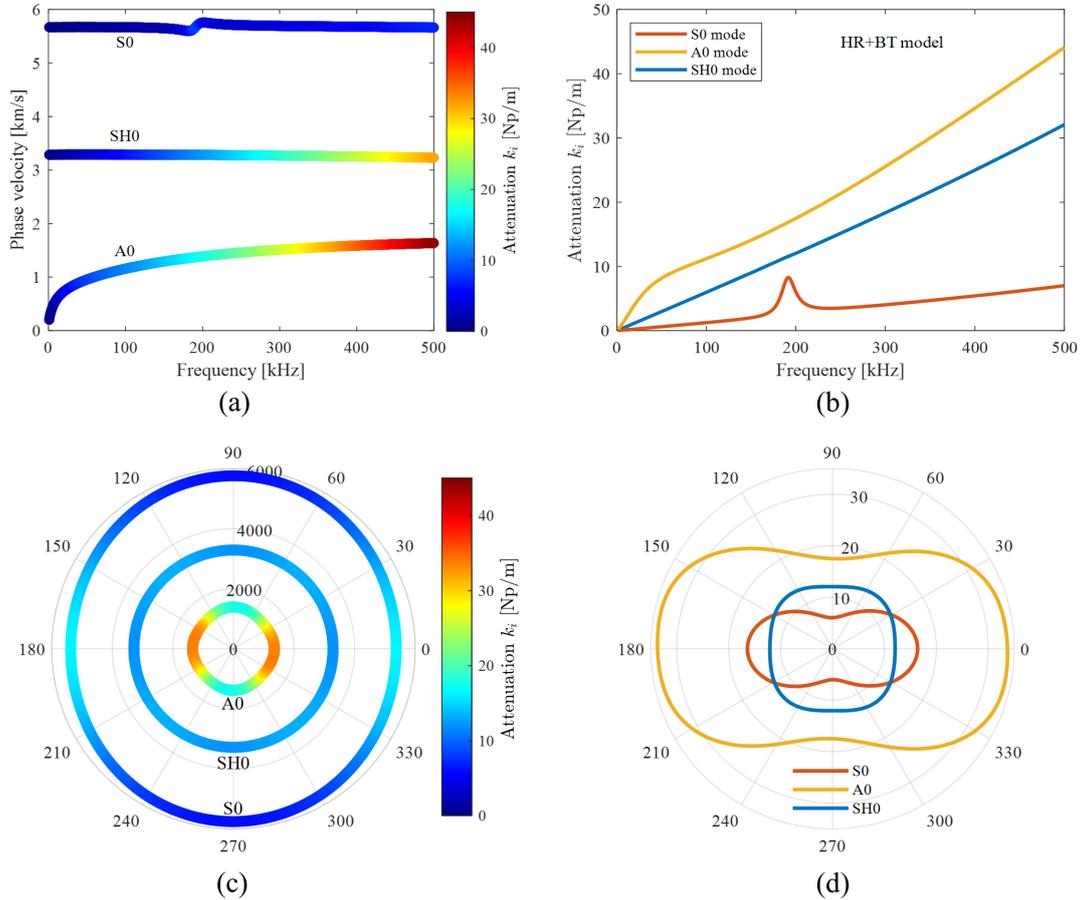


Figure B.14 – Prédiction du modèle HR + BT pour l'IFS non monté: (a) courbe de dispersion de la vitesse de phase à $\theta = 90^\circ$, (b) courbe de dispersion du coefficient d'atténuation à $\theta = 90^\circ$, (c) tracé polaire de la vitesse de phase [m/s] à $f = 200$ kHz, (d) tracé polaire du coefficient d'atténuation [Np/m] à $f = 200$ kHz.

B.4 Conclusion

En résumé, l'utilisation des données réelles et en service des structures aéronautiques réelles pour valider la méthode de prédiction d'atténuation proposée n'est pas une tâche facile mais la rend extrêmement précieuse pour les communautés académiques et industrielles. En ce sens, cette thèse contribue à combler le fossé entre la recherche et le déploiement industriel des technologies de SHM [54].

Résumé : Les plaques composites anisotropes constituées de matériaux composites viscoélastiques sont de plus en plus utilisées dans l'industrie aéronautique et les stratégies basées sur les ondes guidées apparaissent comme un outil très prometteur pour surveiller leur état de santé. Dans ce contexte, ce travail est dédié à l'étude de la propagation et de l'atténuation des ondes guidées dans de telles plaques composites. Les équations classiques des ondes guidées se propageant dans une plaque élastique monocouche sont d'abord passées en revue sur la base de la théorie de l'élasticité tridimensionnelle (3D) et constituent le fondement de l'approche par superposition d'ondes partielles (PWSA). Dans la littérature, cette approche a été étendue à la méthode des matrices de transfert (TMM) et à la méthode des matrices globales (GMM) permettant d'exprimer les caractéristiques de propagation des ondes dans les plaques composites élastiques. En raison de l'anisotropie, des problèmes d'incompatibilité matricielle sont rencontrés lors du traitement de plaques composites arbitrairement orientées pour la TMM et la GMM. Une stratégie originale basée sur des matrices hybrides (HMS) est proposée pour pallier ce problème. Il est en outre démontré que les équations de dispersion construites avec PWSA pour une plaque monocouche et avec TMM et GMM pour un système de plaques multicouches possèdent une propriété de dichotomie dans le cas de matériaux élastiques purs. Cette propriété indique que ces équations a priori à valeurs complexes se réduisent en fait à des équations à valeurs réelles ou imaginaires pures, en fonction du comportement de certains paramètres intermédiaires. Cette propriété est extrêmement utile pour surmonter les instabilités numériques rencontrées au cours du processus de résolution des équations. Le cas élastique est ensuite étendu au cas viscoélastique en introduisant des modèles d'amortissement viscoélastiques (modèles d'hystérésis, de Kelvin-Voigt et de Biot) dans le comportement dynamique des matériaux composites. Ceci forme une méthode appelée « damped GMM » (dGMM) proposé ici pour traiter les plaques composites constituées de matériaux composites viscoélastiques anisotropes orientés arbitrairement. Deux études de cas industrielles, une structure de capot de soufflante (FCS) et une structure fixe intérieure (IFS), toutes deux composantes d'une nacelle d'A380, sont utilisées pour valider expérimentalement la méthode dGMM en comparant la précision des prédictions par dGMM en termes de vitesses et d'atténuation aux mesures expérimentales.

Mots clés : Surveillance de la santé structurelle, Ondes guidées, Matériaux composites aéronautiques et aérospatiaux, Anisotropie, Élasticité et viscoélasticité, Stratifié composite, Approche de superposition d'ondes partielles, Méthode de matrice de transfert, Méthode de matrice globale, Stratégie de matrice hybride, Propriété de dichotomie, Modèles d'amortissement, Équations de dispersion et courbes, Composant de nacelle A380.

Abstract : Anisotropic composite plates made up of viscoelastic composite materials are increasingly used in aeronautic industry and structural health monitoring strategies based on guided waves appear as a very promising tool to monitor their health state. In that context, this work is dedicated to the study of guided waves propagation and attenuation in such composite plates. Classical equations of guided waves propagating in a single layer elastic plate are first reviewed based on the three-dimensional (3D) elasticity theory and form the foundation of the partial wave superposition approach (PWSA). In the literature, this approach has been extended to the transfer matrix method (TMM) and global matrix method (GMM) allowing to express the wave propagation characteristics in elastic composite plates. Due to anisotropy, matrix incompatibility issues are encountered when dealing with arbitrarily orientated composite plates for TMM and GMM. An original hybrid matrix strategy (HMS) is proposed to alleviate this issue. It is furthermore demonstrated that dispersion equations built with PWSA for a single layer plate and with TMM and GMM for a multi-layered plate system possess a dichotomy property in the case of pure elastic materials. This property states that these a priori complex-valued equations collapse to pure real or imaginary valued equations, depending on the behavior of some intermediate parameters. This is extremely helpful for overcoming numerical instabilities encountered during the equation solving process. The elastic case is then extended to the viscoelastic case by introducing viscoelastic damping models (Hysteretic, Kelvin-Voigt and Biot models) in composite materials dynamical behavior. This forms the damped GMM (dGMM) proposed here to deal with composite plates made up of arbitrarily orientated anisotropic viscoelastic composite materials. Two industrial case studies, a fan cowl structure (FCS) and an inner fixed structure (IFS) both which are components of an A380 nacelle, are employed to experimentally validate the dGMM by comparing the accuracy of dGMM predictions in terms of velocities and attenuation to experimental measurements.

Keywords : Structural health monitoring, Guided waves, Aeronautic and aerospace composite materials, Anisotropy, Elasticity and viscoelasticity, Composite laminate, Partial wave superposition approach, Transfer matrix method, Global matrix method, Hybrid matrix strategy, Dichotomy property, Damping models, Dispersion equations and curves, Component of A380 nacelle.